Investigating the role of fast-spiking interneurons in neocortical dynamics

Christoforos A. Papasavvas

Thesis submitted for the degree of
Doctor of Philosophy

Institute of Neuroscience
Newcastle University
October 2016

Abstract

Fast-spiking interneurons are the largest interneuronal population in neocortex. It is well documented that this population is crucial in many functions of the neocortex by subserving all aspects of neural computation, like gain control, and by enabling dynamic phenomena, like the generation of high frequency oscillations. Fast-spiking interneurons, which represent mainly the parvalbumin-expressing, soma-targeting basket cells, are also implicated in pathological dynamics, like the propagation of seizures or the impaired coordination of activity in schizophrenia. In the present thesis, I investigate the role of fast-spiking interneurons in such dynamic phenomena by using computational and experimental techniques.

First, I introduce a neural mass model of the neocortical microcircuit featuring divisive inhibition, a gain control mechanism, which is thought to be delivered mainly by the soma-targeting interneurons. Its dynamics were analysed at the onset of chaos and during the phenomena of entrainment and long-range synchronization. It is demonstrated that the mechanism of divisive inhibition reduces the sensitivity of the network to parameter changes and enhances the stability and flexibility of oscillations.

Next, *in vitro* electrophysiology was used to investigate the propagation of activity in the network of electrically coupled fast-spiking interneurons. Experimental evidence suggests that these interneurons and their gap junctions are involved in the propagation of seizures. Using multi-electrode array recordings and optogenetics, I investigated the possibility of such propagating activity under the conditions of raised extracellular K^+ concentration which applies during seizures. Propagated activity was recorded and the involvement of gap junctions was confirmed by pharmacological manipulations.

Finally, the interaction between two oscillations was investigated. Two oscillations with

different frequencies were induced in cortical slices by directly activating the pyramidal cells using optogenetics. Their interaction suggested the possibility of a coincidence detection mechanism at the circuit level. Pharmacological manipulations were used to explore the role of the inhibitory interneurons during this phenomenon. The results, however, showed that the observed phenomenon was not a result of synaptic activity. Nevertheless, the experiments provided some insights about the excitability of the tissue through scattered light while using optogenetics.

This investigation provides new insights into the role of fast-spiking interneurons in the neocortex. In particular, it is suggested that the gain control mechanism is important for the physiological oscillatory dynamics of the network and that the gap junctions between these interneurons can potentially contribute to the inhibitory restraint during a seizure.

Acknowledgements

First, I would like to thank my two supervisors, Prof Marcus Kaiser and Dr Andrew Trevelyan, for their guidance and support during the three years of the project. Having both of them jointly supervising my project was very beneficial for the development of my interdisciplinary approach in research. Working with Marcus gave me the opportunity to explore different computational approaches and develop my own ideas while learning how to be highly productive. Working with Andy introduced me to the experimental techniques while expanding my knowledge through insightful and intellectually stimulating discussions.

My great appreciation goes to all the members across both labs who provided an educational and supportive environment to work in. I also cherish all the fun moments that we shared during lab meetings and social events. Namely, I want to thank Dr Claudia Racca, Dr Ryley Parrish, Dr Yujiang Wang, Dr Peter Taylor, Dr Rolando Berlinguer-Palmini, Dr Roman Bauer, Dr Sol Lim, Dr Hannah Alfonsa, Dr Edward Merricks, Dr Partow Yazdani, Dr Richard Tomsett, Dr Emily Johnson, Dr Jochen Spanke, Neela Codadu, Eike Joest, Michael Mackay, Frances Hutchings, Chris Thornton, and Emma Craddock. I also want to thank other members of the institute for their support: Prof Jenny Read, Prof Adrian Rees, Prof Mark Cunningham, Dr Andrew Jackson, Dr Fiona LeBeau, and Dr Llwyd Orton. Very special thanks to Neela, Hannah, Ryley, and Rolando who helped me immensely during my long training in experimental techniques. They showed remarkable patience with me, especially during the beginning while I was overwhelmed by all the different aspects of electrophysiological experimentation. Thanks to Eike for the insightful discussions and for showing me how to use the patterned illuminator which proved to be very useful. I also want to thank Yujiang, Sol, and Peter who stood by me as friends and also taught

me many useful things in modelling, analysis, and publishing. Special thanks to my dearest friend Sol with whom I enjoyed fine films at Newcastle's independent cinema.

I would also like to acknowledge the support from the Wellcome Trust. Their studentship was very generous covering fully my PhD studies but also the transitional master's degree that preceded. Their generous support gave me the chance to focus on my research without worrying about my finances. I also appreciate their commitment to enable people like me, from physical, engineering, or mathematical backgrounds, to engage in biomedical research.

Finally, I want to thank my parents for their multifaceted support, especially during the first half of my overall ten-year studies. I appreciate their hard work that enabled me to initiate my studies in the first place. I also thank all my Greek-speaking friends in Newcastle who provided the chance to express myself in my mother language. Special thanks to Dimitris, Dimitra, Harris, and Marialena: I cherish your friendship and all the joyful gatherings we had throughout the years.

Contents

List of Tables

List of Figures

Chapter 1

General Introduction

1.1 Neocortex

Neocortex, or isocortex, is the most recent evolutionary expansion of the cerebral cortex in the mammalian brain (Rakic (2009); Lui *et al.* (2011)). It differentiates from its predecessor, the allocortex, based on a more complex structure. It was introduced in the evolutionary history of the brain during the transition from the Triassic period to the Jurassic period (Rakic (2009)). It emerged in small mammals as a uniform sheet of radially deployed neurons organized in layers with the number of layers varying (5 or 6) depending on the area and the animal (Rakic (2009)). It gradually underwent a regionalization that gave rise to distinct cortical areas with most of them having a specific functional role (Lui *et al.* (2011)). In general, the specialized areas include areas that either process sensory information (visual, auditory, somatosensory) or control the movement of limbs or associate multimodal information to deliver more complex processes (Shepherd (2003)). The evolutionary expansion of neocortex and the formation of specialized areas are considered to underlie every aspect of complex behaviour and cognitive abilities in mammals (Lui *et al.* (2011)).

The organization and connectivity between neocortical layers varies from area to area and from species to species. However, some typical features found in mammalian primary sensory areas are described below (Thomson and Bannister (2003)). The neocortical layers are numbered starting from the most superficial (layer I) to the

deepest (layer VI). They are distinguished between the internal granular layer IV, the supragranular layers I-III which are more superficial and the infragranular layers V-VI which are deeper. The primary functional role of the internal granular layer is to receive afferent input from the thalamus and other cortical areas and feed to other layers, mostly to supragranular layers (Thomson and Bannister (2003); Shepherd (2003)). This is more pronounced in sensory areas which receive major thalamic input (Shepherd (2003)). Supragranular layers receive afferent local connections from layer IV and afferent cortico-cortical connections (Thomson and Bannister (2003)). Layer III is a major source of excitatory connections to other cortical areas and also to infragranular layers (mainly layer V) (Thomson and Bannister (2003)). The infragranular layer V is highly and reciprocally connected with the other layers and it projects efferent connections to subcortical regions like basal ganglia, spinal cord, superior colliculus or the pons depending on the specific cortical area (Wang and McCormick (1993); Thomson and Bannister (2003)). Similarly, layer VI projects to subcortical areas but preferentially to thalamic nuclei (Jones (2001)).

The horizontal organization of the layers is interwoven with a vertical organization of connected neurons, pyramidal and interneurons. This vertically connected group of neurons form a cortical column which is a repeated anatomical structure with diameter ranging from 0.3 to 0.6 mm and spanning across all six layers (Mountcastle (1997)). Despite the initial evidence of its functional significance in somatosensory cortex (Mountcastle (1957); Powell and Mountcastle (1959)), the idea that its functional purpose can be generalized in the whole neocortex was challenged (Horton and Adams (2005)). While the number of neurons in rat neocortex reaches approximately 2 x 10^7, each column has approximately 7500 neurons (Ren *et al.* (1992)). The distribution of these cells across the different layers is as follows: only 1.33% in layer I, 28.67% in layers II/III, 20% in layer IV, 16.67% in layer V and 33.33% in layer VI (Ren *et al.* (1992); Markram *et al.* (2004)). Note the very low number of neurons found in layer I which is mostly populated with glia and extended dendritic and axonal structures that originate from other layers (Shepherd (2003)). The majority of these neurons (approx. 80%) are excitatory pyramidal neurons while the rest are either inhibitory or excitatory interneurons (Markram *et al.* (2004); Shepherd (2003)).

1.2 Neocortical interneurons

Interneurons constitute a minority in the neocortex representing only 10-20% of the neurons while the rest of them are pyramidal cells (White (1989); Markram *et al.* (2004)). The majority of interneurons are inhibitory, using GABA as their neurotransmitter, but notable exemptions are spiny stellate cells and peptidergic interneurons which are glutamatergic (White (1989); Markram *et al.* (2004)). Despite the fact that GABAergic interneurons are less numerous than the excitatory principal neurons, they completely underlie the regulation of spontaneous and evoked cortical activity (for a review, see Isaacson and Scanziani (2011)). Through the plasticity of their synapses, they can provide a homeostatic mechanism that re-balances excitation and inhibition in the network for optimal functionality (Froemke *et al.* (2007); Vogels *et al.* (2011, 2013)). Furthermore, evidence suggests that inhibitory interneurons provide a set of mechanisms that prevent pathological network dynamics such as the hyperexcitability during seizures (for a review, see Trevelyan (2016)). There are many different subclasses of inhibitory interneurons but they have some common features that distinguish them from pyramidal neurons. First, their dendrites are smooth, that is, without spines (Peters and Jones (1984); White (1989)). Second, their somata can receive both excitatory and inhibitory synaptic inputs (Peters and Jones (1984)). Third, their projections are local, either limited inside their cortical column or reaching laterally other columns (Peters and Jones (1984)) with some exceptions of long-range inhibitory cells connecting distant neocortical areas (reviewed in Caputi *et al.* (2013)). Fourth, they are selective in their synaptic targeting with their axon terminals targeting specific subdomains of postsynaptic cells (dendrite, soma, or axon) (Somogyi *et al.* (1998)).

The population of inhibitory interneurons is highly diverse and can be sub-classified in many different subpopulations. Interneuronal subpopulations or classes are characterized by different morphological, electrophysiological, molecular and synaptic properties (Peters and Jones (1984); White (1989); Markram *et al.* (2004); Tremblay *et al.* (2016)). Despite the fact that some morphological classes tend to have specific electrophysiological, molecular or synaptic properties, there is no clear mapping between the different classes and their properties (Markram *et al.* (2004); Tremblay

et al. (2016)). This ambiguity makes the distinction between the subpopulations not a trivial task (Markram *et al.* (2004)). There was a major effort on finding a consensus on the classification of GABAergic interneurons but the result was a set of general guidelines about their most characteristic features (Ascoli *et al.* (2008)). Future advancements in molecular, immunocytochemical and electrophysiological techniques along with better quantitative metrics are expected to help towards a consensus among researchers (Ascoli *et al.* (2008)).

1.2.1 Morphological classification

Interneurons are morphologically classified partly based on their anatomical structure but also on their domain-targeting tendencies (Markram *et al.* (2004); Tremblay *et al.* (2016)). They are classified into: basket cells which are soma- and peri-somatic targeting cells, Martinotti or Cajal Retzius cells which target distant dendrites or tufts, Chandelier cells which are axon-targeting cells, and double bouquet, bipolar, neurogliaform, or bitufted cells which are dendrite-targeting cells (Markram *et al.* (2004)). The morphological classes of interneurons are summarized in Fig. 1.1.

Basket cells are the most numerous inhibitory interneurons (40-50%), specialized on targeting the soma of their targets (Tremblay *et al.* (2016); Markram *et al.* (2004)). They feature diverse dendritic and axonal morphologies but their dendrites are mostly multipolar and their axons have high degree of branching (Kubota (2014); Tremblay *et al.* (2016)). Depending on their dendritic and axonal morphologies, they can be divided into large basket cells (Kisvarday *et al.* (1993)), small basket cells (Kisvarday *et al.* (1985)) and nest basket cells (Wang *et al.* (2002)). Large basket cells have sparse but expansive axonal arborisations typically reaching to neighbouring or distant columns (Kisvarday *et al.* (1993)). They represent the main source for lateral inhibition and disinhibition in neocortex (Kisvarday *et al.* (1993); Markram *et al.* (2004)). Small basket cells have more dense axonal arborisations which are usually limited in their column (Kisvarday *et al.* (1985)). Their somato-dendritic morphology is variable depending mainly on their layer (Markram *et al.* (2004)). Small basket cells is the only subclass of basket cells that express vasoactive intestinal peptide (VIP), along with the expression of cholecystokinin (CCK) (Markram *et al.* (2004); Tremblay *et al.* (2016)).

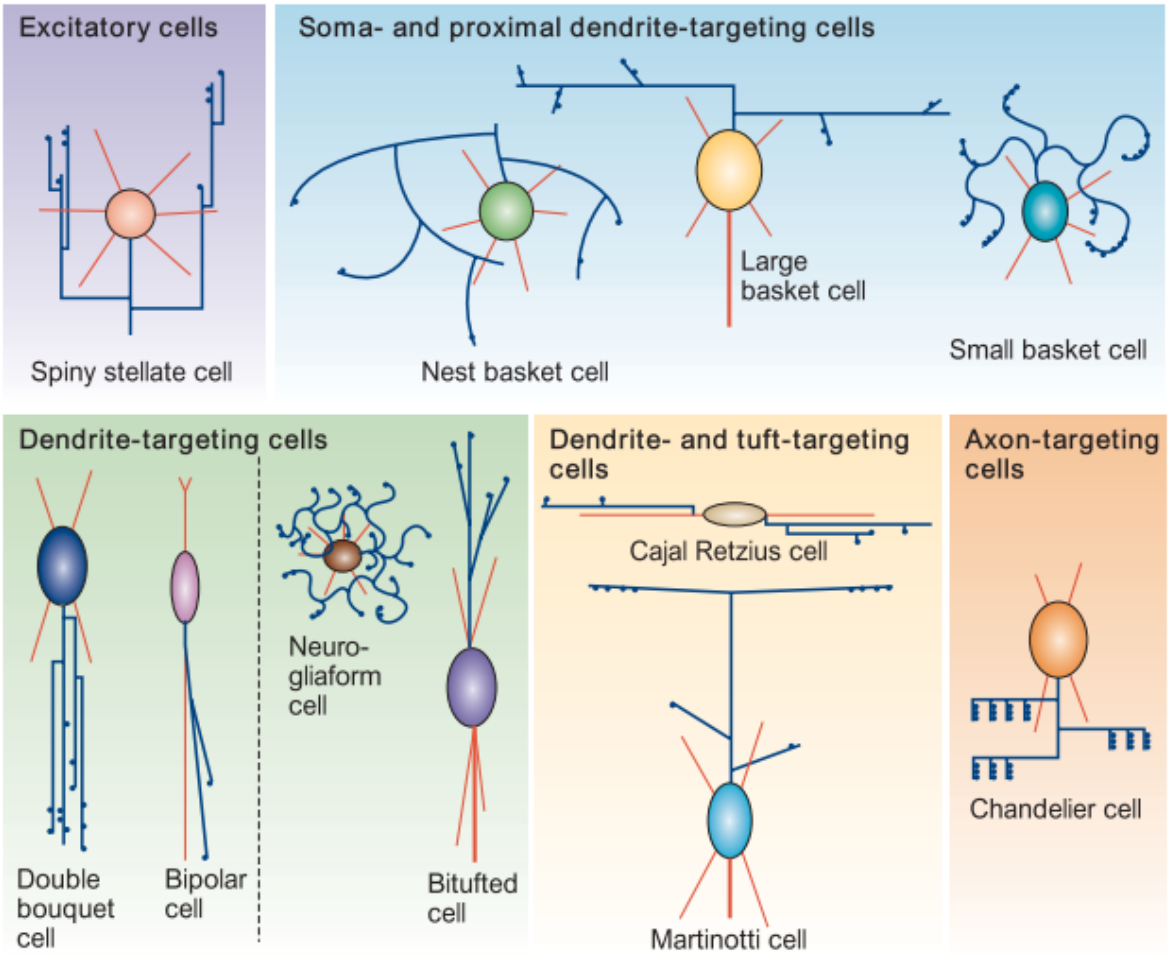

Figure 1.1: Morphological classification of neocortical interneurons. With the exception of spiny stellate cells, all the other interneuronal classes summarized here are inhibitory. Interneurons are morphologically classified based on their dendritic structure (red) and the structure of their axonal arbour (blue). They are also distinguished by their selective targeting of specific domains (dendrite, soma, axon) on their targets. Figure reproduced from Markram *et al.* (2004).

Nest basket cells have more irregular arborisations (Wang *et al.* (2002)). They can be thought as a hybrid between large and small basket cells because their morphological characteristics are a trade-off between those (Markram *et al.* (2004)). They characteristically express the calcium-binding proteins parvalbumin (PV) and calbindin (CB) and various neuropeptides (Markram *et al.* (2004)).

Chandelier cells target the axons of pyramidal cells and specifically the axon initial segments (Kawaguchi and Kubota (1997); Kubota (2014)). The term axo-axonic cells is also used to refer to their specific targeting. With this targeting they are able to intervene and alter the response of a neuron overriding any dendritic integration or gain modulation that was applied (Zhu *et al.* (2004)). Each one can inhibit a cluster of

hundreds of pyramidal cells (Blazquez-Llorca *et al.* (2014); Tremblay *et al.* (2016)). Despite their GABAergic nature, their effect can be excitatory due to the physiological properties of the axon initial segment (Szabadics *et al.* (2006)). They are located mostly in layers II, V, and VI while they are more numerous in frontal than sensory areas (Taniguchi *et al.* (2013); Tremblay *et al.* (2016)). Their axon terminals form vertical rows of boutons giving a chandelier-like appearance (DeFelipe *et al.* (1989); Markram *et al.* (2004)). They typically express CB and PV (DeFelipe *et al.* (1989)) but, unlike basket cells, they do not express neuropeptides like CCK or VIP (Markram *et al.* (2004)).

Martinotti cells, despite their tendency to target dendrites and tufts, were found to innervate through local arborisation peri-somatic domains as well (Kubota (2014); Ma *et al.* (2006); Xu *et al.* (2013); Wang *et al.* (2004)). Their dendrites are either bipolar or multipolar while featuring long ascending axons (Ma *et al.* (2006); Xu *et al.* (2013); Tremblay *et al.* (2016)). They are numerous and spread across layers II-VI but they are most abundant in infragranular layers (Markram *et al.* (2004); Xu *et al.* (2010)). Their targeting is also spread across multiple layers but they are specialized in targeting the tufts of pyramidal cells in layer I (Markram *et al.* (2004); Kubota (2014)). Their axons can expand in layer I and innervate laterally distant columns (Wang *et al.* (2004)). They always express the neuropeptide somatostatin (SOM) but, unlike basket cells or chandelier cells, they never express PV or VIP (Markram *et al.* (2004); Tremblay *et al.* (2016)).

Cajal Retzius cells are also dendrite- and tuft-targeting cells but they are morphologically and functionally distinct from Martinotti cells (Markram *et al.* (2004)). They are only found in layer I and also their axons are confined in the same layer. They provide lateral inhibition across columns by targeting the tufts of pyramidal cells (Anstötz *et al.* (2014)). They are thought to play an important role during development by controlling developmental processes (Marín-Padilla (1998)). There is evidence suggesting their critical role in the formation of the cortical column but after post-natal day 7 they undergo selective cell death and disappear in mice (Anstötz *et al.* (2014)).

Bipolar cells are characterised by a narrow bipolar dendritic structure in most cases

but sometimes it can be bitufted instead (Peters (1990); Prönneke *et al.* (2015); Caputi *et al.* (2009); Cauli *et al.* (2014)). Their somata are small and spindle- or oval-shaped (Peters (1990); Prönneke *et al.* (2015); Caputi *et al.* (2009); Cauli *et al.* (2014)). They are found in layers II-IV but preferentially in layers II/III and their targets are mainly in layers I and VI (Peters (1990); Markram *et al.* (2004); Tremblay *et al.* (2016)). They feature low density of boutons and consequently they have contacts with comparatively few other cells (Peters (1990); Markram *et al.* (2004)). They always express both calretinin (CR) and VIP and in the case of excitatory bipolar cells, VIP is also used a neurotransmitter (Markram *et al.* (2004)). Inhibitory bipolar cells, on the other hand, release GABA instead (Markram *et al.* (2004)).

Double bouquet cells have ovoid somata, a characteristic bitufted dendritic structure and an axon that forms a tight bundle of fibres resembling a horse-tail (DeFelipe *et al.* (1990, 2006)). This axonal structure extends to all layers featuring high density of boutons and targets the pyramidal cells at their basal dendrites (DeFelipe *et al.* (1990, 2006)). They are preferentially located in layers II/III but they are found in layers IV-V as well (Markram *et al.* (2004)). They characteristically express CR and CB simultaneously and sometimes VIP or CCK (Markram *et al.* (2004)).

Bitufted cells have ovoid somata like the bipolar and double bouquet cells (Somogyi *et al.* (1998); Markram *et al.* (2004)). While their dendritic structure is typically bitufted, their axonal structure is characteristically much wider and it can span horizontally the whole cortical column (Markram *et al.* (2004)). Its vertical span, though, is much less extensive reaching the neighbouring layers at most (Markram *et al.* (2004)). They are found in layers II-VI and they express all the common calcium-binding proteins and neuropeptides found in interneurons except PV (Somogyi *et al.* (1998); Markram *et al.* (2004)).

Neurogliaform cells are small cells with numerous short, smooth and rarely branched dendrites radiating around the soma forming a spherical dendritic structure (Overstreet-Wadiche and McBain (2015)). They have a highly branched and intertwined axonal structure with very thin terminals densely packed with boutons (Markram *et al.* (2004)). Their specific targeting was recently challenged by the finding that their synaptic boutons are significantly further away from the targeted dendritic

domain (Oláh *et al.* (2009)). This observation, along with evidence of their highly dense axon terminals, suggest a more target-independent, and cloud-like, inhibitory application mediated by $GABA_A$ and $GABA_B$ (Oláh *et al.* (2009); Overstreet-Wadiche and McBain (2015)). Expression of reelin and neuropeptide Y (NPY) is common among neurogliaform cells whereas neuronal nitric oxide synthase is expressed in a subset of them (Overstreet-Wadiche and McBain (2015)).

1.2.2 Molecular classification

The above classification is primarily based on morphological features; electrophysiological, molecular and synaptic properties can be mapped onto those classes (Markram *et al.* (2004); Tremblay *et al.* (2016)). This strategy was very successful in the classification of hippocampal interneurons because of the simpler laminar architecture of the hippocampus (Somogyi and Klausberger (2005); Klausberger and Somogyi (2008)). However, the architecture of neocortex is much more complex and the ambiguities of morphological features render this classification impractical (Tremblay *et al.* (2016)). An alternative classification strategy is based on molecular markers instead. GABAergic interneurons can be classified in three classes: those expressing PV (∼40%), those expressing SOM (∼30%) and those expressing the ionotropic serotonin receptor 5HT3a (5HT3aR) (∼30%) (Tremblay *et al.* (2016)). These three markers are rarely co-expressed while they represent almost all of the GAD-67 expressing neurons in somatosensory cortex (Lee *et al.* (2010)). A schematic of these classification and the main characteristics of each class is shown in Fig. 1.2.

PV^+ interneurons include the majority of basket cells, which target the soma and peri-somatic domains, and the axon-targeting chandelier cells (DeFelipe *et al.* (1989); Tremblay *et al.* (2016)). The PV^+ basket cells include only those that have a fast spiking firing pattern (see below). SOM^+ cells are also split into two subgroups based on their morphology: Martinotti and non-Martinotti cells (Kubota (2014); Tremblay *et al.* (2016)). Non-Martinotti cells are SOM^+ interneurons lacking the functionally significant characteristic of Martinotti cells: the axonal plexus in layer I (Tremblay *et al.* (2016)). The $5HT3aR^+$ interneurons are again divided into two subgroups based on the expression of the neuropeptide VIP. VIP^+ cells include the majority of bipolar,

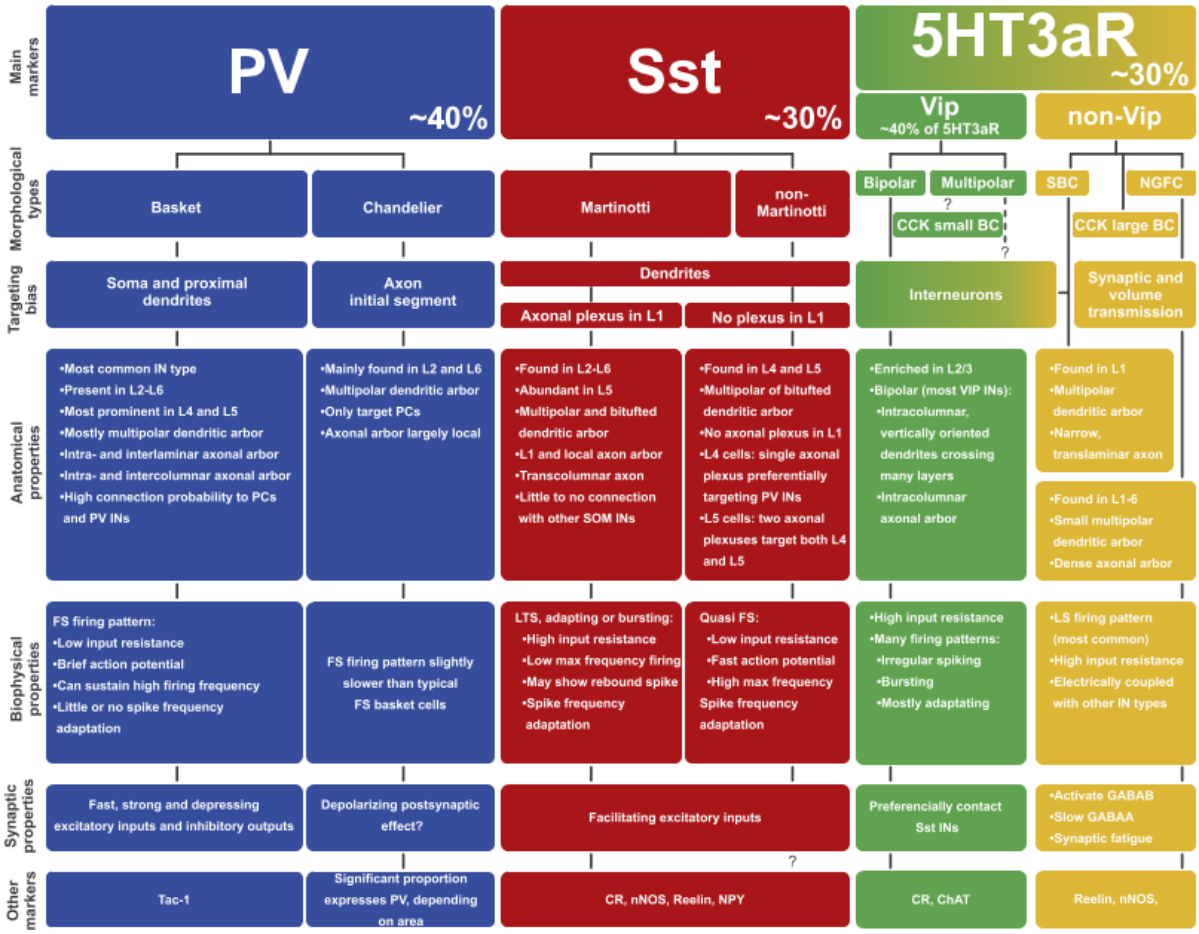

Figure 1.2: Interneuronal classification based on molecular markers. Almost all interneurons can be classified in three classes based on three molecular markers: parvalbumin (PV), somatostatin (Sst or SOM), and 5HT3aR. The co-expression of these markers is very limited (Lee *et al.* (2010)). Figure reproduced from Tremblay *et al.* (2016).

double-bouquet and bitufted cells as described above as well as the CCK-expressing small basket cells (Peters (1990); Prönneke *et al.* (2015); Tremblay *et al.* (2016)). VIP-negative cells include neurogliaform cells as well as the CCK-expressing large basket cells (Overstreet-Wadiche and McBain (2015); Tremblay *et al.* (2016)). Note that these basket cells have a different firing pattern than PV^+ basket cells (see below).

1.2.3 Electrophysiological classification

Neocortical interneurons feature a variety of biophysical properties giving rise to different electrophysiological responses when they are depolarized with a current pulse injected in the soma. Various firing patterns have been reported and sometimes specific morphological or molecular classes are characterized by specific patterns (Kawaguchi and Kubota (1997); Markram *et al.* (2004)). Initial observations of the interneuronal

firing patterns focused on two main types: the fast-spiking (McCormick *et al.* (1985); Connors and Gutnick (1990)) and the low-threshold-spiking or burst-spiking interneurons (Kawaguchi (1993); Kawaguchi and Kubota (1997); Ma *et al.* (2006)). Subsequent work also revealed the existence of regular-spiking interneurons which resemble the regular firing of pyramidal cells (Kawaguchi and Kubota (1997, 1998)), late-spiking cells which fire with a delay (Kawaguchi and Kubota (1996, 1997)), and cells which have irregular spiking after an initial bursting (Porter *et al.* (1998); Cauli *et al.* (1997)).

A classification scheme based on the onset and the steady-state response of the cells was introduced by Gupta et al. (Gupta *et al.* (2000)). The scheme is summarized in Fig. 1.3. The steady-state response to a sustained injection of current can be accommodating, non-accommodating, stuttering, bursting or irregular (Gupta *et al.* (2000); Markram *et al.* (2004)). The bursting patterns can be subclassified as repetitive, initial or transient (see Fig. 1.3). The other steady-state responses can be characterised as classic, bursting or delayed, based on their pattern of onset of firing (Gupta *et al.* (2000); Markram *et al.* (2004)). The accommodating effect refers to a characteristic adaptation of the firing rate during a sustained injection of current at the soma.

The association between the firing patterns and specific morphological or molecular classes is not always clear but some tendencies were reported (Kawaguchi and Kubota (1997); Markram *et al.* (2004); Tremblay *et al.* (2016)). PV^+ cells, both basket and chandelier classes, tend to exhibit a fast-spiking pattern of activity with no accommodation (Markram *et al.* (2004); Tremblay *et al.* (2016)). However, chandelier cells have a slightly slower firing pattern and do not exhibit any delays or pauses, which is common among layer II basket cells (Taniguchi *et al.* (2013)). Fast-spiking was reported in non-Martinotti SOM^+ cells as well, but the pattern is accommodating instead (Xu *et al.* (2013); Tremblay *et al.* (2016)). Low-threshold-spiking interneurons found in infragranular layers were identified as SOM^+ Martinotti cells with accommodating or bursting patterns (Kawaguchi (1993); Kawaguchi and Kubota (1997); Ma *et al.* (2006)). This cannot be generalized, though, to SOM^+ interneurons in other layers or all Martinotti cells (Ma *et al.* (2006)). Regular-spiking interneurons were found to have the morphology of Martinotti, double-bouquet and bipolar cells

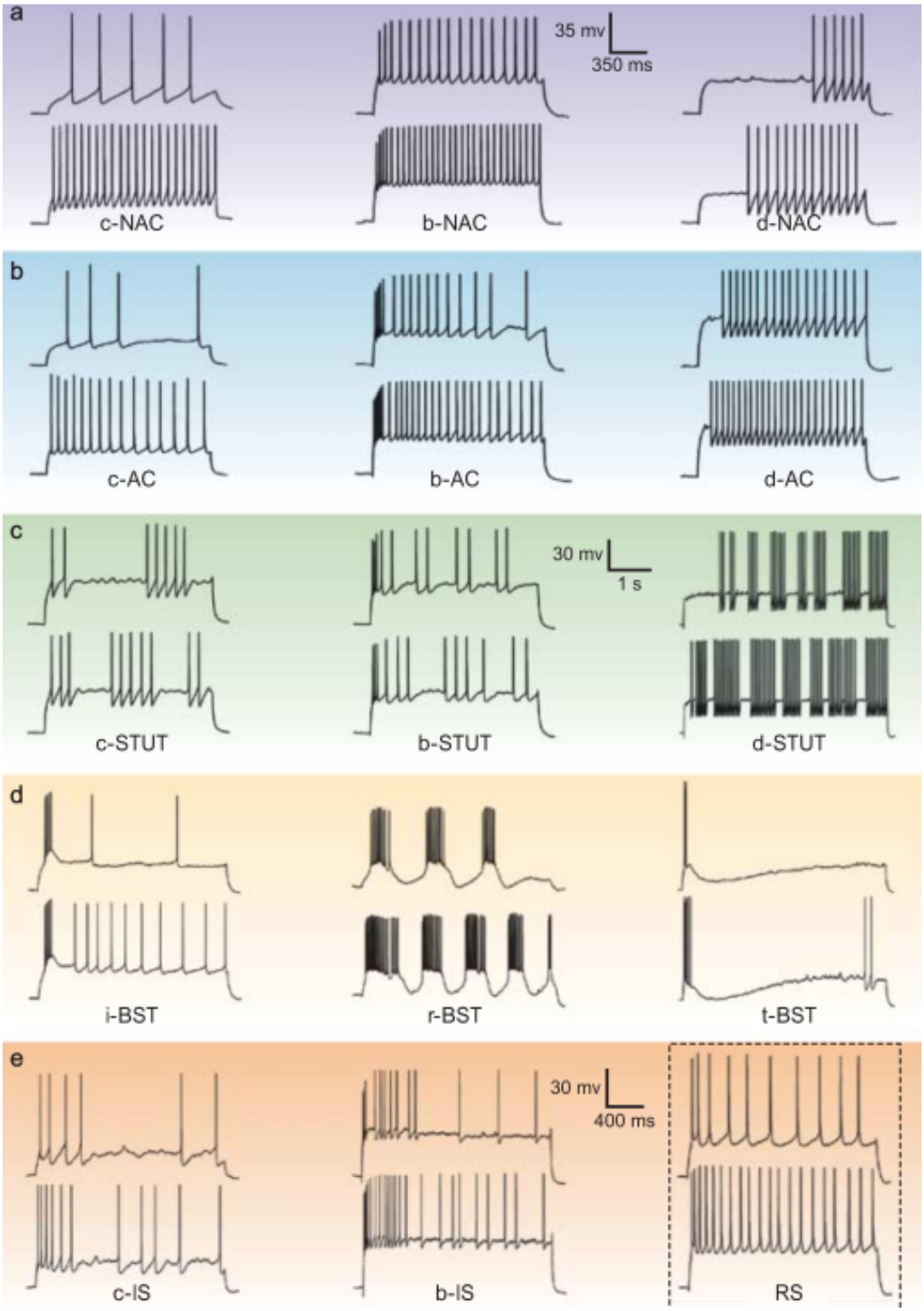

Figure 1.3: Electrophysiological classes of interneurons. Interneurons can be classified in five classes based on their steady-state response: non-accommodating (NAC), accommodating (AC), stuttering (STUT), bursting (BST),and irregular-spiking (IS). Based on the firing onset, interneurons can be characterized as classic (c), bursting (b), delayed (d). The onset of bursting interneurons can be characterized as initial (i), repetitive (r), and transient (t). Figure reproduced from Markram *et al.* (2004).

(Kawaguchi and Kubota (1997, 1998)). The late-spiking pattern of firing found in layers II/III and V were reported to primarily match with neurogliaform cells (Kawaguchi and Kubota (1996, 1997); Tremblay *et al.* (2016)). The irregular-spiking pattern was found in bipolar cells in infra- and supra-granular layers (Porter *et al.* (1998); Cauli *et al.* (1997)).

1.2.4 Interneuronal circuits

Recent studies have examined the connectivity between interneurons based on their molecular markers (Fanselow *et al.* (2008); Adesnik *et al.* (2012); Pfeffer *et al.* (2013)). Such studies show that PV^+ cells deliver strong inhibition on other PV^+ cells along with the inhibition of pyramidal cells (Adesnik *et al.* (2012); Pfeffer *et al.* (2013)). They do not inhibit SOM^+ cells whereas limited inhibition of VIP^+ cells was reported in primary visual cortex (Pfeffer *et al.* (2013)). Interestingly, though, they were reported to inhibit SOM^+ cells in hippocampal CA1 (Lovett-Barron *et al.* (2012)). This connectivity pattern does not apply for PV^+ chandelier cells which are targeting only the axoninitial segments of pyramidal cells (Kubota (2014); Tremblay *et al.* (2016)). The population of SOM^+ cells were found to inhibit every single population, pyramidals and interneurons, except themselves (Pfeffer *et al.* (2013)). They have very limited interconnectivity with chemical synapses as demonstrated with paired recordings and optogenetic approaches (Adesnik *et al.* (2012); Gibson *et al.* (1999); Pfeffer *et al.* (2013)). VIP^+ cells target only the SOM^+ population without inhibiting pyramidal cells (Pfeffer *et al.* (2013)). Due to this connectivity, VIP^+ cells are specialized in providing disinhibition in neocortical circuits (Pfeffer (2014); Tremblay *et al.* (2016)). A schematic of the resulting circuit can be found in Fig. 1.4.

The circuitry described above is limited to the chemical synapses between different populations. However, many interneuronal classes also maintain electrical couplings through gap junctions (Galarreta and Hestrin (1999); Gibson *et al.* (1999); Hestrin and Galarreta (2005)). The predominant gap-junctional channel expressed in neurons is connexin36 (Cx36) (Evans and Martin (2002); Rash *et al.* (2001)). Such connectivity is only found between members of the same class, forming a class-specific syncytium. The syncytia of PV^+ fast-spiking interneurons and SOM^+ low-threshold-spiking

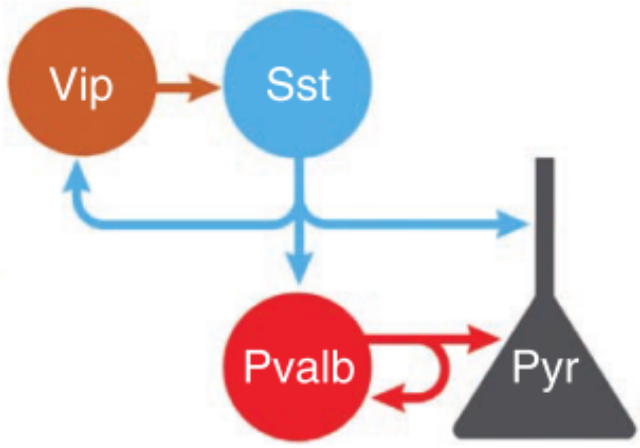

Figure 1.4: Interneuronal circuit in visual circuit. The schematic shows the predominant connectivity between three major interneuronal populations in visual cortex. Note that Sst (SOM) interneurons inhibit everything except themselves. Pvalb (PV) cells inhibit themselves and the pyramidal cells. Vip cells were found to inhibit Sst interneurons only. Figure reproduced from Pfeffer *et al.* (2013).

interneurons were first reported and shown to be electrically distinct (Galarreta and Hestrin (1999); Gibson *et al.* (1999); Hestrin and Galarreta (2005); Fanselow *et al.* (2008)). The PV^+ fast-spiking syncytium includes basket cells and chandelier cells (Hestrin and Galarreta (2005); Woodruff *et al.* (2011)) but it is still unclear whether Martinotti cells are electrically connected with SOM^+ non-Martinotti cells (Tremblay *et al.* (2016)). Another reported syncytium is the one between multipolar bursting cells which target dendritic domains (Blatow *et al.* (2003); Hestrin and Galarreta (2005)). Irregular-spiking interneurons expressing cannabinoid receptors were found to be electrically coupled as well (Galarreta *et al.* (2004); Hestrin and Galarreta (2005)). More recently, VIP^+ cells were reported to function cooperatively through electrical coupling (Karnani *et al.* (2016)). Such homotypic electrical coupling is apparently a common pattern among interneuronal populations of neocortex. However, it is still not clear whether neurogliaform cells are electrically connected in a homotypic way (Tremblay *et al.* (2016)). There is evidence that they are exclusively interconnected in layer I (Chu *et al.* (2003)) but, in contrast, they are promiscuously connected to other cell types in layers II/ III (Simon *et al.* (2005)).

1.3 Fast-spiking, PV$^+$ basket cells

As elaborated above, the three terms fast-spiking interneurons, PV$^+$ interneurons, and soma-targeting basket cells do not refer to exactly the same group of neurons. Despite the popular notion that all PV$^+$ cells are soma-targeting basket cells, or that all fast-spiking interneurons are PV$^+$, this is not the case (Markram *et al.* (2004)). It is rather an approximation of reality. This thesis focuses on the interneuronal population that is formed by the intersection of these classes even though the title refers to fast-spiking interneurons in general. The above notion is usually used in studies to distinguish these cells from the SOM$^+$, low-threshold-spiking, dendrite-targeting interneurons (e.g., Adesnik *et al.* (2012); Wilson *et al.* (2012)) and the same notion is used here for the same reason. So the terms PV$^+$ cells, fast-spiking interneurons and soma-targeting basket cells will be used interchangeably throughout the thesis, referring to the same subpopulation of interneurons.

1.3.1 Ion-channel composition of fast-spiking interneurons

The combination of ion channels expressed in each interneuronal class dictates its electrophysiological phenotype (Markram *et al.* (2004)). Characteristics like the accommodating firing or the bursting are associated with specific ion channels found in the respective interneuronal populations (Ertel and Ertel (1997); Vergara *et al.* (1998)). The ion-channel composition of fast spiking interneurons was also thoroughly investigated leading to the identification of the ion channels responsible for their high frequency, non-accommodating firing and their rapid response (Goldberg *et al.* (2008); Martina *et al.* (1998); Erisir *et al.* (1999); Rudy and McBain (2001); Hu and Jonas (2014); Martina and Jonas (1997); Li *et al.* (2007); Bucurenciu *et al.* (2008)). Kv1.1 channels provide a dampening mechanism at the axon initial segment, filtering out slow depolarizations and allowing fast-spiking interneurons to rapidly respond only to sharp depolarizations (Goldberg *et al.* (2008)). The delayed rectifying Kv3.1 and Kv3.2 channels are highly expressed in fast-spiking interneurons, and they mediate the rapid repolarization of the cells which is crucial for high-frequency firing (Martina *et al.* (1998); Erisir *et al.* (1999); Rudy and McBain (2001)). The afterhyperpolarization is

also large enabling the full recovery of inactivated Na^+ channels thus sustaining the high-frequency of firing without accommodation (Martina *et al.* (1998); Erisir *et al.* (1999); Rudy and McBain (2001)). Furthermore, the gating of Na^+ channels is specialized for maintaining the firing, with slower inactivation and faster recovery than the respective channels in pyramidal cells (Martina and Jonas (1997)). These Na^+ and Kv3 channels are highly expressed in the axon of the cell facilitating the fast and synchronous release of GABA (Hu and Jonas (2014); Tremblay *et al.* (2016)). This is subserved as well by the expression of P/Q-type Ca^{2+} channels, which feature fast kinetics (Martina and Jonas (1997); Li *et al.* (2007); Bucurenciu *et al.* (2008)), at the synaptic terminals. The characteristic ion-channel composition of the fast-spiking interneurons underlies their fast signalling capabilities (Hu and Jonas (2014)).

The specialized Kv3 channels underlie the brief action potentials which characterize fast-spiking interneurons (Erisir *et al.* (1999); Rudy and McBain (2001)). Apart from their short duration, they also have a relatively large afterhyperpolarization (Erisir *et al.* (1999); Rudy and McBain (2001)). These features of single action potentials are widely used to identify the fast-spiking interneurons in local field potential (LFP) recordings (Barthó *et al.* (2004); Mruczek and Sheinberg (2012); Peyrache *et al.* (2012)). The valley to peak duration of these cells is typically lower than 0.4 ms while the typical duration for regular-spiking cells is 0.7 ms (Barthó *et al.* (2004); Mruczek and Sheinberg (2012); Peyrache *et al.* (2012)). In addition, the amplitude ratio between the valley and the peak is lower compared to other classes, reaching sometimes values as low as 0.9, due to the relatively large afterhyperpolarization (Peyrache *et al.* (2012)).

1.3.2 Computational significance of their somatic targeting - Gain control mechanism

The somatic and peri-somatic targeting of basket cells provides proximal inhibition to the pyramidal cell, that is, the postsynaptic inhibitory conductances are injected close to the domain that initiates the action potential. This comes in contrast with the dendritic or distal inhibition which is delivered to the domain where the pyramidal cell receives excitatory conductances and integrates them. Vu and Krasne (1992) showed that this difference between the proximal and distal inhibition had a qualitative

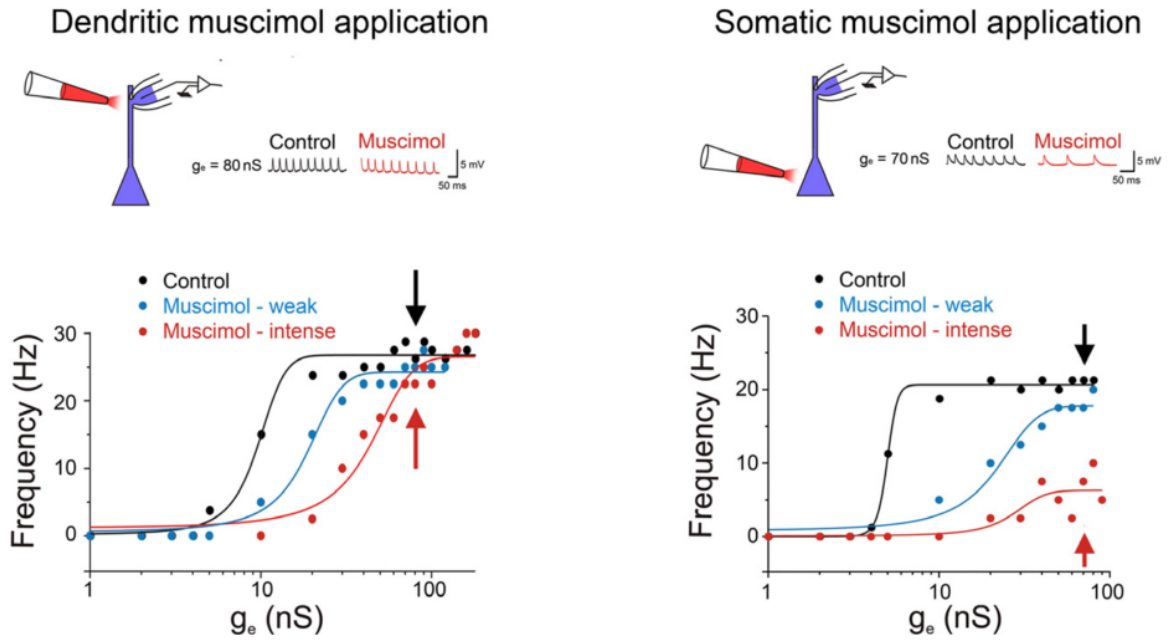

Figure 1.5: Dendritic vs somatic inhibition and the modulation of the input-output function. Inhibition was simulated with the application of muscimol, a $GABA_A$ agonist. It was applied either near the soma or the distal dendrites while the excitatory conductance was varied using dynamic clamping (Pouille *et al.* (2013)). When dendritic inhibition was applied, the sigmoidal input-output function was shifted to higher values without any gain modulation. When somatic inhibition was applied, the slope and maximum value of the sigmoidal function was decreased indicating a gain control mechanism. Figure reproduced from Pouille *et al.* (2013).

difference in the computation carried out by the circuit (Vu and Krasne (1992)). It was shown that increased excitation could override the distal inhibition and generate a spike, while the proximal inhibition could attenuate the excitatory input completely preventing any spike (Vu and Krasne (1992)). They distinguished the two types of inhibition as relative vs absolute and they discussed their functional implications with the latter reducing the dynamic range of the response and the former not (Vu and Krasne (1992)).

In the case of proximal inhibition, inhibitory conductances influence the electrotonic path of the integrated signal by delivering a shunting effect, with the membrane becoming leakier, and the signal attenuating rapidly (Pouille *et al.* (2013)). The maximum achievable firing rate is decreased in this case. In contrast, distal inhibition provides a hyperpolarizing effect that can be overcome with stronger excitation and the cell can reach the same maximum firing rate (Pouille *et al.* (2013)). Both effects can be described by specific modulations of the input-output function of the pyramidal cell. By considering the excitatory input on the x-axis and the firing rate or output of the

cell on the y-axis, the input-output function is typically a sigmoidal function that describes the computational capabilities of the cell (Silver (2010)). Important features of the function include the onset, which is the minimum amount of input that elicits a non-zero output, the slope or neuronal gain, which expresses the sensitivity of the output to varying input intensity, and the maximum output value which gives the value of saturating output for the cell. Examples of input-output functions can be found in Fig. 1.5. The effects of distal and proximal inhibition on the input-output function are shown in the same figure. In that study, distal and proximal inhibitory mechanisms were simulated with the application of muscimol, a $GABA_A$ agonist, close to the distal or proximal dendrites of a pyramidal cell, respectively (Pouille *et al.* (2013)). Note the rightward shift of the function to higher values of input without any modulation of the slope or the maximum firing rate when distal inhibition is applied (Pouille *et al.* (2013)). On the other hand, proximal inhibition decreases the slope (neuronal gain) and the maximum firing rate thus providing a gain control effect (Pouille *et al.* (2013)). Such an effect modulates the dynamic range of the output (Vu and Krasne (1992); Pouille *et al.* (2013)).

Similar results were demonstrated under *in vivo* conditions in mouse visual cortex (Wilson *et al.* (2012)). The activity of pyramidal cells sensitive to the contrast of the visual stimuli was recorded while optogenetically activating different interneuronal populations. In each experiment, either PV^+ or SOM^+ interneurons were activated. The PV^+ interneurons were considered to provide the proximal soma-targeting inhibition while the SOM^+ interneurons were considered to provide the distal dendritic inhibition (Wilson *et al.* (2012)). Examples of how pyramidal input-output functions are modulated with the photoactivation of each interneuronal population are shown in Fig. 1.6. Activating the PV^+ cells resulted into a significant reduction of the slope and the maximum output. Such modulation provides a divisive scaling effect or gain control on the responses of the cell without changing its selectivity (Wilson *et al.* (2012)). Activating the SOM^+ cells, on the other hand, resulted into a shift of the function to higher values without a significant change in the neuronal gain. This modulation sharpens the selectivity of the cell by subtracting the response but keeps its dynamic range the same (Wilson *et al.* (2012)).

In a similar *in vivo* study of neural computation in mouse visual cortex, the PV^+

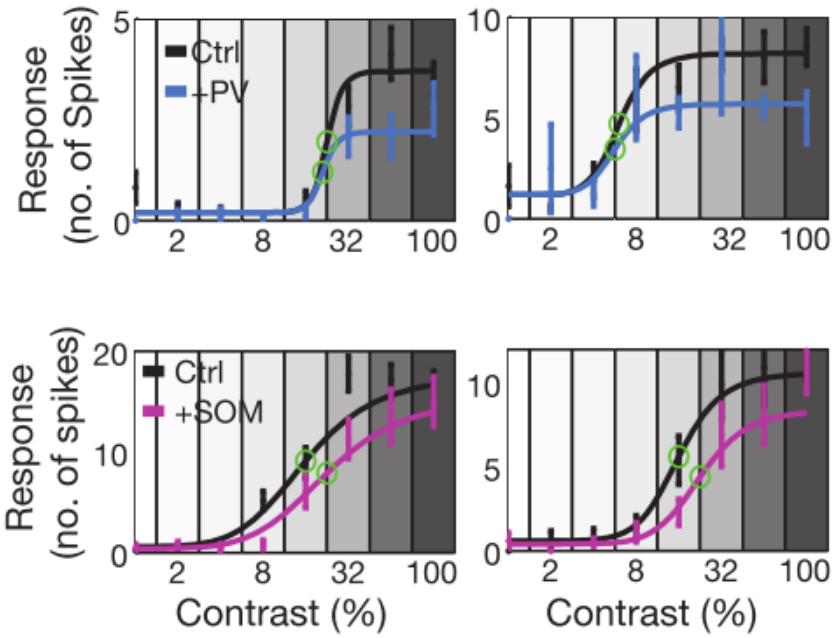

Figure 1.6: Soma-targeting PV$^+$ cells delivering divisive inhibition and dendrite-targeting SOM$^+$ cells providing subtractive inhibition. The input-output function of contrast-sensitive cells in mouse visual cortex is differentially modulated with the optogenetic activation of different interneurons. When PV$^+$ (soma-targeting) cells are activated, there is a divisive modulation on the input-output function. When SOM$^+$ (dendrite-targeting) cells are activated, there is a subtractive modulation on the input-output function instead. Figure reproduced from Wilson *et al.* (2012).

interneurons were either activated or silenced using optogenetic tools (Atallah *et al.* (2012)). Atallah and colleagues (2012) demonstrated that the neuronal gain of pyramidal cells can be either decreased or increased depending on the optogenetic manipulation of PV$^+$ interneurons: there was a divisive decrease with the enhancement of interneuronal activity and there was a multiplicative increase with their silencing (Atallah *et al.* (2012)).

However, the idea that soma-targeting interneurons provide divisive inhibition and dendrite-targeting interneurons provide subtractive inhibition was challenged (Lee *et al.* (2012, 2014); Lovett-Barron *et al.* (2012); Seybold *et al.* (2015); Keller and Martin (2015); El Boustani and Sur (2014)). Lee and colleagues initially reported contradictory results but after a follow-up study concluded that the intensity of the stimulation can influence the results (Lee *et al.* (2012, 2014)). Another study, focusing on the auditory cortex, reported a wide diversity of modulatory effects and suggested that such phenomena arise from more complex mechanisms (Seybold *et al.* (2015)). For instance,

Keller and Martin distinguished experimentally the fast gain control mechanism from the slower adaptation mechanism (subtractive inhibition) while showing that the soma-targeting interneurons are implicated in both (Keller and Martin (2015)). There are many other factors that are expected to influence the modulation of input-output functions including the temporal relations of different inputs, the conductance state of the membrane, the complexity of the dendritic arbour, the active conductances of the dendrite and more (for a review, see Silver (2010)). Indeed, the relative timing between the interneuronal response and the pyramidal response was shown to dictate the quality of inhibition in visual cortex (El Boustani and Sur (2014)).

1.3.3 Functional role of fast-spiking interneurons in cortical circuit motifs

The cortical circuits between pyramidal cells and interneurons are characterised by recurrent connectivity patterns (motifs) (Tremblay *et al.* (2016)). Fast-spiking interneurons are involved in motifs that deliver feedforward and feedback inhibition (Buzsàki and Eidelberg (1981); Pouille and Scanziani (2001); Pouille *et al.* (2009); Geiger *et al.* (1997); Couey *et al.* (2013)). With these circuit-based inhibitory mechanisms, and in combination with their fast signalling capabilities, fast-spiking interneurons have a functional role in the circuits that extends beyond simple inhibition (Hu *et al.* (2014)).

In the case of feedforward inhibition, afferent connections excite both pyramidal cells and interneurons in a microcircuit. The excited interneurons deliver feedforward inhibition onto their local pyramidal cells (Buzsàki and Eidelberg (1981); Pouille and Scanziani (2001); Pouille *et al.* (2009)). Experiments conducted in hippocampal circuits showed that this disynaptic inhibition is delivered primarily by fast-spiking interneurons which target perisomatic domains (Pouille and Scanziani (2001)). Subsequent experiments demonstrated that the fast responses of these interneurons enable them to deliver feedforward inhibition with minimal delay, before the response of other interneurons (Pouille *et al.* (2009)). The rapid feedforward inhibition gives rise to a coincidence detection mechanism in pyramidal cells as a result of a narrower window for temporal integration of excitatory postsynaptic potentials (EPSPs) (Pouille and

Scanziani (2001)). Only the EPSPs that coincide in a shortly after the excitation of the microcircuit are able to produce an action potential (Pouille and Scanziani (2001)).

In the case of feedback inhibition, local excitation activates the interneurons of the microcircuit and those interneurons respond with feedback inhibition either onto the source of excitation (recurrent feedback inhibition) or other principal neurons laterally placed (lateral feedback inhibition) (Geiger *et al.* (1997); Couey *et al.* (2013)). A substantial contribution of fast-spiking interneurons in both types of feedback inhibition was demonstrated in entorhinal cortex (Couey *et al.* (2013)). Through feedback inhibition, a *winner-takes-all* mechanism is enabled: the first group of principal cells that are activated in a microcircuit suppress the initiating of action potential in others through feedback inhibition (de Almeida *et al.* (2009)). The fast signalling of the fast-spiking interneurons is crucial for the efficiency of the mechanism because the short disynaptic delay of their inhibition enables the *winner-takes-all* mechanism with low demands in external input (de Almeida *et al.* (2009)).

1.3.4 Fast-spiking interneurons in physiological and pathological network dynamics

Neuronal networks exhibit a diverse dynamic behaviour and the emerging oscillatory activity has a central role (Wright and Liley (1996); Buzsáki (2006)). Neural oscillations in cortical networks subserve and reflect many cognitive processes including memory (Buzsáki and Draguhn (2004); Klimesch (1999)). During oscillatory activity, the neurons synchronize their firing, producing a network-wide rhythmic coordination and thus enabling synaptic plasticity and information processing (Buzsáki and Chrobak (1995); Buzsáki and Draguhn (2004)). The interneuronal populations, and especially the fast-spiking interneurons, play a primary role in the generation and maintenance of such oscillatory activity (Buzsáki and Chrobak (1995); Bartos *et al.* (2007); Whittington and Traub (2003)).

Networks of fast-spiking interneurons have special features that make them the ideal high-frequency (gamma band) oscillators in cortical networks (for a review, see Bartos *et al.* (2007)). The abundance of these neurons, the reciprocal inhibitory connections

between them, the soma-targeting inhibition that they provide to pyramidal cells and their high-frequency firing all work synergistically to generate and maintain gamma oscillations (Bartos *et al.* (2007)). Experiments carried out in hippocampal slices demonstrated the importance of synaptic inhibition in the generation of such oscillations (Whittington *et al.* (1995)). Synaptically connected interneurons generated gamma oscillations after blocking ionotropic glutamate receptors and activating metabotropic glutamate receptors (Whittington *et al.* (1995)). These oscillations were terminated as soon as the $GABA_A$ receptors were blocked (Whittington *et al.* (1995)). Similar experiments with different pharmacological manipulations showed that GABA-mediated inhibition is necessary and sufficient to generate gamma oscillations (for a review, see Bartos *et al.* (2007)). In addition, rhythmic optogenetic stimulation of the PV^+ interneurons was shown to generate gamma oscillations (Cardin *et al.* (2009); Sohal *et al.* (2009)). The oscillation that emerges among the mutually inhibited fast-spiking interneurons recruits the principal neurons through the synaptic connections between the two neuronal classes (Bartos *et al.* (2007)). Other features of the network like the gap junctions between fast-spiking interneurons (Galarreta and Hestrin (1999); Gibson *et al.* (1999)) and the fast and strong glutamatergic synapses onto these cells (Galarreta and Hestrin (2001); Angulo *et al.* (1999)) promote their synchrony (Vida *et al.* (2006)). Interestingly, a recent study in hippocampal CA1 suggests that interneuronal populations other than the fast-spiking basket cells have a more prominent role in this type of oscillations (Craig and McBain (2015)).

Interneurons are pivotal for the physiological coordination of activity in cortical networks and impairments in these neurons are implicated with the emergence of pathological dynamics (Uhlhaas and Singer (2010); Trevelyan (2016)). Phenomena like hypersynchronous activity or runaway excitation characterize pathologies like epilepsy and Parkinsons disease (Uhlhaas and Singer (2006); Trevelyan (2016)). Interneurons protect the network activity by providing an inhibitory restraint that blocks the propagation of seizures (Trevelyan *et al.* (2006); Schevon *et al.* (2012)). Fast-spiking PV^+ interneurons are crucial in these restraining mechanisms because of their rapid and timely response to excitatory drive and also their targeting specificity (Trevelyan (2016)). Indeed, genetic manipulation of these interneurons increases dramatically the susceptibility of the networks to epileptiform activity (Schwaller *et al.* (2004); Ogiwara *et al.* (2007); Rossignol *et al.* (2013)). Sessolo and colleagues manipulated

optogenetically the population of PV^+ interneurons in a slice model of focal epilepsy and showed that, while the population can block the propagation of seizures away from the focus, it can also generate the seizure at the focus due to postinhibitory rebound spiking in the principal cells (Sessolo *et al.* (2015)). However, this type of interneuronal manipulation has its limitations when it comes to the interpretation of the results due to the uncoordinated activation of the interneurons (Trevelyan (2016)). Molecular alterations in the population of PV^+ interneurons are also involved in schizophrenia pathophysiology (Uhlhaas and Singer (2010); Nakazawa *et al.* (2012); Lewis *et al.* (2012)).

1.4 Outline of the thesis

The purpose of this project was to investigate how different aspects of the PV^+ interneurons influence the neocortical dynamics. Computational and experimental approaches were used for this purpose.

Chapter 2 includes the investigation on how divisive inhibition, as delivered by the soma-targeting interneurons, influences the stability of oscillatory dynamics in neocortical networks. The impact of divisive inhibition on the transition of the network into a state of unstable or paroxysmal (seizure-like) oscillations has never been explored. The aim of this investigation was to determine whether the presence of divisive inhibition in the network can promote or prevent the onset of such oscillations. Neural mass models were used in this investigation.

The same modelling framework was used in Chapter 3 where the impact of divisive inhibition on the phenomena of entrainment and long-range synchronization was explored. These phenomena are indicative of flexible neural dynamics and impairments in these phenomena have been reported in schizophrenics (Schwab *et al.* (2006); Brenner *et al.* (2003); Hamm *et al.* (2015); Pittman-Polletta *et al.* (2015); Schnitzler and Gross (2005)). The aim of this investigation was to determine whether divisive inhibition can enhance or diminish these phenomena in a model neocortical network.

Chapter 4 focuses on the role of the electrical couplings between the PV^+ interneurons

during the state of raised extracellular K^+ concentration. This state is a naturally occurring state at the focus of a seizure (Heinemann and Dieter Lux (1977); Moody *et al.* (1974); Amzica *et al.* (2002); Gnatkovsky *et al.* (2008)). Propagation of seizures through these electrical synapses has been reported under different conditions (drug-induced, see Gigout *et al.* (2006); Louvel *et al.* (2001)). However, the impact of raised extracellular K^+ concentration has never been explored. The possibility of propagating activity through the PV-syncytium under this condition was explored in cortical slices using multi-electrode array (MEA) recordings, optogenetic manipulation and pharmacology. A biophysically detailed model was also used in order to explain some aspects of the experimental results.

Chapter 5 focuses on the interaction of two different oscillations and the potential impact of PV^+ interneurons during such interaction. Interactions between two different oscillations have been reported in slice electrophysiology experiments (e.g., see period concatenation in Roopun *et al.* (2008a,b)) but the role of the inhibitory interneurons has not been investigated during such phenomena. The aim of this investigation was to develop a protocol of interaction between two different oscillations and explore the role of inhibitory interneurons through pharmacological manipulations. A combination of MEA recordings, optogenetics and pharmacology were used in a slice electrophysiology setup for this purpose.

Chapter 6 includes a general discussion on the results of the project and future directions on the study of PV^+ interneurons.

Chapter 2

Gain control through divisive inhibition prevents abrupt transition to chaos in a neural mass model

2.1 Introduction

Neurons can be understood as information processing units that transform synaptic input into a spike train output. This transformation is often described by an input-output function, which can be experimentally measured. Recent experiments have demonstrated that different inhibitory mechanisms can modulate this function (Mitchell and Silver (2003); Wilson *et al.* (2012)). These inhibitory mechanisms can be considered to be either subtractive or divisive based on the modulation that is applied on the postsynaptic neurons. The subtractive modulation shifts the sigmoidal input-output function to higher inputs (hyperpolarizing effect), whereas the divisive modulation decreases the slope of the function (also termed the neuronal gain) (Silver (2010)). Recent studies demonstrated that the two types of modulations are applied on the cortical pyramidal neurons by two distinct inhibitory populations. Dendrite-targeting interneurons provide the subtractive inhibition, whereas divisive inhibition is provided by soma-targeting interneurons (Wilson *et al.* (2012); Pouille *et al.* (2013)). Additionally, the connectivity patterns between these populations were

revealed in recent anatomical study in neocortex, where it was shown that the dendrite-targeting interneurons inhibit the soma-targeting but not the other way around (Pfeffer *et al.* (2013)).

In particular, the role of divisive inhibition (i.e., gain control) has been explored by experimental as well as computational studies, as it is a nonlinear effect that enables more complex functionality into the system. Gain control has been shown to be crucial in human vision (Wilson and Kim (1998)), sensory processing (Schwartz and Simoncelli (2001); Malmierca *et al.* (2005)), gaze direction (Trotter and Celebrini (1999)), selective attention (Hillyard *et al.* (1998)), and motor processing (Treue and Martinez-Trujillo (1999)). In simulated networks of neurons, divisive inhibition was shown to prevent some problems (proximity to unstable behavior, sensitivity of dynamics to connectivity parameters, and slow reaction to fast fluctuating input) caused by the lack of divisive inhibition (Chance and Abbott (2000)). Additionally it was shown that including divisive inhibition can improve storage capacity in neuronal networks without compromising its dynamical stability (Battaglia and Treves (1998)). In terms of network dynamics, the divisive modulation was found to regulate the duration of the active and silent phases during rhythmic bursting activity (Tabak *et al.* (2006, 2011)).

Despite these findings, there are still open questions about the role of divisive inhibition in the overall network dynamics. In particular, the effect on the transition between different network states is unclear. In the present computational work, transitions from low-amplitude oscillations to high-amplitude paroxysmal oscillations are of interest. A high-amplitude paroxysmal oscillation in local neocortical networks is a model of hypersynchronous activity which indicates pathological dynamics, as, for example, in epilepsy (Uhlhaas and Singer (2006)). Experimental studies investigated the role of different elements of neocortical networks and their interaction with the thalamus in the generation of such oscillations (Steriade and Contreras (1998); Bazhenov *et al.* (2004)). These oscillations closely resemble the spike-wave complexes that characterize the pathological activity during seizures. Despite the fact that the interaction between neocortex and thalamus enhances spike-wave complexes, it was shown that the thalamus is not necessary for the generation or propagation of these paroxysmal oscillations in neocortex (Steriade and Contreras (1998); Timofeev *et al.* (2002); Destexhe *et al.* (2001)). Computational studies have used limit cycles or

chaotic attractors to model these paroxysmal oscillations (Wendling *et al.* (2002); Lopes da Silva *et al.* (2003); Suffczynski *et al.* (2004); Huang *et al.* (2011); Freeman (1987)). Despite the fact that chaoticity is a property not always found in this type of pathological activity, the chaotic attractors usually have high-amplitude and complex behavior that resembles such paroxysmal activity. Also a three-dimensional chaotic attractor has the same dimensionality as the seizure attractors analyzed from EEG signals (Babloyantz and Destexhe (1986)). For a review on seizure dynamics and the types of attractors that are used to model this type of activity can be found in Deco *et al.* (2008). In the present work, the transition to paroxysmal oscillations is modeled as a transition from a low-amplitude limit cycle (order) to a high-amplitude chaotic attractor (chaos) in a model of local neocortical networks which were shown to exhibit such activity even in isolation. Furthermore, a recent study on the macroscopic behavior of spiking neural networks verifies the coexistence of order and chaos in local networks (Montbrió *et al.* (2015)).

One intensively studied route to chaos is via a so-called cascade of period-doubling bifurcations (Tresser *et al.* (2014)). During a period-doubling bifurcation, a limit cycle is replaced by a new periodic orbit with double the period of the original orbit. Period-doubling bifurcations are well documented in complex neural systems, both theoretically (Ermentrout (1984); Breakspear *et al.* (2006)) and experimentally (Ishizuka and Hayashi (1996); Crevier and Meister (1998); Perez Velazquez *et al.* (2003)). Additionally, cascades of period-doubling bifurcations are often found preluding the onset of paroxysmal or irregular behavior in these studies. Interestingly, the cascades of period-doubling bifurcations can happen at a constant transition rate, first described by Feigenbaum (Feigenbaum (1978)). The Feigenbaum constant was since found to apply universally in many dissipative systems in nature (Libchaber *et al.* (1982); Testa *et al.* (1982); Makin *et al.* (2008)). The significance of Feigenbaum universality, and particularly of the Feigenbaum constant (Feigenbaum (1978)), is that it provides a prediction for the onset of chaos in parameter space. A system complying with Feigenbaum universality has a well-defined relative boundary between order and chaos, whereas a system with non-Feigenbaum behavior can exhibit abrupt transitions between the two states. Non-Feigenbaum behavior is still an open field of study. Some classes of such behavior have already been characterized, mainly in discrete dynamical

systems (Kuznetsov *et al.* (1997); Kim *et al.* (2001); Kuznetsov *et al.* (2005)). Examples of this behavior in continuous dynamical systems remain poorly understood.

Previous studies of neural population dynamics reported period-doubling transitions (Huang *et al.* (2011); Ermentrout (1984); Breakspear *et al.* (2006); Rodrigues *et al.* (2009)). However, none of them, to our knowledge, focused on the influence of inhibitory mechanisms on the period-doubling cascades. The primary aim of this study is to apply bifurcation theory and investigate the role of divisive inhibition in a neural mass model while it undergoes a period-doubling cascade leading to chaos. In particular, I will explore how the system behaves in relevance to Feigenbaum universality in two different cases: while the model includes divisive inhibition and while it uses only subtractive inhibition.

2.2 Models and Methods

2.2.1 Modeling framework

As in previous studies, neural mass models are used in this work, giving an abstract and macroscopic description of neocortical networks comprised of excitatory and inhibitory populations. The dynamics arise from the interaction of these populations which are expressed by a set of ordinary differential equations (ODEs). In particular, the model used here is an extended version of the spatially localized Wilson-Cowan model (Wilson and Cowan (1972)), which is primarily used to model the oscillatory behavior of neural systems (Tsodyks *et al.* (1997); Deco *et al.* (2009); Wang *et al.* (2012)). This type of model is conceptually simple and well studied and can be easily analyzed using bifurcation theory (Borisyuk and Kirillov (1992); Pinto *et al.* (1996); Monteiro *et al.* (2002)). Therefore it is an ideal choice for investigating how abstract concepts like subtractive or divisive inhibition can change the network's behavior at the population level. The model introduced here can be considered as a generalization of the Wilson-Cowan model (Wilson and Cowan (1972)). This generalization can be used to model not only subtractive inhibition, as featured in the classic model, but also divisive inhibition. In order to achieve this, I consider the excitation and external

inputs to be the *drivers* of the network, whereas the inhibition is used only to *modulate* the sigmoidal input-output functions of all the units in the network. Distinguishing between drivers and modulators in the network is inspired by the Sherman-Guillery proposition (Sherman and Guillery (1998)). This separation of drivers from the modulators comes in contrast to the way that inhibition was previously modeled: as a subtraction from the input, that is, as a negative driver. An equivalent result can be obtained instead by shifting the input-output function to higher inputs (see Fig. 2.1, bottom left), that is, subtractive modulation of the input-output function. This displacement represents the subtractive inhibition in the proposed model. Similarly, the divisive inhibition can be modeled as a gain control mechanism that decreases the slope and maximum output of the input-output functions (see Fig. 2.1, bottom right). By choosing the logistic function as the input-output function, we can model these modulations by promoting the constants for displacement and slope to variables that can be dynamically controlled by the inhibitory populations in the model. This modification results in a function of three variables $F(x, \theta, \alpha)$, $F : \mathbb{R} \times \mathbb{R}_0^+ \times \mathbb{R}_0^+ \to \mathbb{R}$. Variable x represents the input or the driver of the unit, variable θ represents the displacement of the sigmoidal curve along the x axis, and variable α represents the slope of the curve. Thus, the input-output function F(driver, subtractive modulator, divisive modulator) is given by:

$$F_j(x, \theta, \alpha) = \frac{1}{1 + \exp\left[-\frac{\alpha_j}{1+\alpha}(x - (\theta_j + \theta))\right]} - \frac{1}{1 + \exp\left[\frac{\alpha_j \theta_j}{1+\alpha}\right]}, \tag{2.1}$$

where the minimum displacement θ_j and the maximum slope α_j are constants, representing the default case when no modulatory inhibition is delivered to the unit. Specifically, these constants differ for different populations: $j = \{e, s, d\}$ for the excitatory, subtractive, and divisive inhibitory populations, respectively. Note also that the last term in the expression only depends on the variable of slope α and it is used for decreasing the maximum value of the output along with the decrease in slope (see Fig. 2.1 for a schematic).

Using the input-output function F we now have an easy way to express subtractive and divisive modulations in the function arguments.

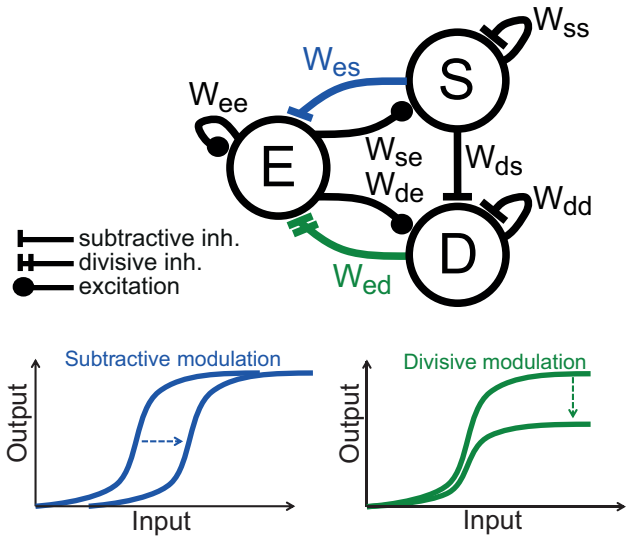

Figure 2.1: Schematic of the ESD model. The model incorporates an excitatory population (E), a subtractive (S), and a divisive (D) inhibitory population. The lower panels show how the two inhibitory mechanisms modulate the input-output function of their target population. Note the nonreciprocal inhibitory connection between S and D. The external inputs to the populations are omitted in this schematic.

ESD model

The model incorporating both subtractive and divisive inhibition (the ESD model, also see Fig. 2.1) is given by the following system of ordinary differential equations (ODEs):

$$\begin{aligned}
\frac{dE}{dt} &= -E + (k_e - E)F_e(w_{ee}E + P_e, w_{es}S, w_{ed}D), \\
\frac{dS}{dt} &= -S + (k_s - S)F_s(w_{se}E + P_s, w_{ss}S, 0), \\
\frac{dD}{dt} &= -D + (k_d - D)F_d(w_{de}E + P_d, w_{ds}S + w_{dd}D, 0),
\end{aligned} \tag{2.2}$$

where

$$k_j = \lim_{x \to +\infty} F_j(x, \theta, \alpha) = \frac{\exp\left[\frac{\alpha_j \theta_j}{1+\alpha}\right]}{1 + \exp\left[\frac{\alpha_j \theta_j}{1+\alpha}\right]}, \tag{2.3}$$

with $j = \{e, s, d\}$. The variables of the system, E, S, and D, express the activity level of the excitatory, subtractive inhibitory, and divisive inhibitory population respectively.

The functions F_j are the sigmoidal input-output functions as presented above. Parameters P_j give the external inputs to the units and they are considered to be independent of time in this study. The refractory period (see Wilson and Cowan (1972)) is assumed to be the same for all populations and equal to 1 (omitted here). The connectivity parameter $w_{ji} \geq 0$ represents the weight of connection from unit i to unit j. The absence of the inhibitory connection w_{sd} is justified by the anatomical findings (Pfeffer *et al.* (2013)). Note that the divisive inhibitory population is considered divisive just because it delivers divisive inhibition to the excitatory population. Its self-inhibition connection w_{dd} remains subtractive; no divisive modulation is evidenced, to our knowledge, in neuronal population other than on the pyramidal cells. All three populations are assumed to work at the same time scale, so all time constants are omitted in this model. A schematic of the model can be found in Fig. 2.1.

$ES\acute{S}$ model

An equivalent model but without the divisive inhibition ($ES\acute{S}$ model) is given by the following system of ODEs:

$$\begin{aligned} \frac{dE}{dt} &= -E + (k_e - E)F_e(w_{ee}E + P_e, w_{es}S + w_{e\acute{s}}\acute{S}, 0), \\ \frac{dS}{dt} &= -S + (k_s - S)F_s(w_{se}E + P_s, w_{ss}S, 0), \\ \frac{d\acute{S}}{dt} &= -\acute{S} + (k_{\acute{s}} - \acute{S})F_{\acute{s}}(w_{\acute{s}e}E + P_{\acute{s}}, w_{\acute{s}s}S + w_{\acute{s}\acute{s}}\acute{S}, 0), \end{aligned} \tag{2.4}$$

with the same input-output functions F_j, $j = \{e, s, \acute{s}\}$, as described in Eq. (2.1). Note that the only thing that changes compared to the ESD model is the quality of inhibition that is provided by the secondary inhibitory population, $\acute{S}$, to the excitatory population, E. Instead of being divisive, denoted by D, now it is subtractive, denoted by $\acute{S}$. This second $ES\acute{S}$ model is created in order to provide a comparison to the ESD model.

Nonideal divisive inhibition

The divisive inhibition in the network can be modeled in a way that is not purely divisive modulation of the input-output function of the excitatory population but rather a combination of divisive and subtractive modulation. This can be thought as a more biologically realistic modulation, which more closely resembles the experimental data (Wilson *et al.* (2012); Pouille *et al.* (2013)). An additional constant parameter $q \in [0, 1]$ is introduced in the model in order to express the fraction of divisive modulation that is delivered to the excitatory population. The rest of the modulation, $1 - q$, is delivered as subtractive. For a schematic see Fig. 2.5(a). The only change in the ESD model [Eq. (2.2)] is the input-output function of the excitatory population:

$$F_e(x, \theta, \alpha) = \frac{1}{1 + \exp\left[-\frac{\alpha_e}{1+q\alpha}(x - (\theta_e + \theta + (1-q)\alpha))\right]} - \frac{1}{1 + \exp\left[\frac{\alpha_e \theta_e}{1+q\alpha}\right]}, \tag{2.5}$$

and, consequently,

$$k_e = \lim_{x \to +\infty} F_e(x, \theta, \alpha) = \frac{\exp\left[\frac{\alpha_e \theta_e}{1+q\alpha}\right]}{1 + \exp\left[\frac{\alpha_e \theta_e}{1+q\alpha}\right]}. \tag{2.6}$$

The input-output functions F_s and F_d remain the same as in Eq. (2.1). I shall use this nonideal divisive inhibition at a later stage in the analysis to simulate mixture models between the ESD and $ES\acute{S}$ models. Table 2.1 summarizes all the model parameters I used in this study.

2.2.2 Feigenbaum number

The Feigenbaum number expresses the rate by which the system undergoes the period-doubling bifurcations en route to chaos. Therefore it can be used as a relative measure of the abruptness of period-doubling cascades. Considering a cascade of

period-doubling bifurcations $R_2, R_4, R_8, \ldots R_{2^n}$, the Feigenbaum number is given by:

$$\delta = \lim_{n \to +\infty} \frac{R_{2^{n-1}} - R_{2^{n-2}}}{R_{2^n} - R_{2^{n-1}}}. \tag{2.7}$$

An approximation of this number, based on the first four period-doubling bifurcations R_2, R_4, R_8, and R_{16}, was calculated by use of the following ratio:

$$\hat{\delta} = \frac{R_8 - R_4}{R_{16} - R_8}. \tag{2.8}$$

This measure can be compared with the Feigenbaum constant $\delta = 4.6692\cdots$ (Feigenbaum (1978)), which was discovered to be a characteristic constant for all one-dimensional maps and many dissipative systems undergoing period-doubling cascades (Cvitanovic (1984); Strogatz (1994)). Values of $\hat{\delta}$ near the Feigenbaum constant are considered as an indication that the system complies with the Feigenbaum universality, whereas values far from this constant indicate a non-Feigenbaum behavior.

Essentially, the number $\hat{\delta}$ estimated from a period-doubling cascade offers us a way to classify the route into chaos. If $\hat{\delta}$ is close to the Feigenbaum constant, then the transition into chaos is well understood and can be reduced to the dynamics of a one-dimensional map. If $\hat{\delta}$ is far from the Feigenbaum constant, then the transition to chaos is underpinned by more complex processes. Particularly, if $\hat{\delta} > \delta$, then the onset of chaos is considered relatively more abrupt.

2.2.3 Bifurcation analysis using numerical continuation

The toolbox MATCONT (Dhooge *et al.* (2003)) was used for the detection of bifurcation points and the numerical continuation of bifurcation curves presented in this work. A fourth-order Runge-Kutta method (ode45) implemented in MATLAB Release 2013b (The MathWorks, Inc., Natick, MA) was used for the numerical integration of the ODEs in all the reported results. Other built-in ODE solvers were also used and produced similar results.

Table 2.1: Parameter sets used for the results shown. For all cases: $P_e = 1.1$, $P_s = P_d = 0$, $\theta_e = 4$, $\theta_s = \theta_d = 3.7$, $\alpha_e = 1.3$, $\alpha_s = \alpha_d = 2$. Note the varying parameters denoted with *var*.

No	w_{ee}	w_{es}	$w_{ed}/w_{e\acute{s}}$	w_{se}	w_{ss}	$w_{de}/w_{\acute{s}e}$	$w_{ds}/w_{\acute{s}s}$	$w_{dd}/w_{\acute{s}\acute{s}}$	Fig.
1	*var*	12	28	14	2	20	21	0	2.2
2	*var*	12	*var*	14	2	20	21	0	2.3(a-b)
3	20.7	12	19	14	2	20	21	0	2.3(c)
4	19.6	12	19	14	2	20	21	0	2.3(d)
5	*var*	12	28	14	2	20	*var*	0	2.4
6	*var*	12	*var*	*var*	2	20	*var*	0	2.5(b) black
7	21	*var*	28	14	*var*	*var*	21	*var*	2.5(b) red
8	*var*	12	28	14	2	20	21	0	2.5(d)
9	21	11.5	24	*var*	1.5	20	21.5	6	2.6
10	21	11.5	*var*	15	1.5	20	*var*	8	2.7(a)
11	21	11.5	24	*var*	1.5	19.5	*var*	6	2.7(b)
12	21.5	12	*var*	16	2	20	18	0	2.10

2.3 Results

In this work, the role of divisive inhibition in the transition from order to chaos through a period-doubling cascade is examined. For this purpose, the model introduced in the previous section was used. The connectivity between the two inhibitory populations is unidirectional and follows the experimental findings in neocortical networks (Wilson *et al.* (2012); Pfeffer *et al.* (2013)). A schematic of the model with all the connectivity parameters can be found in Fig. 2.1. A numerical approach was used for its analysis throughout.

The introduced model can exhibit transitions from a limit cycle (order) to a chaotic attractor through a cascade of period-doubling bifurcations. Figure 2.2(a) shows the bifurcation diagram of such a transition. The cascade parameter used in this example is the self-excitation synaptic weight, w_{ee}. The limit cycle emanates from a supercritical Andronov-Hopf bifurcation and the amplitude of the oscillation increases with the increase of the cascade parameter. The first four period-doubling bifurcations are labeled as R_2, R_4, R_8, and R_{16}, denoting the beginning of the period-2, period-4, period-8, and period-16 cycles, respectively. Instances of the phase space at different stages of the transition can be seen in Fig. 2.2(b), including the chaotic attractor appearing at the end of the cascade. The strange attractor is topologically similar to the Rössler attractor (Rössler (1976)), the Sprott D attractor (Sprott (1994)), and the

Genesio-Tesi attractor (Genesio and Tesi (1992)) exhibiting a stretching and folding mechanism (Gilmore *et al.* (2008)). The period-doubling cascade shown in Fig. 2.2(a) has a Feigenbaum number close to the Feigenbaum constant, $\hat{\delta} \approx \delta$.

The behavior during the transition in this model, which includes divisive inhibition, is compared with an equivalent one which does not include divisive inhibition. All the parameters of the model are the same; the only thing that changes is the quality of inhibition delivered by the secondary inhibitory population. The two versions of the model are labeled as ESD and $ES\acute{S}$ and are expressed by the sets of ODEs Eq. (2.2) and Eq. (2.4), respectively. The first four period-doubling bifurcations R_2, R_4, R_8, and R_{16} were numerically calculated in both ESD and $ES\acute{S}$ models using the MATCONT toolbox (Dhooge *et al.* (2003); see Models and Methods). The same toolbox was used to produce the period-doubling bifurcation curves by varying both the cascade parameter and another connectivity parameter. This way it is possible to explore whether the transition from order to chaos is sensitive to changes in network connectivity. The resulting bifurcation diagrams are shown in Figs. 2.3(a) and 2.3(b).

As shown in the lower panels of Figs. 2.3(a) and 2.3(b), the rate of bifurcation $\hat{\delta}$ was calculated for each value of the varying parameter on the abscissa (see Models and Methods). This measure was plotted alongside the Feigenbaum constant $\delta = 4.6692\cdots$ (Feigenbaum (1978)) represented by the dashed line in the same panels. This plot reveals whether the behavior of the model follows Feigenbaum universality. In Fig. 2.3, an example of the comparison between ESD and $ES\acute{S}$ is shown with self-excitation w_{ee} being the cascade parameter and w_{ed} (respectively $w_{e\acute{s}}$ for $ES\acute{S}$) being the varying connectivity parameter.

From the example in Fig. 2.3, it is obvious that the two versions of the model, ESD and $ES\acute{S}$, can exhibit a significantly different behavior. While the $\hat{\delta}$ value is always near the Feigenbaum constant in the ESD model, the $\hat{\delta}$ value for the $ES\acute{S}$ model is sensitive to changes of the parameter $w_{e\acute{s}}$ and can take a wide range of values. There is actually a linear increase as the parameter $w_{e\acute{s}}$ is increased. The results indicate that the ESD model complies with the Feigenbaum universality and has always smooth transition from order to chaos, whereas the $ES\acute{S}$ model exhibits a non-Feigenbaum behavior with transitions which can be much more abrupt. Similar observations can be

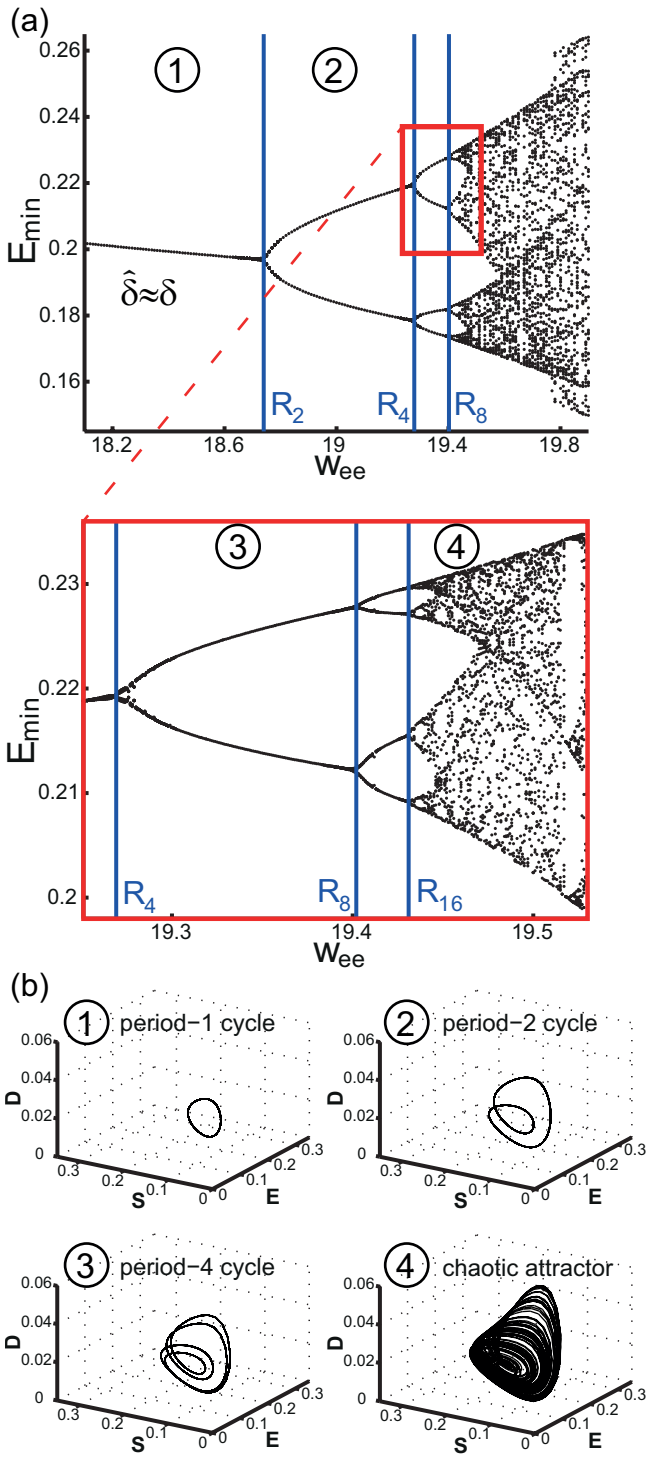

Figure 2.2: Example of a period-doubling cascade in the ESD model and the different oscillatory states of the system. (a) The bifurcation diagram, where local minima of variable E are plotted against the cascade parameter w_{ee}, shows the successive period-doubling bifurcations R_2, R_4, R_8, and R_{16} occurring at a rate $\hat{\delta}$ close to the Feigenbaum constant $\delta \approx 4.67$. (b) The phase space plots show the different oscillatory states of the system from a period-1 cycle up to the chaotic attractor. The value ranges for these oscillatory states are marked in (a) by corresponding Arabic numerals.

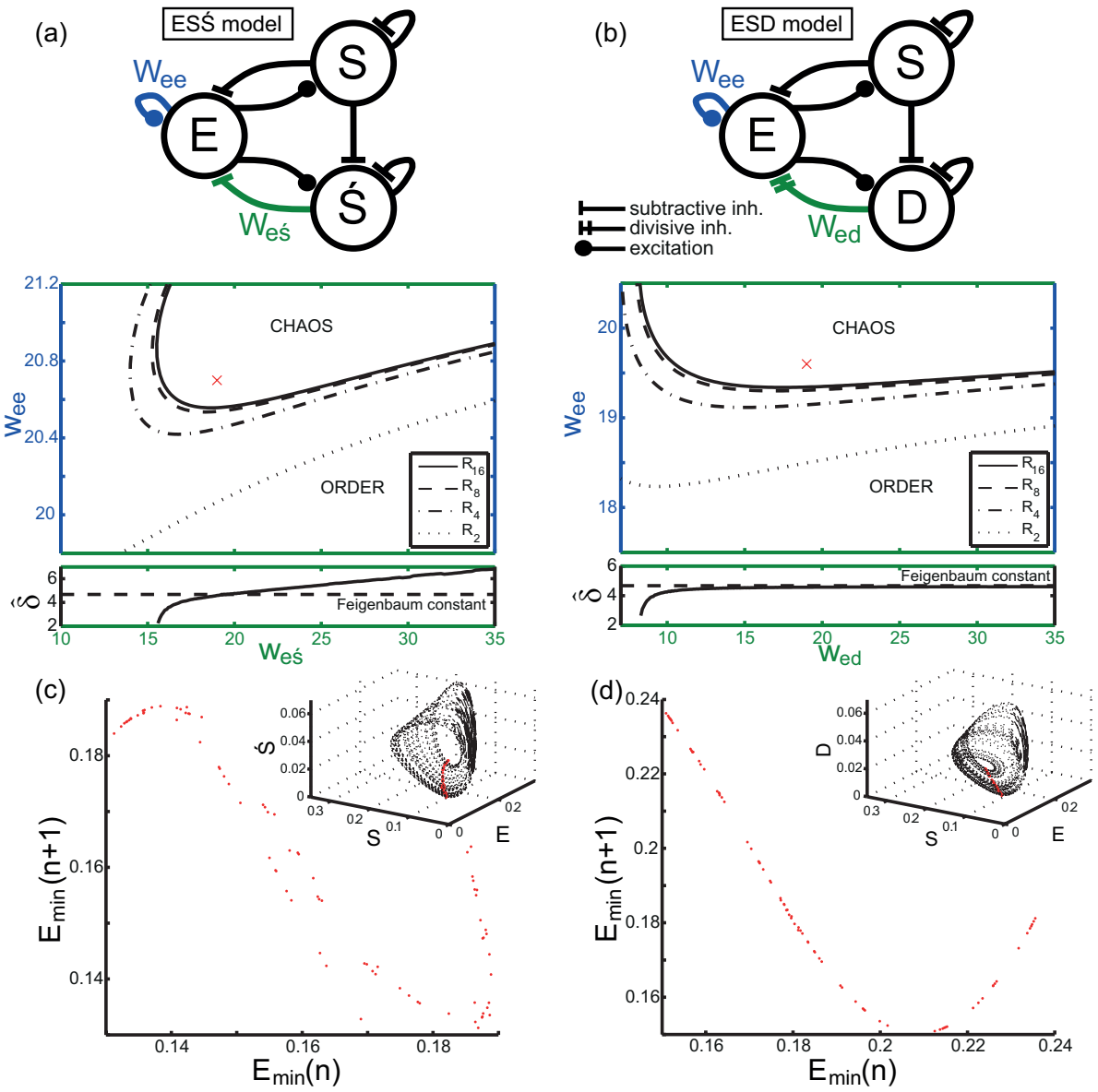

Figure 2.3: Comparison between the $ES\acute{S}$ and ESD model in terms of their Feigenbaum behavior and their first return maps. [(a)-(b)] Bifurcation diagrams for the $ES\acute{S}$ and ESD models showing the first four period-doubling curves. The parameter w_{ee} was used as the cascade parameter in both cases. The lower panels show the calculated $\hat{\delta}$ of the cascades for varying $w_{e\acute{s}}$ and w_{ed}, respectively. [(c)-(d)] First return maps of typical chaotic attractors produced by the $ES\acute{S}$ and ESD model, respectively. The maps are produced by taking the local minima of the variable E (red dots on the attractors in the inset plots). The parameter values used to produce the chaotic attractors are marked with a red cross in the respective bifurcation diagram in (a) or (b) (see also Table 2.1).

made using other cascade parameters, like w_{ds} or w_{se}, and other varying connectivity parameters (see also Appendix A).

This difference in behavior between $ES\acute{S}$ and ESD model can be also seen in the first return maps of their chaotic attractors [see Fig. 2.3(c) and 2.3(d)]. By taking the local minima of the chaotic activity of excitatory population E, I constructed the first return maps $E_{min}(n+1)$ vs $E_{min}(n)$ where $E_{min}(n)$ the n-th local minimum. In particular, the chaotic activity was produced using the parameters marked with a red cross in Figs. 2.3(a) and 2.3(b). As shown in Figs. 2.3(c) and 2.3(d), only the return map of the ESD attractor is one-dimensional and unimodal, indicating compliance to Feigenbaum universality (Strogatz (1994)). This type of return map is typical of attractors resulting from a stretching and folding mechanism (Gilmore *et al.* (2008)). In contrast, the $ES\acute{S}$ model produces a two-dimensional and bimodal return map, indicating that the attractor is not *folded* completely upon the first return; that is, its dynamics cannot be described by a one-dimensional map as the universality requires.

The question that arises is how does the divisive inhibition in the ESD model ensure Feigenbaum behavior preventing any abrupt transitions? Can this observation be generalized to all possible parameter sets that produce transitions to chaos through period-doubling cascade? Studies on non-Feigenbaum behavior suggest that phenomena of codimension-2 or higher can disturb the period-doubling curves in their neighborhood, resulting in arbitrarily abrupt transitions (Kuznetsov *et al.* (1997)). In Fig. 2.4, the bifurcation diagrams include also the Andronov-Hopf bifurcation curve and the saddle-node (also known as fold) bifurcation curve along with the period-doubling bifurcation curves. The $ES\acute{S}$ diagram reveals a codimension-2 bifurcation called zero-Hopf bifurcation (or fold-Hopf) at the point where the two bifurcation curves tangentially intersect (Guckenheimer and Kuznetsov (2007)). As the $\hat{\delta}$ value indicates, the period-doubling bifurcation curves are disturbed near the zero-Hopf bifurcation resulting into a non-Feigenbaum behavior. For higher values of w_{ds}, though, away from the zero-Hopf bifurcation point, the $\hat{\delta}$ value returns to values near the Feigenbaum constant. A branch of subcritical Neimark-Sacker bifurcation also appears in Fig. 2.4(a), originating from the zero-Hopf point as expected (Guckenheimer and Kuznetsov (2007)). This results in the appearance of an unstable torus in phase space for parameter values between the Andronov-Hopf and Neimark-Sacker bifurcation

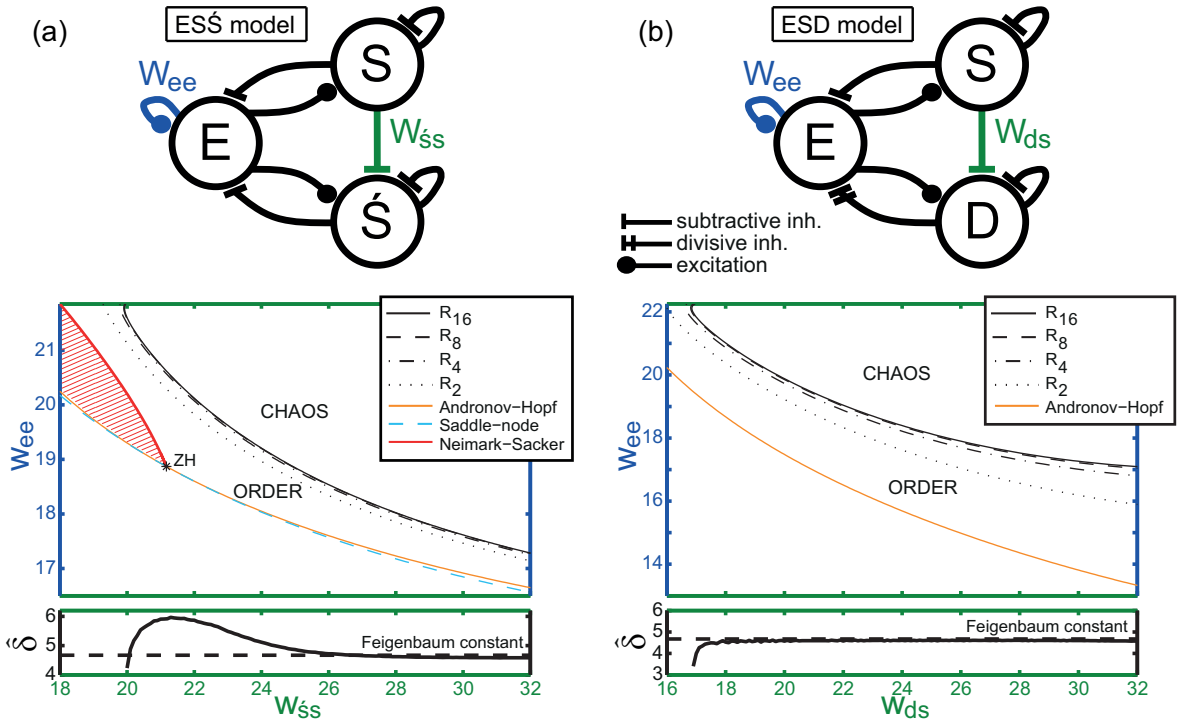

Figure 2.4: Zero-Hopf (ZH) and Neimark-Sacker bifurcations are implicated in the non-Feigenbaum behavior of the $ES\acute{S}$ model. The Andronov-Hopf bifurcation curves (orange) are plotted alongside the period-doubling bifurcation curves for both the $ES\acute{S}$ and ESD model. A saddle-node bifurcation curve (cyan) was also found near the Andronov-Hopf curve only in the case of $ES\acute{S}$. These two bifurcation curves tangentially intersect and produce a zero-Hopf (ZH) bifurcation point. Near the ZH point, the value of $\hat{\delta}$ is increased indicating a non-Feigenbaum behavior in the $ES\acute{S}$ model. In contrast, the ESD model does not exhibit any interaction between Andronov-Hopf and saddle-node curves (at least in this example) and the model continues to obey Feigenabum universality. The shaded area indicates the existence of a torus. Other plotting conventions are the same as in Figs. 2.3(a)-2.3(b).

curves (shaded area). Tori (stable and unstable) and quasiperiodic activity are features easily found in the $ES\acute{S}$ model and they are always linked with the zero-Hopf and Neimark-Sacker bifurcations in this model. This and similar findings (see Appendix A) suggest that the appearance of such bifurcations (zero-Hopf and Neimark-Sacker) can be responsible for the non-Feigenbaum behavior and abrupt transitions in our model. The implication of Neimark-Sacker bifurcation in non-Feigenbaum behavior is also documented in another study in which such phenomena are found in a two-dimensional model map (Kuznetsov *et al.* (2005)). Apparently these bifurcations can appear in the $ES\acute{S}$ system but what about the ESD? Does the divisive inhibition prevent such bifurcations for all possible parameter settings?

To address this question I introduce an additional parameter in the ESD model. The

parameter $q \in [0, 1]$ creates a continuum between the two extremes: $ES\acute{S}$ at $q = 0$ and ESD at $q = 1$. With any other value within this range, the secondary inhibitory population of the model exhibits a combination of subtractive and divisive inhibition [for a schematic see Fig. 2.5(a)]. Using this model, it is possible to incorporate the results shown in Figs. 2.3 and 2.4 in a single plot and examine what is the behavior of the model between the two extremes. As shown in Fig. 2.5(d), the behavior of the system switches gradually from non-Feigenbaum ($q < 0.2$) to Feigenbaum ($q > 0.4$). The saddle-node bifurcation curve and also the zero-Hopf bifurcation point are found for low values of q, near the $ES\acute{S}$ extreme. Starting from $q = 0$, the saddle-node bifurcation curve is very close to the Andronov-Hopf bifurcation curve. They tangentially meet each other at the zero-Hopf point and then they diverge rapidly from each other for values of q higher than 0.2. The saddle-node bifurcation curve reaches a cusp point (CP) at around $q = 0.51$ and returns back to lower values of q, preventing any subsequent interactions with the Andronov-Hopf bifurcation curve for high values of q ($q > 0.5$). Note also that at around $q = 0.4$ and $w_{ee} = 18.3$ the two bifurcation curves seem to intersect again but actually they do not; two different fixed points bifurcate separately in this case so no zero-Hopf is produced there. Despite the fact that the cusp point does not always appear in such bifurcation diagrams and therefore the saddle-node bifurcation curve can sometimes reach high values of q (depending on the parameter set used), the two bifurcation curves always seem to diverge from each other for high values of q (data not shown). If this is true for all possible parameter sets, then the appearance of a zero-Hopf bifurcation is impossible for high values of q (near the ESD extreme). Also the presence of the cusp point (CP) indicates that the phenomenon of hysteresis is also possible for low q values. During this phenomenon the whole period-doubling cascade can be skipped and the system can directly transition from a resting state to chaos through a saddle-node bifurcation instead (see Appendix B for an example). Note that the saddle-node bifurcation is considered as the most common transition into seizure dynamics (Jirsa *et al.* (2014)).

Next I examined if it is possible to find any zero-Hopf bifurcation points in the parameter space for high values of q. For this purpose, a numerical optimization approach was used to search for such points in the parameter space for different values of q. In particular, the search starts from random points in the parameter space and tries to converge to a fixed point which undergoes simultaneously saddle-node and

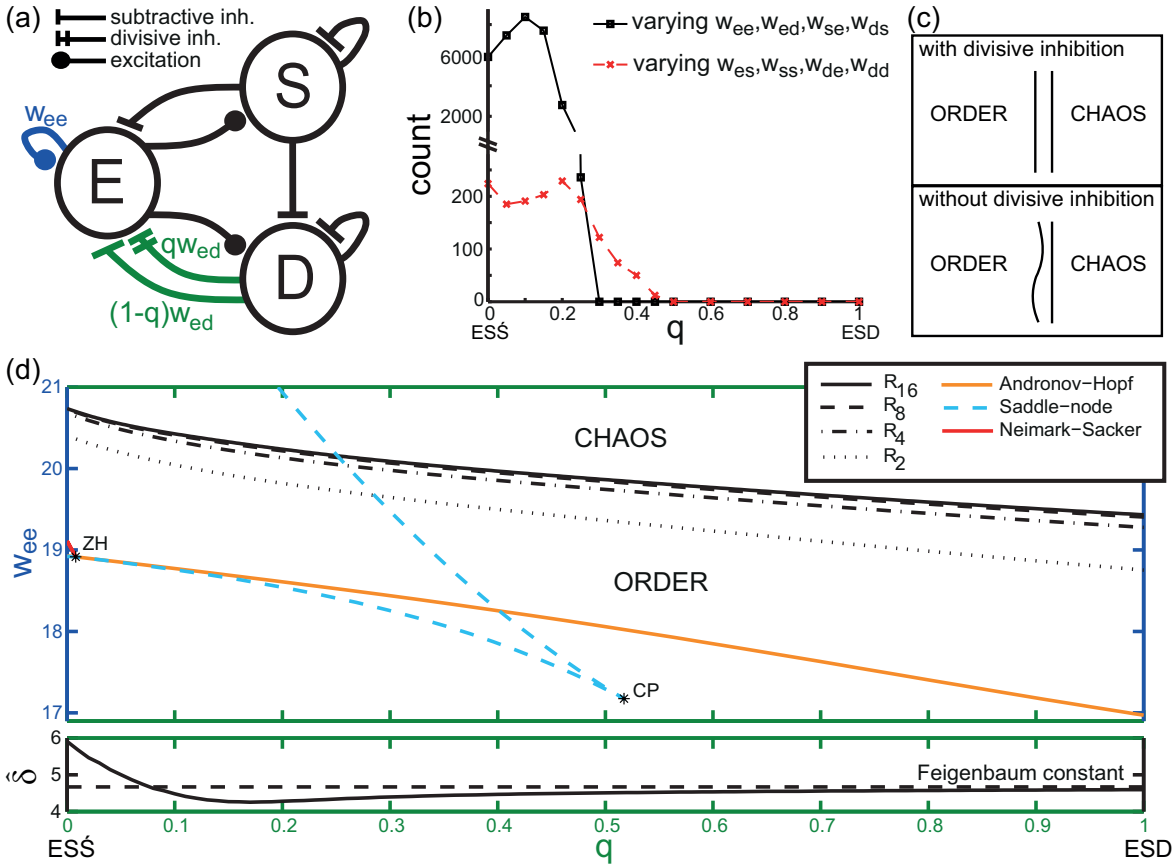

Figure 2.5: Zero-Hopf (ZH) bifurcations can only be found when divisive inhibition is far from being purely divisive (low values of q). (a) Schematic of the model incorporating the q parameter which enables the modeling of nonideal divisive inhibition and creates a spectrum between $ES\acute{S}$ and ESD. (b) Counting the zero-Hopf bifurcations found for different values of q using a random search in the parameter space. (c) Intuitive schematic of how the presence or the absence of the divisive inhibition shapes the boundary between order and chaos. (d) Bifurcation diagram showing an example of the spectrum between $ES\acute{S}$ (for $q = 0$) and ESD (for $q = 1$). Note the presence of the saddle-node curve (cyan) near the Andronov-Hopf curve (orange) only for low values of q.

Andronov-Hopf bifurcations by varying the connectivity parameters. More precisely, the search tries to find fixed points where one of the eigenvalues of the Jacobian matrix is zero, $\lambda_1 = 0$, and the other two are purely imaginary conjugates, $\lambda_{2,3} = \pm i\omega$ (Izhikevich (2007); see Appendix C for details). Running the algorithm multiple times with these criteria, it is expected to reveal multiple occurrences of zero-Hopf bifurcation in the parameter space. The algorithm was tested and successfully managed to find the particular zero-Hopf bifurcation points that were first found by MATCONT and shown in Figs. 2.4 and 2.5, demonstrating its reliability. After multiple runs (10^7 for each q value), the overall results of this search are shown in Fig. 2.5(b). The two curves show all the occurrences of zero-Hopf bifurcation which were found for different values of q. Each curve corresponds to a different subset of varying parameters (see Appendix C for details). Apparently all the zero-Hopf points found in the system are limited in the region near the $ES\acute{S}$ extreme, with $q < 0.5$. This plot clearly shows that it is impossible for the random search algorithm to find any fixed points undergoing a zero-Hopf bifurcation for values of $q \geq 0.5$. This result coupled with some further analysis on the distribution of the zero-Hopf points (see Appendix D) indicates that pure or almost pure divisive inhibition can prevent phenomena like zero-Hopf and Neimark-Sacker bifurcations. Therefore it prevents non-Feigenbaum behavior and abrupt transitions into chaos.

2.4 Discussion

The comparison between a model of neocortical networks with divisive inhibition (ESD, $q = 1$) and an equivalent one without divisive inhibition ($ES\acute{S}$, $q = 0$) suggests that gain control plays a special role in the dynamics of such networks. The present numerical study of the transition from order to chaos in this type of networks shows that pure or almost pure divisive inhibition ensures that the transition always complies with Feigenbaum universality. Complying with Feigenbaum universality means that there is always a well-defined boundary (in relative terms) that separates the regions of order and chaos in the parameter space regardless of the specific values of connectivity weights. In contrast, when the divisive inhibition is replaced by subtractive, the transition can be abrupt or smooth depending on the exact parameter settings of the

network. Without divisive inhibition, the period-doubling transition to chaos can be considered unpredictable. An intuitive representation of the difference between the two cases is depicted in the schematic of Fig. 2.5(c). As outlined in the Introduction, similar findings about divisive inhibition (preventing instabilities and the sensitivity to parameter changes) were found in a recurrent network of interconnected neurons with firing rate dynamics (Chance and Abbott (2000)). This indicates that this effect of divisive inhibition is not limited only to the abstract Wilson-Cowan type of models. Consequently, the role of divisive inhibition is worth investigating also in spiking neural networks that feature gain modulation (e.g., Vogels and Abbott (2005); Litwin-Kumar *et al.* (2016)).

The non-Feigenbaum behavior, which is only found when the inhibition is far from being divisive (low q values), is linked with the appearance of zero-Hopf and Neimark-Sacker bifurcations. In general, when the model lacks divisive inhibition, it seems to have a more diverse dynamic repertoire with the possibility of exhibiting phenomena of codimension-2 or higher. This increased effective dimension of the dynamics might be the underlying explanation for the non-Feigenbaum behavior found in the model, as suggested in Kuznetsov *et al.* (1997). The gain control mechanism prevents these phenomena and therefore prevents non-Feigenbaum critical behavior. Additionally, the simple generic structure of this system suggests that gain control might have a similar effect in structurally equivalent systems.

The model is capable of incorporating mixed effects from divisive and subtractive inhibition (using the parameter q). This is because different factors have been suggested to enable and modulate (possibly in combination) divisive inhibition. Such factors include synaptic noise (Chance *et al.* (2002); Fellous *et al.* (2003)) and target positions on the principal cells of the inhibitory input (Pouille *et al.* (2013)). As both the synaptic noise variance and the target position can vary in a continuous fashion, it is reasonable to include the degree of divisive inhibition as a continuous parameter. I shall elaborate on the implications of linking synaptic noise to our parameter q.

Experimental studies investigated how synaptic noise influences the gain control mechanism of shunting inhibition which is provided primarily by soma-targeting interneurons (Wilson *et al.* (2012)). By simulating the background synaptic noise with

a dynamic clamping technique, it was shown that highly variable synaptic input is required for the modulation of neuronal gain (Chance *et al.* (2002)). A similar *in vitro* approach was taken in Fellous *et al.* (2003), where they controlled the magnitude and the variance of the excitatory and inhibitory conductances independently. In agreement with the previous study, the input-output relationship of pyramidal neurons was divisively modulated proportionally with the variance of the injected conductances. A computational study of this mechanism also demonstrated the importance of highly variable synaptic noise in gain modulation with a biophysically detailed neuron model (Prescott and De Koninck (2003); for a review, see Silver (2010)). In our model, high values of the q parameter can indicate that the network is functioning under high synaptic noise conditions, that is, high variance of the synaptic currents. By linking the parameter q with high synaptic noise, our model provides hypotheses which can be tested either experimentally with electrophysiological setups or computationally with detailed networks of spiking neuron models. For instance, I predict that when the synaptic noise is increased, the possible dynamic phenomena in the network are more limited (no codimension-2 bifurcations), structures such as tori are less likely to arise, the transition to chaos through period-doubling bifurcations follows a Feigenbaum behavior, and the chaotic attractor can be described by a one-dimensional first return map. In experimental setups, the prediction about tori might prove most interesting, as they would correspond to quasiperiodic oscillations or amplitude modulated oscillations (also observed in experiments, Díaz *et al.* (2007)).

Our findings might also have implications in the understanding of pathological dynamics in the brain and the role that gain control may play on their onset. The dynamics in pathologies like epilepsy and Parkinson's disease are characterized by hypersynchronous activity in local networks (Hammond *et al.* (2007); Uhlhaas and Singer (2006)) and, consequently, reduced entropy (Trevelyan *et al.* (2013)). This activity can be either regular or irregular but the common feature is the excessive synchronous activity that is detected in electroencephalogram (EEG) or local field potential (LFP) recordings. Such abnormally synchronous oscillations are also characterized as paroxysmal events, that is, featuring rapid fluctuations between extremely high and low values in the mean-field potential. The transition into chaos in our model can be considered as such a transition to a pathological state exactly because of the paroxysmal oscillations that emerge (e.g., see Fig. 2.8 in Appendix B).

Figure 2.2(a) shows how the local minima get more and more extreme as we progress through the cascade and into the chaotic regime. A similar plot can be produced for the local maxima of the system (not shown) indicating that the range of activity increases while the oscillation becomes more complex. These observations are typical among period-doubling cascades and the resulting chaotic attractors as dictated by the α constant of the Feigenbaum universality (Feigenbaum (1978)). Through these cascades, the activity is pushed to its limits and, consequently, becomes increasingly paroxysmal. Many computational studies modeled pathological dynamics and in particular seizure like activity with chaotic attractors that produce complex paroxysmal oscillations resembling the spike-wave or polyspike-wave complexes usually seen in epilepsy patients' EEG (Freeman (1987); Huang *et al.* (2011); Breakspear *et al.* (2006); Rodrigues *et al.* (2009)). In addition, some of these models feature period-doubling cascades at the onset or offset of the paroxysmal activity (Huang *et al.* (2011); Breakspear *et al.* (2006); Rodrigues *et al.* (2009)). Period-doubling cascades were also detected in the analysis of EEG taken from patients of temporal lobe epilepsy (Perez Velazquez *et al.* (2003)). Hence I suggest that the low-dimensional chaotic attractor as introduced here could be identified as a paroxysmal state, with gain control serving as a way to prevent relatively rapid transitions into such a state.

In more general terms, chaotic dynamics in local networks imply a failure of stable periodic activity that is necessary for long-range synchronization at specific frequencies. Hence, any brain function that relies on stable periodic activity of local neocortical networks would be impaired by the onset of chaos. It is well established that long-range synchronization at α and θ frequencies are crucial for memory and other cognitive functions (Klimesch (1999)). Furthermore, failure in long-range synchronization at β and γ frequencies is associated with pathologies like schizophrenia (Uhlhaas and Singer (2006)). The results presented here suggest that divisive inhibition is responsible for maintaining stable periodic behavior and thus enabling synchronization. Indeed, preliminary simulation results in a paradigm of long-range synchronization between two local networks suggest that the inclusion of divisive inhibition prevents chaotic activity and enhances synchronization. Hence, by preventing abrupt transition into chaos, divisive inhibition could act to prevent the onset of pathological neural dynamics.

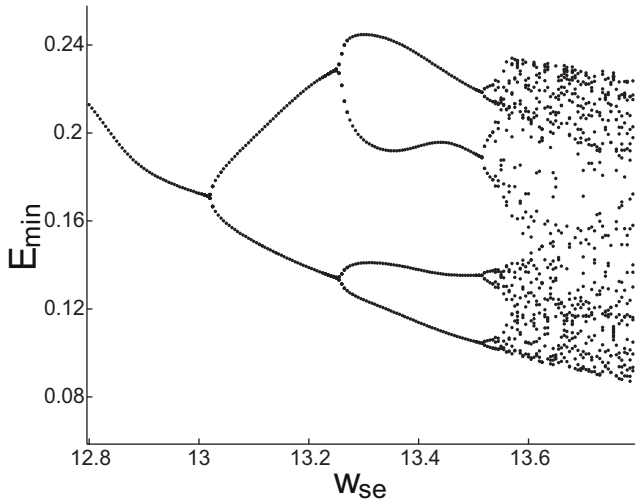

Figure 2.6: Example of an abrupt period-doubling cascade in the $ES\acute{S}$ model. The fourth period-doubling bifurcation comes relatively much more abruptly compared to the previous one ($\hat{\delta} \approx 12.35$).

Appendix A Abrupt period-doubling cascade and non-Feigenbaum behavior in the $ES\acute{S}$ model

Figure 2.6 shows an example of an abrupt period-doubling cascade leading to chaos taken from the $ES\acute{S}$ model. The specific parameters used are given in Table 2.1, Parameter Set 5. Comparing it to the typical, fractal in nature, Feigenbaum cascade in ESD (see Fig. 2.2), this cascade can be considered as a much more abrupt transition into chaos with $\hat{\delta} \approx 12.35$ which is much higher than the Feigenbaum constant (Feigenbaum (1978)).

Figures 2.7(a) and 2.7(b) are showing two more examples of non-Feigenbaum behavior produced by the $ES\acute{S}$ model. The specific parameters used in both cases are given in Table 2.1. The period-doubling bifurcation curves, in both of these examples, are found to be distorted or twisted resulting into values of $\hat{\delta}$ that can vary widely. The presence of the saddle-node bifurcation curves near these cascades is hypothesized to be interfering locally with limit cycles in phase space. This prevents the neighboring limit cycles to bifurcate in a typical Feigenbaum way. Saddle-node and Andronov-Hopf bifurcation curves are also interacting producing the phenomena of zero-Hopf (ZH) and

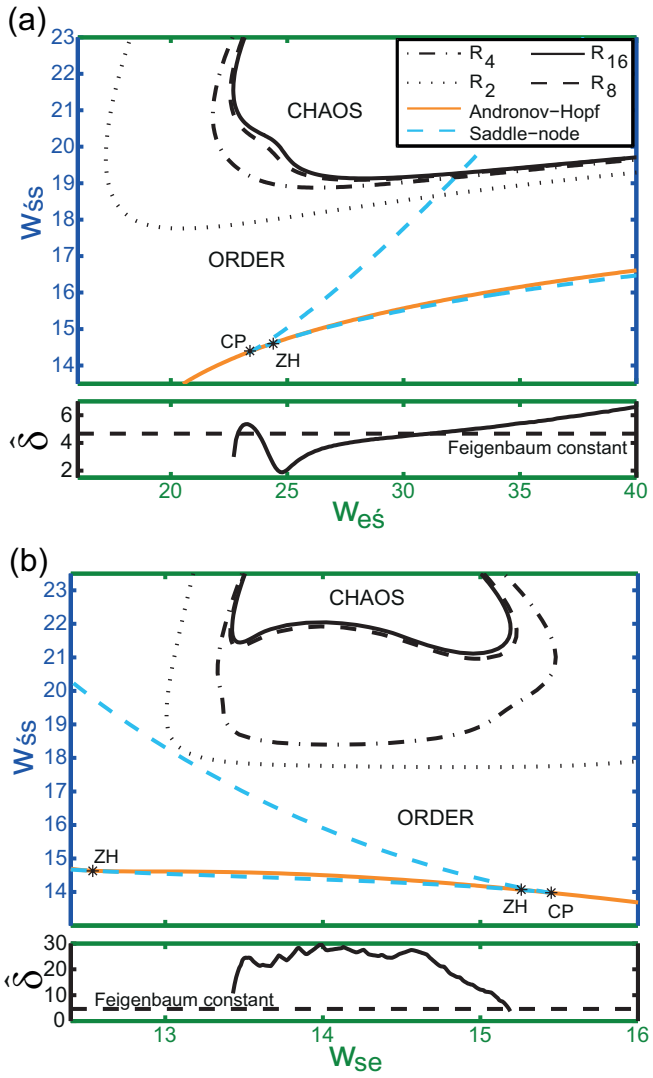

Figure 2.7: Zero-Hopf bifurcation found near the non-Feigenbaum critical behavior in the $ES\acute{S}$ model. The parameter sets for these examples can be found in Table 2.1. The legend applies for both (a) and (b). Other plotting conventions are the same as in Fig. 2.4.

Neimark-Sacker (torus) bifurcations. Such phenomena were implicated in non-Feigenbaum behavior in previous works (Kuznetsov *et al.* (1997, 2005)).

Appendix B Transition to chaos through a saddle-node bifurcation (hysteresis phenomenon)

As shown in Fig. 5(d), the system can enter the chaotic region through a saddle-node bifurcation at low values of q. This is possible as a result of a hysteresis phenomenon.

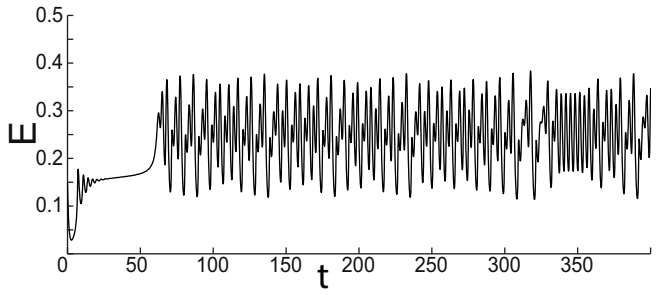

Figure 2.8: Example of the activity entering chaos directly from the resting state. At time point 50, a saddle-node bifurcation occurs and the node on which the activity was resting vanishes. After that point the trajectory converges to the chaotic attractor.

Consider the following scenario. I keep q constant at 0.2. By increasing the parameter w_{ee} from 17 to 19, the activity starts from a resting state (i.e., converges to a stable fixed point) and remains in the resting state despite the appearance of a limit cycle at the Andronov-Hopf curve (at $w_{ee} \approx 18.7$). The system is bistable at this point. Then, by increasing w_{ee} even more, the limit cycle undergoes the period-doubling cascade while the activity remains at rest. At $w_{ee} \approx 21$ the stable fixed point collapses on the saddle point and vanishes (saddle-node bifurcation), leaving the system monostable again with the chaotic attractor as the only attractor in phase space. At this point the system transitions from a resting state to a chaotic state directly. A trace of such a transition can be seen in Fig. 2.8. Until time point 50, the activity is at rest. The saddle-node bifurcation occurs at time point 50 and the activity is chaotic after that. At that time point, the value of the parameter w_{ee} reaches 21. See also Table 2.1 for the rest of the parameters [same as Fig. 5(d)]. Note that this type of bifurcation, the bistable nature of the behavior, and the direct current shift that is present resemble the experimental signature of seizure like event onset (Jirsa *et al.* (2014)).

Appendix C Random search in parameter space for zero-Hopf bifurcations

A nonlinear optimization method was used to find zero-Hopf bifurcations starting from random points in the parameter space. In particular, fminsearch function was used in MATLAB Release 2013b for the reported results. The search tries to find fixed points where one of the eigenvalues of the Jacobian matrix is zero, $\lambda_1 = 0$, and the other two

are purely imaginary conjugates, $\lambda_{2,3} = \pm i\omega$ (Izhikevich (2007)). The algorithm starts from a random point p_0 in the parameter space and tries to solve the optimization problem $\min_p z(p)$ where the function $z(p)$ is given by:

$$z(p) = \sum_i g_i^2 + \prod_i |\lambda_i|^2 + \sum_i \Re(\lambda_i)^2 + (\sum_i \Im(\lambda_i))^2 + l. \tag{2.9}$$

The set p is a set of parameters including the three variables E, S, and D and four connectivity weights w. The functions g_i, $i = \{1, 2, 3\}$, are the right-hand side of the ODEs in Eq. (2.2) in combination with the input-output function in Eq. (2.5). Minimizing these functions to 0 is equivalent as solving the system of the three nullclines and therefore finding a fixed point in the phase space. The eigenvalues λ_i, $i = \{1, 2, 3\}$, are the eigenvalues of the Jacobian matrix of the system. Minimizing the product $\prod_i |\lambda_i|^2$ ensures that at least one of the eigenvalues is 0 which is the criterion for the saddle-node bifurcation. Given that one of the eigenvalues is 0, minimizing the sum $\sum_i \Re(\lambda_i)^2 + (\sum_i \Im(\lambda_i))^2$ ensures that the other two eigenvalues are complex conjugates with zero real parts. This is the criterion for the Andronov-Hopf bifurcation. The penalty term l is a positive number only when the search algorithm diverges outside the valid parameter space in which the search is limited. This number is proportional to the divergence from the valid parameter space. In all other cases $l = 0$.

The valid parameter space is enclosed in the range [0 0.5] for each of the three variables E, S, and D and the range [0 50] for each of the varying connectivity parameter w. The results shown in Fig. 2.5(b) are produced for two different cases, for either $p = \{E, S, D, w_{ee}, w_{ed}, w_{se}, w_{ds}\}$ or $p = \{E, S, D, w_{es}, w_{ss}, w_{de}, w_{dd}\}$. Note that both combinations of the connectivity parameters involve all three nullclines of the system. Given that the parameter space is a seven-dimensional space, for each q value the algorithm was run 10^7 times in order to achieve a reasonably comprehensive search.

Appendix D Distribution of the zero-Hopf phenomena in the parameter space

This section reports some supporting results about the random search which was performed to find zero-Hopf bifurcation points for different values of the parameter q. As shown in Fig. 5(b), the points were only found for low values of q. Varying the parameters w_{es}, w_{ss}, w_{de}, and w_{dd} (red dashed line) all the zero-Hopf points were limited at $q \leq 0.45$. Figure 2.9(a) shows the distribution of these points across the four connectivity parameters. It is evident that all zero-Hopf points are found in a limited range of values below 50 for each parameter. The search was actually limited to values below 50, but even if this limit was higher, it would not return more points. This is true assuming that all zero-Hopf points are lying on a single continuous hypersurface in the parameter space.

Figure 2.9(b) shows the distribution of the same points across the varying parameters w_{ee}, w_{ed}, w_{se}, and w_{ds} [black solid line in Fig. 5(b)]. In this case it is apparent that as the q value increases, the zero-Hopf points are found at increasingly higher values of w_{ed}. At $q = 0.25$, the ZH points are actually found near the arbitrarily chosen upper limit of 50 for w_{ed}. This suggests that our results might be biased. The other three parameters (w_{ee}, w_{se}, and w_{ds}) are clearly limited to values lower than 50 so they do not raise any concerns. In order to check whether more ZH points can be found for higher values of q by varying these parameters, the valid ranges for parameter values were expanded to [0 200] for w_{ed} and [0 100] for the other three parameters. The random search was run again and indeed a few more ZH points were found for $q = 0.3$ and $q = 0.35$. For these additional ZH points, w_{ed} has very high values (in the range [150 200]), whereas the other three parameters remain very limited to values below 50 (data not shown). Apparently, the hypersurface that accommodates the ZH points collapses on just one parameter, namely w_{ed}. This result suggests that it might be possible to produce zero-Hopf phenomena even for high values of q just by keep increasing disproportionally w_{ed} while the other parameters remain stable at low values. It is also evident from the previously reported results [e.g., see Figs. 2.3 and 2.7(a)] that the chaotic region can actually be extended for high values of w_{ed}. But as Fig. 2.10 shows, the chaotic attractor quickly flattens out as w_{ed} increases. The

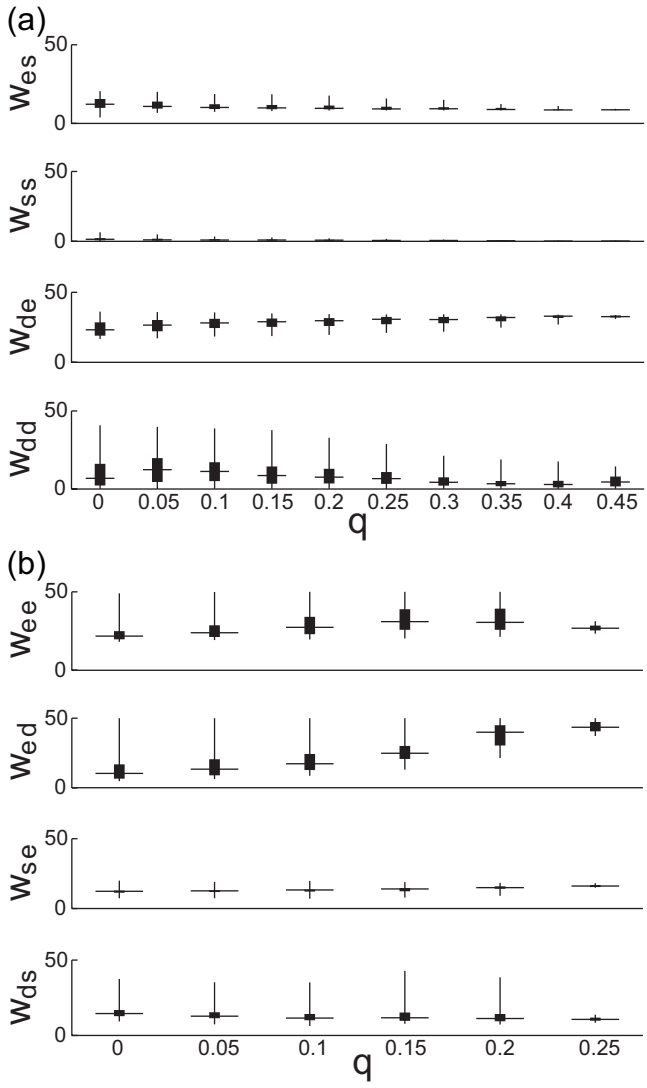

Figure 2.9: Box plots showing the distribution of ZH points found in the parameter space for the four varying parameters (a) $\{w_{es}, w_{ss}, w_{de}, w_{dd}\}$ and (b) $\{w_{ee}, w_{ed}, w_{se}, w_{ds}\}$. The horizontal line indicates the median value, the box edges indicate the 25th and 75th percentiles and the whiskers extend to include the whole range of values. (a) As q increases, the ZH points are found in an increasingly limited range of values below 50. (b) In contrast, the values for the parameter w_{ed} are increasing as q increases and they reach the upper limit of 50.

max-min amplitude along the dimension D decreases much faster than the max-min amplitude along the other two dimensions making the attractor almost a two-dimensional object in phase space. This flattening of the attractor defeats its modeling purpose. Assuming that all the parameters have the same order to magnitude, ZH points cannot be found for high values of q.

So based on these results and assuming that all zero-Hopf points are lying on a single continuous hypersurface and also assuming that all connectivity parameter values have the same order of magnitude, no zero-Hopf bifurcations can be found in a model with

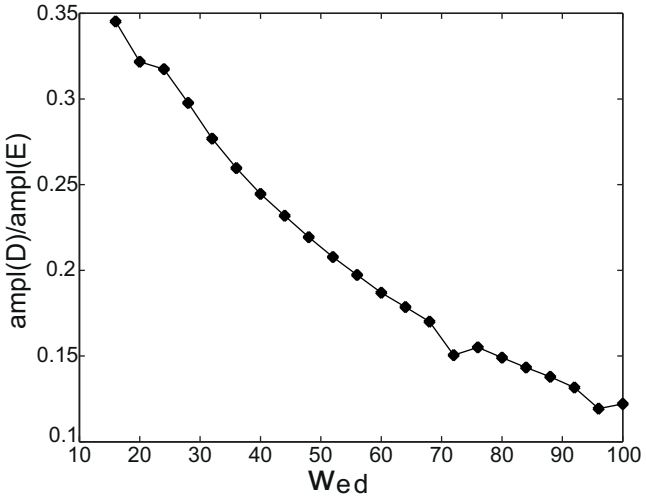

Figure 2.10: Increasing w_{ed} and keeping everything else constant quickly flattens out the chaotic attractor. Ampl(X) denotes the max-min amplitude in dimension X. Note that $q = 1$ in this case. See also Table 2.1 for the rest of the parameter values.

strong divisive inhibition (high q value) and therefore any abrupt period-doubling transition to chaos is prevented.

Chapter 3

Gain control through divisive inhibition enhances entrainment and long-range synchronization in a neural mass model

3.1 Introduction

Neural networks exhibit a diverse dynamic repertoire at macroscopic and microscopic scales as evidenced in electrophysiological recordings or through imaging (Wright and Liley (1996); Chialvo (2010); Buzsáki (2006); Vogels *et al.* (2005)). The oscillatory activity often seen in such data is part of this repertoire and it is understood that it plays a crucial role in information processing and many cognitive processes (Klimesch (1999); Buzsáki and Draguhn (2004); Buzsáki (2006)). Neural oscillations are considered an efficient way to achieve temporal coordination among neurons (Laurent (2002)) and, thus, a way to enable the integration of information and the facilitation of synaptic plasticity (Buzsáki and Draguhn (2004)). Specific frequency bands of oscillations are known to subserve specific cognitive processes. Studies showed, for example, that memory and attention are associated with gamma oscillations (30-80 Hz)

and deficiencies of such oscillatory behaviour are linked to neurological and psychiatric disorders (Schnitzler and Gross (2005); LeBeau (2013)).

Neural networks were found to resonate in particular frequencies, that is, their oscillations are stronger in these frequencies (Herrmann (2001); Hutcheon and Yarom (2000)). The resonant frequencies of the networks depend on factors like the resonance of the neurons that compose the network, the connectivity between them and the size of the network (Pike *et al.* (2000); Stark *et al.* (2013); Lea-Carnall *et al.* (2016); Masuda and Aihara (2004)). It has been demonstrated through electroencephalogram (EEG) or magnetoencephalogram (MEG) recordings that the frequency of oscillation can be adjusted to match the stimulation frequency and this is usually done by external stimulation, like photic driving or transcranial magnetic stimulation (TMS) (Schwab *et al.* (2006); Thut *et al.* (2011)). This phenomenon is called entrainment. The ability of the networks to be entrained is not limited only under the conditions of external stimulation. It has been demonstrated that endogenous electric fields that are generated in neocortex can entrain network activity as well (Froehlich and McCormick (2010)). It has also been shown that the phenomenon of entrainment can emerge in a network model with a biologically realistic spike-timing-dependent plasticity with asymmetric learning windows, demonstrating its universality (Masuda and Kori (2007)). Networks' ability of entrainment is an indication of functional flexibility and consequently of healthy brain dynamics (Schwab *et al.* (2006); Spiegler *et al.* (2011)).

Distributed neural networks have also the ability to synchronize despite long conduction delays. The oscillatory activity of distant networks interacting through long-range connections, with axonal conduction delays of tens of milliseconds (Swadlow and Waxman (2012)), can be synchronous in particular frequency bands (Belluscio *et al.* (2012); Linkenkaer-Hansen *et al.* (2001)). The synchronization between two signals is traditionally considered in terms of their similarity in the time domain. In particular cases of connectivity, cortico-cortical or cortico-thalamic circuits are able to diminish any phase shift or time lag in long-range synchronization through the self-organizing process of dynamical relaying (Fischer *et al.* (2006); Vicente *et al.* (2008)). However, synchronization can be also defined as an interdependency or correlation between other aspects of the signals, such as amplitude, frequency or phase (Quian Quiroga *et al.* (2002)). The widely documented phase synchronization

phenomenon, for example, is known to subserve memory and cognition as evidenced by EEG studies (for a review, see Fell and Axmacher (2011)).

Dynamic phenomena such as these were extensively investigated through computational models (Vogels *et al.* (2005); Deco *et al.* (2008)). Neural mass models like the Wilson-Cowan oscillators (Wilson and Cowan (1972); Cowan *et al.* (2016); Lea-Carnall *et al.* (2016); Spiegler *et al.* (2011); Gollo *et al.* (2014)) and the Jansen-Ritt model (Jansen and Rit (1995); Moran *et al.* (2007)) are considered appropriate for this purpose because of their ability to model easily such abstract and macroscopic phenomena. Lea-Carnall *et al.* (2016) used coupled Wilson-Cowan oscillators to explore how network size, connectivity and delays influence the resonance properties of a cortical area. Spiegler *et al.* (2011) investigated the mechanisms of entrainment in a Jansen-Rit neural mass model and reproduced the phenomenon as seen in EEG. Borisyuk *et al.* (1995) used coupled Wilson-Cowan oscillators to investigate their synchronization using different types of long-range connections. Other studies focused on how different cortical motifs can achieve zero-lag synchronization across different scales of abstraction (Viriyopase *et al.* (2012); Gollo *et al.* (2014)) or how the coupling strength and the conduction delays influence the synchronization between two coupled networks (David and Friston (2003); Huang *et al.* (2011)).

Despite the fact that there is an extensive literature about this topic, the role of different inhibitory mechanisms has not been investigated computationally, perhaps because the classic neural mass models feature only subtractive inhibition. The difference between subtractive inhibition, which provides a hyperpolarizing effect, and divisive inhibition, which provides gain control, is well established for decades now (Silver (2010); Ayaz and Chance (2012)). Recent experimental findings in cortical circuits, though, linked these mechanisms with the dendrite-targeting (somatostatin-positive) and the soma-targeting (parvalbumin-positive) interneurons (Wilson *et al.* (2012); Atallah *et al.* (2012); Pouille *et al.* (2009)), respectively, reviving the interest in them (Litwin-Kumar *et al.* (2016)). In addition, recent experimental and computational studies showed that it is precisely this difference in their targeting that enables their different effects (Jadi *et al.* (2012); Pouille *et al.* (2013)). So, considering the fact that divisive inhibition was shown to have a positive impact on the stability of the dynamics and robustness of oscillations in local recurrent networks (Chance and

Abbott (2000); Vida *et al.* (2006); Papasavvas *et al.* (2015)), it would also be appropriate to explore its effect on entrainment and global long-range synchronization in particular while incorporating the new experimental findings.

As mentioned above, abnormalities in the oscillatory behaviour of neural networks are usually indicative of a psychiatric or neurological disorder (Schnitzler and Gross (2005); LeBeau (2013)). More specifically, the phenomena of entrainment and long-range synchronization are known to be deficient in pathologies like schizophrenia and Alzheimer's disease. In fact, impairment in entrainment is suggested as a biomarker for the pathology of schizophrenia (Brenner *et al.* (2003); Hamm *et al.* (2015)). In addition, long-range synchronization was repeatedly found impaired in schizophrenics, especially in beta and gamma frequency bands (Uhlhaas and Singer (2010); Pittman-Polletta *et al.* (2015); Schnitzler and Gross (2005)). Similar deficiencies were reported for Alzheimer's disease as well (Uhlhaas and Singer (2006); Stam *et al.* (2003); Schnitzler and Gross (2005)).

In this study I investigate the role of divisive inhibition in the phenomena of entrainment and long-range synchronization in a neural mass model. The model used is an extended and more versatile version of the Wilson-Cowan model that incorporates gain control through divisive inhibition (Papasavvas *et al.* (2015)). A network model with divisive inhibition is compared with a model without divisive inhibition in both entrainment and long-range synchronization. The effect of divisive inhibition is then generalized across the parameter space by random generation of the parameter sets.

3.2 Methods

3.2.1 Modelling framework

Modulation of the input-output function The models used in this study are an extended version of the spatially localized Wilson-Cowan model (Wilson and Cowan (1972)). These models feature one excitatory population and two inhibitory populations. They also feature divisive inhibition in addition to the subtractive inhibition that the original Wilson-Cowan model uses. This modelling framework was

introduced in Papasavvas *et al.* (2015). The divisive inhibition is possible by using a more versatile input-output function that accepts three variables: the input x, the subtractive modulation θ, and the divisive modulation α.

$$F_j(x, \theta, \alpha) = \frac{1}{1 + \exp\left[-\frac{\alpha_j}{1+\alpha}(x - (\theta_j + \theta))\right]} - \frac{1}{1 + \exp\left[\frac{\alpha_j \theta_j}{1+\alpha}\right]}, \tag{3.1}$$

for $j \in \{e, i\}$, where e stands for excitatory and i stands for inhibitory. Note that this equation is the same as Eq. (2.1). With this definition for the sigmoidal input-output function, the model can exhibit a dynamic gain control, through divisive inhibition, in addition to the hyperpolarizing effect of the subtractive inhibition. For more details on how this definition relates to and expands on the original Wilson-Cowan formulation see Papasavvas *et al.* (2015).

Single local network for the scenario of entrainment Using the input-output function F_j in Eq. (3.1), we can now describe a recurrent local network with one excitatory population ($E(t)$) and two inhibitory populations: one representing the dendrite-targeting interneurons providing subtractive inhibition ($I_{dend}(t)$) and the other representing the soma-targeting interneurons providing divisive inhibition ($I_{soma}(t)$). Note that the divisive inhibition is provided only onto the excitatory population. The three populations and their connectivity between them (based on the anatomical study of primary visual cortex in Pfeffer *et al.* (2013)) is described by the following system of ordinary differential equations (ODEs):

$$\begin{aligned}
\tau \frac{dE(t)}{dt} &= -E(t) + (k_e - E(t)) F_e(w_1 E(t) + P(t), w_2 I_{dend}(t), w_3 I_{soma}(t)), \\
\tau \frac{dI_{dend}(t)}{dt} &= -I_{dend}(t) + (k_i - I_{dend}(t)) F_i(w_4 E(t), 0, 0), \\
\tau \frac{dI_{soma}(t)}{dt} &= -I_{soma}(t) + (k_i - I_{soma}(t)) F_i(w_5 E(t), w_6 I_{dend}(t) + w_7 I_{soma}(t), 0).
\end{aligned} \tag{3.2}$$

For comparison, another local network was designed which differs in only one

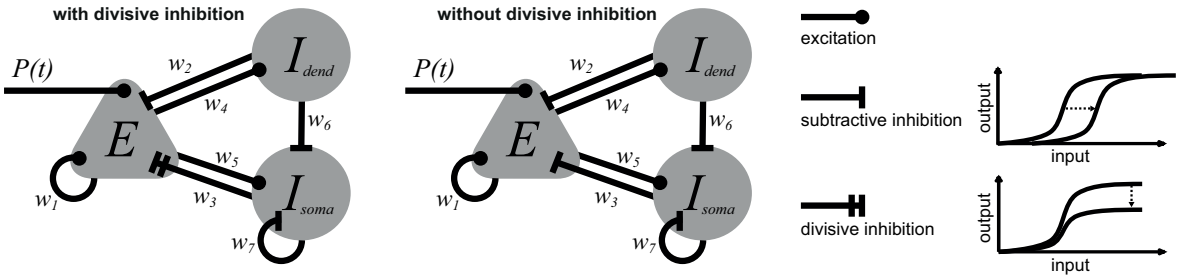

Figure 3.1: The models under comparison: with and without divisive inhibition. Schematics of the local network models that are being compared. They feature one excitatory (E) and two inhibitory populations (I_{dend} and I_{soma}). Note the different quality of inhibition that is delivered by I_{soma} onto E. The panels on the right show how the input-output function is modulated by the subtractive and divisive inhibition.

qualitative aspect: it does not feature divisive inhibition, that is, the soma-targeting interneurons (I_{soma}) provide subtractive inhibition instead. This is modelled using the following system:

$$\begin{aligned}
\tau\frac{dE(t)}{dt} &= -E(t) + (k_e - E(t))F_e(w_1E(t) + P(t), w_2I_{dend}(t) + w_3I_{soma}(t), 0),\\
\tau\frac{dI_{dend}(t)}{dt} &= -I_{dend}(t) + (k_i - I_{dend}(t))F_i(w_4E(t), 0, 0),\\
\tau\frac{dI_{soma}(t)}{dt} &= -I_{soma}(t) + (k_i - I_{soma}(t))F_i(w_5E(t), w_6I_{dend}(t) + w_7I_{soma}(t), 0),
\end{aligned} \tag{3.3}$$

where

$$k_j = \lim_{x\to+\infty} F_j(x,\theta,\alpha) = \frac{\exp\left[\frac{\alpha_j\theta_j}{1+\alpha}\right]}{1+\exp\left[\frac{\alpha_j\theta_j}{1+\alpha}\right]}, \tag{3.4}$$

for $j \in \{e, i\}$, which applies for both Eqs. (3.2) and (3.3). In Fig 3.1 you can see a schematic for each local network. The parameters chosen for the input-output functions F_j (Eq. (3.1)) are: $\theta_e = 4$, $\theta_i = 3.7$, $\alpha_e = 1.3$, and $\alpha_i = 2$ for both models.

The time constant τ in both systems (Eqs. (3.2) and (3.3)) was set to $\tau = 0.05$. This value was chosen based on the response of both systems to an instantaneous input, as shown in Fig 3.8. The figure shows both networks responding with an exponential

decay after an instantaneous input at time $t_0 = 100$ ms. This decay has a characteristic half-life $t_{1/2} = 39.8$ ms. Based on this, the value of time constant τ was chosen to yield $t_{1/2} \approx 40$ ms which is a good approximation of the response of electrically stimulated neocortical networks in electrophysiological experiments (Alfonsa *et al.* (2015)). Coincidentally, this value of τ sets the range of intrinsic frequencies for the model of cortical networks to the physiologically relevant theta range (Stark *et al.* (2013)).

The connectivity parameters between the populations were set to $w_1 = 14.5$, $w_2 = 12$, $w_4 = 14$, $w_5 = 20$, and $w_6 = 16$ for both systems whereas $w_3 = 15$ and $w_7 = 8$ for the case of the network with divisive inhibition (Eq. (3.2)) and $w_3 = 8$ and $w_7 = 20.5$ for the case of the network without divisive inhibition (Eq. (3.3)). This difference in the connectivity parameters between the two cases is used to set the two networks in a comparable dynamic regime. Their dynamic regime is explored by their bifurcation diagram shown in Fig 3.8 (produced using the toolbox MATCONT; Dhooge *et al.* (2003)). This diagram shows the bifurcations of the two systems by varying the value of a time-independent input, $P(t) = P$. Moreover, Fig 3.8 shows the frequency of oscillation for each network against its relevant values of P; note that the range of values P that cause oscillations are different for each network. These frequencies, which belong to theta band, can be considered as the frequencies at which the networks resonate; they are thought as the preferred or intrinsic frequencies. Fig 3.8 shows that the two networks have comparable oscillating behaviour, at least in the interval $2 \leq P \leq 4.5$. Specifically, their oscillatory behaviour is comparable in terms of frequency, amplitude, and offset for the chosen set of connectivity parameters w_j. Note that these comparable settings can only serve as an illustrative example for the comparison. The main findings of this comparison will be generalized at the end by randomly sampling the parameter space.

Coupled local networks for the scenario of synchronization For the scenario of long-range synchronization, in which two local networks interact with each other, a six-dimensional system of delayed differential equations (DDEs) was used instead. The set of variables in this case is $\{E(t),\, I_{dend}(t),\, I_{soma}(t),\, \bar{E}(t),\, \bar{I}_{dend}(t),\, \bar{I}_{soma}(t)\}$ where barred variables represent the second local network. The system that features divisive inhibition, using Eq. (3.2) as a building block, is given by:

$$
\begin{aligned}
\tau\frac{dE(t)}{dt} &= -E(t) + (k_e - E(t))F_e(w_1E(t) + c_1\bar{E}(t-t_{del}) + P, w_2I_{dend}(t), w_3I_{soma}(t)),\\
\tau\frac{dI_{dend}(t)}{dt} &= -I_{dend}(t) + (k_i - I_{dend}(t))F_i(w_4E(t), 0, 0),\\
\tau\frac{dI_{soma}(t)}{dt} &= -I_{soma}(t) + (k_i - I_{soma}(t))F_i(w_5E(t), w_6I_{dend}(t) + w_7I_{soma}(t), 0),\\
\tau\frac{d\bar{E}(t)}{dt} &= -\bar{E}(t) + (k_e - \bar{E}(t))F_e(w_1\bar{E}(t) + c_2E(t-t_{del}) + P, w_2\bar{I}_{dend}(t), w_3\bar{I}_{soma}(t)),\\
\tau\frac{d\bar{I}_{dend}(t)}{dt} &= -\bar{I}_{dend}(t) + (k_i - \bar{I}_{dend}(t))F_i(w_4\bar{E}(t), 0, 0),\\
\tau\frac{d\bar{I}_{soma}(t)}{dt} &= -\bar{I}_{soma}(t) + (k_i - \bar{I}_{soma}(t))F_i(w_5\bar{E}(t), w_6\bar{I}_{dend}(t) + w_7\bar{I}_{soma}(t), 0).
\end{aligned}
\tag{3.5}
$$

Note the long-range connections c_1 and c_2 connecting the two local networks with conduction delay t_{del}. These connections are between the excitatory populations. Note also that I consider the case of coupled identical oscillators here, that is, both local networks have the same connectivity parameters w_j (same values as above) and receive the same constant input $P = 2$ to produce a baseline oscillatory activity.

Similarly, I used another six-dimensional system of DDEs comprising two local networks without divisive inhibition using Eq. (3.3) as a building block.

The simulations were carried out in MATLAB Release 2013b (The MathWorks, Inc., Natick, MA) using the built in integrators `ode45` and `dde23` for the ODEs and DDEs, respectively.

Nonideal divisive inhibition For the purpose of generalizing the results at the final stage of this study, another version of the model is used. This version, with the inclusion of an extra parameter q, produces a spectrum between the two extremes described by the Eqs. (3.2) and (3.3). In this version, the soma-targeting interneurons, I_{soma}, can provide both subtractive and divisive inhibition to the excitatory population at the same time and the proportion of each quality is dictated by the parameter q. By varying the parameter q from 0 to 1, it is possible to scan the spectrum from the case of a purely subtractive to the case of a purely divisive inhibition being delivered from

the soma-targeting interneurons. With any other value in between, the modulation has a mixture of subtractive and divisive quality with proportions $1-q$ and q, respectively. Note that the overall weight of the connection between I_{soma} and E remains the same and is given by w_3. This model can be considered as a model featuring a nonideal, more biologically realistic version of divisive inhibition. To implement this, only the input-output function of the excitatory population, $F_e(x,\theta,\alpha)$, needs to be updated:

$$F_e(x,\theta,\alpha) = \frac{1}{1+\exp\left[-\frac{\alpha_e}{1+q\alpha}(x-(\theta_e+\theta+(1-q)\alpha))\right]} - \frac{1}{1+\exp\left[\frac{\alpha_e\theta_e}{1+q\alpha}\right]}, \tag{3.6}$$

and, consequently,

$$k_e = \lim_{x\to+\infty} F_e(x,\theta,\alpha) = \frac{\exp\left[\frac{\alpha_e\theta_e}{1+q\alpha}\right]}{1+\exp\left[\frac{\alpha_e\theta_e}{1+q\alpha}\right]}. \tag{3.7}$$

This updated input-output function of the excitatory population can be used in conjunction with the systems of ODEs or DDEs described in Eqs. (3.2) and (3.5), respectively.

3.2.2 Entrainment measure

The entrainment of a local network to an oscillatory input (sinusoidal) with frequency f_{in} is measured by calculating the discrete Fourier transform (using `fft` in MATLAB) of the response of the network (after the initial transient activity) and specifically the response of the excitatory population, $E(t)$. After removing the harmonics, the transform E_k is then normalized so that $\sum_k E_k = 1$. Finally, the entrainment of the network to an input frequency f_{in} is given by $E_{f_{in}}$. This measures the proportion of the power concentrated at the input frequency f_{in} in the power spectrum. This can take values from 0 to 1 with 0 denoting no entrainment and 1 denoting complete entrainment.

3.2.3 Synchronization measures

In order to measure synchronization between two local networks, two synchronization measures were used: cross-correlation and phase synchronization. Both of these measures quantify the interdependence between two signals based on different aspects (Quian Quiroga *et al.* (2002)). The signals on which these measures were applied are the activities of the two excitatory populations, $E(t)$ and $\bar{E}(t)$ in Eq. (3.5).

Cross-correlation Cross-correlation is a linear measure that quantifies similarities of the two signals in the time domain. The cross-correlation between two signals, x_n and y_n $(n = 1, \ldots, N)$, is given by:

$$r(m) = \frac{1}{N-m} \sum_{n=1}^{N-m} \frac{(x_n - \mu_x)(y_{n+m} - \mu_y)}{\sigma_x \sigma_y}, \tag{3.8}$$

where μ_x and σ_x are the mean and standard deviation of the signal x, respectively. In the results, the reported value of cross-correlation is the maximum value of $r(m)$. The respective lag $m = \arg\max_m r(m)$ at which the maximum occurs is reported as well.

Phase synchronization Phase synchronization measures can detect interdependencies between two signals in an alternative way. They are based on a flexible measure of the phase difference between the signals. Instead of focusing on the time domain, phase synchronization can detect any *locking* between the phases of the two signals even if the signals are composed of completely different frequencies.

In this study, it was measured by calculating first the Hilbert transformation (phase ϕ) of the signals using the `hilbert` function in MATLAB and then the phase difference between them:

$$\phi_{xy}(t) = u\phi_x(t) - v\phi_y(t) \tag{3.9}$$

with u, v some integers. The phase synchronization index is thus given by:

$$\gamma = \sqrt{\langle \cos \phi_{xy}(t) \rangle_t^2 + \langle \sin \phi_{xy}(t) \rangle_t^2} \tag{3.10}$$

In every case, the γ reported as a result is the maximum across the different ratios of

integers u and v. The ratios $u : v$ that are used are $\{1{:}1,\ 1{:}2,\ 2{:}1,\ \ldots,\ 3{:}4,\ \ldots,\ 5{:}1\}$. For more information on phase synchronization see Quian Quiroga *et al.* (2002).

3.3 Results

3.3.1 Entrainment

First I investigated the role of divisive inhibition in the scenario of entrainment. In this scenario, a local network, with its own resonant or preferred frequency of oscillation, receives a sinusoidal input and its entrainment to the input frequency is measured. This is carried out with both networks: with and without divisive inhibition. See Fig 3.2A for a schematic of this scenario and Methods for a description of the two models and the measurement of entrainment.

The sinusoidal input was modelled as $P(t) = P + A\sin(2\pi f_{in} t)$. The entrainment was measured in the interval of input frequencies, f_{in}, from 0.25 to 40 Hz. The average oscillating input $\langle P(t) \rangle$, or equivalently its offset P, is varied in the interval $[1.5,\ 4.3]$ and $[1.9,\ 4.3]$ for the cases of the networks with and without divisive inhibition, respectively. These intervals are the intervals in which the two networks produce oscillatory behaviour in the presence of a steady, time-invariant input P (see Fig 3.8). The amplitude A of the sinusoidal input is equal to 0.5 for this set of results.

The two models behave differently under this scenario. The model featuring divisive inhibition exhibits enhanced entrainment compared to the other. The results comparing the two models can be found in Fig 3.2B. The green lines represent the preferred frequencies of oscillation for each different value of P. These preferred or intrinsic frequencies are the same frequencies presented in Fig 3.8. As expected, both models can be completely entrained to input frequencies f_{in} that are close to their preferred as shown by the white areas in the heat maps. Note that for the model with divisive inhibition the white area is wider especially for low values of f_{in} and P. In contrast, both models fail to get entrained in the black areas and in this case these areas are wider for the model without divisive inhibition. Note that these black areas are close to the harmonics of the preferred frequencies. Finally, the coloured areas

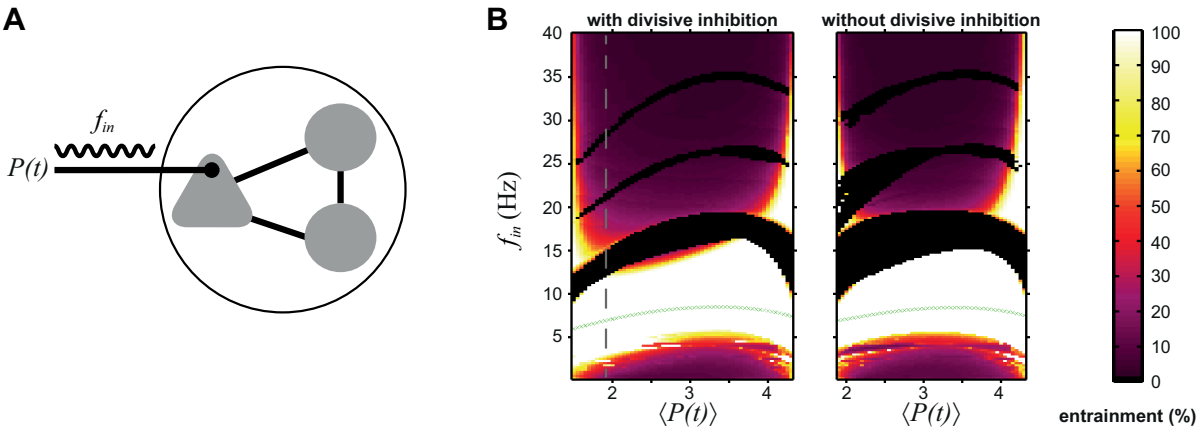

Figure 3.2: Entrainment of the network with and without divisive inhibition. (A) Schematic of the entrainment scenario: a local network with three populations receiving an oscillating input with frequency f_{in}. This input is delivered only to the excitatory population. Note that the details about the connectivity between the populations are not included in this schematic: this local network can be considered as either featuring divisive inhibition or not (see Fig. 3.1 for the connectivity details). (B) Measured entrainment for different values of input frequency f_{in} and input average $\langle P(t) \rangle$ for both local networks: with and without divisive inhibition. The green lines represent the intrinsic frequencies of the networks (see also Fig 3.8). The white areas close to the intrinsic frequencies indicate a complete entrainment in which the networks respond with an oscillation that matches the input frequency. The black areas indicate a failure in entrainment whereas any other colour indicates partial entrainment: the input frequency is just one among many frequencies found in the power spectrum of the activity. Examples of partial and failed entrainment can be found in Fig 3.9. Note that the range of values on the x-axis is different between the two networks (see also Fig 3.8). For comparison, the grey dashed line on the left heat map matches the lower x-value on the right heat map. The two heat maps suggest that, at least for low values of $\langle P(t) \rangle$ ($\langle P(t) \rangle < 3.2$), the model with divisive inhibition achieves entrainment in a wider range of input frequencies f_{in}.

indicate partial entrainment, which means that the power spectrum of the network's response features multiple peaks and one of them is located at f_{in}. In these cases the activity is usually quasi-periodic (see also *phase drift*; Ermentrout and Kopell (1991)) and sometimes chaotic featuring a complex waveform with many different frequencies. The heat maps reveal many areas where the network with divisive inhibition exhibits partial entrainment whereas the model without divisive inhibition fails completely. An example of such waveforms can be seen in Fig 3.9 where both models receive the same input ($f_{in} = 16$ Hz and $P = 2$) but only the model with divisive inhibition achieves partial entrainment with quasi-periodic activity whereas the model without divisive inhibition oscillates at its intrinsic frequency alone.

In general, the network with divisive inhibition can be entrained, completely or partially, to a wider range of input frequencies f_{in} as compared with the network

lacking divisive inhibition. This is apparent especially for $P < 3.2$. For higher values of P the two heat maps look very similar with no obvious difference between the two cases. This can be explained by the fact that with increasing P, the activity of the populations E and I_{dend} is increasing, but the activity of I_{soma} is decreasing for both models (see Fig 3.8). The contribution of the relevant population I_{soma} to the network's dynamics is monotonically decreasing from approximately 10% at $P = 2$ to approximately 2% at $P = 3.2$ and this is due to the disinhibitory connection w_6. So by diminishing the effect of the relevant population I_{soma}, which either delivers divisive inhibition or not, it is expected that the behaviour of the two models will become almost identical. This diminishing effect is true at least for this specific parameter set which is used as an illustrative example for the comparison.

3.3.2 Long-range synchronization

In the scenario of long-range synchronization, two local networks are coupled with excitatory connections between their excitatory populations. The weights of these connections are given by c_1 and c_2. These connections are considered to be long-range connections so they introduce a conduction delay into the system. More specifically, in this study, they are considered to have the same conduction delay. In addition, the excitatory populations receive the same external input P inducing the same oscillatory behaviour in each local network. A schematic of this scenario can be seen in Fig 3.3A.

Cross-correlation with symmetrical long-range connection weights without delay. The comparison between the models with and without divisive inhibition for the synchronization scenario starts considering the case of symmetry and no delay. In the case of symmetry, I consider the long-range connections to be equal, $c = c_1 = c_2$. In the case of no delay, I consider the same connections introducing a delay of 0, $t_{del} = 0$. As expected, when these apply and additionally the local networks have the same initial conditions ($\{E(0), I_{dend}(0), I_{soma}(0), \bar{E}(0), \bar{I}_{dend}(0), \bar{I}_{soma}(0)\} = \{0, 0, 0, 0, 0, 0\}$), the system exhibits zero-lag synchronization between the local networks regardless of the presence of divisive inhibition, as seen in Fig 3.3B. In this case, because the local networks have the same initial conditions, they are initially in synchrony and remain in

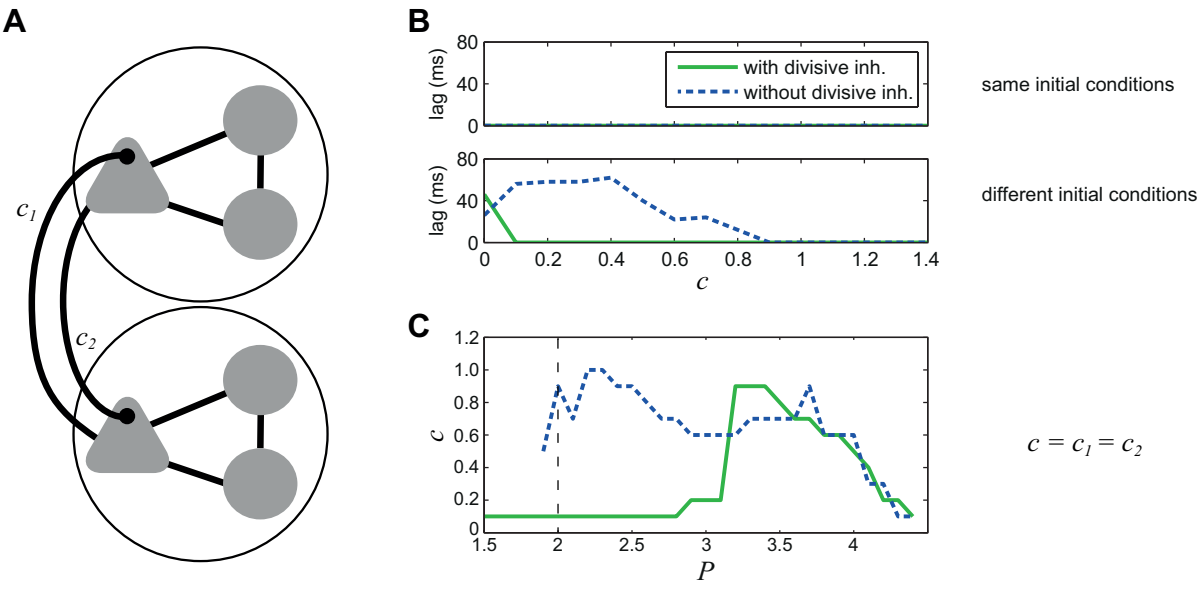

Figure 3.3: Long-range synchronization scenario and zero-lag synchronization in the case of symmetry ($c = c_1 = c_2$) and no delay ($t_{del} = 0$). (A) Schematic of the long-range synchronization scenario: two local networks coupled with excitatory connections between their excitatory populations. The excitatory populations also receive the same external input P which produces the baseline oscillatory activity (not shown). Note that the details about the connectivity within each local network are omitted in this schematic: the two local networks can be considered as either featuring divisive inhibition or not (see Fig. 3.1 for the connectivity details). (B) Lag between the two local networks for the cases of with and without divisive inhibition and for low values of c. When the initial conditions of the local networks are the same, they start in synchrony and remain in synchrony regardless of the value c. When the initial conditions are different though, and the local networks are initially out of synchrony, only the system with divisive inhibition achieves zero-lag synchronization with low values of c. (C) The minimum value of c that is needed for the systems to achieve zero-lag synchronization for different values of P. Note the different behaviour of the two systems for values of $P < 3.2$. The dashed line at $P = 2$ represents the example shown in panel (B).

synchrony for whatever value of the connection weight c. This is shown with a zero lag between them as derived from the cross-correlation measure.

In the same figure, though, it is apparent that the results between the models with and without divisive inhibition differentiate when the initial conditions of the two local networks are different ($\{E(0),\ I_{dend}(0),\ I_{soma}(0),\ \bar{E}(0),\ \bar{I}_{dend}(0),\ \bar{I}_{soma}(0)\} = \{0,\ 0,\ 0,\ 0.3,\ 0,\ 0\}$). The simulation starts with them being out of synchrony. The local networks remain out of synchrony, with a non-zero lag, when they are isolated, $c = 0$. For $c > 0$, the system that exhibits divisive inhibition manages to synchronize the local networks with zero lag after the initial transient phase of the simulation. On the other hand, when the system does not exhibit divisive inhibition, the local networks achieve

zero-lag synchronization only for values of c higher than 0.8. For lower values, a non-zero lag is maintained between them. In fact, for $0.1 < c < 0.4$, the system without divisive inhibition tends to an anti-phase synchronization with a lag close, but not always equal, to half of the period. This tendency of a system of weakly coupled Wilson-Cowan oscillators (without divisive inhibition) to an anti-phase synchronization was reported previously in Borisyuk *et al.* (1995). The same behaviour was found in similar oscillating systems of coupled pendulums (Bennett *et al.* (2002)). At least in this example, divisive inhibition cancels this tendency and can enable zero-lag synchronization even with a weak coupling between the local networks, $0 < c < 0.8$. Qualitatively the same results were found for other initial conditions as well. For all the remaining results, though, I consider that the simulation starts with the local networks out of synchrony by setting the initial conditions to $\{E(0),\ I_{dend}(0),\ I_{soma}(0),\ \bar{E}(0),\ \bar{I}_{dend}(0),\ \bar{I}_{soma}(0)\} = \{0,\ 0,\ 0,\ 0.3,\ 0,\ 0\}$.

The results shown in Fig 3.3B are for the case of constant input $P = 2$ which is the chosen value for all the remaining results for the long-range synchronization. In Fig 3.3C, it is shown that the same qualitative results are found for other values of P. This plot shows the minimum value of c that is needed to achieve zero-lag synchronization against different values of constant input P. Apparently, the two systems, with and without divisive inhibition, behave differently for values of $P < 3.2$: the one achieves zero-lag synchronization even with near zero values of c whereas the other demands much higher values of c ($c \approx 0.7$). For $P \geq 3.2$ the two systems behave similarly demanding relatively high values of c to achieve zero-lag synchronization. This difference between high and low values of P can once again be explained by the diminishing contribution of the soma-targeting population I_{soma} in the network's dynamics as the value of P increases (see Entrainment above and Fig 3.8).

Note that the results reported here focus on the qualitative difference between the two network models: the one with divisive inhibition achieves zero-lag synchronization even with weak coupling whereas the other does not. This is evidenced for $P < 3.2$ when divisive inhibition is stronger and it applies with different initial conditions as well. It is true that for $3.2 < P < 3.5$ in Fig 3.3C the system without divisive inhibition achieves zero-lag synchronization with slightly lower values of c, but this is a quantitative difference that is sensitive to the initial conditions.

Cross-correlation with asymmetrical long-range connection weights without delay. Next, I consider the case where there is still no delay in the system, $t_{del} = 0$, but there is no longer symmetry in the connectivity between the local networks: the long-range connections c_1 and c_2 can vary independently. The synchronization between the local networks is still measured using cross-correlation and the lag as described in Methods. The comparative results of cross-correlation and lag between the systems with and without divisive inhibition can be found in Fig 3.4. In both cases, the synchronization is generally higher when the long-range connectivity is close to symmetry, that is, close to the diagonal $c_1 = c_2$. The synchronization is diminished, though, when we move away from the diagonal. Note that the values on the diagonal are the same as the values presented in Fig 3.3B. Note also that the system without divisive inhibition has particularly low synchronization with weak coupling, $c_1 < 1$ and $c_2 < 1$ as it was shown earlier. In general these heat maps have similar characteristics between the two cases, with and without divisive inhibition, but the synchronization is measured to be higher across the map when divisive inhibition is included in the system. This is shown clearly in the respective distributions of the values next to the colourbars. The areas in the maps that are grey represent parameter sets that do not produce oscillations.

Phase synchronization with asymmetrical long-range connection weights and variable delay. The synchronization between the local networks was also measured using phase synchronization. Phase synchronization was chosen as an alternative measure at this stage based on the fact that it is a widely used measure in EEG synchronization and it was found to be weakly correlated with cross-correlation thus giving complementary information (Dauwels *et al.* (2010)). This measure quantifies synchronization in a more informative way than cross-correlation being able to detect relationships between the phases of the signals (see Methods). The phase synchronization results and the comparison between the systems with and without divisive inhibition can be found in Fig 3.5. These results include also different values for the delay parameter t_{del}. When $t_{del} = 0$, the heat maps of phase synchronization are similar to the respective ones of cross-correlation in Fig 3.4 with higher synchronization close to the diagonal and lower synchronization away from it. Both maps are symmetric about the diagonal. The system exhibiting divisive inhibition once again

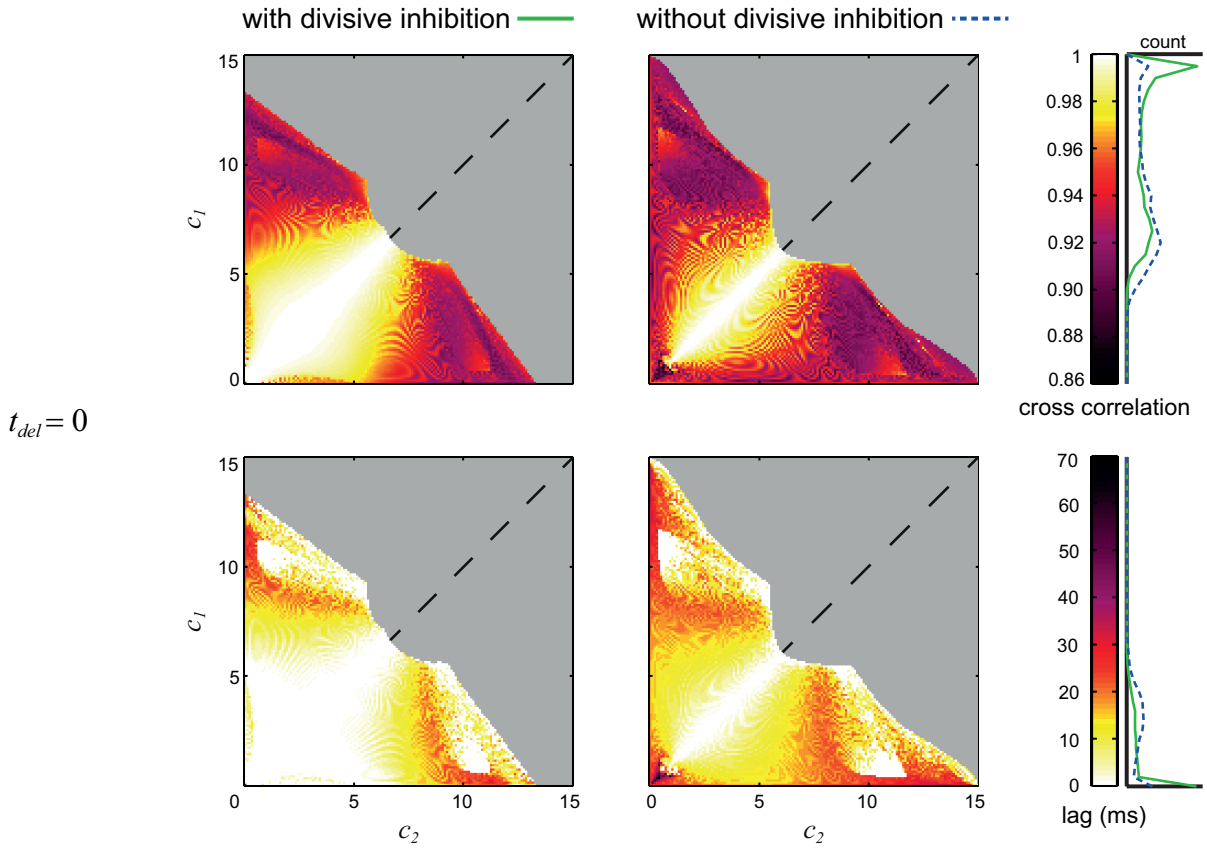

Figure 3.4: Synchronization with no delay ($t_{del} = 0$) as measured with cross-correlation and lag. The heat maps show the cross-correlation and lag between the local networks for the two cases: with and without divisive inhibition. Synchronization is generally higher close to the diagonal for both cases. The system with divisive inhibition though achieves higher measured synchronization across the map as shown by the distributions next to the colourbar.

achieves higher synchronization across the map. With $t_{del} = 10$ ms, the areas with high synchronization (white areas) shrink into more limited areas around the diagonal especially in the case of the network without divisive inhibition. This value of delay would correspond to approximately 70 mm of myelinated and 7 mm of non-myelinated axons considering conduction velocities approximately 7 m/s and 0.7 m/s, respectively (Swadlow and Waxman (2012). Increasing the delay to 20 ms (corresponding to approximately 140 mm of myelinated and 14 mm of non-myelinated axons), the phase synchronization is being decreased in general, as expected. However in the case of divisive inhibition the heat map is not symmetric any more and it features discontinuities: notice, for example, the areas of red and white being next to each other. The map seems to have a two-layer morphology with another layer of high synchronization appearing unexpectedly. What is happening in this case is that the algorithm detects a 2:1 phase synchronization (with the activity being quasi-periodic)

rather than the more common 1:1 phase synchronization. The reported result is always the maximum phase synchronization among all the different combinations (see Methods). This is an example of how the phase synchronization measure can be more informative than cross-correlation. In the case of the system without divisive inhibition, the heat map is symmetric and more homogeneous. The difference between the two cases can be summarized by the distributions of phase synchronization values plotted on the right of the colourbar. Note the bimodality of the distribution for the case with divisive inhibition which represents its double layered heat map. These results show that the system with divisive inhibition achieves, at least in this illustrative example, better phase synchronization even with the introduction of different values of conduction delay and this continues to apply for values of t_{del} as high as 30 ms (corresponding to 210 mm of myelinated and 21 mm of non-myelinated axons).

The distributions of phase synchronization indices presented in Fig 3.5 can be plotted against the delay parameter to investigate how sensitive the systems are to the increase of t_{del}. Fig 3.6 shows clearly how the distribution of phase synchronization values changes with the increase of the delay parameter for both cases, with and without divisive inhibition. Firstly, in both cases the systems achieve and maintain relatively high synchronization for values of t_{del} up to approximately 20 ms whereas higher values of delay cause a dramatic decrease in synchronization indices. Secondly, this dramatic decrease in synchronization indices is more pronounced when the system does not have divisive inhibition. Thirdly, the system with divisive inhibition, while its synchronization indices are decreasing with increasing delay $t_{del} > 20$ ms, maintains a bimodal distribution with a second peak lying at high values of phase synchronization (see also Fig 3.5).

3.3.3 Generalizing the results

The comparison presented above between a network incorporating divisive inhibition and another one without divisive inhibition serves as an illustrative example but in order to generalize to findings across the parameter space I introduce an extra parameter, q, to the model. This parameter expresses the divisiveness of the modulation that I_{soma} provides and varies from 0 (purely subtractive) to 1 (purely

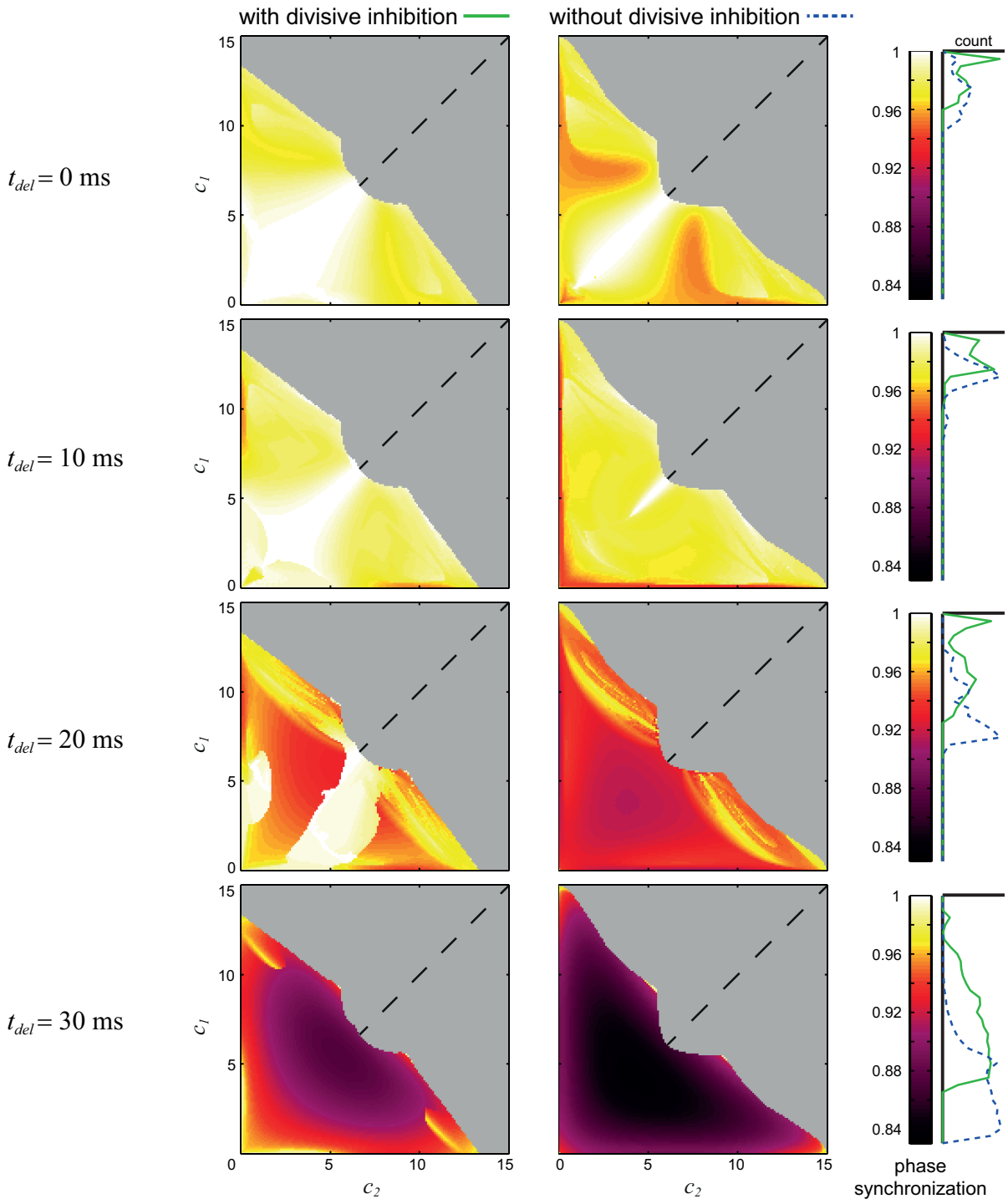

Figure 3.5: Phase synchronization with different values of conduction delay t_{del}. The heat maps show the phase synchronization for the two cases of distributed networks, with and without divisive inhibition, at different values of conduction delay. As expected, the increase of conduction delay has a negative impact on the synchronization between the two local networks. Nevertheless, the presence of divisive inhibition enhances the synchronization between the local networks (see the distributions of synchronization indices on the right of the colourbars). Notice that both 1:1 and 1:2 phase synchronization was detected in the same map, as indicated by the bimodal distribution of the synchronization indices, when the system incorporates divisive inhibition at $t_{del} = 20$ ms.

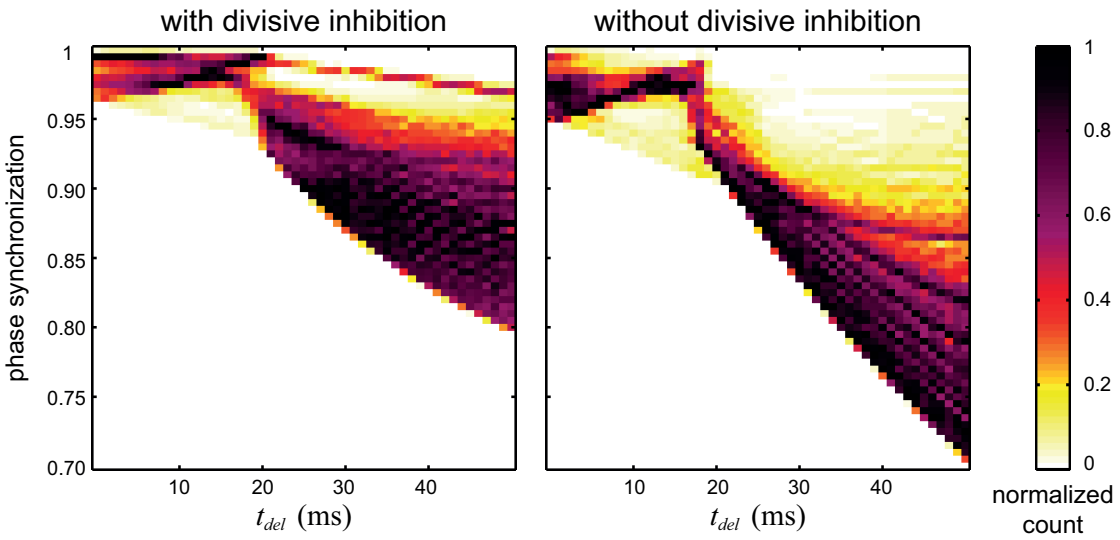

Figure 3.6: Distribution of phase synchronization indices for different values of conduction delay t_{del}. The heat maps show the distribution of phase synchronization indices for the two cases of networks, with and without divisive inhibition, for different values of conduction delay. Each column is a normalized histogram of these indices derived from maps like the ones presented in Fig 3.5. The network with divisive inhibition is less sensitive to the increase of the delay parameter and maintains a bimodal distribution for high values of t_{del}.

divisive). See Fig 3.7A of a schematic of this model and Methods for its implementation.

First, I generalize the results in the phenomenon of long-range synchronization. A repeated random sampling of the parameter space was used to achieve this (see Appendix B). An illustrative example of the process is shown in Figs 3.7B and 3.7C. In Fig 3.7B it is shown how the q parameter can create a spectrum between the two extremes and their respective synchronization maps like the ones presented in Fig 3.5. The way to generalize the results is to investigate what is happening for intermediate values of q in terms of phase synchronization. Thus, in Fig 3.7C the slope λ is calculated using linear regression based on the values of phase synchronization for $q =$ 0.4, 0.45, 0.5, 0.55, 0.6. In this case, which comes from the example in Fig 3.5 at $t_{del} =$ 30 ms, there is an increase with increasing values of q and is characterized with $\lambda = 0.0214$.

From the 10^5 samples taken from the parameter space, only 3.1% (3084) produced oscillations and the calculation of a well-fitted slope was possible. The distribution of the calculated slopes can be found in Fig 3.7D. This distribution has a mean of 0.0429 and a strong positive skewness of 2.209. The fact that most of the slopes, and their

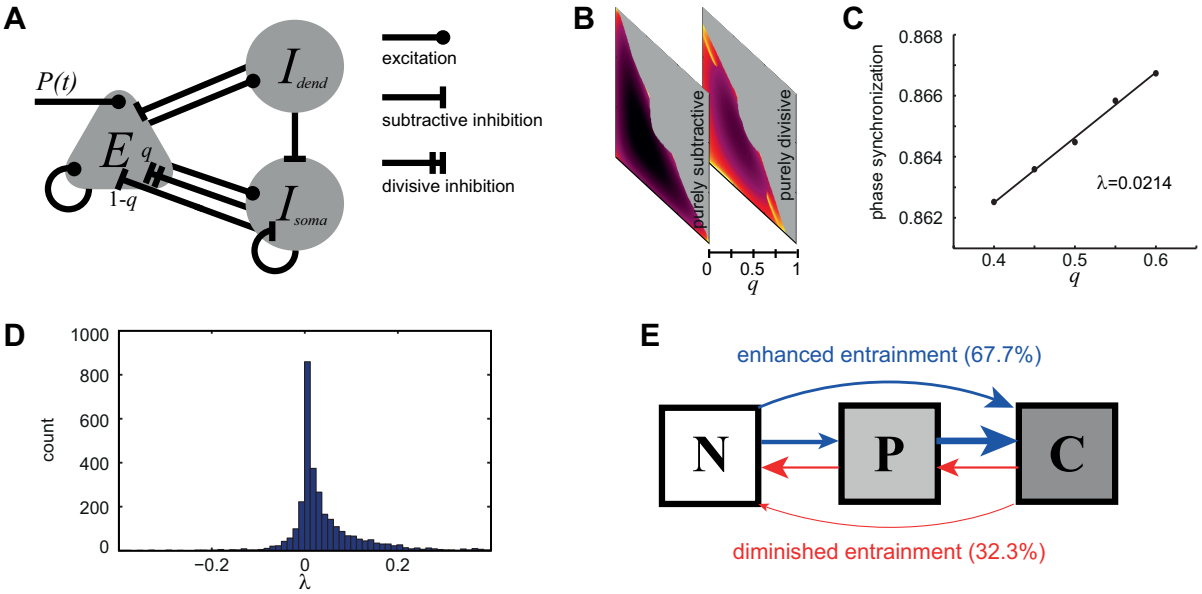

Figure 3.7: Introducing parameter q to the model and generalizing the results across the parameter space. (A) Schematic of the model incorporating the parameter q which expresses the divisiveness of the inhibition provided by I_{soma}. (B) Illustrative example of how parameter q can create a spectrum between the two extremes: a model with purely subtractive inhibition ($q = 0$) and a model with purely divisive inhibition ($q = 1$) provided by I_{soma}. (C) Calculation of the slope λ using linear regression on the phase synchronization indices at different values of q. (D) Distribution of all the slopes calculated after a random sampling of the parameter space for the purpose of generalizing the results of long-range synchronization. Notice the strong skewness (2.209) of the distribution towards positive values which indicates that, with increasing divisiveness, synchronization tends to increase too. (E) Schematic illustrating the overall results for the generalization of the effect of divisive inhibition on entrainment. The direction of the arrows indicate increasing q. The thickness of the arrows expresses how strong is the tendency of the system to transit from one state of entrainment to another. The states are N for no entrainment, P for partial entrainment, and C for complete entrainment. In the majority of cases (67.7%) the entrainment is qualitatively enhanced with increasing divisiveness (increasing q).

mean, are close to 0 is expected because it was shown above that the slope should be very close to zero whenever c_1 and c_2 are approximately equal and the delay is relatively low (see Fig 3.5). The positive skewness of this distribution indicates that increasing the divisiveness of the inhibition provided by the soma-targeting population increases the phase synchronization across the parameter space.

A similar approach was used to check whether entrainment is enhanced by divisive inhibition across the parameter space (see Appendix B). The results include the cases with a monotonic increase or decrease of the entrainment in a qualitative sense. Thus, there are six different cases: (i) increase from no entrainment to partial entrainment, (ii) increase from no entrainment to complete entrainment, (iii) increase from partial entrainment to complete entrainment, (iv) decrease from complete entrainment to partial entrainment, (v) decrease from complete entrainment to no entrainment, and (vi) decrease from partial entrainment to no entrainment. After taking 10^6 samples from the parameter space, only 0.15% (1494) would produce oscillations and a monotonic increase or decrease of the entrainment with increasing q. From these 1494 samples, 67.7% (1011) had a monotonic increase and 32.3% (483) had a monotonic decrease. The schematic in Fig 3.7E illustrates the results. The six arrows represent the six cases (i)-(vi) and the thickness of each arrow is proportional to the number of samples that represents each case. These results demonstrate that increasing the divisiveness of the inhibition generally enhances the entrainment of a local network across the parameter space.

Discussion

The findings demonstrate how divisive inhibition can promote the phenomena of entrainment and long-range synchronization in a neural mass model. The presence of this gain control mechanism in the model enhances the entrainment of a local network by enabling its entrainment to a wider range of frequencies (see Fig 3.2). Additionally, the divisive inhibition enhances long-range synchronization for different values of coupling strength and delay. In fact, the model exhibiting divisive inhibition has lower sensitivity to the change of such parameters as shown in Figs 3.5 and 3.6. This link

between divisive inhibition and low sensitivity in parameter changes has been demonstrated in different models and phenomena in the past (Chance and Abbott (2000); Papasavvas *et al.* (2015)).

As shown in Fig 3.6, regardless of the presence of divisive inhibition in the network, the long-range synchronization is much more sensitive to increasing values of delay beyond 20 ms. The network is able to achieve, in general, higher synchronization with delays below 20 ms, which is approximately 1/7 of the intrinsic period of 141 ms, but with a delay beyond this value, there seems to be a transition in another state in which synchronization is relatively much more deficient. Studies on the connectome suggests that this threshold at 20 ms delay is enough at least for the distribution of conduction delays found in the rhesus monkey. Considering its cortico-cortical connections, including interhemispheric, the values of conduction delay range up to 18 ms (Swadlow and Waxman (2012). Additionally, considering a mean conduction velocity of 7 m/s (Swadlow and Waxman (2012)) and the distribution of intrahemispheric connection lengths in human cortex which ranges up to 0.1 m (Kaiser (2011)), the mean delay ranges up to 14.3 ms. This verifies that the threshold of 20 ms delay found by simulating the model is consistent with the distribution of functional delays found in primates, considering, of course, cortical networks that resonate at theta frequencies.

The main findings of the comparison were generalized across the parameter space using an extra parameter q, expressing the divisiveness of inhibition, revealing its general impact to the system regardless of the specific parameters used (see Fig 3.7). In general, both entrainment and long-range synchronization were found to be enhanced with increasing divisiveness using randomly generated parameter sets. This generalization suggests that the same effects of divisive inhibition can be found in networks with widely different connectivity settings. Note that these results do not demonstrate that increased divisiveness is beneficial for every single different parameter set: there are cases in which entrainment or long-range synchronization are getting worse with increased value of q. Actually, what is shown in Fig 3.7 is that, with increased divisive inhibition, these phenomena are enhanced *on average* across the parameter space.

The reported results reveal, in addition to the quantitative enhancement, a qualitative

effect of divisive inhibition in such network models. The results in Figs 3.3B and 3.3C demonstrate that divisive inhibition enables zero-lag synchronization even with weak coupling when there is symmetry and no delay. As far as I know, this is the first time to observe such behaviour in two weakly coupled identical oscillators. The failure of zero-lag synchronization with weak coupling was reported in the past for neural and mechanical systems of coupled oscillators (Borisyuk *et al.* (1995); Bennett *et al.* (2002)). Despite the fact that this qualitative effect is true for different initial conditions, it is still unknown whether the effect can be generalized for different connectivity settings of the identical local networks. This can potentially be a future direction of the study by focusing on symmetrical weak couplings without delay between the networks and applying analytical approaches to test whether gain control ensures zero-lag synchronization.

As shown in Fig 3.2, the local network with divisive inhibition tends to exhibit more readily quasi-periodic activity when it is driven with high frequency oscillation, thus achieving partial entrainment. In situations like the one shown in Fig 3.9, the network with divisive inhibition has more flexible oscillations that can include the high input frequency and the low intrinsic frequency in the same waveform. This type of oscillations are phenomenologically similar to the well documented phenomenon of cross-frequency coupling, which is usually observed between theta and gamma frequencies (Belluscio *et al.* (2012); Lodge *et al.* (2009); Pastoll *et al.* (2013)). This does not suggest, however, that this model can serve as a mechanistic model of cross-frequency coupling; it suggests that the flexibility that gain control provides can subserve this type of phenomena as well.

It is evidenced that long-range synchronization between distant areas is crucial for information processing (see Introduction). This is especially true for the integration of information at a global scale where substantial delays are involved. Despite the fact that the long-distance connections found in neural systems can reduce the delays by minimizing the processing steps (Kaiser and Hilgetag (2006)), delays of up to 18 ms are unavoidable in the primate cortex (Swadlow and Waxman (2012)). The robust synchronization between multiple distant areas is a requirement for the processing of different features of an object according to the synchronization theory of the binding problem(von der Malsburg (1995)). According to this theory, synchronous oscillations

between these areas serve as the feature binding mechanism which produces a complete and distinct perception of an object. Thus, the enhancement of long-range synchronization by divisive inhibition could promote the integration of information at a global scale.

Considering the positive impact of divisive inhibition on the phenomena of entrainment and long-range synchronization which are crucial for physiological brain dynamics, it is fair to suggest that any deficit in divisive inhibition can possibly lead to pathological brain dynamics. No direct causal link has been found so far experimentally between the phenomenon of divisive inhibition and any measurable pathological phenotype. However, there is a plethora of evidence linking deficits in soma-targeting interneurons, the population that predominantly provides divisive inhibition (Wilson *et al.* (2012); Atallah *et al.* (2012)), with the phenotype of schizophrenia (for a review, see Nakazawa *et al.* (2012)) and other neurological conditions, such as epilepsy (Rossignol *et al.* (2013); Tan *et al.* (2012)). Studies on brain tissue recovered from schizophrenia patients provide evidence of molecular alterations in soma-targeting interneurons resulting into lower expression of GAD67 and higher expression of μ opioid receptor which leads to deficient synthesis and release of GABA (Curley and Lewis (2012); Lewis *et al.* (2012)). Similar postmortem studies verified that these abnormalities of the population are mostly molecular and not structural (Glausier *et al.* (2014)). Additionally, loss of these interneurons in entorhinal cortex was reported in LPA1-deficient mice which serve as an animal model of schizophrenia (Cunningham *et al.* (2006)). Other studies investigated whether these alterations are exclusively found in the soma-targeting population or whether there is an implication of the dendrite-targeting population (somatostatin-positive) as well. The results are contradictory with one study implicating the dendrite-targeting interneurons (Morris *et al.* (2008)) while another reported no implication (Mellios *et al.* (2009)). The soma-targeting population of interneurons is referred to as parvalbumin-positive basket cells or fast-spiking GABAergic neurons in these studies.

The cognitive deficits found in schizophrenia patients are thought to result from the failure of the soma-targeting interneurons to generate high frequency oscillations exactly because of these abnormalities in the population (Nakazawa *et al.* (2012); Lewis *et al.* (2012); Uhlhaas and Singer (2006); Cunningham *et al.* (2006)). Indeed, it is well

established that this population is the single most important inhibitory population for the generation of gamma frequency oscillations because of their highly specialized synapses (Bartos *et al.* (2007)). But is the failed rhythmogenesis at gamma frequencies the only causal link between the molecular alterations in soma-targeting interneurons and the deficits in entrainment and long-range synchronization in schizophrenia? It is evidenced that these deficits are not limited only to gamma frequencies but also at the lower range of beta frequencies (Yeragani *et al.* (2006); Vierling-Claassen *et al.* (2008); Uhlhaas and Singer (2006)). Entrainment and synchronization were found to be impaired even at alpha frequencies (White *et al.* (2010); Rice *et al.* (1989); Jin *et al.* (2000)). In fact, long-range interactions were reported to rely predominantly on middle-frequency rhythms (4-12 Hz) rather than high (von Stein *et al.* (2000); Bressler *et al.* (1993); Lakatos *et al.* (2008)). I hypothesize that impaired divisive inhibition could be contributing as another causal link between the molecular alterations in the soma-targeting interneurons and the deficiencies in entrainment and long-range synchronization in schizophrenia. An initial experiment towards testing this hypothesis would be to measure and compare the divisive inhibition in animal models of schizophrenia (e.g., LPA1-deficient mice in Cunningham *et al.* (2006) or chronically exposed to phencyclidine rats in Bullock *et al.* (2009)) and control animals using the same methodology as in Wilson *et al.* (2012).

By using an extended version of the Wilson-Cowan model, we showed that a gain control mechanism can have a positive impact on the dynamics of neocortical networks. Simulating the divisive inhibition provided by the soma-targeting interneurons in neocortex yielded enhanced entrainment and long-range synchronization. The enhancement in entrainment reflects more flexible oscillatory dynamics which is considered to be crucial for the adaptive functionality of the network (Schwab *et al.* (2006); Spiegler *et al.* (2011)). The ability of distributed networks to synchronize better is also important for their dynamic coordination which underlies many cognitive functions (Uhlhaas and Singer (2006, 2010)). The findings were generalized across the parameter space demonstrating the universality of the effect. Future directions of the study can potentially test whether the effect persists with noise in the system or with different patterns of long-range connectivity. The results in this study suggest that the soma-targeting interneurons and the divisive inhibition that they provide make the physiological dynamics of neocortical networks more robust.

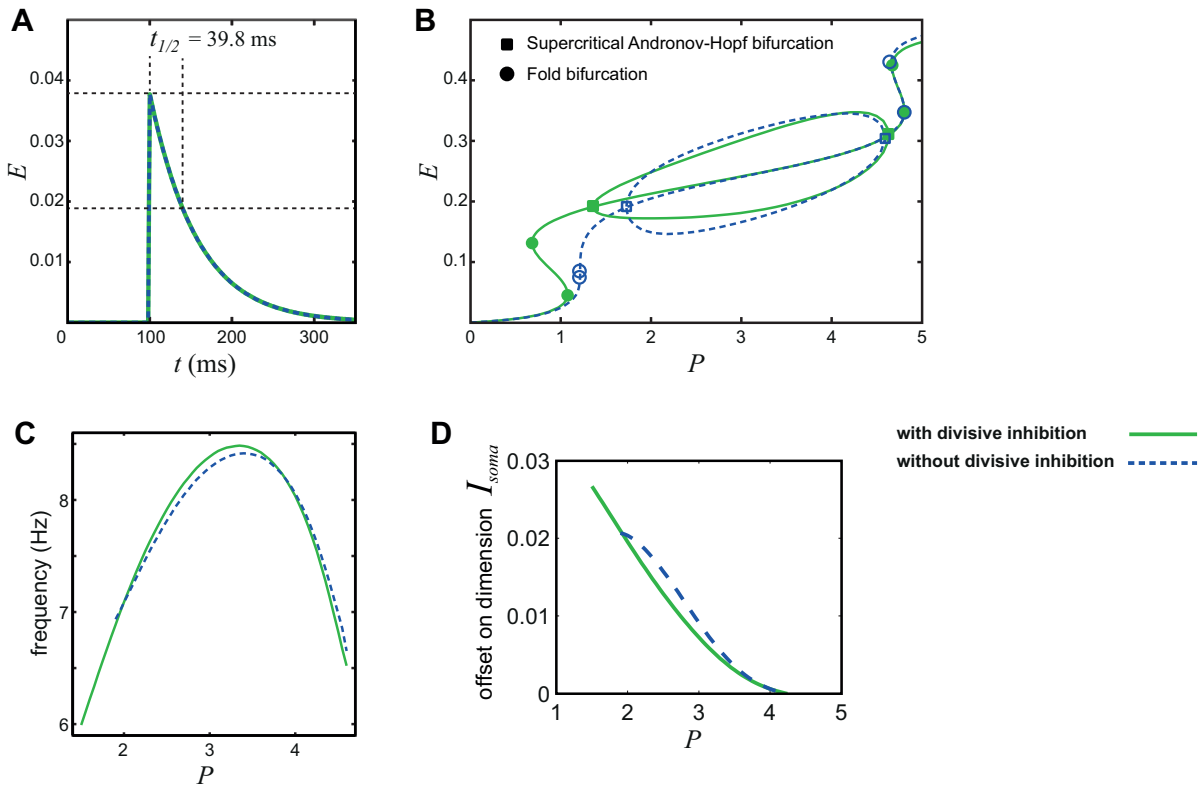

Figure 3.8: Calibration of the two network models. (A) The response of both models to an instantaneous input is an exponential decay with half-life $t_{1/2} = 39.8$ ms. (B) Bifurcation diagrams showing a comparable dynamic regime in which the networks are calibrated to. (C) The two network models respond with similar frequencies of oscillation for different values of constant input P. (D) The activity of population I_{soma} in both models is diminished with increasing values of P making the models converge to exactly the same behaviour.

Appendix A Supplementary figures

The two local networks, with and without divisive inhibition, were calibrated before the comparison. The specific parameters for each case were chosen to produce similar oscillatory behaviour in terms of the frequency, the offset and the amplitude of oscillation. The results of the calibration are shown in Fig 3.8. The small discrepancies between the oscillations of the two systems after the calibration were shown not to influence the main findings of the study due to fact that those findings were generalized across the parameter space.

The activity of the systems during the entrainment scenario was analysed based on their power spectrum. An example of the analysis procedure is shown in Fig 3.9. The system with divisive inhibition produces a complex waveform (quasi-periodic) with multiple peaks in the spectrum. Some of the power in the spectrum is concentrated on

the input frequency, thus the entrainment of the system is considered to be equal to the proportion of that power (i.e. partial entrainment). The system without divisive inhibition in this example has a simpler activity with just a single peak in the power spectrum. This frequency is close to its resonant frequency. It fails to accommodate the much higher input frequency in its spectral composition, thus there is no entertainment at all.

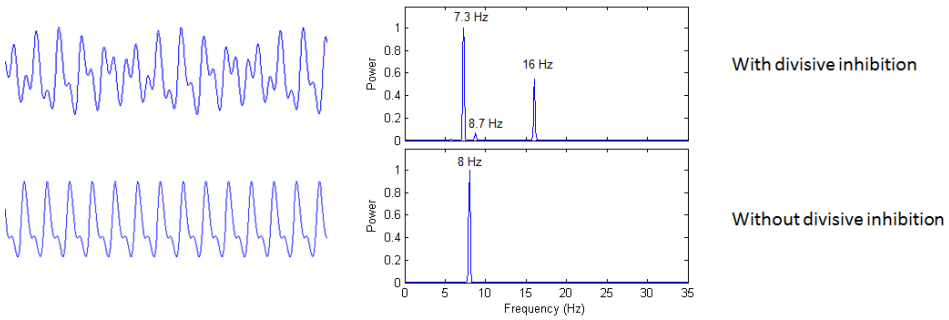

Figure 3.9: An example of waveforms in the entrainment scenario. Both models receive oscillating input with frequency $f_{in} = 16$ Hz and offset $P = 2$. The model with divisive inhibition responds with a complex waveform featuring multiple frequencies including f_{in} and its intrinsic frequency. In contrast, the model without divisive inhibition fails the entrainment because it exhibits a simple waveform featuring only the $f_{in}/2$ which is close to its intrinsic frequency. The power spectrums are plotted after the removal of the harmonics but before the normalization (see Methods).

Appendix B Random sampling algorithms

For the purpose of generalizing the results across the parameter space, we employ an unbiased random sampling of the parameter space to check what is the impact, if any, of increasing divisiveness of the soma-targeting inhibition on the entrainment and long-range synchronization. This divisiveness is given by the parameter q.

For the scenario of long-range synchronization, the following algorithm was used to sample the parameter space.

Algorithm for generalizing long-range synchronization

Repeat N times:

1. Randomly select a set of values $S_1 = \{P, w_1, w_2, w_3, w_4, w_5, w_6, w_7\}$ with

uniform distribution from the intervals $0 \leq P \leq 6$ and $0 \leq w_j \leq 30$, $j = 1, 2, \ldots, 7$.

2. Build a local network using S_1, $q = 0.5$ and simulate.

3. If there is no oscillation, then reject S_1 and return to step 1 to continue iteration. Otherwise, continue with next step.

4. Randomly select a set of values $S_2 = \{c_1, c_2, t_{del}\}$ with uniform distribution from the intervals $0 \leq c_1 \leq 20$, $0 \leq c_2 \leq 20$ and $0 \leq t_{del} \leq 40$ ms.

5. Build a distributed network with two coupled identical local networks using S_1, S_2, $q = 0.5$ and simulate.

6. If there is no oscillation, then reject S_1, S_2 and return to step 1 to continue iteration. Otherwise, continue with next step.

7. Calculate phase synchronization indices for $q = 0.4$, 0.45, 0.5, 0.55, 0.6.

8. Apply linear regression on the calculated phase synchronization indices to calculate the slope λ.

9. If the goodness-of-fit of the linear regression is less than 0.9, then reject S_1, S_2 and return to step 1 to continue iteration. Otherwise, continue with next step.

10. Save S_1, S_2, and λ and continue iteration.

End of algorithm

For the scenario of entrainment, the following algorithm was used to sample the parameter space.

Algorithm for generalizing entrainment

Repeat M times:

1. Randomly select a set of values $S_1 = \{P, w_1, w_2, w_3, w_4, w_5, w_6, w_7\}$ with uniform distribution from the intervals $0 \leq P \leq 6$ and $0 \leq w_j \leq 30$, $j = 1, 2, \ldots, 7$.

2. Build a local network with constant input using S_1, $q = 0.5$ and simulate.

3. If there is no oscillation, then reject S_1 and return to step 1 to continue iteration. Otherwise, continue with next step.

4. Randomly select a set of values $S_2 = \{A,\ f_{in}\}$ with uniform distribution from the intervals $0 \leq A \leq 1$ and $1 \leq f_{in} \leq 40$ Hz.

5. Build a local network with oscillating input using S_1, S_2, $q = 0.5$ and simulate.

6. If there is no oscillation, then reject S_1, S_2 and return to step 1 to continue iteration. Otherwise, continue with next step.

7. Calculate the entrainment values for $q = 0.4,\ 0.45,\ 0.5,\ 0.55,\ 0.6$.

8. Transform the entrainment values into qualitative values by setting all values of the open interval (0, 1) equal to 0.5 which represents partial entrainment. Values 0 (no entrainment) and 1 (complete entrainment) remain the same.

9. If there is neither monotonic increase nor decrease in the qualitative values of entrainment with increasing q, then reject S_1, S_2 and return to step 1 to continue iteration. Otherwise, continue with next step.

10. Save S_1, S_2, the qualitative entrainment values and continue iteration.

End of algorithm

Note that, for generalizing the entrainment results, the algorithm focuses on qualitative differences rather than quantitative. Also the number of repetitions N and M were chosen to be 10^5 and 10^6, respectively. These numbers were verified to be sufficient by running again each algorithm and yielding almost the same overall results, in terms of their statistics, as presented in the main text.

Chapter 4

Optogenetic manipulation of PV^+ interneurons and propagation of activity through the PV-syncytium

4.1 Introduction

4.1.1 Gap junctions and the PV-syncytium

Gap junctions form a syncytium between cells permitting the transfer of ions and small molecules from one cell to the other. Gap junctions function as electrical synapses enabling the rapid communication of information between cells with ionic currents traversing the syncytium. They have a critical role in the physiology of the peripheral and central nervous system but also in the myocardial cells and smooth muscle cells. Due to the gap junctions, action potentials propagate through electrically coupled phasic smooth cells causing the contraction of smooth musculature (Garfield *et al.* (1978); Sims *et al.* (1982); Brink *et al.* (1996)). Similarly, the myocardium functions as a syncytium: a wave of depolarization spreads through the electrically coupled myocardial cells producing a contraction whenever the syncytium is stimulated (Goodyer (1968); Brink *et al.* (1996)). Gap junctions mediate the coordination of activity in such tissue which is characterized by broad action potentials (Brink *et al.*

(1996)). Additional functional roles of the gap junctions are associated with wound healing (Moyer *et al.* (2002); Coutinho *et al.* (2003)) and cell death (Andrade-Rozental *et al.* (2000)).

Gap junctions play a major role in the peripheral and central nervous system as well. They are particularly crucial during the development of the central nervous system. They are involved in the regulation of cell growth and then the migration of the cells (Bruzzone and Dermietzel (2006)). Gap junctions are prevalent during the initial developmental stages, coupling cells and coordinating their activity well before the formation of chemical synapses (Kandler and Katz (1995)). Their prevalence decreases sharply during differentiation (Walsh *et al.* (1989)), and continues to decrease during the later developmental stages as, for example, in the formation of circuits (Peinado *et al.* (1993)). Nevertheless, the adult brain features electrical synapses between specific cell types which provide specific functionality (see below). One of the highly functional syncytia is the astroglial syncytium which has an important role during development but also in the adult brain (Kandler and Katz (1995); Dermietzel (1998)). Electrically coupled glia cells provide signal transmission and metabolic support to neurons by mediating Ca^{2+} waves (Cornell-Bell *et al.* (1990)). This constitutes a phenomenon of intercellular volume transmission and the gap junctions between glia provide the most critical mechanism for such functionality (Dermietzel (1998)).

The adult brain features gap junctions between interneurons and these connections are largely maintained through development and into adulthood (Connors *et al.* (1983); Peinado *et al.* (1993)). Electrical coupling between fast-spiking interneurons has been demonstrated using both electrophysiological and anatomical studies (Bernardo (1997); Galarreta and Hestrin (1999); Gibson *et al.* (1999); Amitai *et al.* (2002); Fukuda and Kosaka (2003); Fukuda *et al.* (2006)). Patch-clamping was used on neighbouring fast-spiking cells in infragranular layers of neocortex and a high percentage of such pairs were found to be electrically coupled (Galarreta and Hestrin (1999); Gibson *et al.* (1999)). The probability of two interneurons being electrically coupled decreased with the distance between their somata and the probability dropped to 0 at approximately 200 μm (Amitai *et al.* (2002)). In such experiments, the electrotonic coupling between the paired cells was demonstrated with the manipulation of the membrane potential of one cell by the injection of current in the other (Galarreta and Hestrin (1999); Amitai

et al. (2002)). Dye coupling was also used to demonstrate the syncytium between neocortical interneurons (Bernardo (1997)).

The proteins that form gap junctions between neurons are connexin36 (Cx36) and connexin45 (Cx45) (Evans and Martin (2002)). From these two, Cx36 is widely used to identify gap junctions in neurons exactly because the protein is found exclusively in neurons (Rash *et al.* (2001)). A study applying Cx36 immunohistochemistry found that large PV^+ interneurons have approximately 60 gap junctions distributed along their dendrites with the majority of them lying up to 150 μm from the soma (Fukuda *et al.* (2006)). Nevertheless, their distribution can reach longer distances, close to 400 μm, and establish intercolumnar connections (Fukuda *et al.* (2006)). The electrical synapses established by a PV^+ interneuron are almost exclusively on to other PV^+ cells (Galarreta and Hestrin (1999)). GABA-ergic chemical synapses are established between some of these pairs as well, producing a complex response at the presynaptic cell (Galarreta and Hestrin (1999)).

The junctional conductance between these cells was estimated using different methodologies. Fukuda and Kosaka used anatomical data from electron microscopy to estimate the junctional conductance to be about 2.15.3 nS, based on the morphological size of gap junctions (Fukuda and Kosaka (2003)). Gibson and colleagues used an electrophysiological methodology with their estimation lying in a similar range of 0.45.5 nS, and verified that the coupling conductance was practically the same between the two different directions of measurement (Gibson *et al.* (1999)). Galarreta and colleagues reported a similar range of values using the same methodology (Galarreta and Hestrin (1999)). However, Amitai and colleagues suggest that, considering that these cells are electrically coupled with multiple cells, the average junctional conductance that each cell receives from its neighbours is approximately 10 nS (Amitai *et al.* (2002)).

It is well understood that interneuronal populations, like the fast-spiking interneurons, are critical for the coordination of activity in neocortex, including synchronous and oscillatory activity (Cobb *et al.* (1995); Whittington *et al.* (1995); Lytton *et al.* (1997)). The gap junctions between these cells were shown to promote their synchronized firing with high precision of spike timing (Gibson *et al.* (1999); Galarreta and Hestrin (1999)). This can be thought as an excitatory signalling mechanism in the distributed

network of electrically coupled interneurons that coordinates their firing (Galarreta and Hestrin (1999)). Consequently, this coordinated release of $GABA_A$, from multiple coupled interneurons, is able to synchronize the firing of principal cells after a short period of silence (Whittington *et al.* (1995)). The emergence of oscillatory activity is considered to rely on this coordinated interaction (Bartos *et al.* (2007)). The electrical coupling was also shown to act as a low-pass filter enhancing the synchronization between a pair of cells mostly at lower frequencies (Galarreta and Hestrin (1999)).

Gap junctions have also been implicated in the onset and propagation of seizures. Gap junction blockers were successfully used to block focal seizures induced by tetanus injection in an *in vivo* study (Nilsen *et al.* (2006)). Another study suppressed the high-frequency oscillations in hippocampus again by applying gap junction blockers (Draguhn *et al.* (1998)). These high-frequency oscillations are thought to originate from the axo-axonic gap junctions between pyramidal neurons (Schmitz *et al.* (2001); Draguhn *et al.* (1998)) and they are associated with seizure onset. Although, it is conceivable that the mechanisms behind the reported high frequency oscillations (Draguhn *et al.* (1998)) are completely different from those characterizing seizure onset (Trevelyan (2009); Foffani *et al.* (2007); Trevelyan (2016)). Furthermore, genetic studies linked epileptogenesis with increased expression of Cx36 (Gajda *et al.* (2003)). In contrast, other studies report that blocking the gap junctions with mefloquine can trigger seizures (Bem *et al.* (1992); Rouveix *et al.* (1989)). This might be explained as a side effect of mefloquine in high doses: partial blockade of Cx43 between astroglia is possible resulting into a deficient regulation of Ca^{2+} and metabolic instability (see above).

Gap junctions were suggested to play a critical role in such pathological phenomena even in seizure models where only the electrically coupled GABAergic interneurons are involved. Such epileptiform activity is widely modelled by blocking Kv channels with 4-aminopyridine (4AP) and this activity can persist even after the blockade of ionotropic glutamate receptors indicating that it is due to discharges of the inhibitory interneurons alone (Gigout *et al.* (2006); Louvel *et al.* (2001)). Furthermore, backpropagating action potentials were found to be enhanced in basket cells during sharp wave oscillations (Chiovini *et al.* (2010)). In such experiments, blocking the gap junctions between them also abolished the discharges, indicating an antiepileptic effect

(Gigout *et al.* (2006)). But this effect can alternatively be demonstrated by blocking other features of the network. Using the same model of epileptiform events, these events were blocked in a reversible manner by antagonizing the $GABA_A$ receptors (Uva *et al.* (2009)). In fact, a study that used the same model in slices from wild-type and Cx36 knockout mice showed that this effect can be better explained by the blockade of $GABA_A$ receptors, which is a known side effect of the gap junction blocker carbenoxolone (Tovar *et al.* (2009)), rather than the blockade of gap junctions (Beaumont and Maccaferri (2011)).

All these results, with some being contradictory, indicate that the role of gap junctions in epilepsy is still poorly understood. Such studies reveal the difficulties introduced in the investigation of gap junctions when using pharmacological agents to block them. These drugs are well-known for their non-specific effect and this is especially pronounced in the case of the widely used carbenoxolone (Rozental *et al.* (2001); Tovar *et al.* (2009); Beaumont and Maccaferri (2011)). Carbenoxolone can be considered a drug with low specificity for many reasons including: blocking many different connexins (Rozental *et al.* (2001)), blocking NMDA receptors (Chepkova *et al.* (2008)), blocking voltage gated Ca^{2+} channels (Vessey *et al.* (2004)), blocking AMPA and $GABA_A$ receptors (Tovar *et al.* (2009)) and decreasing input resistance (Tovar *et al.* (2009)) (for a commentary see Connors (2012)).

In this study, I used several different gap junction blockers, because of the low specificity and limitations of each blocker. As indicated above, carbenoxolone is non-specific in its actions, however, it was used during the initial stages of the study. Other more specific blockers were preferred, namely, mefloquine (Cruikshank *et al.* (2004)) and quinine (Srinivas *et al.* (2001)). Mefloquine is considered more specific, targeting Cx36 and Cx50 (Cruikshank *et al.* (2004)), with limited side effects. It was found having no impact on the cells resting membrane potential or input resistance but it did alter the action potential dynamics in hippocampal pyramidal cells, thus, affecting their excitability (Behrens *et al.* (2011)). Mefloquine was produced as an improvement over quinine (Cruikshank *et al.* (2004)). Quinine is the drug from which mefloquine was derived and there is evidence that, other than gap junctions, it affects voltage-gated and ligand-gated channels as well (Cruikshank *et al.* (2004); Yatani *et al.* (1993); Snyders *et al.* (1992)). Nevertheless, quinine was used in this study because of

its reversible effect on gap junctions: quinine is less lipophilic than mefloquine, thus, it can be washed out.

4.1.2 Cable theory

Cable theory is the mathematical analysis of signal propagation within neurons. Through this theory, we can simulate spread of electrical current in cable-like structures, that is, structures with elongated, cylindrical geometry. The attenuation and delay of propagating signals is greater when they traverse such cable-like structures. Its use in neuroscience has been successful exactly because the vast majority of dendrites and axons of neurons have this type of geometry. Abstracting the complex morphology of neuronal structures into a series of connected cylindrical compartments is essential in the application of cable theory.

Historically, cable theory has its roots in the middle of the 19^{th} century with the work of Lord Kelvin on the spread of potential along the submarine telegraph cable (Koch (2004)). Later, the concept of the core conductor was formulated by Hermann which refers to a thin membrane surrounding an electrically conducting cylindrical core placed in a solution of electrolytes (Hermann (1881)). This concept was introduced to understand the propagation of current in nerve axons, and cable theory emerged from its systematic study (Koch (2004)). Elements of cable theory were applied in the study of squids giant axon in the 1930s and 1940s (Hodgkin and Rushton (1946); Davis Jr and Lorente (1947)), but the theory reached its full potential with the work of Rall in the 1960s and 1970s (Rall (1989)).

The problem of calculating the current flow i_i through a cylindrical axon with radius α can be described in terms of an equivalent electrical circuit. Such a circuit is shown in Fig. 4.1. The membrane is characterised by two parameters: the membrane resistance r_m and the membrane capacitance c_m. These two elements are connected in parallel and they traverse the membrane connecting the intracellular with the extracellular space. In addition, r_i is the resistance of the cytoplasm, r_o is the resistance of the extracellular medium and x expresses the distance along the cylinder. Any current injected in the cylinder will flow down two paths: across the membrane as leak current

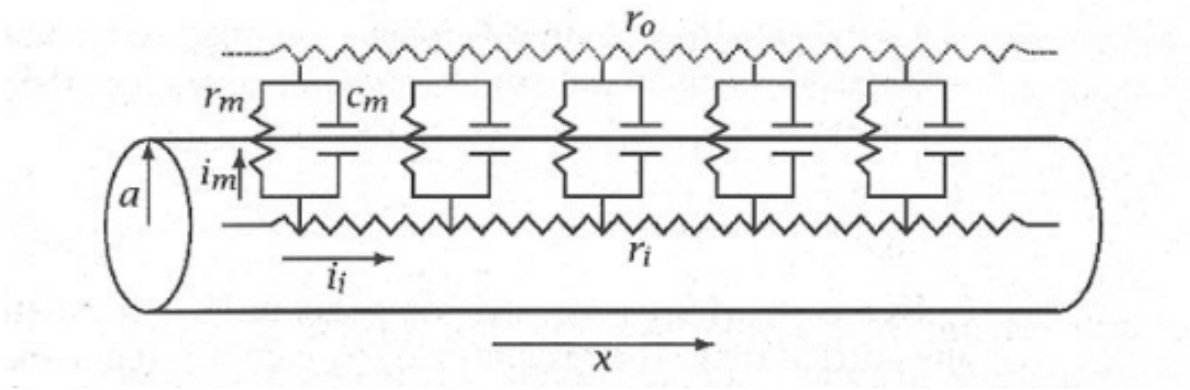

Figure 4.1: Schematic of the circuit describing the flow of current inside a cable in the context of cable theory (schematic from Johnston and Wu (1995)).

i_m and along the cylinder as intracellular current i_i. The assumptions made for this circuit are:

1) The intracellular current flow is limited to one spatial dimension x, along the cable. Currents along its radius are neglected (one-dimensional cable theory).

2) The extracellular resistance is 0 for simplicity.

With the second assumption we consider the extracellular space to be isopotential, that is, constant potential along the dimension x. This is a reasonable assumption in most cases but in some cases, such as cases of tightly packed axons or significant extracellular currents, the assumption is an oversimplification (Johnston and Wu (1995)). The first assumption is also fair considering that the majority of dendrites and axons are very narrow. The radial variations of the potential are negligible compared to the longitudinal variations (Dayan and Abbott (2001)).

In the case of linear cable theory we consider the membrane to be linear and uniform. This means that the parameters characterising the membrane are the same throughout the cylinder and they are independent of the membrane potential. This is a significant constraint considering that all the nonlinear, voltage-depended properties of the dendrites and axons are ignored. Such active properties are expected to boost the signal along the cylinder and they influence the dynamics significantly. For that reason, these properties are included in the context of nonlinear cable theory. Nevertheless, this introduction focuses on the linear cable theory which provides a conceptual framework introducing the most important parameters that are relevant for the study.

Considering now the above assumptions and the circuit in Fig. 4.1, a current injected somewhere along the cylinder will produce a membrane potential V_m with an evolution which is described by the following partial differential equation:

$$\frac{\partial V_m(x,t)}{\partial x} = -r_i i_i.$$

The spatial variable x denotes the distance from the site of injection and the equation is Ohms law expressing the decrease in membrane potential with distance is equal to the current times the resistance. The intracellular current i_i, however, is not constant along the cylinder because some is leaking out through r_m and c_m, that is, leak current i_m. The decrease in intracellular current with distance is thus given by the equation:

$$\frac{\partial i_i}{\partial x} = -i_m.$$

Combining the above equations yields:

$$\frac{\partial^2 V_m}{\partial x^2} = -r_i \frac{\partial i_i}{\partial x} = r_i i_m.$$

The leak current is the sum of the current flowing through the membrane resistance and the current flowing through the membrane capacitance:

$$i_m = i_C + i_{ionic} = c_m \frac{\partial V_m}{\partial t} + \frac{V_m}{r_m}.$$

Combining the last two equations, we obtain:

$$\frac{1}{r_i}\frac{\partial^2 V_m}{\partial x^2} = c_m \frac{\partial V_m}{\partial t} + \frac{V_m}{r_m}.$$

This is called the *cable equation* describing how the membrane potential changes in time and along the cylinder. It is the single most important equation in linear cable theory from which other equations are derived for special cases. There are other forms of the equation one of which is derived by multiplying everything with the membrane resistance r_m:

$$\lambda^2 \frac{\partial^2 V_m}{\partial x^2} = \tau_m \frac{\partial V_m}{\partial t} + V_m,$$

where $\tau_m = r_m c_m$ represents the time constant of the membrane and:

$$\lambda = \sqrt{\frac{r_m}{r_i}} = \sqrt{\frac{\alpha R_m}{2R_i}},$$

where α is the radius of the cable. This is the length constant and it is useful because the electrotonic distance X can be easily expressed as $X = x/\lambda$.

Cable theory is relevant in this study because the gap junctions form a syncytium between the interneurons. This syncytium can be considered as an extended neuronal structure with many nodes (neuron somata) connected with long branching cables. The gap junctions can be considered as ohmic resistances connecting the neighbouring cables. Any activity propagating through the syncytium is either flowing passively through the cables or it can be regenerated at the nodes of the network. If the latter applies, then the propagation of activity will mainly depend on the electrotonic distance between the nodes. As long as the nodes are electrotonically close enough, the activity can continue propagating. Factors like the cable length, the leakiness of the membrane, the thickness of the dendrite and the linear conductance of the gap junctions are expected to play the most important role in this phenomenon. All these factors of the system can be manipulated in an *in silico* experimental environment in order to explore their influence on the phenomenon of propagating activity through the syncytium.

4.1.3 Rationale behind the experiments

All previous demonstrations of propagating activity through the PV-syncytium involved states that are not naturally occurring (i.e., induced by drugs; Gigout *et al.* (2006); Louvel *et al.* (2001)). In this study, the question was whether naturally occurring states can exhibit such propagation. Thus, the possibility of propagation during a state of elevated concentration of extracellular K^+ was explored. The increase of this concentration during seizures has been reported repeatedly (Heinemann and Dieter Lux (1977); Moody *et al.* (1974); Amzica *et al.* (2002); Gnatkovsky *et al.* (2008), see also Discussion). In this study, the extracellular concentration of K^+ was gradually increased while an area in layer V was illuminated with blue light. The PV^+ cells in

the slice are stimulated by the light through the expression of ChR2. In order to detect any propagation, I used a linear MEA placed along layer V.

In addition, I ran another series of experiments where I applied optogenetic silencing of the PV^+ cells during bursts of activity. This was achieved with the expression of Halorhodopsin (eNpHR) in PV^+. These bursts were spontaneously initiated while the slice was bathed in a solution with low-Ca^{2+} (Sanchez-Vives and McCormick (2000)). The purpose was to investigate whether the silencing of these interneurons has an impact on the bursting activity of the local network.

4.2 Methods

4.2.1 Cortical expression of optogenetic proteins

All animal handling and experimentation were done according to UK Home Office guidelines. Cortical channelrhodopsin-2 (ChR2) expression was achieved by using genetically engineered transgenic mice. Brain slices were prepared from first generation cross-breeding of homozygous floxed-channelrhodopsin mice (B6; 129S-Gt(ROSA)26Sor$^{tm32(CAG-COP4*H134R/EYFP)Hze}$/J; Jackson Laboratory, stock number 012569) with homozygous PV-cre mice (B6; 129P2-Pvalb$^{tm1(cre)Arbr}$/J; Jackson Laboratory, stock number 008069). Cortical halorhodopsin (eNpHR) expression was achieved with the same strategy. Brain slices were prepared from first generation cross-breeding of the homozygous floxed-halorhodopsin mice (Ai39; B6; 129S-Gt(ROSA)26Sor$^{tm39(CAG-HOP/EYFP)Hze}$/J; Jackson Laboratory, stock number 014539) with PV-cre mice (B6; 129P2-Pvalb$^{tm1(cre)Arbr}$/J; Jackson Laboratory, stock number 008069). Wild-type mice (C57BL/6J) not expressing any optogenetic protein were also used for control experiments.

4.2.2 Preparation of brain slices

For the ChR2 experiments, young mice (6-12 weeks) were perfused. They were first anesthetised using Ketamine (0.3 mL / 30 g) and then perfused with ice-cold

sucrose-based artificial cerebrospinal fluid (ACSF: $NaHCO_3$ 24mM, KCl 3 mM, NaH_2PO_4 1.25 mM, sucrose 227.8 mM, glucose 10mM, $MgCl_2$ 4 mM) before the brain was removed to prepare coronal brain slices. For the eNpHR experiments, young to mature mice (2-8 months) were sacrificed by cervical dislocation, and the brain was removed to prepare coronal brain slices. For the extracellular recordings, I used 400 μm thick slices, and for intracellular recordings, 350 μm thick slices. The slices were cut on Leica VT1200 vibratome (Leica Microsystems, Wetzlar, Germany) either in ice-cold oxygenated (95% O_2 / 5% CO_2) ACSF (NaCl 125mM, $NaHCO_3$ 26mM, glucose 10mM, KCl 3.5 mM, NaH_2PO_4 1.26 mM, $MgCl_2$ 3mM) for the eNpHR experiments or in ice-cold oxygenated (95% O_2/ 5% CO_2) sucrose-based ACSF as above for the ChR2 experiments. After cutting, the slices were transferred to an incubation, interface chamber (room temperature) perfused with oxygenated (normal) ACSF (NaCl 125 mM, $NaHCO_3$ 26 mM, glucose 10 mM, KCl 3.5 mM, NaH_2PO_4 1.26 mM, $CaCl_2$ 2 mM, $MgCl_2$ 1 mM) for at least 1 hour before transferring them to a recording interface chamber. In the recording interface chamber, the ACSF used was either normal ACSF as above for the ChR2 experiments or low-Ca^{2+} ACSF (NaCl 125 mM, $NaHCO_3$ 26 mM, glucose 10 mM, KCl 3.5 mM, NaH_2PO_4 1.26 mM, $CaCl_2$ 1.1mM, $MgCl_2$ 1mM) (Sanchez-Vives and McCormick (2000)) for the eNpHR experiments. The ACSF was perfused at 1.5 2.5 ml /min and its temperature was kept at 33-36 ^{o}C. In the case of the ChR2 experiments, the concentration of extracellular K^+ was systematically being increased during the recording by adding KCl to the perfused ACSF. Figs 4.2 and 4.3 show details about the experimental setup for the ChR2 and eNpHR experiments, respectively.

4.2.3 Extracellular recordings

Multichannel extracellular recordings were collected at 25 kHz unless otherwise stated, using a linear 16-channel-probe configuration (A16x1-2mm-100-177; NeuroNexus; electrode separation, 100 μm) for the ChR2 experiments or a four tetrode 16-channel-probe configuration (A4x1-tet-3mm-150-121; NeuroNexus; tetrode separation, 150 μm) for the eNpHR experiments. This was connected to an ME16-FAI-μPA-system and MC-Rack software (Multichannel Systems, Reutlingen). Data acquisition was carried out using a 1401-3 Analog-Digital converter (Cambridge

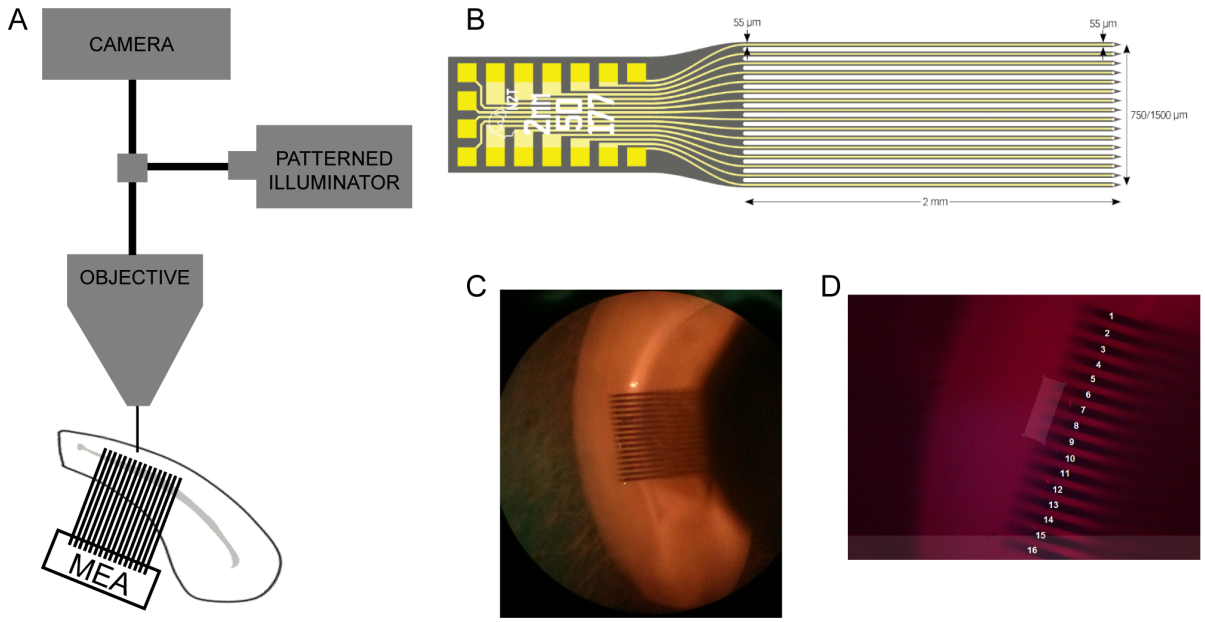

Figure 4.2: Schematic of the experimental setup and equipment used in the ChR2 study of the PV-syncytium.(A) Schematic of the experimental setup during the extracellular recordings using a linear 16-electrode array. The photostimulation was delivered using patterned illumination through the objective. (B) Schematic of the linear 16-electrode array used in the experiments. The image was taken from the NeuroNexus catalogue. Note that the distance between adjacent electrodes is 0.1 mm. (C) The recordings were taken from the dorsal area of the slice, targeting the primary visual area. (D) Example of an experiment where the illumination was delivered to a 4-electrode wide area in the centre of the array. The electrodes E6 up to E9 were considered to be in the photostimulated area while the propagation of activity was recorded at a distant electrode.

Electronic Design, Cambridge) and Spike2 software (Cambridge Electronic Design, Cambridge). The electrode array was placed along layer V in the occipital dorsal area of neocortex (see Fig. 4.2), approximately corresponding to primary visual cortex (Allen Mouse brain atlas, Goldowitz (2010)).

4.2.4 Optogenetic illumination

Channelrhodopsin was activated by a 470nm LED delivering light through the objective using the patterned illuminator Polygon400 (Mightex Systems, Pleasanton, CA, USA). The system was controlled and the patterns were designed through the PolyScan 2 software from the same company. The light intensity was measured at approximately 2 mW/mm^2 *(courtesy of Mr. Eike Joest).*

Halorhodopsin was activated by a 561nm, 50mW solid-state laser (Cobolt) connected

to a fibre optic with a fine cannula (400 μm core, 0.20 NA; Thorlabs). The illumination was controlled by a SR475 laser shutter (Stanford Research Systems). After optimizing the optic fibre coupling, the total light power at the cannula tip was measured at 15-30 mW. The light intensity was adjusted by adding different neutral density filters (ND filters 0.2-0.6; Thorlabs) placed in the light path between the laser and the optic fibre. Different filters could be used for different slices, however it was always constant at any given slice. After adding neutral density filter, laser output power ranged between 3-20 mW measured at the tip of the cannula.

Desensitization of the eNpHR protein was minimized, as described by Han and Boyden (2007), by co-illumination also with blue light (epifluorescent illumination through bandwidth excitation filter (460nm, halfwidth 40nm), through a 4x air objective (0.28 NA, Nikon; approximately 12mW/mm^2 at the tissue). This was used only during the extracellular recordings.

4.2.5 Patch-clamp experiments

Recordings were made using a laser spinning disc confocal microscope (Visitech) fitted with Patchstar micromanipulators (Scientifica) mounted on a Scientifica movable top plate. Electrophysiological data was collected using a Multiclamp 700B amplifier (Molecular Devices) and Digidata acquisition boards connected to Dell desktop computers running pClamp software (Molecular Devices). During the entire recording, cells were bathed in oxygenated (95% O_2/ 5% CO_2) ACSF solution (perfusion at 13 ml/min) heated to 3337C by a sleeve heater element (Warner Instruments) around the inflow tube. Whole cell recordings were made using 3-7M pipettes made of borosilicate glass (Harvard apparatus). The electrode filling solution used was: K-methyl-SO_4 125 mM, Hepes 10 mM, Mg-ATP 2.5 mM, NaCl 6mM; 290 mOsM and pH 7.35.

4.2.6 Pharmacology

For the purpose of blocking the glutamate currents both NBQX and D-APV were used. NBQX (HelloBio) was used at 20 μM concentration to block the AMPA receptors.

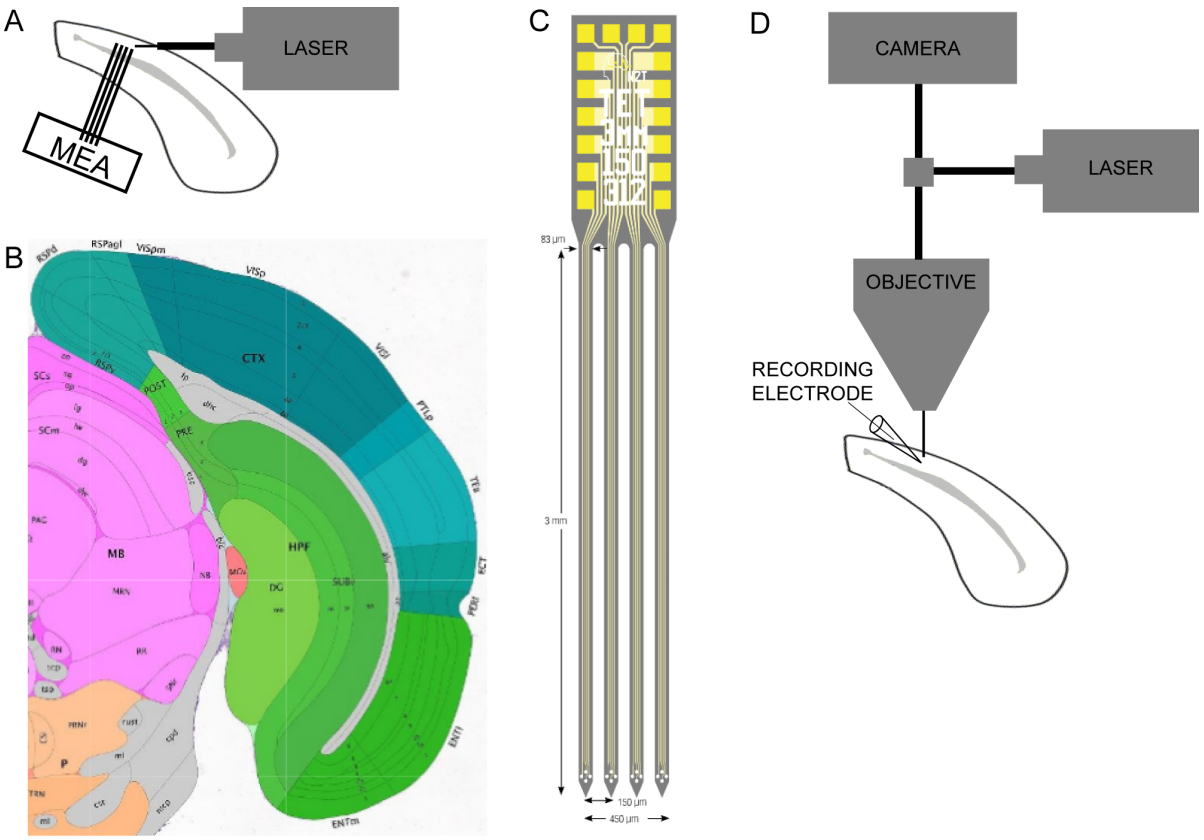

Figure 4.3: Schematic of the experimental setup and equipment used in the eNpHR study.(A) Schematic of the experimental setup of the extracellular recordings using a 4-tetrode MEA. The illumination was delivered by a solid-state laser through a fine cannula. (B) The recordings were taken from the dorsal area of the slice, targeting the primary visual area (VISp). The image was downloaded from the Allen Mouse Brain Atlas (Goldowitz (2010)). (C) Schematic of the 4-tetrode array used in the experiments. The image was taken from the NeuroNexus catalogue. (D) Schematic of the experimental setup used for intracellular recordings using a glass micropipette as the recording electrode. Note that the illumination in this case is delivered through the objective.

D-APV (Abcam Biochemicals) was used at 50 μM concentration to block the NMDA receptors. In addition, the gap junction blockers Mefloquine (50 μM, (Cruikshank *et al.* (2004)); Sigma), Quinine (100 μM, (Srinivas *et al.* (2001)); Aldrich), Carbenoxolone (100 μM, (Rozental *et al.* (2001)); Tocris Bioscience) were used.

4.2.7 Network model

A network model of the PV-syncytium was developed and simulated in NEURON 7.4 (Hines and Carnevale (1997)). The simulations were carried out on a Windows 10 (64-bit) computer with an Intel Core i5-3337U processor. The network comprised identical fast-spiking interneurons as used by Konstantoudaki *et al.* (2014) (see also

Durstewitz and Gabriel (2007)). The model of fast-spiking interneuron used in the present study was obtained from ModelDB (accession number 168310). These cells are biophysically detailed but morphologically simple. The biophysical mechanisms featured by the soma include: fast Na^+ channel, A-type K^+ channel, delayed-rectifier K^+ currents, Ca^{2+} buffering mechanism, slow K^+ current, N-type high-threshold activated Ca^{2+} current, and the hyperpolarization-activated cation current. The mechanisms of the dendrite include the fast Na^+ channel, the A-type K^+ channel, and the delayed-rectifier K^+ currents whereas the axon has only the fast Na^+ channel and the delayed-rectifier K^+ currents. For modelling the membrane random fluctuations, artificial current with Poisson characteristics was injected in the soma (Konstantoudaki *et al.* (2014)). The neuron model used in this study had the same biophysics as described in (Konstantoudaki *et al.* (2014)). The morphology was slightly modified, though, with each cell having two rather than just one dendrite of length 0.2 mm (Amitai *et al.* (2002); Fukuda *et al.* (2006)). The dendrites are composed of 10 segments. Each dendrite features a gap junction at a distance d from the soma. These are used to electrically connect the cells in a chain formation with 0.1mm spacing between the cells (see Fig. 4.12). One gap junction is used to electrically connect the cell with the neighbouring cell up the chain whereas the other is used to connect it with the neighbouring cell down the chain. The first cell is only connected with one cell down the chain and receives input directly to its soma from a current clamp mechanism instead.

4.2.8 Statistical analysis

In order to test whether the optogenetic silencing in the eNpHR experiments had a significant effect on the firing rates of active neurons, a paired Wilcoxon signed-rank test was used. This is a non-parametric statistical hypothesis test applied on paired differences, in this case, the difference in the firing rate before and during as well as during and after the illumination. It is an alternative to the paired t-test when the assumption of normality in the data is violated (McDonald (2009)). This test has three other assumptions:

1. The dependent variable is either ordinal or continuous.

2. The independent variable consists of two categorical groups (e.g., before and after).

3. The distribution of the differences between the pairs is symmetrical in shape.

As with any other statistical hypothesis testing, the effect is considered statistically significant if the null hypothesis can be rejected as improbable. The null hypothesis in this case is that the differences between the pairs come from a distribution with median 0. This analysis was carried out in MATLAB Release 2013b (The MathWorks, Inc., Natick, MA) using the function `signrank`.

4.3 Results: Optogenetic activation of PV^+ cells

I investigated the propagation of activity through the PV-syncytium in occipital cortical brain slices in different levels of extracellular K^+. Extracellular recordings were made from 29 mouse brain slices prepared from 10 young adult mice which expressed ChR2 under the PV promoter. I recorded extracellular field potentials using a linear multi-electrode array (MEA; 1.5 mm wide array of 16 electrodes with 0.1 mm spacing between the shafts) placed along layer V (see Fig. 4.2). I focused in layer V in which a dense network of electrically coupled PV^+ cells is well documented (Galarreta and Hestrin (1999); Fukuda and Kosaka (2003)). The photostimulation was a 3-second long train of pulses with frequency of 20 Hz (50% duty cycle), repeated every 20 seconds. The rationale of the experiments was to deliver a focal activation of PV^+ interneurons, and record any propagating activation away from that focus. Precise photostimulation was crucial for the control and reproducibility of the experiment, and to achieve this, I used a patterned illuminator (see Materials and Methods). For instance, see Fig. 4.2D for an example of photostimulation which is limited to an area of 400×100 μm, that is, equivalent to the extent of 4 adjacent microelectrodes.

I first assessed the ability of photoactivation of PV^+ cells in the photostimulation area as recorded by adjacent electrodes (usually 2 to 4) under the conditions of normal ACSF (3.5 mM extracellular K^+). Reliable activity was indeed recorded at those electrodes and the activity was limited in the specific area. The concentration of extracellular K^+ was increased, by adding KCl in the perfused ACSF during the

experiment, with small increments of 1 or 2 mM (in some of the earlier experiments, larger increments of up to 4 mM were used). The resting membrane potential of the cells was gradually depolarized due to the increase of the concentration making the cells more excitable (Somjen (2004)). After each K^+ increment, activity was recorded for at least 5 min. As expected, spontaneous activity increased as the levels of extracellular K^+ were increased (Jensen and Yaari (1997); Korn *et al.* (1987)).

4.3.1 Propagation of activity with increased extracellular K^+

I observed that there was a threshold of extracellular K^+ above which local field potential activity propagated out from the photostimulation area. This was observed by events recorded at distant electrodes outside the illuminated area. While the photo-induced activity of PV^+ cells was limited to the illumination area at low extracellular K^+, additional induced activity was recorded at distant electrodes outside the illumination area at high extracellular K^+. The firing outside the illumination area was time-locked with the firing inside the illumination area, indicating propagating waves of activation.

An example of such propagation arising under conditions of high extracellular K^+ is shown in Fig. 4.4. The blue traces come from electrodes, 8^{th} and 9^{th} along the linear array, in the photostimulation area where reliable activity is induced throughout the experiment even at normal K^+ levels (3.5 mM). The black traces come from the 11^{th}, 12^{th} and 13^{th} electrodes which are 200 400 μm away from the photostimulation area. Note that all these traces come from high-pass filtered channels with cutoff frequency at 300Hz. As Fig. 4.4 shows, at normal K^+ levels the induced activity is limited to the photostimulation area whereas at high K^+ levels the activity seems to propagate to the 11^{th} electrode (E11) as well (see zoomed-in traces). Notice also the increased spontaneous activity between the photostimulation periods at high K^+ levels.

This phenomenon was observed in multiple slices, approximately 1 in 3 slices, in which the induced activity was propagating to distant electrodes up to 0.6 mm away from the photostimulation area (n=10 propagations, range 0.1 0.6 mm with a median of 0.4 mm). In one of these propagations, more than one distant electrodes were involved.

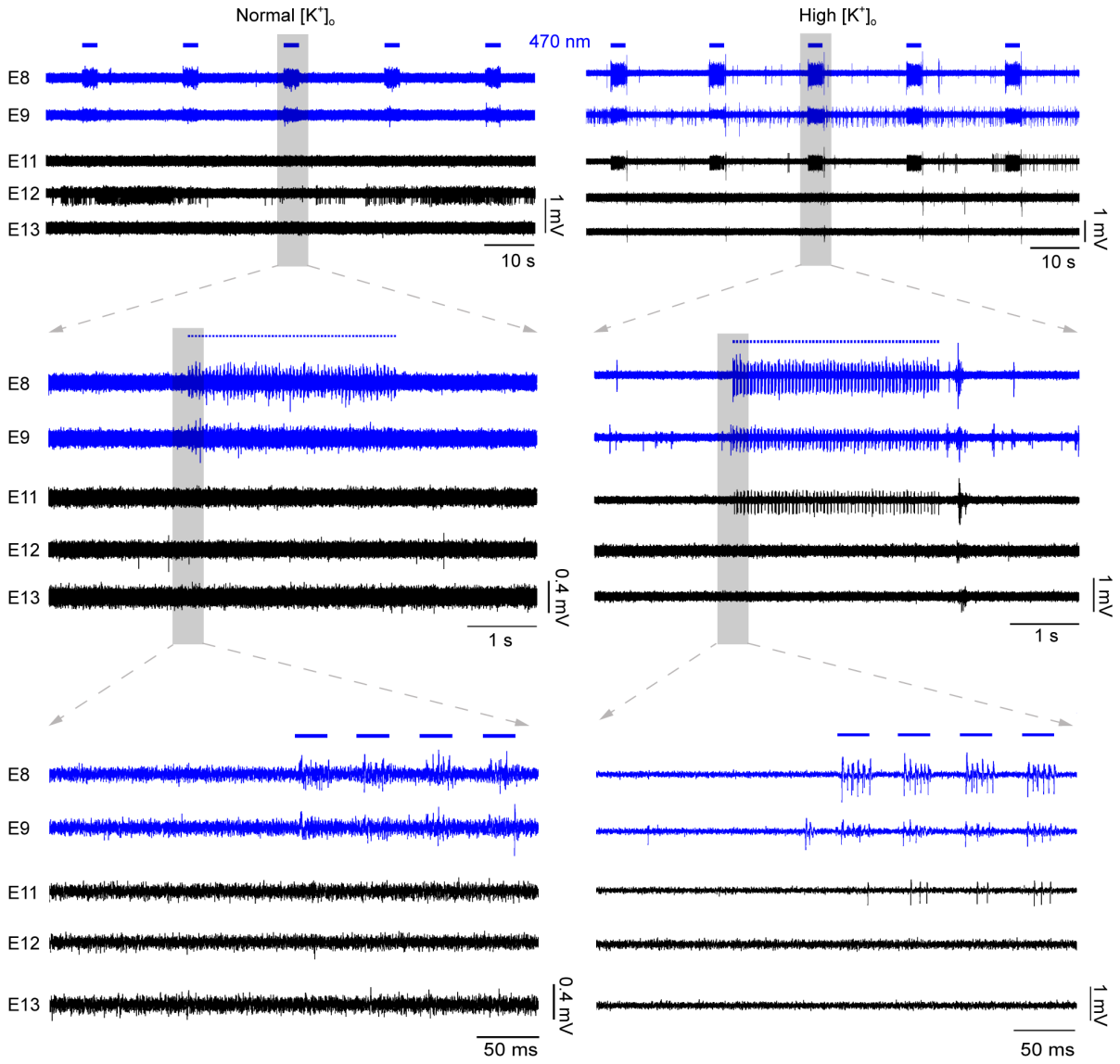

Figure 4.4: Propagating activity arising with raised extracellular K^+. The area around electrodes E8 and E9 is photostimulated (marked with blue) with 3 seconds long train of 20Hz pulses which repeat every 15 s. PV^+ cells around these electrodes are responding with 4-5 spikes per pulse (see zoom-in traces). After raising the extracellular K^+ concentration (from 3.5mM to 7.5mM), induced activity is recorded in a distant electrode as well, namely at E11. The activity recorded at E11 has lower spike rate compared to the activity in E8 and E9. It is also delayed compared to the activity recorded in the photostimulated area. The activity at the distant electrode is hypothesized to propagate through electrical synapses considering that the stimulated cells are GABAergic in nature.

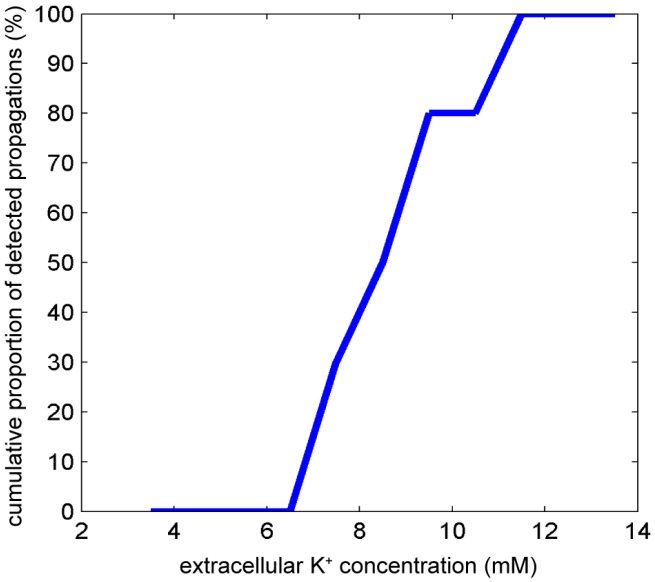

Figure 4.5: Concentration of extracellular K^+ needed to observe propagation of activity. The plot shows the cumulative proportion of detected propagations at different values of extracellular K^+ concentration. The majority of propagations (8 out of 10) were observed with an increase of the extracellular K^+ up to 9.5 mM.

The pooled data is reported in Fig. 4.5 where the cumulative proportion of detected propagations is plotted against the extracellular K^+ concentration. The concentration of extracellular K^+ needed to enable the propagation of activity at a distant area was calculated by fitting a sigmoidal function (logistic) to the pooled data: the 50% threshold is reached at 8.49 mM. As mentioned above, during the early stages of the study, large increments of K^+ concentration were applied (e.g., from 7.5 mM to 11.5 mM). This is the reason why some propagations reported here needed a concentration of 11.5 mM to be detected. That proved to be unnecessarily high and was later avoided because of the possible spreading depression which interfered with the experimental process.

4.3.2 Pharmacological manipulations

The hypothesis was that the induced activity at the photostimulation area propagates to the distant electrodes through the PV-syncytium. In order to test whether the propagated activity goes through the electrical synapses between PV^+ cells, pharmacological manipulations were used. Note that from all the propagations reported in Fig. 4.5, only 6 of them were confirmed to travel through the gap

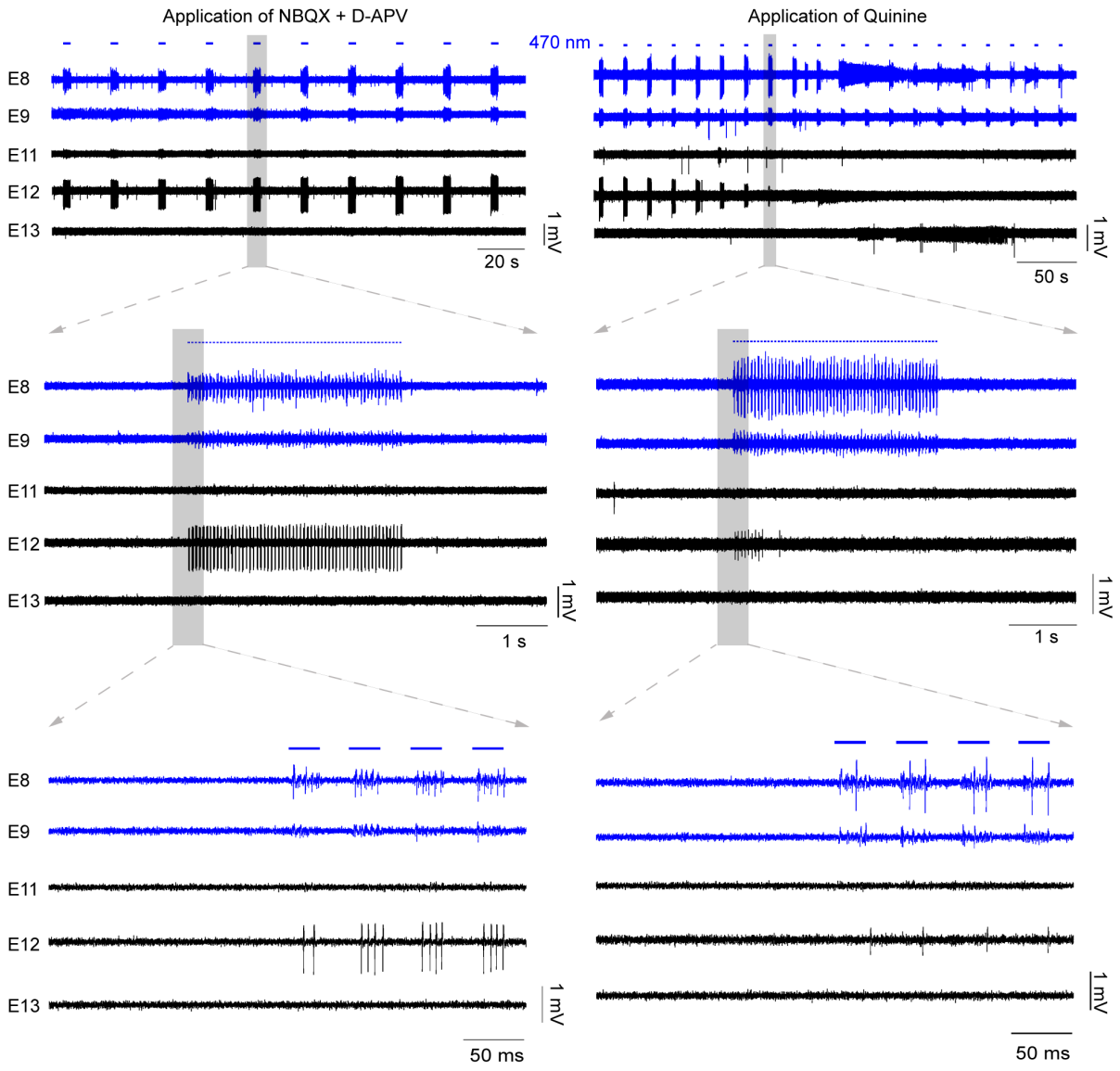

Figure 4.6: Pharmacological manipulation of the propagating activity. To test whether the activity at the distant electrode seen in Fig. 4.4 is propagating through gap junctions, I applied some pharmacological agents. First, the glutamate receptors were blocked by applying NBQX and D-APV. The spontaneous activity is decreased but the induced activity remains strong at the distant E12 indicating that glutamate is not involved in the propagation. Then, the gap junction blocker quinine was applied. The induced activity in E12 was suppressed evidenced by decreasing amplitude and spike rate. It was gradually silenced.

junctions. The rest, recorded early on during the study, were not pharmacologically tested so they are considered as putative propagations through the gap junctions.

First, glutamatergic currents were suppressed with the application of NBQX and D-APV. The purpose of this application is twofold: to decrease the spontaneous activity so the induced would be more pronounced and to eliminate the possibility of a multi-synaptic propagation involving glutamate release. Indeed, as observed in 4 different slices, the suppression of glutamatergic currents was found to suppress the propagation too. In such cases, the propagated activity gradually diminishes along with the suppressed spontaneous activity, indicating a multi-synaptic propagation involving ionotropic glutamate receptors. In contrast, in the example of Fig. 4.6 left panel, the propagation to E11 and E12 remains strong while the spontaneous activity diminishes in E8 and E9, indicating that no glutamate is involved in this propagation.

A gap junction blocker was then applied to test whether the putative propagation through the gap junctions would cease. For this purpose, the gap junction blockers quinine, mefloquine and carbenoxolone were used in different experiments. Quinine and mefloquine were preferred because of their ability to block specifically the relevant channels Cx36 and Cx50 with minor side effects (Cruikshank *et al.* (2004); Srinivas *et al.* (2001)). In contrast, carbenoxolone was used only once because of its low specificity (Rozental *et al.* (2001)). Following the same experiment, Fig. 4.6 right panel shows how the propagated activity is suppressed after the application of quinine. This suppression is characterized by a decrease in the amplitude and the firing rate of the recorded activity at E12 (see zoomed-in traces).

The advantage of quinine over mefloquine is that its effects are reversible by washing it out (Srinivas *et al.* (2001)). The expected result of the washout in this experiment was the reappearance of the propagated activity, and indeed this is exactly what happened, as shown in Fig. 4.7 left panel when quinine, NBQX and D-APV were washed out. In the example shown, the propagated activity reappeared first in E11 and E12 for a short time and then the propagated activity built up and remained strong in E13 for several minutes. Interestingly, despite the fact that the propagation was recorded in E11 and E12 before, now that the activity reached E13, both E11 and E12 were silent (see Discussion). After a persistent propagation of the activity as recorded in E13, a second

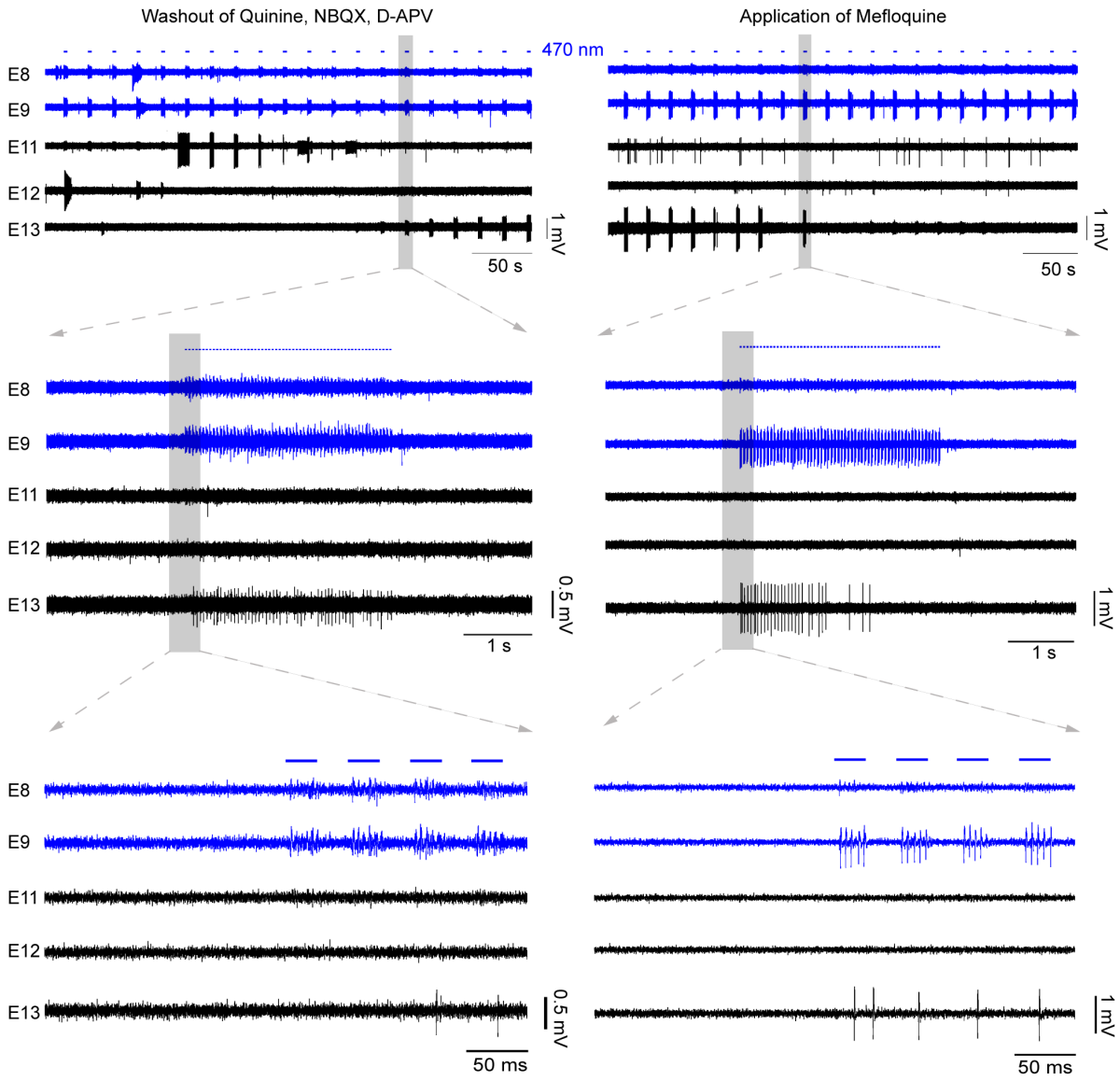

Figure 4.7: Validating the implication of gap junctions by applying multiple gap junction blockers. The propagated activity silenced in Fig. 4.5 was recovered by washing out quinine. In this case, NBQX and D-APV were also washed out. Induced activity was recorded at E11 and E12 but it was limited in time. Stable activity with increasing amplitude was recorded at E13. This activity remained strong for several minutes until another gap junction blocker was applied, namely mefloquine. The propagated activity was once again blocked but this time through a decrease in spike rate without a gradual decrease in amplitude.

blockade was achieved after applying mefloquine (see Fig. 4.7 right panel). Note that the second blockade of the propagation was achieved in the absence of the glutamate blockers indicating that they are not required for the effect.

As mentioned above, the blockade of gap junctions, shown in Fig. 4.6 was characterized by a significant and gradual decrease in amplitude. This was a common effect found in 4 out of 6 propagations when a gap junction blocker was used. In Fig. 4.7, though, the second blockade on the same slice was not characterized by this significant and gradual decrease in amplitude. Instead, it just exhibited a decrease in firing rate. The same effect was observed in another experiment where only mefloquine was used. Fig. 4.8 shows the entire protocol of that experiment. The two electrodes E13 and E9 were sufficient to show the propagation and its blocking with E13 being in the photostimulation area and E9 away from it. Initially, at normal K^+ levels, induced activity was recorded only at E13. Then, the extracellular K^+ concentration was increased to 8.5 mM and the activity was propagating to E9. Notice the very high levels of spontaneous activity at this stage. It seems that the activity at E13 was being silenced completely during each photostimulation but actually only the spontaneous activity was silenced; the induced activity in E13 remains the same (see zoomed-in traces). After the application of NBQX and D-APV the spontaneous activity was reduced massively and the propagating induced activity was recorded clearly between E13 and E9 (see zoomed-in traces). At the final stage, mefloquine was applied and the propagation was blocked by a gradually decreasing firing rate. Note, though, that some lower amplitude activity remained in E9 even after the blockade.

The working hypothesis behind these propagations was that they initiate from PV^+ cells in the photostimulation area, they travel through the gap junctions between these cells and the activity is regenerated through action potentials in PV^+ cells outside the photostimulation area. If this is true, then the activity recorded from outside the photostimulated area would have a spike waveform characteristic of PV^+ cell firing. Analysis of spike waveforms was carried out to check this. A demonstration of this analysis is shown in Fig. 4.9 where the average spike waveforms are calculated from the signals E13 and E9 from Fig. 4.8 after NBQX and D-APV were applied. In this example, the valley-to-peak width t and the valley-to-peak amplitude ratio v/p are relatively low, consistent with the action potential signature of fast-spiking

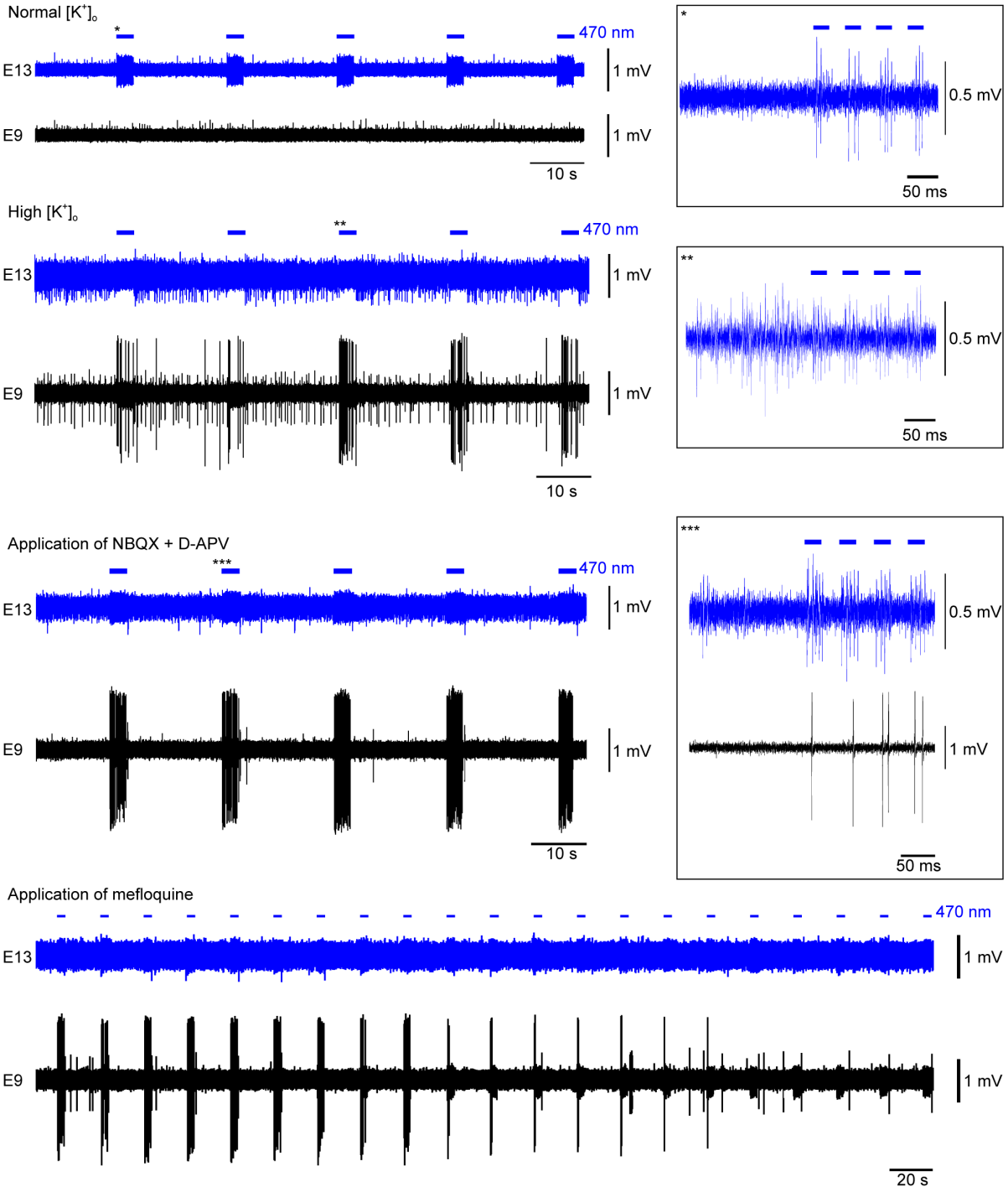

Figure 4.8: Blocked propagation of activity with a gradual decrease of firing rate rather than gradual decrease of amplitude. The activity at two different electrodes is plotted: electrode E13 in the illuminated area (blue) and electrode E9 outside the illumination area (black). When the extracellular K^+ has a normal concentration, there is induced activity only at E13. With the rise of extracellular K^+ has concentration, induced activity is observed in E9 as well. Blocking the AMPA and NMDA receptors diminishes the spontaneous activity but leaves the induced activity strong. Subsequent application of the gap junction blocker mefloquine diminishes the propagated activity in E9. The blockade of the activity is characterized by a gradual decrease in firing rate.

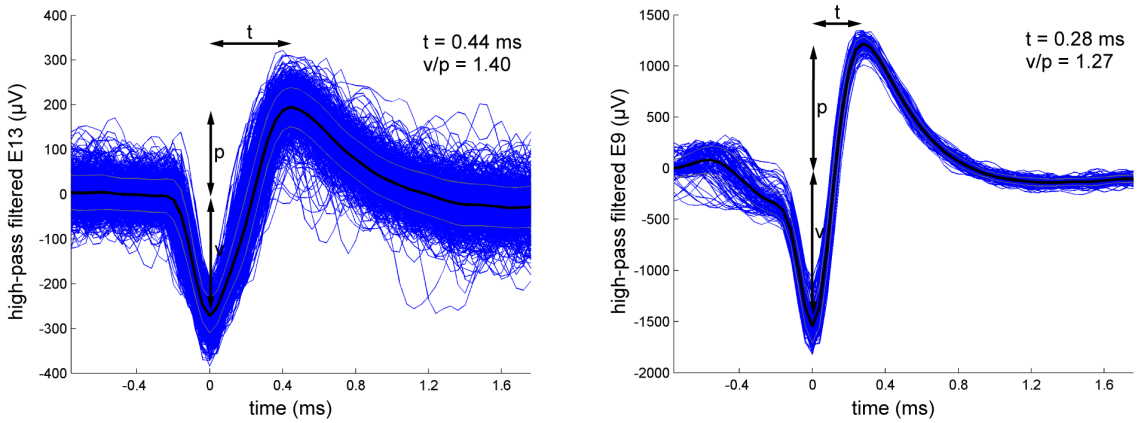

Figure 4.9: Analysing the waveforms of recorded spikes. In order to test whether the propagated activity is indicative of fast-spiking interneurons, the spike waveforms were analysed using two metrics: the spike width *t* (valley to peak) and the valley-peak amplitude ratio *v/p* (Peyrache *et al.* (2012)). The spikes plotted here are taken from example in Fig. 4.7. The activity on the left was recorded at the photostimulated area and the activity on the right was recorded at the distant electrode. The propagated activity on the right has an indicative waveform of a fast-spiking interneuron with very low *t* and *v/p* (Barthó *et al.* (2004); Peyrache *et al.* (2012); Mruczek and Sheinberg (2012)).

interneurons (Peyrache *et al.* (2012)). The same analysis was carried out for all propagated activity yielding a valley-to-peak width t ranging from 0.24 to 0.36 ms (0.30 ± 0.02 ms) and a valley-to-peak amplitude ratio v/p ranging from 1.01 to 1.94 (1.48 ± 0.14). These results support the idea that the propagated activity is recorded from fast-spiking interneurons rather than regular-spiking cells (Barthó *et al.* (2004); Peyrache *et al.* (2012); Mruczek and Sheinberg (2012)). They also support the idea that recorded activity represents action potentials rather than inhibitory post-synaptic potentials (IPSPs) which have significantly longer waveforms.

The speed of propagation can be calculated analysing the timing of the spikes recorded and considering the distance between the electrodes involved. As mentioned above, the photostimulation is delivered as a 20 Hz train of pulses with 50% duty cycle: this gives a period of 50 ms during which the light is on for 25 ms and off for the remaining 25 ms. Analysing the timing of spikes during this period for both electrodes E13 and E9 of the previous example, produces the spike time histograms shown in Fig. 4.10. Clearly the spikes recorded in E9 outside the photostimulation area are delayed compared to the ones recorded inside the photostimulation area (E13). Taking the time points of the average first spike (marked with asterisk) and considering 0.4 mm distance between the electrodes, the speed is calculated at 52.2 mm/s. The same approach was carried

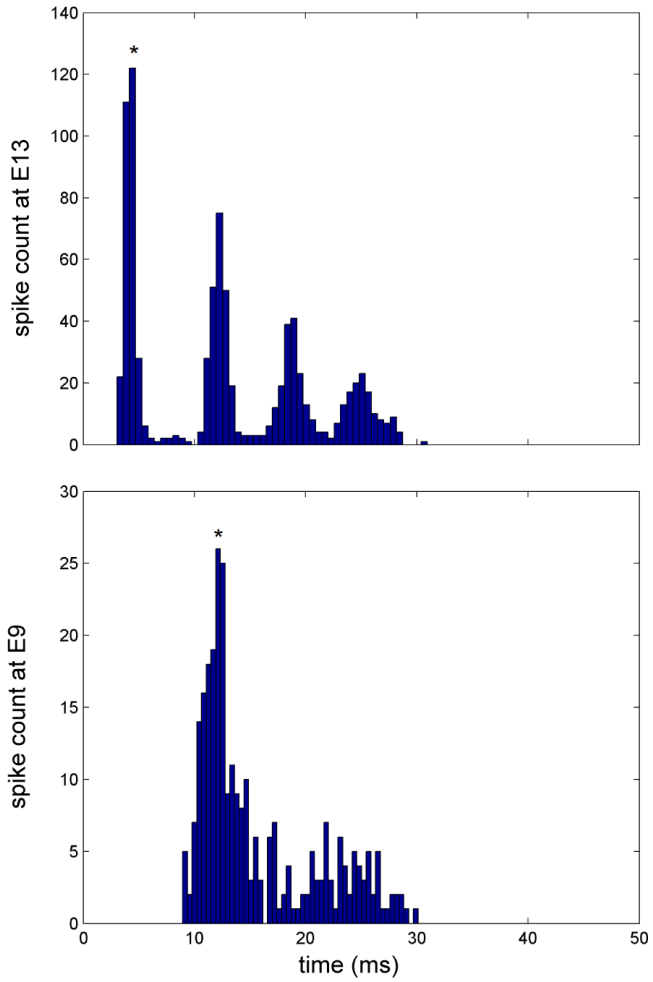

Figure 4.10: Calculating the speed of propagation from the spike time histograms. The propagation speed was calculated by first plotting the spike histograms during the illumination pulse period of 50 ms (25 ms light on and 25 ms light off) at two electrodes. The first peaks, marked here with asterisks, were then chosen for both the photostimulated electrode and the distant electrode. The propagation speed was directly calculated from the time difference between these peaks and the known distance between the electrodes (0.4 mm in this example).

out for all recorder propagations and the distribution of propagation speeds is plotted in Fig. 4.11. This plot includes 6 propagations through the gap junctions that were confirmed with pharmacological manipulations and 4 putative propagations through gap junctions that were collected in the early stages of the study without any pharmacological manipulation. The calculated propagation speeds are relatively consistent with the exception of one putative propagation (135.1 mm/s), which lies 3.6 interquartile ranges away from the median (63.6 mm/s). After excluding the outlier, the experimental results yield a propagation speed of 58.9 $\pm$ 5.3 mm/s.

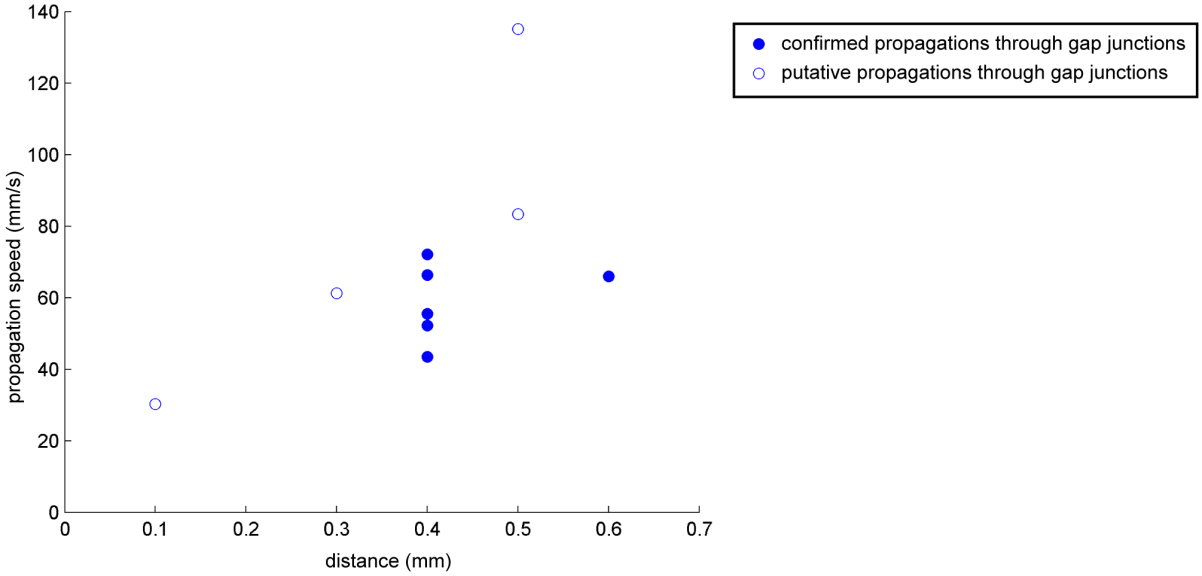

Figure 4.11: Distribution of calculated propagation speeds. Scatter plot of all the propagation speeds including 6 that were confirmed to propagate through gap junctions using gap junction blockers and 4 that were not tested and are considered putative. The x-axis gives the distance covered by the propagating activity.

4.3.3 Computational modelling of the phenomenon

In order to explore the phenomenon in the context of cable theory (see Introduction), the experiment was modelled in the NEURON 7.4 environment (see Methods). A schematic of the model can be found in Fig. 4.12, where fast-spiking interneurons are electrically coupled in a chain formation. The cells were depolarized,to simulate the effect of high extracellular K^+, by setting their resting membrane potential V_m to -49 mV. Random fluctuations of the membrane potential were modelled with an injected noise signal. The first cell in the chain was stimulated with current with the same characteristics as in the experiment: 20 Hz with 50% duty cycle. As shown in Fig. 4.12, the first cell responds to the stimulation with a comparable firing rate (3-4 spikes per 25ms pulse) to the one seen in the experiments and the activity propagates down the chain through the gap junction with conductance g_{gap} which is placed at distance d from the soma. These and other parameters were manipulated to investigate their role in the propagation (see below). The example shown in Fig. 4.12 is based $g_{gap} = 18.18$ nS and $d = 0.1$ mm and the activity propagates successfully down the chain. The probability of spike regeneration decreases rapidly as the activity propagates from one cell to the next. As a result, the activity dies out at a distance of 0.3 mm in this example. The histograms on the right reveal the massive decrease of firing rate as the

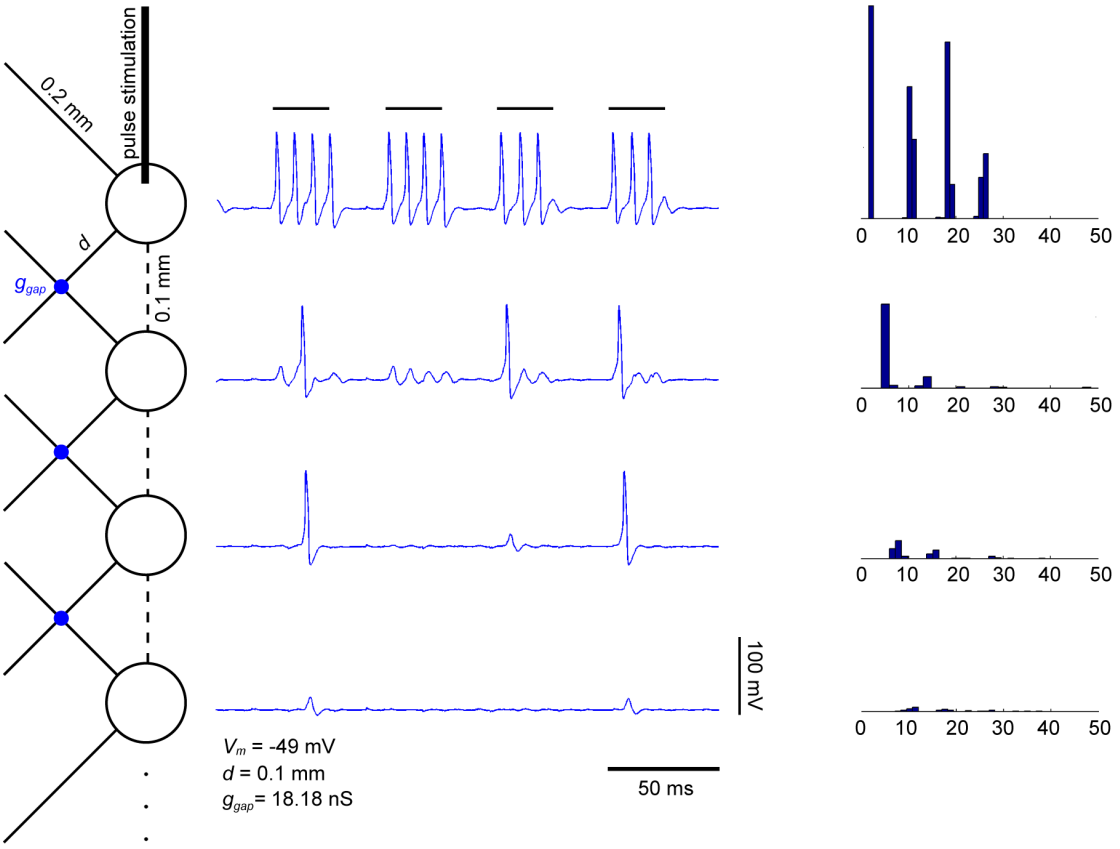

Figure 4.12: Simulating the propagation of activity in a chain of electrically coupled fast-spiking interneurons. A model network of electrically coupled fast-spiking interneurons was developed. The cells were connected in a chain formation with a distance of 0.1 mm between each pair. The cells feature detailed biophysics (see Methods) but their morphology is reduced to a compartment of soma and two dendrites composed of 10 segments. The dendrites feature a gap junction with conductance g_{gap} placed at a distance d from the soma. The cells feature a noisy membrane potential and are depolarized to -49 mV to simulate the effect of high extracellular K^+. The first cell receives stimulating pulses of 25 ms width and 50 ms period and the activity propagates down the chain through the gap junctions. Some spikes are regenerated from node to node but the overall spike rate drops sharply as the number of intermediate nodes increases. The spike time histograms on the right are used to calculate the propagation speed in the same way as above (see Fig. 4.10).

activity propagates through the syncytium and it also shows the timing of spikes relative to the 50 ms period of stimulation. Notice that, during each 50 ms stimulation period, 4 spikes are usually induced in the first cell of the chain from which the first one has the highest probability of regeneration at the next node. The same behaviour was found during the experiments (see Fig. 4.10). The propagation speed reported below is calculated from the spike-time histograms using the same approach used in the analysis of the experimental results (see Fig. 4.10).

The distance d of the gap junctions from the soma is one of the parameters manipulated in the chain model. The speed of propagation was calculated for different

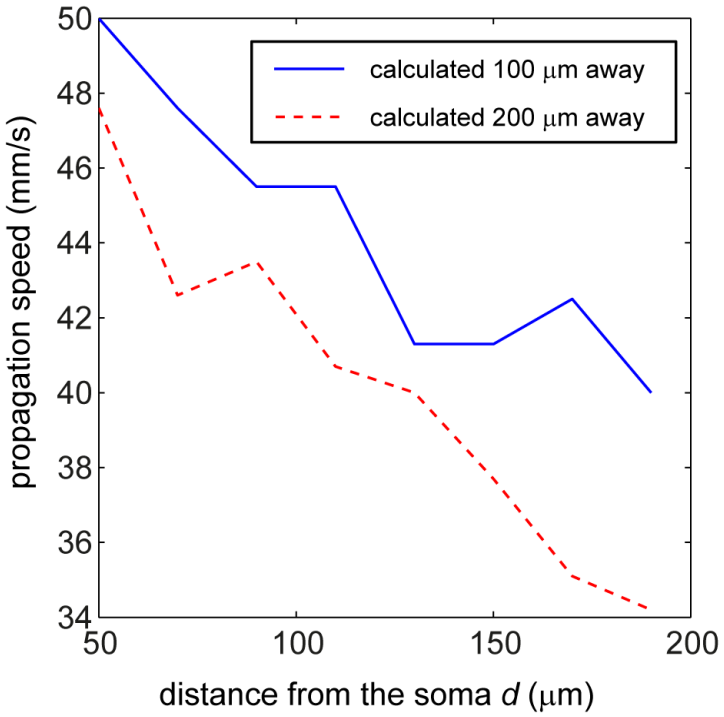

Figure 4.13: Calculating the propagation speed for different values of distance from the soma, d. The speed of propagation varies with values comparable to the experimental results. Increasing the distance d of the gap junction from the soma increases the length of the cable through which the activity has to travel. This results into greater delays of regeneration and therefor lower speeds of propagation from cell to cell. The speed calculated 200 μm away from the stimulated cell is lower that the speed calculated 100 μm away. This indicates that the intermediate spike regenerations introduce delays in the propagation.

values of the parameter d. It was varied from 0.05 mm to 0.2 mm which represents a physiological range of values as measured in visual cortex (Fukuda *et al.* (2006)). The results in Fig. 4.13 include the speed of propagation as calculated at 0.1 mm and 0.2 mm away, that is, from the first to the second or the third cell, respectively. As expected, the propagation speed is decreasing with increasing d: the action potential travels through a longer cable and the regeneration is delayed at each next node. Notice, however, that the speed calculated at 0.2 mm down the chain (range: 34-48 mm/s) is lower than the speed calculated at 0.1 mm (range: 40-50 mm/s) indicating that the regeneration of the spike at intermediate nodes introduces some delay in the propagation. This suggests that the propagation, at least in this example, has a regenerative nature rather than a passive propagation of depolarization.

The successful regeneration and continued propagation of the activity is expected to depend heavily on some cable parameters of the system (see Introduction). These parameters include the membrane resistance r_m, the diameter of the dendritic cross

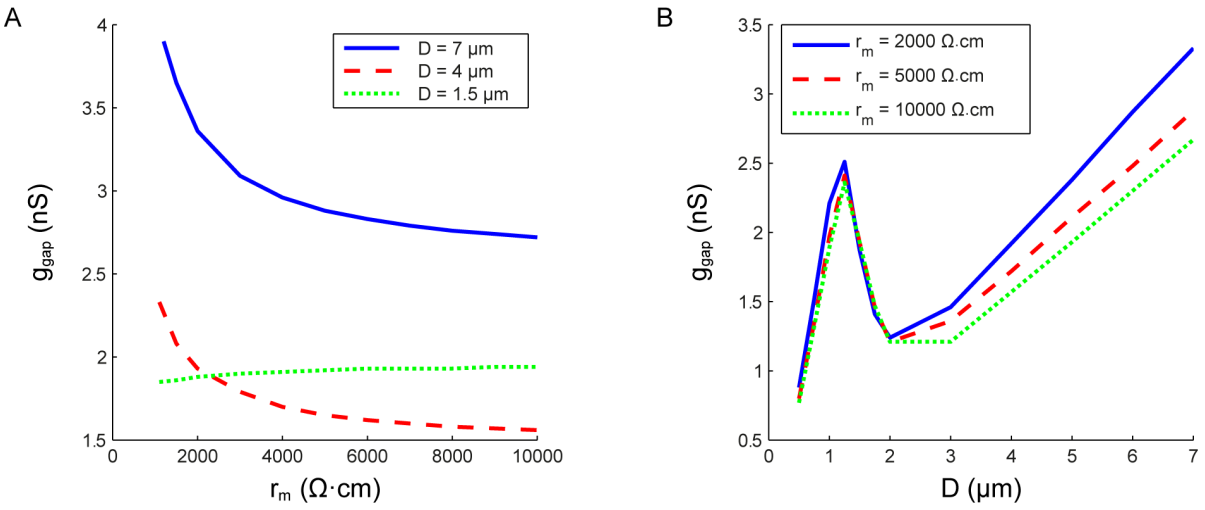

Figure 4.14: Relationship between the minimum gap-junctional conductance, g_{gap}, needed for the propagation and other parameters. (A) The minimum g_{gap} that enables propagation is inversely proportional to the membrane resistance, r_m, for medium or high values of dendritic diameter D. This does not apply when the dendrite is thin ($D = 1.5$ μm) in which case the minimum g_{gap} remains almost constant with the increase of r_m. (B) The minimum g_{gap} has a linear relationship with the dendrite diameter for D higher or equal to 3 μm. The slope of this linear relationship increases slightly with the decrease of r_m. Their relationship becomes nonlinear for D lower than 3 μm. The results suggest a qualitatively different propagation of activity between low and high values of D.

section and the conductance of the gap junction g_{gap}. The values of such parameters should yield, in combination, an electrotonic distance that is high enough for the action potential to travel through the coupled dendrites and reach the next soma in the chain. These parameters were systematically varied in the network model to reveal the trade-offs between them. More specifically, the membrane resistance, r_m, and the diameter of the dendrite, D, were varied and the minimum gap-junctional conductance, g_{gap} needed for successful propagation was calculated (see Fig. 4.14). The following results were produced with the noise disabled and the resting membrane potential was arbitrarily set to -48 mV to simulate the effect of increased extracellular K^+ concentration.

The results in Fig. 4.14A show that the minimum value of gap-junctional conductance needed for propagation is inversely proportional to the membrane resistance as long as the diameter of the dendrite is higher or equal to 3 μm (see below). This relationship indicates that when the membrane is leaky (low membrane resistance) the gap-junction conductance needs to be higher for the activity to propagate. On the other hand, with high membrane resistance, as in the case of the 4AP model (see Discussion), the

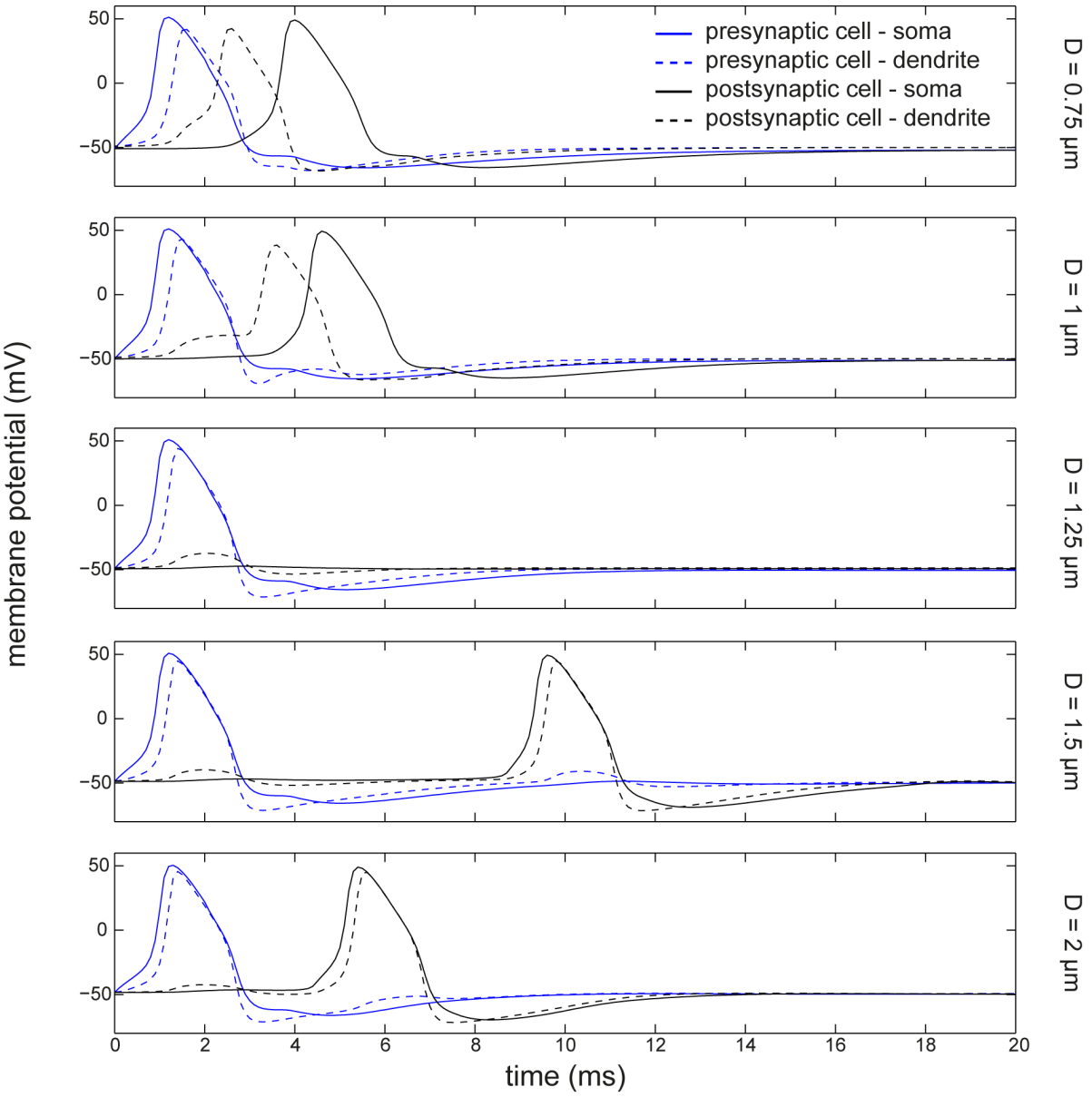

Figure 4.15: Qualitatively different types of spike propagation for different values of dendritic diameter D. The plots show the somatic and dendritic membrane potential in two electrically coupled cells for different values of D. The dendritic membrane potential is measured at the same compartment where the gap junction is located with its conductance g_{gap} set to 2 nS. When the dendrite is very thin ($D \leq 1$ μm) there is a dendritic spike preceding the somatic spike of the postsynaptic cell. In contrast, the somatic spike slightly precedes the dendritic spike when $D \geq 1.5$ μm. At $D = 1.25$ μm the propagation fails. The membrane resistance, r_m, is set to 5000 Ω·cm.

propagation can exist even with low gap-junction conductance. In addition, having thicker dendrites increases the leak current and demands higher values of g_{gap} for the propagation of activity. However, the relationship changes when we have a thin dendrite (1.5 μm). The minimum g_{gap} needed seems to be almost constant at approximately 1.9 nS for whatever value of membrane resistance. Actually, in contrast to the previous observations, the minimum g_{gap} is slightly decreased when membrane resistance is low.

This strange behaviour of the system when the dendrite is thin is demonstrated in Fig. 4.14B as well. The diameter of the dendrite is varied and the minimum gap-junctional conductance is plotted for three different values of membrane resistance. The minimum g_{gap} needed for propagation increases linearly with the increase of diameter beyond 3 μm in all three cases. The slope of this increase is slightly increased as the membrane resistance decreases. However, when the dendrite is thin with a diameter up to 2 μm, the minimum g_{gap} has a nonlinear relationship to the diameter. The minimum g_{gap} has a higher value than expected with a peak at 2.5 nS when the diameter is approximately 1.25 μm. Yet, at very low values of diameter (0.5 μm) the minimum g_{gap} drops to values as low as 0.75 nS. Interestingly, the behaviour of the system in this regime of thin dendrites seems to be qualitatively the same whatever the value of the membrane resistance. Even the values of g_{gap} are almost the same. These results suggest that the dynamics of the propagating activity are qualitatively different between high and low values of the dendrite diameter.

To further investigate this unexpected behaviour, I examined the traces of the simulation. In particular, the membrane potential at the somata and the dendrites of the first two cells was investigated. The dendritic compartments used were the ones featuring the gap junctions, which were placed 0.1 mm away from the soma. In these simulations, the g_{gap} was set to 2 nS and the traces were extracted for the diameter values 0.75, 1, 1.25, 1.5, and 2 μm. According to Fig. 4.14B, the propagation fails only in the case of $D = 1.25$ while it is successful in all the other cases. Indeed, as shown in Fig. 4.15, there is no propagation of the action potential when $D = 1.25$ μm but propagation is achieved in the rest. However, the propagation for values lower than 1.25 μm is qualitative different than the propagation for values higher than that. When the dendrite is very thin, the postsynaptic dendritic compartment, which features

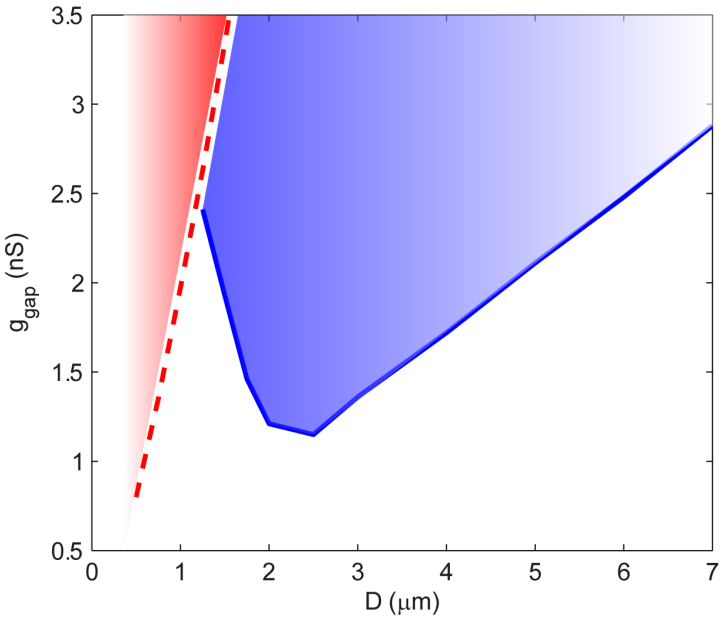

Figure 4.16: The two different regimes of propagating activity. This plot explains the curves shown in Fig. 4.14B. The area above the curves indicate the parameter settings that produce propagating activity and, as shown here, there are two different regimes for such propagation. The red area represents the regime of dendrite-first propagation, where the dendritic spike precedes the somatic spike. In this regime the minimum g_{gap} needed for the propagation increases linearly with the increase of the diameter, D. On the other hand, the blue area represents the regime of soma-first propagation. The relationship between g_{gap} and D is non-linear in this case. Note that the red area supersedes the blue area because the dendrite is always the first that is depolarized through the gap junction and has the chance of spiking.

voltage-dependent conductances, generates an action potential that precedes the action potential recorded at the soma (dendrite-first propagation). In contrast, when the dendrite is thicker, the slight depolarization of the postsynaptic dendrite generates an action potential at the postsynaptic soma which then travels back to the dendrite (soma-first propagation).

Further investigation reveals the two different regimes of activity that can explain the curves in Fig.4.14B. As shown in Fig. 4.16, there are two distinct regimes of propagating activity in the parameter space. The two different types of propagation shown in the traces of Fig. 4.15 are represented by the red and blue areas of the parameter space in Fig. 4.16. Parameters from the red area produce the dendrite-first propagation where the depolarization on the postsynaptic dendrite is strong enough to generate a dendritic spike which then generates a somatic spike. The minimum g_{gap} needed for the direct generation of a dendritic spike increases linearly with the increase of the dendrite's diameter. In contrast, parameters taken from the blue area generate a soma-first propagation where the dendrite is depolarized and this depolarization generates, with some delay, a somatic spike which then travels back to the dendrite. As shown in the figure, there is a non-linear relationship between the minimum conductance of the gap junction and the diameter of the dendrite. Notice that the red regime supersedes the blue regime exactly because the depolarization starts from the dendrite and if the depolarization is strong enough it will produce a dendritic spike that always precedes the spike at the soma.

As shown in Fig. 4.15, the propagation fails when the g_{gap} is set to 2 nS and the diameter is set to 1.25 μm. Considering the two different regimes of propagating activity shown in Fig. 4.16, this can be explained as follows. The g_{gap} is neither strong enough to generate directly a dendritic spike (as in the red regime) nor it is strong enough to travel down the dendrite and generate a somatic spike (as in the blue regime).

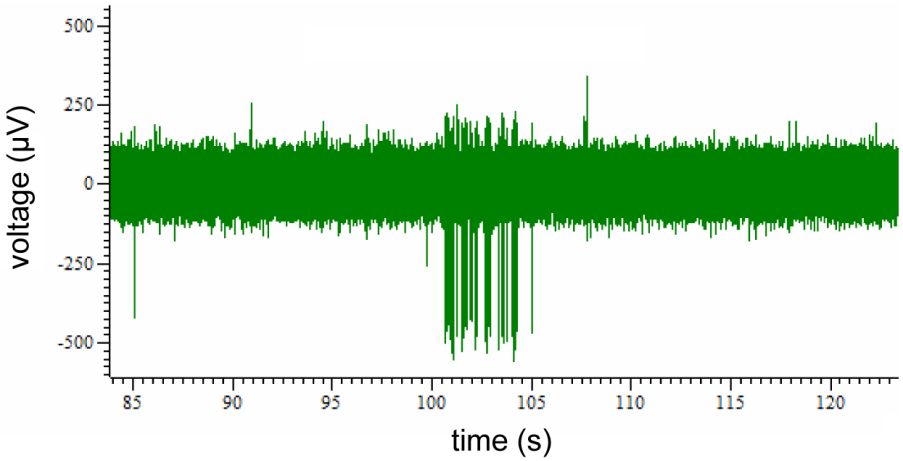

Figure 4.17: Extracellular recording of an exemplar short burst of activity in the low-Ca^{2+} solution. Spontaneous bursting activity such as this was repeatedly recorded in layer V of slices bathing in low-Ca^{2+} solution. Though, this type of activity did not match the expected activity as described in previous studies (Sanchez-Vives and McCormick (2000); Shu *et al.* (2003)). The bursts of activity recorded were usually much longer than expected and did not have low (delta) frequency of occurrence.

4.4 Results: Optogenetic silencing of PV^+ cells

Recordings were made from layer V of neocortical brain slices (n=19), bathed in ACSF modified to induce spontaneous UP and DOWN state transitions (Sanchez-Vives and McCormick (2000)). Indeed, the solution induced some activity but it had different characteristics than expected. Instead of short and slowly oscillating bursts of activity, usually shorter than 2 s (Sanchez-Vives and McCormick (2000); Shu *et al.* (2003)), the activity was longer without any oscillating behaviour. An example of the spontaneous activity during this experiment is shown in Fig. 4.17. Bursts of activity persisted for several seconds with a relatively stable firing rate. The activity was either single unit or multi-unit. The example in Fig. 4.17 is an example of short single unit activity lasting for approximately 5 seconds but much longer activity was also recorded, sometimes persisting for more than 40 seconds. In order to examine the effect of the illumination on these bursts, only a subset of them was considered. The following analysis includes only bursts of single unit activity with a firing rate of at least 5 spikes/s that were long enough to receiving at least 2 consecutive illuminations (15 s apart). From all the slices used (n=19) only a subset of them exhibited long enough activity to be analysed (n=8). These slices provided 11 long bursts of activity that were later analysed (see below).

The optogenetic silencing of the PV^+ interneuronal population during this type of

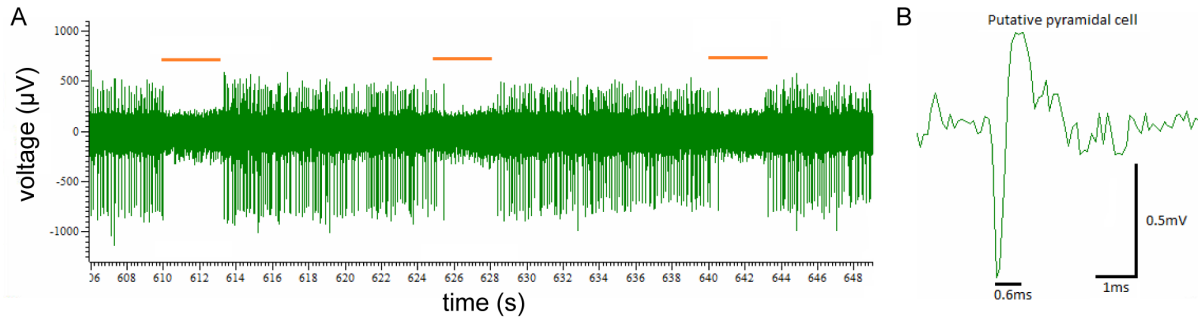

Figure 4.18: Extracellular recording of a putative pyramidal cell that was repeatedly silenced by optogenetic silencing of the PV$^+$ cells. (A) High-pass extracellular recording from layer V featuring bursting activity persisting for several seconds. The activity was repeatedly silenced by yellow light illumination (yellow bars) which was expected to silence exclusively the PV$^+$ cells. (B) A typical waveform (in terms of amplitude and width) of a spike taken from the single unit activity in (A). The spike-width of the cell is long (0.6 ms) indicating a putative pyramidal cell rather than putative PV$^+$ interneuron. This observation rendered the silencing effect as paradoxical.

activity yielded a paradoxical effect. Instead of an increase in the firing rate, as expected from the decreased inhibition (disinhibition) in the local network, what was observed was a decrease of firing rate and even complete silencing of the activity in some cases. An example of such a silencing is shown in Fig. 4.18A. This silencing would be trivially explained only if the recorded neurons were PV$^+$ cells, that is, the cells that express eNpHR. I found this phenomenon to be potentially interesting, though, because it was found multiple times in the recordings (see below) and the trivial explanation would be statistically improbable considering that the PV$^+$ cells are only approximately 10% of the cells in neocortical layer V (Markram *et al.* (2004)). So, this raised the question: does the low Ca^{2+}solution in these preparations induce bursts of activity mainly in the PV$^+$ population rather than any other population? In order to address this question, the spike waveforms for these bursts were analysed. Based on the spike width cells were classified as putative PV$^+$ cell or not. As an example, Fig. 4.18B shows a typical spike waveform of the activity shown in Fig. 4.18A with a spike width of 0.6 ms which is much longer than the typical fast-spiking interneuron waveform (shorter than 0.4 ms valley to peak; Barthó *et al.* (2004); Peyrache *et al.* (2012); Mruczek and Sheinberg (2012)).

The same spike waveform analysis was applied on all the recorded bursts of activity that fulfilled the criteria described above. The purpose was to identify putative PV$^+$ cell activity, based on the spike width metric as used in Chapter 4, and exclude it from

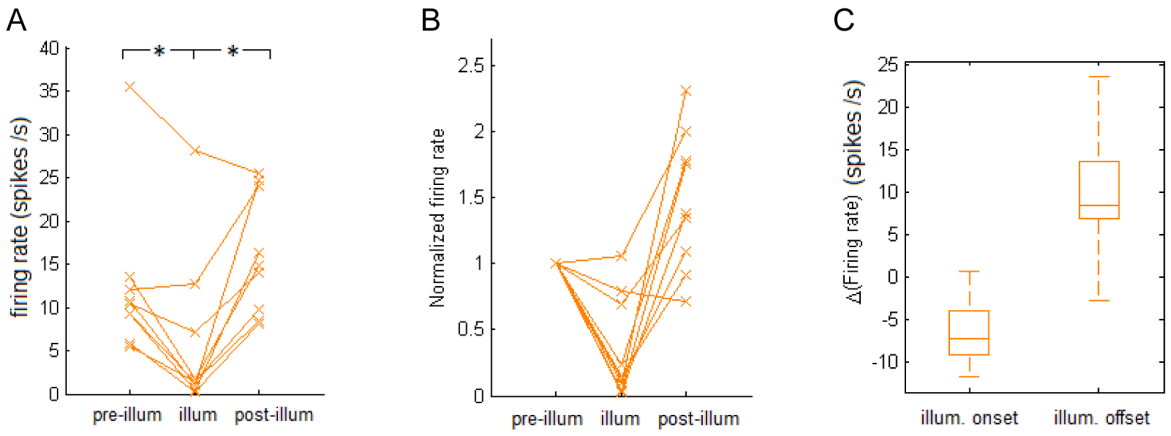

Figure 4.19: The effect of silencing the PV$^+$ interneurons on the activity of putative pyramidal cells (n=9). (A) Firing rate before, during and after the illumination. The paradoxical effect of illumination is evident with a decreased firing rate during the illumination and a subsequent increase after the illumination. These firing rates for each cell are averaged over at least two consecutive illuminations. This effect was found to be significant both at the onset and the offset of illumination with p<0.001 in a paired Wilcoxon signed-rank test (-6.44 ± 1.26 spikes/s, range -11.77 - 0.67 spikes/s; 9.19 ± 2.07, range -2.73 - 23.67 spikes/s, respectively). (B) Firing rates were normalized on the pre-illumination firing rate to show the percentage of change. Note that the firing rate after the illumination is higher than the initial firing rate in most cases. (C) The distribution of the firing rate difference at the onset and offset of illumination shown with box plots.

the statistical analysis. Indeed 2 out of 11 bursts had a particularly short spike waveform (0.2 ms and 0.24 ms) and these cells were removed from the pooled data as putative PV$^+$ cells (Erisir *et al.* (1999); Barthó *et al.* (2004)). The remaining 9 bursts had a spike width of at least 0.4 ms and were considered to be not putative PV$^+$ cells. The firing rate was calculated pre-illumination, during illumination, and post-illumination for the remaining 9 bursts to test whether there was a robust paradoxical effect when silencing the PV$^+$ cells. The results in Fig. 4.19A show that there is a consistent effect of the illumination with a decrease in the activity during the silencing of PV$^+$ interneurons. A paired Wilcoxon signed-rank test was applied between the pre- and the during-illumination firing rates as well as between the during- and post-illumination. In both cases the effect was found to be significant with p ¡ 0.001 (-6.44 ± 1.26 spikes/s, range -11.77 - 0.67 spikes/s; 9.19 ± 2.07, range -2.73 - 23.67 spikes/s, respectively). Notice that one of the cells had a particularly high initial firing rate which is more common to PV$^+$ cells than pyramidal cells. Nevertheless, because only the spike width metric was used to identify and exclude putative PV$^+$ cells, this outlier remained in the analysis. The firing rates were normalized based on the pre-illumination value to reveal the percentage of change in Fig. 4.19B. The box

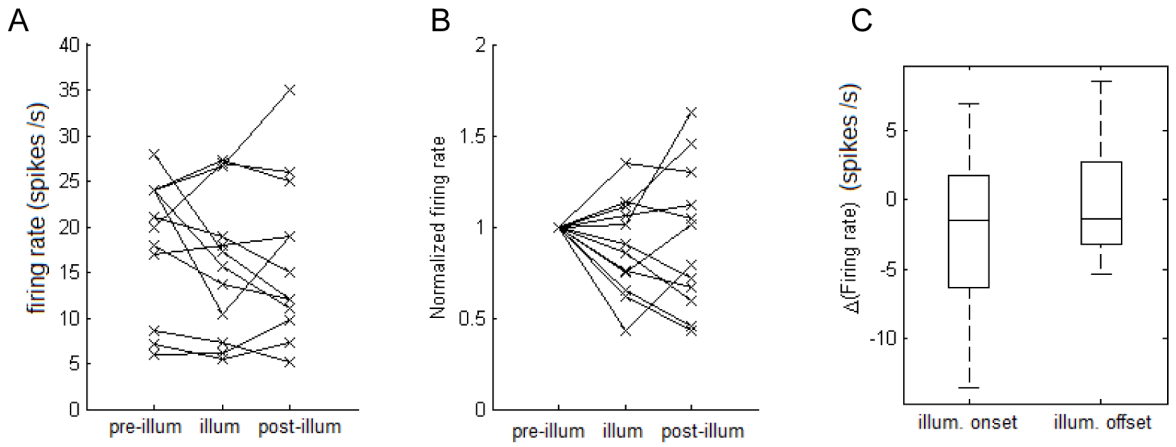

Figure 4.20: Testing whether the photovoltaic effect is involved in the paradoxical effect seen in the eNpHR experiments. (A) Firing rate before, during and after the illumination. The illumination has no impact on the firing rate of the recorded cells indicating that the photovoltaic effect cannot explain the paradoxical effect seen above. A paired Wilcoxon signed-rank test yielded no significant result with p = 0.30 (-2.33 ± 1.74 spikes/s, range -13.66 - 7.01 spikes/s) and p = 0.79 (0.19 ± 1.36 spikes/s, range -5.34 - 8.66 spikes/s) for the illumination onset and offset, respectively. (B) Firing rates were normalized on the pre-illumination firing rate to show the percentage of change. (C) The distribution of the firing rate difference at the onset and offset of illumination shown with box plots. Note that the median value is very close to 0 indicating no significant effect.

plots in Fig. 4.19C show the distribution of change in firing rates on the onset and offset of the illumination. Note that the firing rates tend to increase right after the illumination to values even higher than the initial, pre-illumination values (2.92 ± 1.75 spikes/s, range -9.99 - 14.00 spikes/s). This rebound activity can potentially be due to hyperpolarizing-activated currents (see Discussion).

One possible explanation for this paradoxical effect is the photovoltaic effect (Becquerel effect). We therefore examined whether the results may arise from a non-biological source, by running some control experiments. For these control experiments, the whole procedure was the same but, instead of running it on tissue with the expression of eNpHR in PV^+ cells, it was run on tissue from wild-type animals (n=11 slices) from which only a subset of them exhibited long enough bursting activity to be analysed (n=5). Because of the limited number of slices shorter bursts were also considered. The selected bursts were at least 9 seconds long: 3 seconds before, 3 seconds during and 3 seconds after the illumination. Seeing the same effect would mean that the illumination alone can induce these changes in firing rate through the photovoltaic effect. The same analysis was applied as in Fig. 4.19 but the results of the control experiments yielded

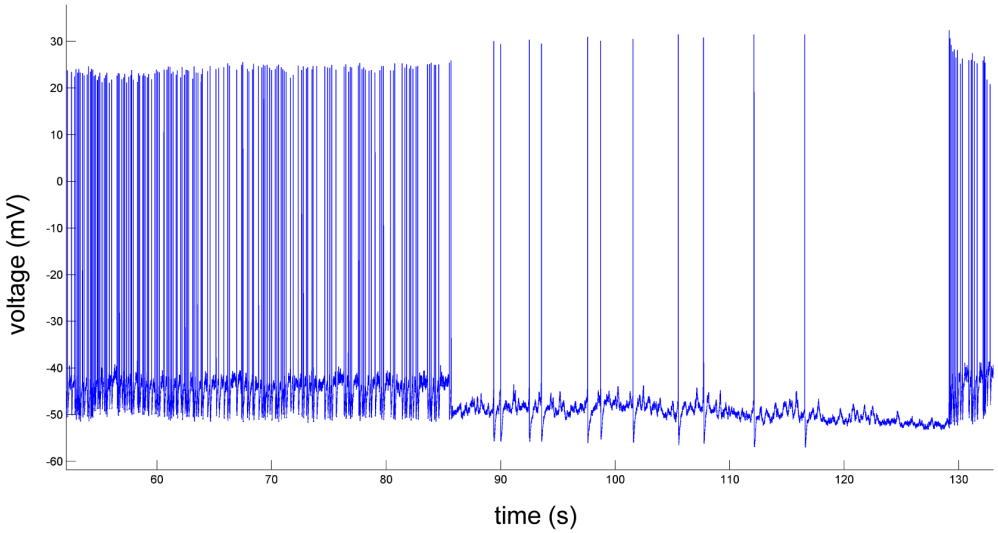

Figure 4.21: Intracellular recording of a putative pyramidal cell undergoing spontaneous transitions between depolarized and hyperpolarized states. Current-clamp recording from a putative pyramidal cell (based on its morphology) bathing in low-Ca^{2+} solution. During the depolarized state it maintains a firing state of approximately 5 spikes/s. It spontaneously transitions to a hyperpolarized state with a step-wise decrease of the membrane potential (approximately 6 mV). The firing rate during the hyperpolarized state is less than 1 spike/s. It spontaneously returns to a depolarized state at the end of this sample.

no significant effect (n=12 bursts). Fig. 4.20 shows the results on which the paired Wilcoxon signed-rank test returned p = 0.30 (-2.33 ± 1.74 spikes/s, range -13.66 - 7.01 spikes/s) and p = 0.79 (0.19 ± 1.36 spikes/s, range -5.34 - 8.66 spikes/s) for the illumination onset and offset, respectively.

The paradoxical phenomenon remained unexplained after the control experiments. Then a new hypothesis was introduced. I hypothesized that the activity recorded was similar to the UP states as described in (Sanchez-Vives and McCormick (2000)) despite the fact that the recorded bursts of activity had different characteristics (see above). If this is the case, it is expected that both pyramidal neurons and interneurons simultaneously transition into an UP state (step-wise depolarization of their membrane potential) resulting into a burst of activity. Then the optogenetic silencing, that is, hyperpolarization of the PV^+ interneurons, induces a DOWN state for the duration of the illumination at least for the PV^+ cells. According to the theory behind the UP states, the depolarization of both cell types is self-maintained by the balance of excitation and inhibition during this activity. Thus, the idea behind the hypothesis is

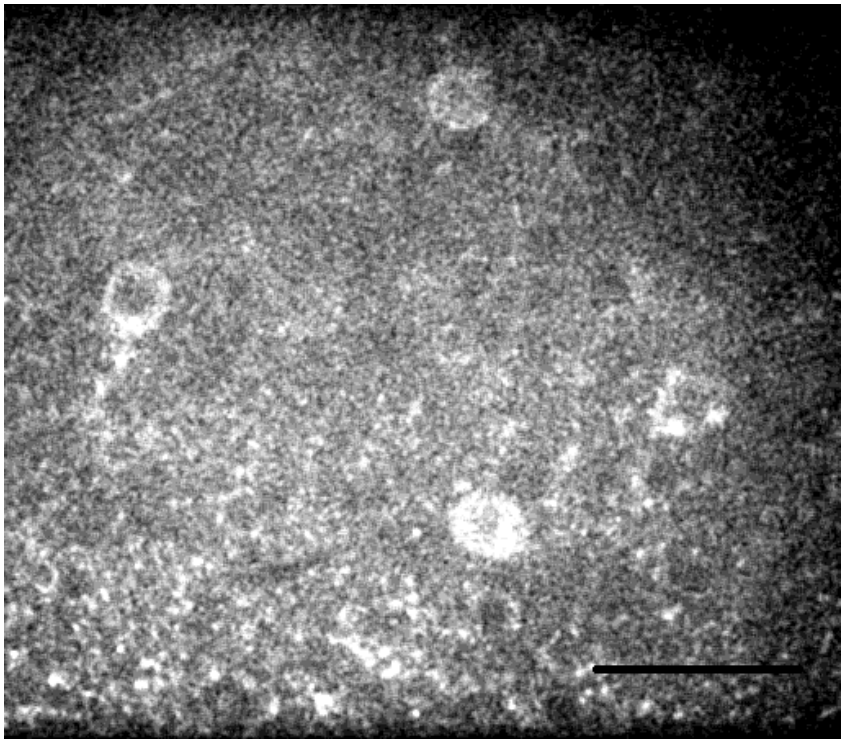

Figure 4.22: Sparse expression of eNpHR tagged with GFP. Example of a slice with a sparse expression of eNpHR and GFP in PV^+ cells (Ai39; B6; 129S-Gt(ROSA)26Sortm39(CAG-HOP/EYFP)Hze/J; Jackson Laboratory, stock number 014539). The imaging was carried out during the intracellular recordings. Scale bar = 50 μm.

that disturbing this balance, even by silencing the interneurons, would silence the activity of the local network that depends on it.

In order to test this hypothesis, though, intracellular recordings were needed to monitor the membrane potential of the cells and identify any depolarized states in low-Ca^{2+} conditions. Preliminary recordings were carried out in slices expressing no opsin for this purpose. Indeed depolarized states were detected in 2 cells, one of which is shown in Fig. 4.21. The transitions between the depolarised and hyperpolarized states were spontaneous with a step wise increase or decrease of the membrane potential. In this example, the change in membrane potential was approximately 6 mV. Note the relatively stable firing rate (approximately 5 spikes/s) during the depolarized state.

The preliminary results described above were followed by experiments targeting pyramidal cells in slices where eNpHR is expressed only in PV^+ cells. An example of this sparse expression can be found in Fig. 4.22 where the expression of eNpHR is labelled with green fluorescent protein (GFP). The patching was always targeted to cells that would have the typical pyramidal shape but in order to make sure that the

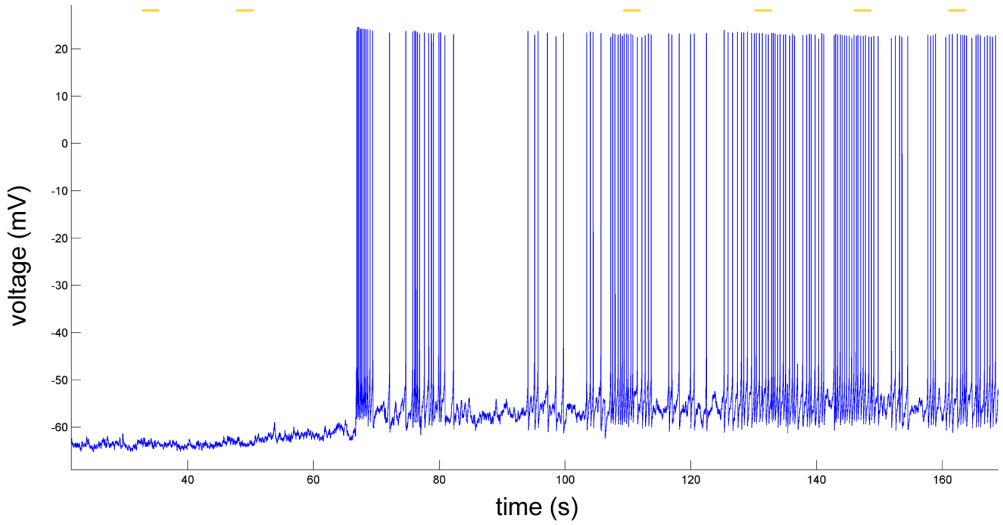

Figure 4.23: Activating eNpHR-currents by illumination had no effect on the membrane potential of a putative pyramidal cell. This current-clamp recording was taken from a putative pyramidal cell in layer V. The whole neighbourhood of the patched cell was illuminated with 561 nm light (yellow bars) in order to silence the PV^+ cells in its local network. The fact that the illumination had no effect on the membrane potential of the cell during the hyperpolarized state (before 65 s) indicates that this cell is indeed not a PV^+ interneuron. The illumination had no effect on its membrane potential during the depolarized state (after 65 s) either. Assuming that during its depolarized state this cell was taking part to a collective UP state across the local network, there is no indication that silencing the neighbouring PV^+ cells can also silence the collective activity of the network.

cell was not expressing any eNpHR, I would illuminate with yellow light during a hyperpolarized state to check whether it hyperpolarizes even more. If there was no such response, then I waited for the putative pyramidal cell to spontaneously transition into a depolarized state with persistent activity and used the illumination again to check whether it induces a hyperpolarized state and silences the activity. Fig. 4.23 shows an example of such a recording in the current-clamp mode. Neither the activity nor the membrane potential was influenced by the illumination of light. The same qualitative results were collected from 4 cells (2 whole-cell and 2 cell-attach recordings) providing no support for the hypothesis that silencing the PV^+ interneurons can also silence the pyramidal cells during a depolarised state.

4.5 Discussion

The study with the eNpHR experiments was terminated without a solid finding or a clear conclusion. The main reason is that the experimental setup used was not the appropriate setup to explore the effect of silencing the PV^+ cells during an active state of a local network. The experiments were designed to produce recurrent local network activity in the neocortex using the same solution (yet not the same cortical area) as described in Sanchez-Vives and McCormick (2000). However, the bursting activity recorded did not resemble the recurrent, slow oscillating activity that was expected (Sanchez-Vives and McCormick (2000); Shu *et al.* (2003)). Thus, the assumption that the recorded activity was a manifestation of a balanced interaction between excitation and inhibition, was not grounded. An alternative experimental setup with *in vivo* electrophysiology and optogenetics would be more appropriate to explore the question. Such recurrent activity is reliably produced during sleep (Steriade *et al.* (1993)).

The ChR2 experiments yielded some interesting results regarding the propagation of activity when electrically coupled PV^+ cells are photostimulated. First, I found that there is a threshold of extracellular K^+ concentration above which the activity does propagate in the slice preparations. This threshold is at approximately 8.5 mM. Second, pharmacological manipulations showed that these propagations involved gap junctions and persisted even after blocking glutamatergic currents (see schematic in Fig. 4.24). This suggests that the activity propagates through the PV-syncytium and does not rely on chemical synaptic transmission. Spike waveform analysis of the propagated activity was found to be indicative of the characteristic action potentials of fast-spiking interneurons.

The speed measured during the experiments might be overestimated. The propagation speed was measured with the assumption that the activity recorded at the distant electrode is a propagation of the activity recorded at the electrode close to the borders of the illumination area. But as shown in Fig. 4.2D, the illumination area can extend around 0.05 mm away from that electrode and the propagated activity might originate from the border of the illumination area instead. Having this in mind, the propagations recorded might actually represent shorter propagations, shorter by approximately

0.05mm, thus the mean speed measured drops from 58.9 mm/s to 51.6 mm/s considering the median distance 0.4 mm (see Fig. 4.11).

Simulating the experiment in NEURON provided primarily a qualitative description of the behaviour seen in the brain slices. The quantitative results of the simulation might not be accurate enough considering all the different factors that influence the phenomenon. The speed of propagation, as measured from the simulation, is comparable to the one measured from the experiments. However, the specific values for parameters like, the membrane resistance, gap junction conductance or the dendritic morphology were shown to influence greatly the dynamics of spike propagation in the simple chain network (see Figs. 4.14 and 4.15). Simulation of a larger network with biologically realistic connectivity can potentially reproduce better the phenomenon: the network parameters are possibly more important in the phenomenon rather than the cellular parameters.

Another phenomenon that raises questions is the evidence of the propagated activity in different electrodes at different times. This was actually observed only once and it is the example shown in Figs. 4.5 4.7. In this example, the propagated activity is recorded in multiple electrodes located 0.2 to 0.4 mm away. The propagation to the electrodes closer to the illumination area was observed during the early stages of the experiment. The propagation to the most distant electrode was observed in later stages instead. The propagation travels further in the later stages but when it does reach the most distant electrode, it seems to skip the intermediate electrodes that were active before. How can the activity propagate to a more distant electrode while skipping previously active electrodes? If there was no activity in the intermediate electrodes from the beginning, the explanation would be that there was no interneuron actively involved in the propagation near those electrodes. The propagation can potentially use a route other than the shortest which passes through every intermediate electrode. But in this case there is evidence that propagated activity can reach the intermediate electrodes as well. Is it possible for the propagated activity to skip some intermediate nodes? I hypothesize that the activity propagates through all cells but regenerates only in the last cell of the chain under the conditions of depolarization block in the intermediate nodes. Under these conditions the activity might propagate passively

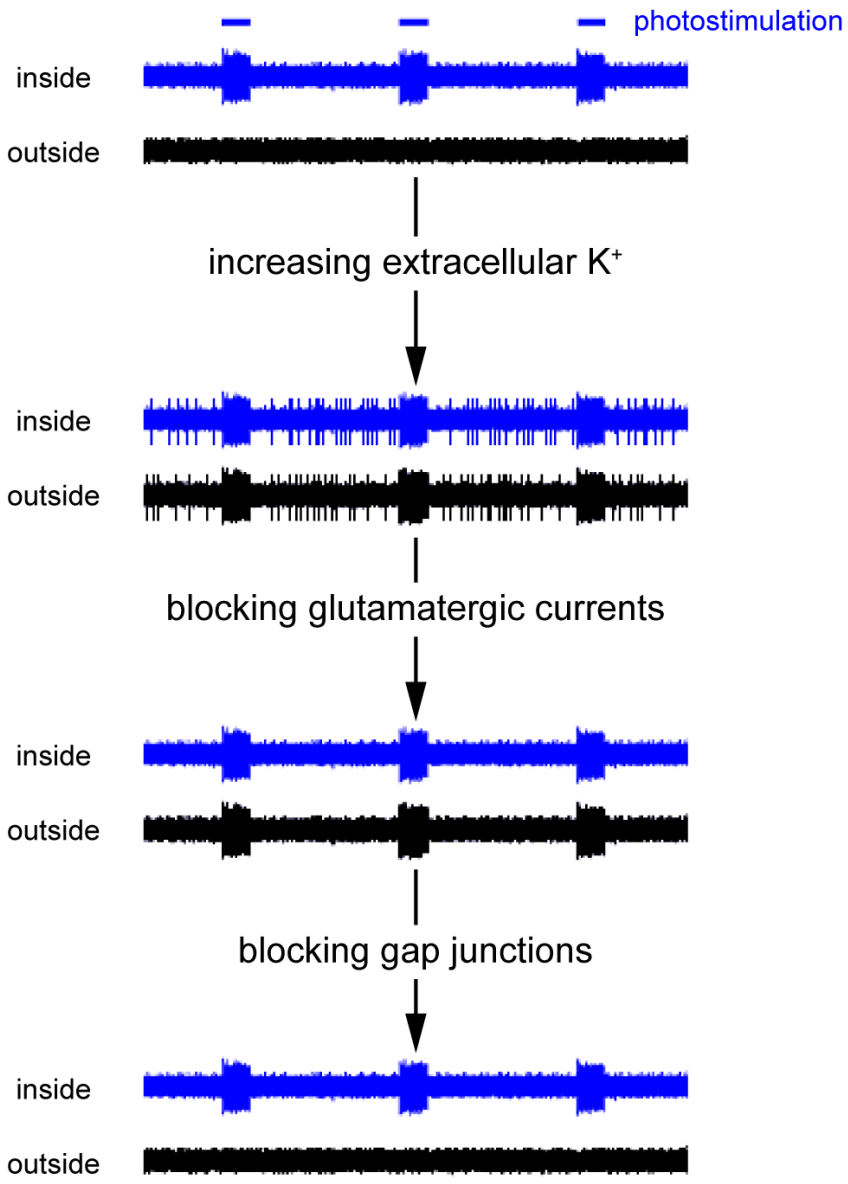

Figure 4.24: **Schematic summarizing the experimental procedure used to demonstrate the propagation of activity through the PV-syncytium under the condition of increased extracellular K^+.** PV^+ cells expressing ChR2 were photostimulated inside the illumination area (blue trace). Induced, time-locked activity was recorded outside the illumination area (black trace) after raising the concentration of extracellular K^+, indicating propagation. Blocking the glutamatergic currents did not influence the induced activity; it suppressed only the spontaneous activity. The propagated activity was blocked only after applying gap-junction blockers.

through the intermediate interneurons without regeneration and finally regenerate the spike at the end of the chain.

As mentioned in Introduction, experiments using gap junction blockers can be difficult to interpret, because of their multiple other side effects (Connors (2012); Behrens *et al.* (2011); Cruikshank *et al.* (2004); Yatani *et al.* (1993); Snyders *et al.* (1992)). In order to overcome this problem, the strategy usually followed is to apply different gap junction blockers during the replication of the experiment (Middleton *et al.* (2008); Uusisaari *et al.* (2002); Gigout *et al.* (2006)). Following this strategy, the involvement of the gap junctions is verified through the convergence of the different blockers effect (Middleton *et al.* (2008)). Similarly in this study, three blockers were used. The same qualitative effect was seen with the broad-spectrum blocker carbenoxolone, which targets neuronal and glial connexins at the same time (Rozental *et al.* (2001)), and the more specific Cx36 blockers quinine and mefloquine (Srinivas *et al.* (2001); Cruikshank *et al.* (2004)). All of them have side effects but none of the known side effects is common to all three of them (see Introduction). The fact that there was successful blockade of the propagation with all different blockers strengthens the evidence that the propagating activity depends on the gap junctions.

In this study, the gap junctions were considered to be nonplastic and nonrectifying. This assumption was applied also in the simulations of the network model. However, there is experimental evidence, from vertebrates and invertebrates, that gap junctions can also be rectifying (Furshpan and Potter (1959); Auerbach and Bennett (1969)); that is, the coupling coefficient between two electrically coupled cells is different depending on the direction of measurement. This is believed to be due to structural asymmetries of the junction (Verselis *et al.* (1994)). The conductance of a gap junction can also be regulated either indirectly by non-junctional factors (membrane properties, other chemical synapses) or directly by the modification of the channel itself (Pereda *et al.* (2013)). Such channel modifications were firstly observed in horizontal cells in the retina (Piccolino *et al.* (1984)), but more recently synaptic depression and potentiation was reported in electrical couplings of the Mauthner cell (Pereda and Faber (1996); Smith and Pereda (2003)). The functional implications of the gap-junctional plasticity is still poorly understood (Pereda (2014)).

Regarding the connectivity between fast-spiking interneurons, there is a coexistence of chemical and electrical synapses (Galarreta and Hestrin (1999); Gibson *et al.* (1999); Pfeffer *et al.* (2013)) (see also Introduction). The electrical coupling delivers an excitatory signal whereas the chemical delivers an inhibitory signal. When a presynaptic PV^+ interneuron fires, the electrically and chemically postsynaptic cell receives a complex postsynaptic potential consisting of a sharp spikelet followed by a long hyperpolarization (Gibson *et al.* (1999)). Computational studies explored the functional role of each type of synapse but also the potential of their combination in terms of synchronization and dynamics (Lewis and Rinzel (2003); Nomura *et al.* (2003); Kopell and Ermentrout (2004); Pfeuty *et al.* (2007)). Lewis and Rinzel used electrically and chemically connected pairs of leaky integrate-and-fire neurons to explore their synchronization and the results suggest that the combination of both types of coupling actually undermines their synchronous firing (Lewis and Rinzel (2003)). Simulations of paired interneurons and extended interneuronal networks featuring both electrical and bidirectional chemical synapses suggest that a bistability between synchronous and asynchronous firing is possible (Nomura *et al.* (2003)). Kopell and Ermentrout concluded that they have complementary roles: while the inhibitory couplings are important to make the network dynamics more stable by reducing sensitivity to initial conditions, the electrical couplings can synchronize much more efficiently the network when there is heterogeneity of currents (Kopell and Ermentrout (2004)). In another study, the two types of coupling were found to cooperate and increase the synchronous firing of the network only under the conditions of strong inhibitory synapses (Pfeuty *et al.* (2007)). In particular, the finding of this study was that the synchronization capabilities of the electrical synapses are modulated by the strength of the chemical synapses (Pfeuty *et al.* (2007)). As yet, the role of this combination of coupling and the complex postsynaptic potential is still unclear and limited to the phenomena of synchronization and oscillatory dynamics. Investigations in other phenomena, such as synaptic plasticity or sensory information processing, can potentially reveal additional functionalities of the coupling between PV^+ cells.

The functional role of gap junctions in excitable tissue like in musculature and myocardium was reviewed briefly in Introduction. In addition, their important role in development was also mentioned. In those cases, the action potentials that traverse the syncytium through the gap junctions seem to be appropriately broad for the

functionality of contraction or the regulation of cell growth and migration. Note that these broad action potentials resemble the low frequency component of the 4AP-models burst in the PV-syncytium (Gigout *et al.* (2006); Louvel *et al.* (2001)). This type of coarse activity though seems to contradict the signalling norms of neural systems. Except for the metabolic support of the astroglial syncytium, the signalling is characterized by high information content and temporal precision. Despite the fact that these bursts of activity are not part of the physiological repertoire of the system, the gap junctions between fast-spiking interneurons enable such pathological activity undermining the normal function of the network.

4.5.1 Extracellular K^+ concentration and seizures

The relation between the concentration of extracellular ions and seizures is still unclear (Devinsky *et al.* (2013); Somjen (2004)). Seizure dynamics and fluctuations of extracellular K^+ are correlated but there is still a debate whether these fluctuations can cause a seizure or merely contribute to its evolution (Somjen (2004)). Artificial increases of extracellular K^+ were shown to induce seizures or promote paroxysmal activity (Zuckermann and Glaser (1968); Somjen and Giacchino (1985); Jensen and Yaari (1997); Korn *et al.* (1987)). Concentrations of 7-8 mM were enough to observe these results but all of these studies involved epileptiform activity in hippocampus where the interstitial space is smaller compared to neocortex (McBain *et al.* (1990)). The elevated concentration of extracellular K^+ depolarizes the cells rendering them more excitable (Somjen (2004)). It is expected to have a major impact especially on the dendrites of PV^+ interneurons because of their high dendritic expression of K channels (Hu *et al.* (2010)). It also causes the increase of intracellular Cl^- which results in less effective synaptic inhibition thus promoting paroxysmal activity (Korn *et al.* (1987); Alfonsa *et al.* (2015); Somjen (2004)).

The accumulation of extracellular K^+ under physiological conditions was hypothesised to generate seizures (Green (1964); Fertziger and Ranck (1970)). It was described as a positive feedback loop where the release of excess K^+ from overexcited neurons reinforced paroxysmal activity making the seizure self-sustaining (Fertziger and Ranck (1970)). Indeed, the use of potassium-selective microelectrodes enabled researchers to

record the significant elevation of extracellular K^+ concentration during seizures induced by electrical stimulation or drugs (Heinemann and Dieter Lux (1977); Moody *et al.* (1974); Amzica *et al.* (2002); Gnatkovsky *et al.* (2008)). The concentration was shown to reach 8-12 mM, which is high enough to trigger seizures by itself (Jensen and Yaari (1997); Korn *et al.* (1987)), thus supporting the potassium hypothesis of seizure generation. However, there are some observations, such as the concentration increase lagging behind the electrographic seizures, which do not support the hypothesis (Somjen (2004)).

Whether or not the elevated extracellular K^+ concentration can initiate a seizure, it is evidenced that it contributes to its course because of the effect on the neurons and synapses (Hablitz and Heinemann (1987, 1989); Heinemann *et al.* (1990)). The results in this chapter suggest a special functionality of the PV-syncytium at the core of a seizure where the extracellular K^+ concentration can rise above 8 mM. Recruited PV^+ interneurons in the ictal core can potentially signal, through the fast medium of gap junctions, members of the syncytium in the surrounding area around the core, that is, the penumbra. Such mechanism might enhance the surround inhibition and contribute to the activity in the penumbral territories which restricts the propagation of a seizure (Trevelyan *et al.* (2006); Schevon *et al.* (2012); Trevelyan (2016)).

Chapter 5

Interaction between two oscillations

5.1 Introduction

Oscillating activity in neural networks is a pivotal phenomenon of neural dynamics (Buzsáki (2006)). Electrophysiological and imaging techniques revealed oscillating behaviour of neural networks ranging from very low frequencies, below 1 Hz (Steriade (1999)), to very high, exceeding 100 Hz (Grenier *et al.* (2003); Ylinen *et al.* (1995)). Neural oscillations are organized in discrete frequency bands and each band is associated with psychophysical processes or states (Roopun *et al.* (2008b)). This rhythmic behaviour enables the synchronization of neuronal activity that mediates information processing, synaptic plasticity, and cognitive functions (for reviews, see Buzsáki and Draguhn (2004); Klimesch (1999)).

Experimental evidence shows that oscillations of different frequency bands can occur simultaneously and interact in hippocampal and neocortical networks (Penttonen and Buzsáki (2003); Roopun *et al.* (2008b); Canolty *et al.* (2006); Cunningham *et al.* (2003); Bragin *et al.* (1995); Colgin *et al.* (2009); Belluscio *et al.* (2012); Akam *et al.* (2012)). This co-occurrence was usually observed between the bands delta, theta, and gamma (Penttonen and Buzsáki (2003); Roopun *et al.* (2008b)). Canolty and colleagues reported an interaction between theta (4-8 Hz) and high gamma frequencies (80-150 Hz) in neocortex (Canolty *et al.* (2006)). The power of the fast oscillation was modulated by the slower oscillation and the spatial profile of the interaction was found

to be task-dependent (Canolty *et al.* (2006)). This cross-frequency coupling phenomenon was also reported in entorhinal cortex (Cunningham *et al.* (2003)) and in hippocampus where theta oscillations were found to interact with slow gamma (30-80 Hz) as well (Bragin *et al.* (1995); Colgin *et al.* (2009); Belluscio *et al.* (2012)). This type of interaction is common between frequencies that differ by a factor of 2 or more and the fast oscillation is usually nested in the slow oscillation (Roopun *et al.* (2008a)). Another phenomenon was observed in cortical slices where two different oscillations, a gamma (40 Hz) and a high beta (25 Hz), interacted and produced a slower oscillation (Roopun *et al.* (2008a)). The periods of the two fast oscillations, one expressed in infragranular layers and the other in supragranular layers, were concatenated and produced a slower oscillation with a period equal to their sum (Roopun *et al.* (2008a)). This transition was triggered with a decrease in excitatory drive after the application of an AMPA-receptor blocker (Roopun *et al.* (2008a)). Note that, in this case, the ratio between the frequencies is non-integer and lower than 2 (Roopun *et al.* (2008a,b)).

The functional role of such interactions is still unclear but there are indications that they are implicated in neural communication and computation (Canolty and Knight (2010)). For instance, cross-frequency coupling between theta and gamma was shown to be correlated with the performance in a learning task (Tort *et al.* (2009)). It was also shown to change according to behavioural events (Tort *et al.* (2008)). Considering that high-frequency oscillations reflect information processing at a local level (von Stein *et al.* (2000)) whereas slow oscillations can synchronize distributed areas for multi-sensory processing (von Stein *et al.* (2000); Lakatos *et al.* (2008)), cross-frequency coupling was suggested as a mechanism for information transfer between global and local functional networks (Canolty and Knight (2010)). Similar explanation was suggested for the period concatenation phenomenon (Roopun *et al.* (2008a,b)). Period concatenation can provide a mechanism for hierarchical organization and transformation of the different frequencies and enable parallel information processing across multiple temporal and spatial scales (Roopun *et al.* (2008b); see also, spectrally distributed processing in Palva *et al.* (2005)).

The experiments described in this chapter were designed to investigate the interaction of two slow oscillations in a cortical slice preparation. The oscillations, featuring different frequencies (3 and 4 Hz), were generated by optogenetic stimulation of the

pyramidal cells in supragranular layers. Note that, the two frequencies have a non-integer ratio lower than 2 which suggests the possibility of period concatenation during the interaction (Roopun *et al.* (2008a,b)). The purpose of this study was also to explore any implications of the interneurons in the interaction by applying pharmacological manipulations.

5.2 Methods

5.2.1 Cortical expression of optogenetic proteins

All animal handling and experimentation were done according to UK Home Office guidelines. Cortical channelrhodopsin-2 (ChR2) expression was achieved by using genetically engineered transgenic mice. Brain slices were prepared from first generation cross-breeding of homozygous floxed-channelrhodopsin mice (B6; 129S-Gt(ROSA)26Sor$^{\mathrm{tm32(CAG\text{-}COP4*H134R/EYFP)Hze}}$/J; Jackson Laboratory, stock number 012569) with homozygous Emx1-cre mice (B6; 129S2-Emx1$^{\mathrm{tm1(cre)Krj}}$/J; Jackson Laboratory, stock number 005628). Wild-type mice (C57BL/6J) not expressing any optogenetic protein were also used.

5.2.2 Preparation of brain slices

Young to mature mice (2-8 months) were sacrificed by cervical dislocation, and coronal brain slices were prepared for extracellular recordings in the same way as described in the previous chapter. Normal ACSF was used during these experiments.

5.2.3 Extracellular recordings

Multichannel extracellular recordings were collected at 25 kHz, using a linear 16-channel-probe configuration as described in the previous chapter. It was placed along layer V as in the previous chapter.

5.2.4 Optogenetic illumination

Channelrhodopsin was activated by a 470nm LED delivering light through the objective using the patterned illuminator Polygon400 (Mightex Systems, Pleasanton, CA, USA). The system was controlled and the patterns were designed through the PolyScan 2 software from the same company. The light intensity used was approximately 1 - 1.5 mW/mm^2 *(courtesy of Mr. Eike Joest).*

In order to produce two different frequencies of illumination with the same illuminator (i.e. single blue light source), a protocol of illumination had to be designed. The goal was to deliver simultaneously a 3 Hz and a 4 Hz illumination in two separate areas: let us call them the red and the yellow areas. The protocol of illumination used is shown in Fig. 5.1A. Each second is composed by 24 frames, that is, the Nyquist frequency of the least common multiple between the desired frequencies. Each column in Fig. 5.1A can be considered covering a time bin of a 24$^{\text{th}}$ of a second, that is, approximately 42 ms. During each time bin, a frame is projected and it is either projecting to both areas or to the yellow area alone or the red area alone or to none. Fig. 5.1A shows how a 3 Hz illumination is composed in the yellow area and the 4 Hz illumination is composed in the red area. The same figure also shows with orange colour when the two illuminations coincide.

5.2.5 Pharmacology

Pharmacological manipulations were carried out using the following substances: D-APV (50 μM), ZD7288 (50 μM), scopolamine (30 μM), baclofen (5 μM), NBQX (20 μM), TTX (1 μM).

5.3 Results

During the experiments, the protocol of illumination described above was projected onto a cortical slice in which ChR2 is expressed under the Emx1 promoter (pyramidal cells and glia) (see Methods). A medial area in the supragranular layers was considered

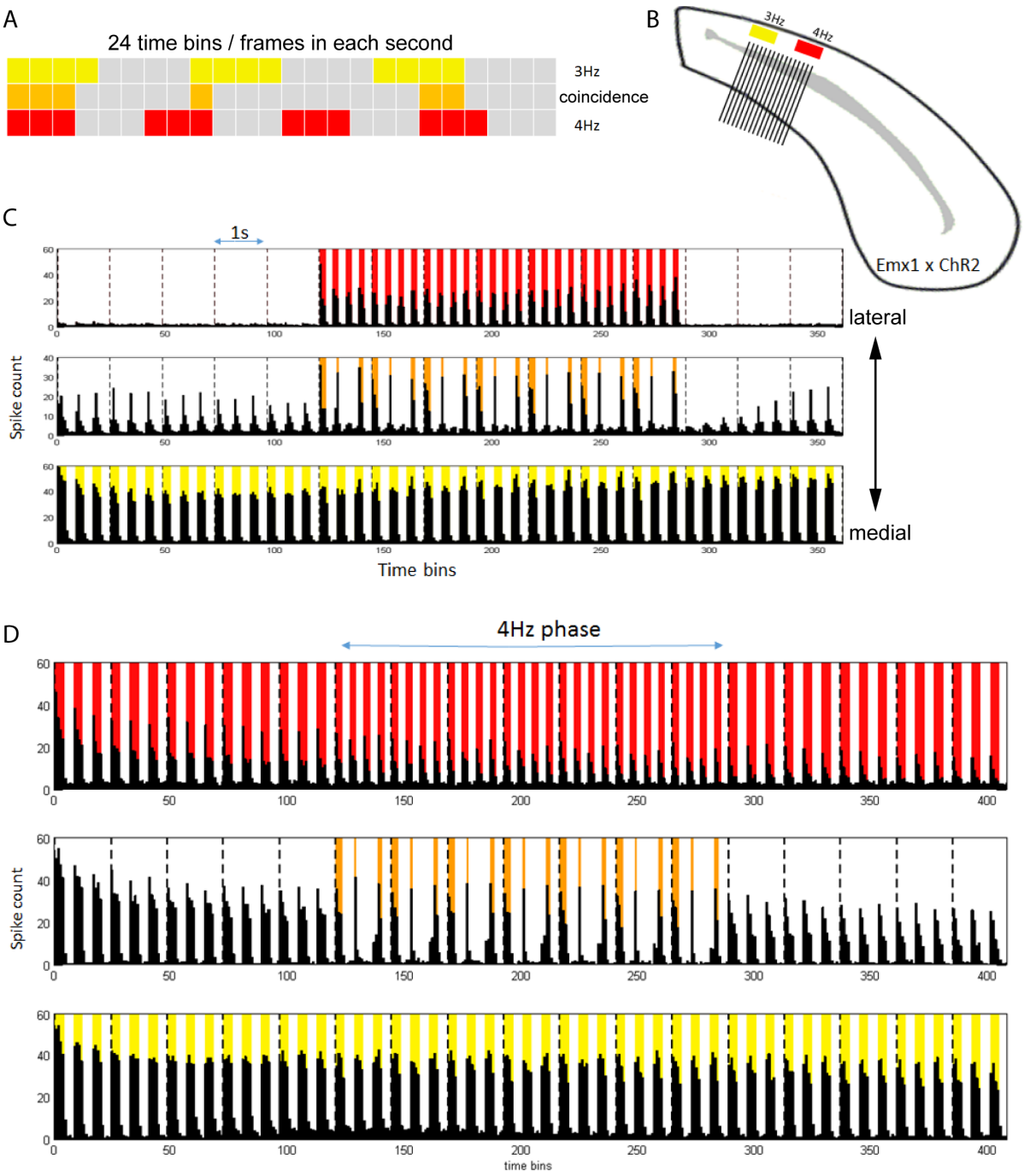

Figure 5.1: Illumination protocol producing two oscillations and the coincidence detection effect during their interference.(A) The design of the illumination protocol producing simultaneously a 3 Hz and a 4Hz illumination. The two illuminations are assigned to different areas: the yellow (1st row) and the red (3rd row). Each second is split into 24 time bins (columns). A frame is projected during each time bin dictating which areas are illuminated. The middle row indicates when the two illuminations coincide. (B) Schematic of the experimental setup. The linear MEA is placed along layer V in a cortical slice with the expression of ChR2 in pyramidal cells and glia. (C) Recordings taken from three electrodes: one on the medial side, one on the lateral side and one in between. The activity in the middle follows initially the baseline activity on the medial side. Then, the two different oscillations interfere, giving rise to a coincidence detection pattern in the middle. After the interference, the activity returns to the baseline with some delay. (D) The baseline activity (3Hz) is now induced in both red and yellow areas. The red area is oscillating with 4 Hz only during the interference period. The same effect is found in the middle but the recovery now is instantaneous due to the stable overall stimulation used. All spike counts are averaged over 15 repetitions of the illumination protocol.

to be the yellow area and a lateral area was considered to be the red area receiving a 3 Hz and a 4 Hz illumination, respectively. The recordings were made using a linear MEA placed along layer V. As Fig. 5.1B shows, the illumination was covering approximately 5-6 electrodes wide areas on either side, leaving a 4-6 electrodes wide area in the middle without any illumination.

As expected, a 3 Hz oscillation was recorded at the medial side of the array and a 4 Hz oscillation was recorded at the lateral side of the array but the activity recoded in the middle had a more complex pattern with frequency 1 Hz. The majority of spikes recorded in the middle area were limited to the time bins when there was coincidence between the two illuminations. An example of this effect can be found in Fig. 5.1C, which shows the spikes recorded at three different electrodes in the array which was placed in layer V: one electrode immediately deep to the red area (lateral), another immediately deep to the yellow area (medial), and another from the deep middle area. Note that, in this example, the 3 Hz illumination was used as a baseline activity, that is, the medial area was receiving the illumination before the interference period and continued to receive the same illumination after the interference period. As Fig. 5.1C shows, the activity in the middle responds to the baseline activity initially and the same baseline activity recovers slowly after the interference period. Note that the coincidence detection pattern of activity in the middle is characterized by higher spike count (during the active time bins) compared to the baseline activity. Note also that the protocol was always repeated 15 times and the spike count reported is the average between the repetitions.

I hypothesised that the increased spike count during the interference, and the slow recovery after that, can be explained by the increased overall photostimulation that the slice receives: during the interference of the two oscillatory illuminations, the area in the middle receives twice the input per second on average. In order to test this hypothesis, the photostimulation protocol was changed to feature the baseline activity in both areas before and after the interference phase. This makes the overall illumination being constant from phase to phase. An example of this experiment is shown in Fig. 5.1D in which both illuminated areas receive a 3 Hz baseline photostimulation initially, then the red area switches to a 4Hz illumination, and finally the illumination returns to the baseline in both areas. The recovery after the

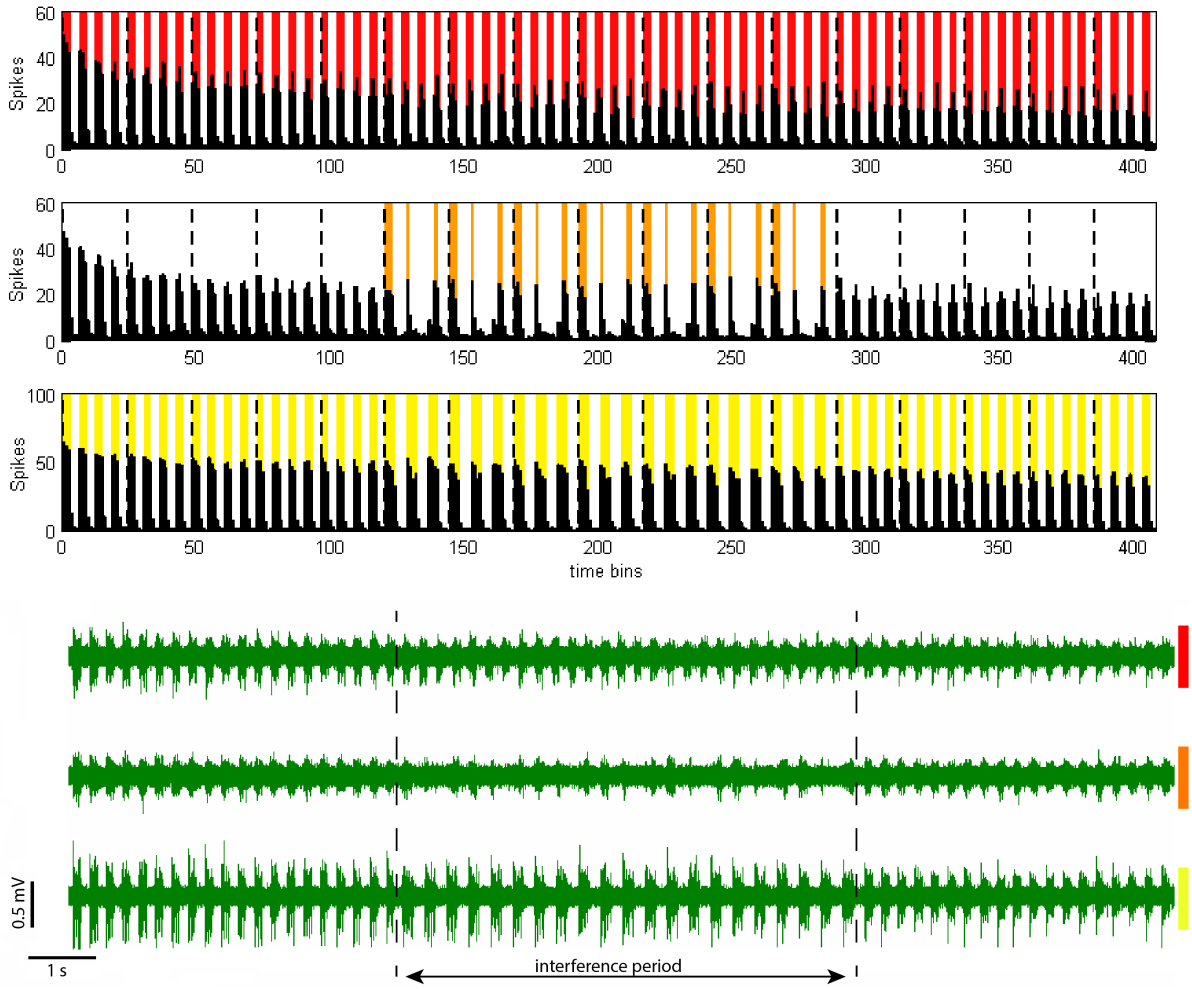

Figure 5.2: Variation of the illumination protocol yielding the same qualitative result. This variation is labelled as *4Hz lateral*, that is, the baseline activity is 4Hz on the lateral side (red). Notice that the medial side (yellow) changes from 4Hz to 3Hz and back to 4Hz. The same coincidence detection pattern arises in the middle during the interference of the two different frequencies. The phenomenon is also evident in the raw traces in green.

interference is now instantaneous and the spike count per time bin during the interference is not significantly higher compared to the baseline activity, as expected. However, the coincidence detection pattern that arises during the interference is still unexplained. Why would the activity be limited to the time bins when both illuminations are ON simultaneously, and not extending into the periods when only one area is illuminated?

This effect proved to be very robust. The coincidence detection pattern was reproduced in 8 slices with different variations of the illumination protocol. The same pattern of activity was recorded when the baseline activity was 4 Hz rather than 3 Hz or when the 3 Hz illumination was assigned to the lateral side rather than the medial. These

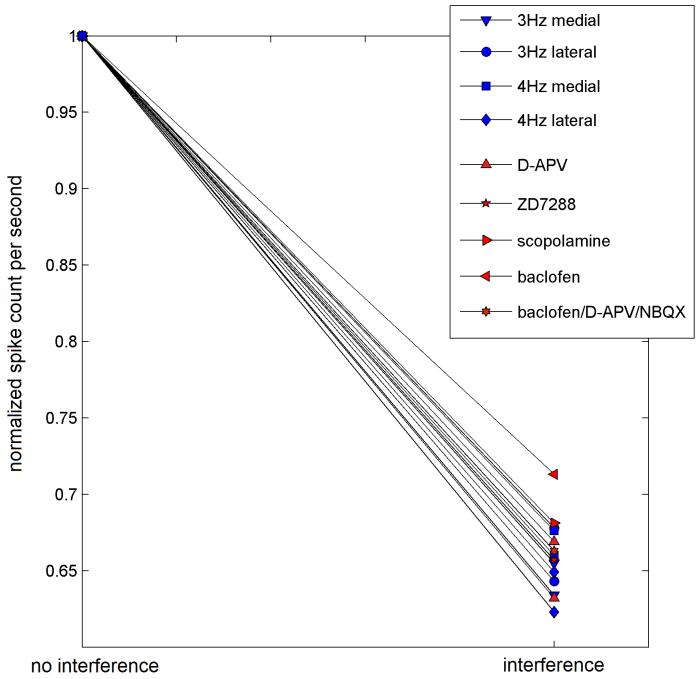

Figure 5.3: The average activity in each second is reduced when there is interference between the two different frequencies. The normalized spike count per second is reduced to approximately 66% of the baseline activity during the interference. The same result stands for all the different experiments including the variations of the protocol (blue) and the pharmacological manipulations (red).

four variations are labelled based on the frequency (3Hz or 4Hz) and the side (medial or lateral) of the baseline activity. The examples in Fig. 5.1 are labelled as *3Hz medial* whereas the variation in Fig. 5.2 is labelled as *4Hz lateral*.

Pharmacological manipulations were then used to investigate the role of specific ion channels and receptors in the phenomenon. First, the NMDA receptors were investigated by applying D-APV (n=2 slices). Blocking the NMDA receptors had no qualitative effect on the pattern: the coincidence detection pattern was still recorded in the middle area. Subsequently, I blocked the HCN channels which mediate the hyperpolarization-activated (I_h) currents by applying ZD7288 (n=1 slice). Blocking these currents had no qualitative effect on the pattern. In addition, scopolamine was used to block the muscarinic acetylcholine receptors (mAChRs) (n=1 slice). The effect persisted in the middle area. The $GABA_B$ agonist baclofen was also used without any qualitative effect (n=1 slice). A combination of baclofen, D-APV and NBQX was used blocking both NMDA and AMPA receptors while simulating the release of $GABA_B$ (n=1 slice). The pattern was still recorded in the middle area. Only the application of

TTX managed to block the coincidence detection pattern along with all other activity in the slice (n=1 slice).

Neither the different variations of the illumination protocol nor the pharmacological manipulations described above had any impact on the pattern of coincidence detection. The qualitative effect during the interference is also characterized by a quantitative change: the spike count per second is reduced during the interference phase. In the example seen in Fig. 5.1D, the activity during the baseline phase is 367.1 spikes/s and it drops to 240.4 spikes/s during the interference. The interference pattern has only 65.5% of the baseline spike count in the specific example. Approximately the same reduction was found in all the experiments described above. The normalized spike count per second before and during the interference is plotted in Fig. 5.3 for all the different experiments. The experiment with TTX was not included in this figure due to the complete absence of activity.

This persistence of the phenomenon even after pharmacologically blocking major synaptic mechanisms suggested that it might be manifested through other means, like the emergence of electric fields (Froehlich and McCormick (2010); Qiu *et al.* (2015)). Such electric fields can arise in the two illumination areas and interact in the middle area bypassing all synaptic mechanisms. Electric fields (ephaptic effects) generated from population activity were shown to propagate through slice preparations of hippocampus without the need of synaptic connections (Zhang *et al.* (2014); Qiu *et al.* (2015)). However, this hypothesis of ephaptic transmission was controversial knowing the limited strength of these fields, even in the densely packed hippocampus, much less in neocortex (Zhang *et al.* (2014); Qiu *et al.* (2015)). Nevertheless, in order to test it, I used a double slice experimental setup where one slice had the expression of ChR2 as before and the other had no opsin expressed (wild-type). The electrodes were placed in the supragranular layers of the wild-type tissue and the illumination was delivered to the genetically enhanced slice that was laying next to it. The arrangement can be seen in Fig. 5.4. The hypothesized electric fields were expected to emerge from the ChR2 slice on the left and excite the cells in the wild-type slice with some recorded activity as evidence. No such activity was recorded indicating that the interfering electric fields are not a viable explanation for the phenomenon.

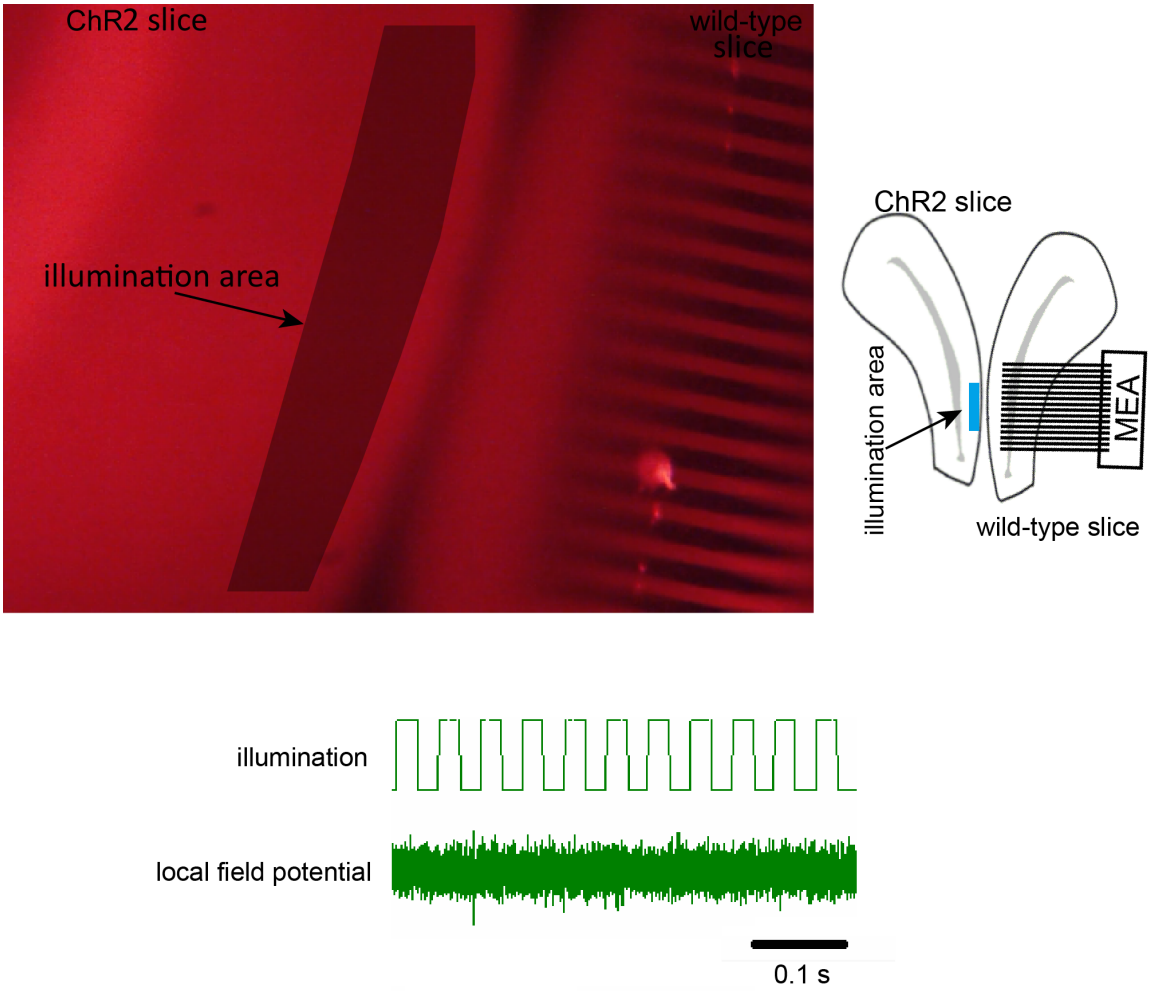

Figure 5.4: Testing whether electric fields are involved in the phenomenon using a double slice setup. A ChR2 (left) and a wild-type (right) cortical slice are placed against each other with their layer I areas almost touching each other (see also schematic on the right). The electrodes are placed in the wild-type slice and the illumination is targeted on the supragranular layers of the ChR2 slice (shaded area). There was no activity recorded in the wild-type slice (see local field potential) indicating that the electric fields emerging in the ChR2 slice are not strong enough to induce activity in cells approximately 400 μm away.

The next hypothesis was that the phenomenon could be explained by an imprecise delivery of light. This was supported by two subsequent experiments where the slices were cut in a way that the three areas (lateral, medial and the middle) were physically separated. The slices were cut across all layers to eliminate all synaptic connections between the illumination areas and the area in the middle. An example of such preparation is shown in Fig. 5.5. Note that the cuts reach the white matter. Even in this case the phenomenon occurred. This observation suggests that the illumination is not precise enough with the light either directly hitting the middle area or it reaches the middle area through scattering.

In order to test the precision of the illumination, I ran an experiment with a moving

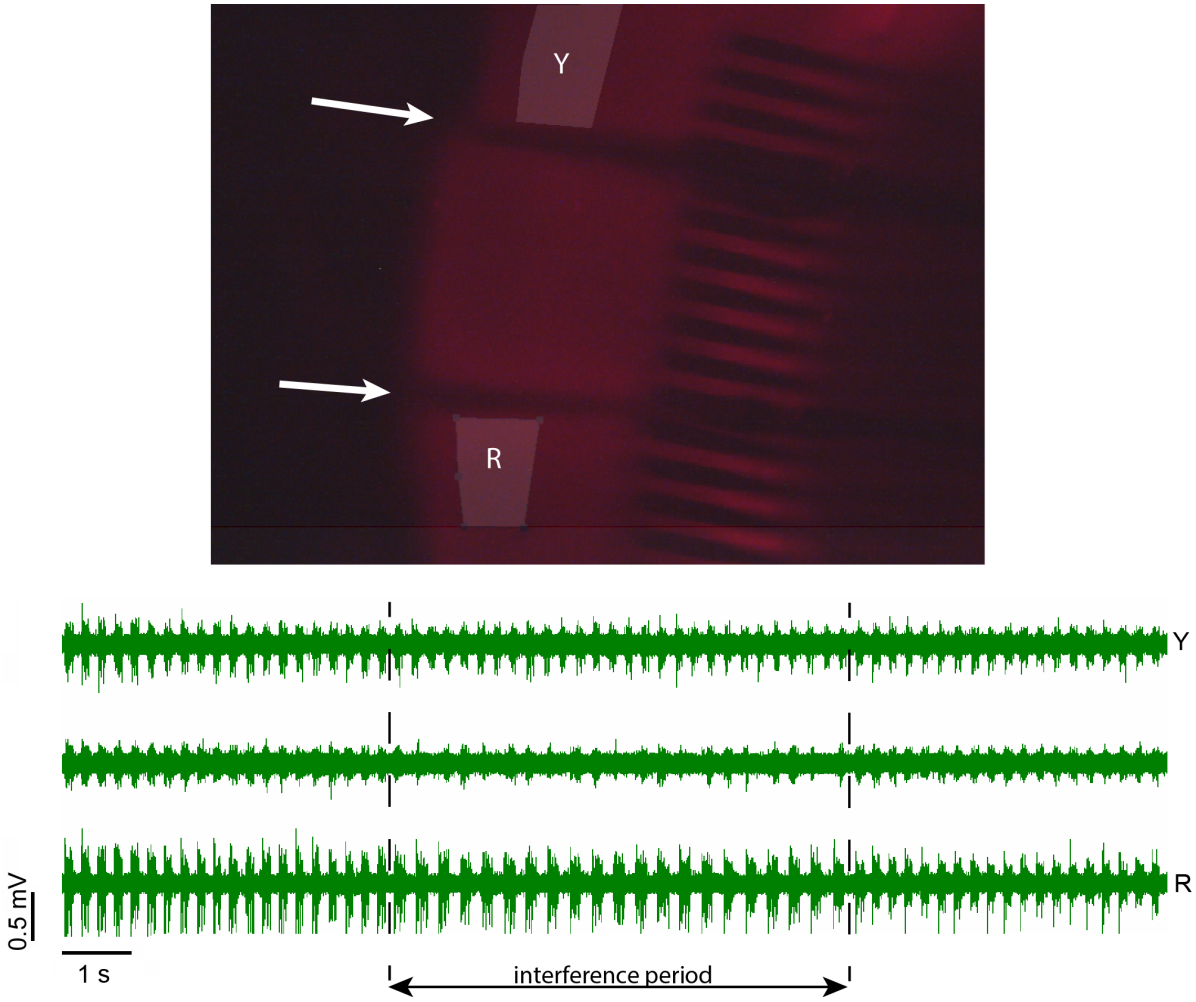

Figure 5.5: Eliminating all synaptic interactions by cutting the slice (ChR2) and separating the three different areas. The cortical area in the middle is physically separated from the medial and lateral sides where the illumination is targeted (yellow and red areas marked). Note that the cuts (white arrows) in the slice are reaching the white matter eliminating any synaptic connection between the different areas. Even under these conditions, the coincidence detection pattern is evident in the raw traces during the interference period.

box of illumination over a severed slice. Part of the neocortical area of the slice was removed. The results show that the illumination is precisely delivered to the moving box. The partial slice in Fig. 5.6 responded only when the illumination area is actually covering a part of the slice (Fig. 5.6B) but not when it is approximately 50 μm away (Fig. 5.6A). This indicates that the illumination is precise enough at least in terms of direct light illumination but poor precision is still possible due to the scattering of light.

Double slice experiments were once again used to test the scattering of light. As before, a ChR2 slice and a wild-type slice were used in the same experiment but in this case, instead of illuminating on the ChR2 slice, the illumination was delivered on the wild-type slice. The ChR2 slice, with the MEA placed along its supragranular layers,

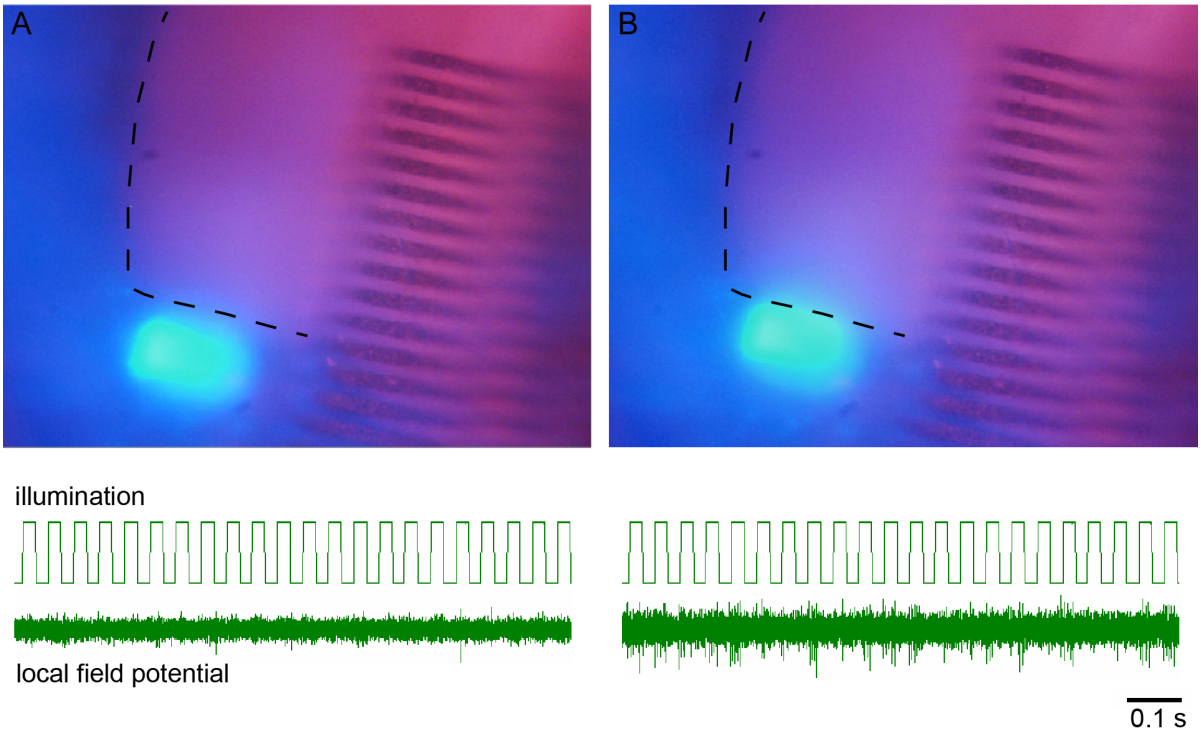

Figure 5.6: Testing the precision of the illumination. A rectangular area of illumination is moved parallel to the array of electrodes on a slice (ChR2) which is partly missing. The dashed lines show the boundaries of the cut slice. The illumination in A does not induce activity despite the fact that it is close to the boundary of the slice. In contrast, the illumination in B, which actually touches the boundary of the slice, induces activity (see local field potential traces). The displacement of the illuminated area between A and B is approximately equal to the width of the electrode shaft which is 55 μm.

was set next to the wild-type one. The arrangement is shown in Fig. 5.7A. The light-sensitive cells in the ChR2 slice were indeed activated through the scattering of light on the wild-type slice. Notice also that there is a significant distance between the slices; they are not touching. Nevertheless the scattered light is able to produce activity in the supragranular layers of the ChR2 slice efficiently. This is not the case when the wild-type slice is removed (see Fig. 5.7B). The absence of the tissue prevents any scattering of light in this case (similar to Fig. 5.6A).

5.4 Discussion

The experiments described in this chapter yielded unexpected results which were only partly explained. The interaction of the two oscillations did not produce an activity comparable to the period concatenation phenomenon (Roopun *et al.* (2008a,b)).

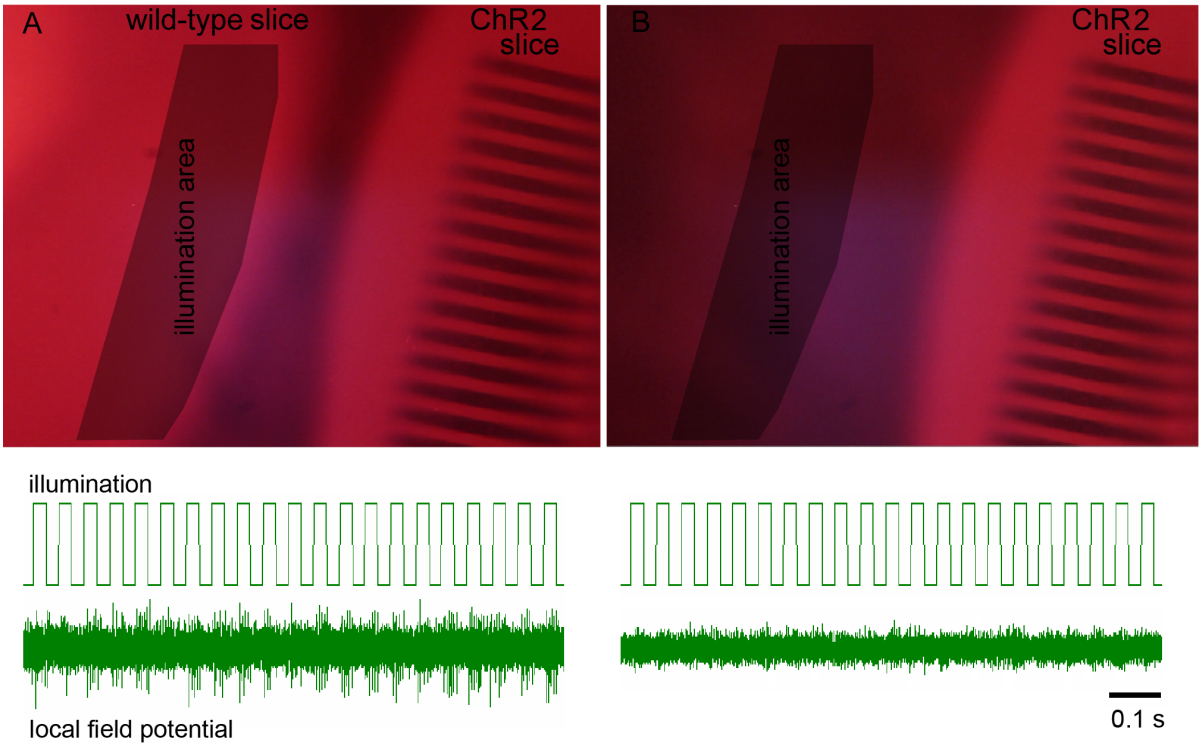

Figure 5.7: Demonstration of the significant scattering of light with a double slice setup. (A) The wild-type slice on the left receives photostimulation (shaded area) and the scattered light reaches the ChR2 slice on the right from where the activity is recorded (see local field potential). The scattering is enough to activate the ChR2 cells despite the distance between illumination area and the ChR2 slice (0.3-0.4 mm). (B) The wild-type slice is removed and no more activity is recorded (see traces). The light is not scattered in this case.

Instead, a coincidence detection pattern was produced during the interference of the two oscillations. The activity recorded in the middle during the interference was limited to the periods of time when both medial and lateral areas were active. Despite the fact that some proposed explanations were proven to be wrong, I still cannot explain the phenomenon with confidence. Some speculations and a proposed experiment to test them are described below. Through pharmacological manipulations, and especially through the blockade of glutamatergic currents, I showed that the phenomenon cannot be explained due to synaptic activity and thus the implication of fast-spiking interneurons (e.g., through feed-forward inhibition, Pouille and Scanziani (2001); Pouille *et al.* (2009)) is unlikely. I also showed that the phenomenon does not occur due to the interference of electric fields originating from the photostimulated areas.

The results suggest that the scattering of light is much more significant than expected. Areas located 0.4 mm away from the illuminated area can be activated through the scattered light (see Fig. 5.7). This introduces a significant issue regarding the precision

of photoactivation in similar experimental setups. A possible solution to this issue would be to decrease the intensity of light or to shrink the illumination area. Ideally, the intensity of light should be the bare minimum for the direct activation of the cells in the illuminated area. In that case, the scattered light is expected to be too weak to activate significant numbers of cells outside that area. Alternatively, the scattered light can be decreased significantly by shrinking the illumination area.

Considering the significant scattering of light in these experiments, the coincidence detection pattern recorded could be the result of direct activation of the horizontally extended dendritic structures of layer V pyramidal cells. I hypothesize that the activity recorded in layer V comes mainly from pyramidal cells with wide dendritic structures in layers I and II. Their tufts were activated through scattered light and the coincidence detection pattern reflects the interaction of the two currents flowing from either side (Larkum *et al.* (2009); Schaefer *et al.* (2003)). The interaction between propagating and backpropagating signals might be responsible for the average reduction of activity during the interference (Williams and Stuart (2000)). This suggests that the effect is a result of subcellular mechanisms and this is also supported by the fact that pharmacological blockade of synaptic activity did not influence the pattern in any qualitative way. This hypothesis can be tested with whole cell recordings from layer V pyramidal cells in cortical slices. The same illumination protocol as described above can be used on the slice. The same coincidence detection pattern is expected to arise. Alternatively, simulations of a biophysically detailed neuron model of layer V pyramidal cell can be used. This strategy will also enable an easy investigation of the subcellular mechanisms involved.

Chapter 6

General Discussion

6.1 Overarching discussion on the theoretical chapters

The work presented in chapters 2 and 3 is a theoretical investigation of the functional role of divisive inhibition in neocortical dynamics. The fast-spiking, soma-targeting interneurons are the primary source of this type of inhibition due to their selective targeting on the somatic and peri-somatic domain of pyramidal cells (Wilson *et al.* (2012); Pouille *et al.* (2013); Atallah *et al.* (2012)). The results in these chapters show that the mechanism of divisive inhibition renders the network dynamics less sensitive to changes in certain anatomical features. This was demonstrated in two different phenomena using the same neural mass model. First, the onset of chaotic activity was shown to follow a universal transition regardless of the specific connectivity settings (Papasavvas *et al.* (2015)). Second, the long-range synchronization between two neocortical areas was found to be less sensitive to the increase of conduction delay and the asymmetry of their long-range connections. Simulating the phenomenon of entrainment using the same neural mass model revealed another interesting effect of divisive inhibition. The oscillatory dynamics were more flexible and the network was entrained to a wider range of frequencies.

These effects were observed by introducing divisive inhibition, as a gain control

mechanism, in a neural mass model. In particular, it was introduced in an extended version of the spatially localized Wilson-Cowan model which had originally two populations, one excitatory and one inhibitory (Wilson and Cowan (1972)). The neural mass model of a local neocortical network was modelled here as three populations, one excitatory and two inhibitory. The fact that the dimensionality of the network was increased from 2 to 3 is potentially important. The first inhibitory population, representing the dendrite-targeting interneurons, was always delivering a subtractive inhibition to the excitatory population. The other inhibitory population, representing the soma-targeting interneurons, was either delivering divisive inhibition or subtractive inhibition or a combination of the two. Note that there were two different interneuronal populations (variables) delivering the two types of inhibition. The input-output function of the excitatory population was dynamically modulated in two different ways by two different variables. In addition, the first inhibitory population was inhibiting the second, consistent with the anatomical evidence (Pfeffer *et al.* (2013)). I speculate that having this increased dimensionality, from 2 to 3, was important for the investigation and the observations made. It was possible to introduce the mechanism of divisive inhibition in a two-population network instead, with the inhibitory population delivering at the same time a combination of subtractive and divisive inhibition. In that case, the chaotic activity would not be possible, because it demands a dimensionality of at least 3, but the phenomena of entrainment and long-range synchronization would be possible to simulate. I speculate that the introduction of divisive inhibition in this way, with its dynamics being exactly the same with subtractive inhibition, would fail to have the same positive effect on the two phenomena. The input-output function needs to be modulated in two different ways independently in order to enable more flexible dynamics and thus the enhancement of entrainment and long-range synchronization.

6.2 Overarching discussion on the experimental chapters

One of the main findings from chapter 5 is that the scattering of light is significant and can stimulate cells, in the case of ChR2 expression, outside the illumination area. This observation calls for a reconsideration of the results reported in chapter 4 where

activity was found to originate and propagate from inside the illumination area to neighbouring territories. Can the results be interpreted differently considering the significant scattering of light? Is it possible that the cells outside the illumination area were stimulated sufficiently by scattered light thus producing action potentials after the increase of extracellular K^+ and the depolarization of their membrane?

First, it is worth noting that the illumination areas in the ChR2 experiments of chapter 4 are significantly smaller than the ones in chapter 5 (see Figures 4.2 and 5.5), suggesting that the issue of scattering light was not as significant. Furthermore, ChR2 in chapter 4 was expressed only in PV^+ cells which have less excitable dendrites than the pyramidal cells in chapter 5 (Martina *et al.* (2000); Goldberg *et al.* (2003); Stuart and Sakmann (1994)). It is true that the propagations reported had a median distance of 400 μm from the illumination area which, as shown in chapter 5, is a distance that scattered light can reach easily. However, the fact that the time-locked activity outside the illumination area was always recorded with a significant delay compared to the activity inside the illumination area excludes the possibility of their somata being directly stimulated by the scattered light.

Is it possible that their distant dendrites, which can typically reach 200 μm away from the soma, were stimulated by the scattered light? This possibility is also excluded because it cannot explain the suppression effect of gap junction blockers on the activity outside the illumination area. Gap junction blockers would either have no effect in that case or the effect would be the opposite because they are expected to make the cell electrotonically more compact.

As discussed in chapter 4, some results, and in particular the speed of propagation through the PV-syncytium, might not be accurate. The scattering of light supports the idea that the calculated speed of propagation was potentially overestimated. PV^+ cells, located outside the illumination area but close enough to receive sufficient scattered light, could initiate a propagation that was shorter than what was initially considered.

6.3 Future directions in the study of fast-spiking, PV^+ interneurons

Recent advances in the study of fast-spiking, PV^+ interneurons opened up new avenues and introduced new questions for further research. Research is increasingly turning towards questions about their impact on a network and behavioural level, and, in particular, the functional role of their specialized cellular physiology and connectivity on those levels (for a review, see Hu *et al.* (2014)). This thesis can be considered as a contribution to this endeavour with investigations on how their gain modulatory capabilities and their electrical synapses influence the dynamics of neocortical networks. Further investigations on the specific properties of these interneurons will potentially enable the clinicians to target them for therapeutic interventions in many conditions (Hu *et al.* (2014)).

PV^+ interneurons were implicated in learning paradigms and synaptic plasticity mechanisms in sensory cortices (Yazaki-Sugiyama *et al.* (2009); Kuhlman *et al.* (2013); Wolff *et al.* (2014); Letzkus *et al.* (2011); Sparta *et al.* (2014); Donato *et al.* (2013)). The function of these cells in the circuits of visual cortex was found to be temporarily suppressed after monocular deprivation and this suppression enabled the re-wiring of the circuit for the establishment of ocular dominance (Yazaki-Sugiyama *et al.* (2009); Kuhlman *et al.* (2013)). A similar disinhibitory mechanism was also found between amygdala interneurons and cortical PV^+ interneurons in an associative fear learning paradigm (Wolff *et al.* (2014)). Learning was achieved by the suppression of activity of PV^+ interneurons in auditory cortex (Wolff *et al.* (2014); Letzkus *et al.* (2011)). In contrast, optogenetic stimulation of these interneurons in prefrontal cortex facilitated the extinction of reward-associated behaviour (Sparta *et al.* (2014)). Furthermore, it was recently suggested that not only the activity of PV^+ interneurons has an impact on learning, but also that learning has an impact on the interneuronal network plasticity as well (Donato *et al.* (2013)).

PV^+ interneurons are characterized by a pronounced polarity in terms of the excitability of their dendrites and axons (Hu *et al.* (2014)). While their dendrites feature a low ratio between the Na^+ and K^+ channels (Hu *et al.* (2010)), in contrast,

their axons have a distinctively high ratio (Hu and Jonas (2014)). This makes their dendrites weakly excitable whereas their axons are highly excitable, and this polarity distinguishes PV^+ interneurons from pyramidal neurons or other interneuronal classes (Martina *et al.* (2000); Goldberg *et al.* (2003); Stuart and Sakmann (1994)). This characteristic distribution of the ion channels, and especially the high expression of Na^+ channels at the axon, is critical for the fast signalling of PV^+ cells (Hu *et al.* (2014)). Links between impaired signalling or abnormal distribution of ion channels and the phenotype of neuropsychiatric diseases were established recently (Hu *et al.* (2014); Ogiwara *et al.* (2007); Mashimo *et al.* (2010); Fazzari *et al.* (2010)).

The subcellular and connectivity features of PV^+ cells are implicated in epilepsy in different ways as recent studies show (Hu *et al.* (2014); Ogiwara *et al.* (2013); Mashimo *et al.* (2010)). Nonsense and missense mutations of the $Na_v1.1$/SCN1A gene give rise to different functional impairments of these interneurons and consequently to different phenotypes of epilepsy (Ogiwara *et al.* (2013); Mashimo *et al.* (2010)). The $Na_v1.1$ channel is highly expressed in the axonal compartment of these cells and any mutation has a significant effect on their electrophysiological responses (Ogiwara *et al.* (2007)). The nonsense mutation impairs both the high-frequency firing and the fast propagation of the signal along the axon (Ogiwara *et al.* (2007)). These impairments are suggested to cause severe myoclonic epilepsy of infancy (Dravet syndrome) after it was shown that the nonsense mutation can replicate the phenotype of the disease in mouse models (Ogiwara *et al.* (2013)). The missense mutation of the gene alters the inactivation properties of the $Na_v1.1$ channel resulting into a decreased excitability of the axon (Mashimo *et al.* (2010)). This was shown to produce the phenotype of generalized epilepsy with febrile seizures plus (GEFS+) in rats (Mashimo *et al.* (2010)). As described in chapter 4, the electrical synapses between the PV^+ interneurons are implicated in epileptogenesis and seizure propagation (Gajda *et al.* (2003); Gigout *et al.* (2006); Louvel *et al.* (2001); Uusisaari *et al.* (2002)). Furthermore, the results reported in the same chapter demonstrate that activity can propagate through the PV-syncytium during a seizure due to the elevated concentration of extracellular K^+. These observations suggest that the population of PV^+ interneurons should be considered as a potential target for the treatment of epilepsy.

Subcellular and electrophysiological alterations in PV^+ cells are also implicated in

schizophrenia (Lewis *et al.* (2012, 2005); DelPino *et al.* (2013)). Altered expression of different genes was reported in schizophrenia patients (Lewis *et al.* (2012, 2005)). The upregulation of μ opioid receptor and the downregulation of GAD67 were reported for PV^+ interneurons in the prefrontal cortex (Curley and Lewis (2012); Lewis *et al.* (2012)). The synthesis and release of GABA is impaired due to these alterations (Curley and Lewis (2012); Lewis *et al.* (2012)). Similarly, mutations in both ErbB4 and Nrg1 genes were reported in schizophrenia patients (Lewis *et al.* (2005)). These are exclusively expressed in PV^+ interneurons and their mutation lead to electrophysiological deficiencies in these cells (Fazzari *et al.* (2010)). Both their excitatory synaptic inputs and their inhibitory synaptic outputs are affected (Fazzari *et al.* (2010); DelPino *et al.* (2013)). The dysregulation of Na^+ and K^+ channels causes an impairment of the fast-spiking and fast signalling phenotypes of these cells (Janssen *et al.* (2012)). Such molecular alterations in the soma-targeting, PV^+ interneurons are hypothesized to impair the mechanism of gain control in the cortical circuits. As discussed in chapter 3, these subcellular alterations can potentially cause the impairment in entrainment and synchronization which characterizes schizophrenia due to a deficient divisive inhibition. Further investigation of these interneurons is still necessary to understand how molecular aberrations influence the functionality of the system at a network and behavioural level.

6.4 Towards multi-scale modelling

The dynamics of neural systems can be studied at different spatial scales: from the microscopic scale of subcellular and cellular elements, to the mesoscopic scale of the circuits and the macroscopic scale of global networks. Churchland and Sejnowski used the term *levels of organization* to refer to these different spatial scales (Churchland and Sejnowski (1992)). The examples of pathological dynamics described above suggest that, in order to fully understand a condition, we need to consider its phenotype at multiple levels (Lytton (2008); Jirsa *et al.* (2010)). The same applies for the understanding of complex physiological functions of the brain, such as memory and multi-modal sensory processing (Djurfeldt *et al.* (2008); Coombes (2010)). In the case of disorders, a mechanistic understanding of how alterations in one level (e.g.,

molecular) can produce pathological dynamics in another level (e.g., circuit) is pivotal for the development of effective treatments (Nakazawa *et al.* (2012); Lytton (2008)). Such multi-scale phenomena have been described in all major neurological and psychiatric disorders (Nakazawa *et al.* (2012); Lytton (2008); Uhlhaas and Singer (2006)). Multi-scale models that include two or more interacting levels of organization can assist towards a comprehensive understanding of the causal links between the different levels of the pathology.

Models of neural systems that focused on a single level proved to be useful in explaining simpler phenomena observed in experimental data. Depending on the questions posed, single-level models with the appropriate degree of abstraction were developed to explain phenomena at the microscopic, mesoscopic or macroscopic scale (Hodgkin and Huxley (1952); Wilson and Cowan (1972, 1973); Jansen and Rit (1995)). The abstraction of irrelevant aspects, either at the same or another level of organization, is crucial for the development of tractable models, that is, models which are easily analysed and interpreted (Jirsa *et al.* (2010); Djurfeldt *et al.* (2008)). Hodgkin and Huxley, working at the microscopic level, applied abstraction to ignore the irrelevant ion channels in order to explain the mechanism of an action potential based on the function of Na^+ and K^+ channels alone (Hodgkin and Huxley (1952)). This type of models, focusing on a single cell or a small group of coupled cells, can be used to explore phenomena which rely on the biophysics of ion channels and synaptic activity. Whole cell recordings are usually used to inform these models or test any hypotheses that are formulated after the simulation of the model. In the case of mesoscopic or macroscopic models, the membrane potentials and the synaptic activity between large neuronal populations are abstracted by applying the mean-field approximation (Renart *et al.* (2004); Deco *et al.* (2008)). To preserve the tractability of the model, the models dimensionality is reduced by representing a large number of variables with their average. Emergent population phenomena, such as oscillations or the resonance of a network, can be easily modelled as the interaction of excitatory and inhibitory populations (Wilson and Cowan (1972, 1973); Jansen and Rit (1995)). Mesoscopic models are usually related to local field potential (LFP) recordings which represent the activity of a localized network. The macroscopic models resemble the dynamics of distributed networks as recorded in electroencephalograms (EEG) or functional magnetic resonance imaging (fMRI) (Deco *et al.* (2008)).

Over the last decade, advances in high performance computing enabled the development of multi-scale models which combine two or more levels of organization (Breakspear and Stam (2005); Kiebel *et al.* (2008); Breakspear and Knock (2008); Markram (2006)). Three different strategies have been employed (Jirsa *et al.* (2010)). The first strategy uses a hierarchical organization of the networks elements taking advantage of the modular and recursive topological patterns of the functional networks (Meunier *et al.* (2009); Echtermeyer *et al.* (2011)). This produces an explicit multi-scale framework where there are level-specific equations describing the relation of each level with the next one (Jirsa *et al.* (2010)). Theoretical frameworks to explore spatial and temporal correlations were proposed using this architecture and predictions about function-structure relationship were produced (Breakspear and Stam (2005); Kiebel *et al.* (2008)). A second approach, which was termed *multi-scale minded*, focuses predominantly on a single level, while also incorporating dynamics with reduced complexity from adjacent levels (Jirsa *et al.* (2010); Breakspear and Knock (2008)). The reduction in complexity is typically achieved by applying the mean-field approximation as mentioned above (Jirsa *et al.* (2010); Deco *et al.* (2008)). The third approach, which is termed as the *brute force* approach, follows a bottom-up construction of a circuit based on a highly detailed microscopic scale in terms of its biophysics and anatomy (Jirsa *et al.* (2010)). Multiple circuits can be used as building blocks for a larger network but the cellular detail is preserved (Jirsa *et al.* (2010)). This strategy was introduced with the Blue Brain project, with a realistic cortical column as its goal (Markram (2006)). Some emergent phenomena were recently reported in the first draft of the project (Markram *et al.* (2015)). The major concern about this strategy, however, other than its very high demands in computational power, is the interpretability of the results due to its very high complexity (Jirsa *et al.* (2010)).

Multi-scale modelling can help us transcend levels of understanding and explore the role of different populations in cortical microcircuits or even global brain networks. Following these approaches, it is possible to support the investigation on how fast-spiking interneurons, or any other neuronal class, influence neocortical dynamics in health and disease. Alterations at the molecular level, as the ones described in the previous section, can be introduced at the lower level of a multi-scale model in order to simulate their impact on the functionality of the neuronal circuit. This will help formulate new hypothesis or refine existing ones that can be tested through

experimentation. I believe, such synergistic application of theory and experimentation is the only way forward in our struggle to solve the increasingly hard problems in neuroscience.

Bibliography

Adesnik, H., Bruns, W., Taniguchi, H., Huang, Z.J. and Scanziani, M. (2012). A neural circuit for spatial summation in visual cortex. *Nature*, **490**, 226–31.

Akam, T., Oren, I., Mantoan, L., Ferenczi, E. and Kullmann, D.M. (2012). Oscillatory dynamics in the hippocampus support dentate gyrusCA3 coupling. *Nat. Neurosci.*, **15**, 763–771.

Alfonsa, H., Merricks, E.M., Codadu, N.K., Cunningham, M.O., Deisseroth, K., Racca, C. and Trevelyan, A.J. (2015). The Contribution of Raised Intraneuronal Chloride to Epileptic Network Activity. *J. Neurosci.*, **35**, 7715–7726.

Amitai, Y., Gibson, J.R., Beierlein, M., Patrick, S.L., Ho, A.M., Connors, B.W. and Golomb, D. (2002). The spatial dimensions of electrically coupled networks of interneurons in the neocortex. *J. Neurosci.*, **22**, 4142–4152.

Amzica, F., Massimini, M. and Manfridi, A. (2002). Spatial buffering during slow and paroxysmal sleep oscillations in cortical networks of glial cells in vivo. *J. Neurosci.*, **22**, 1042–1053.

Andrade-Rozental, A.F., Rozental, R., Hopperstad, M.G., Wu, J.K., Vrionis, F.D. and Spray, D.C. (2000). Gap junctions: the kiss of death and the kiss of life. *Brain Res. Rev.*, **32**, 308–315.

Angulo, M.C., Staiger, J.F., Rossier, J. and Audinat, E. (1999). Developmental synaptic changes increase the range of integrative capabilities of an identified excitatory neocortical connection. *J Neurosci*, **19**, 1566–1576.

Anstötz, M., Cosgrove, K.E., Hack, I., Mugnaini, E., Maccaferri, G. and Lübke, J.H.R. (2014). Morphology, inputoutput relations and synaptic connectivity of CajalRetzius

cells in layer 1 of the developing neocortex of CXCR4-EGFP mice. *Brain Struct. Funct.*, **219**, 2119–2139.

Ascoli, G.A., Alonso-Nanclares, L., Anderson, S.A., Barrionuevo, G., Benavides-Piccione, R., Burkhalter, A., Buzsáki, G., Cauli, B., Defelipe, J., Fairén, A., Feldmeyer, D., Fishell, G., Fregnac, Y., Freund, T.F., Gardner, D., Gardner, E.P., Goldberg, J.H., Helmstaedter, M., Hestrin, S., Karube, F., Kisvárday, Z.F., Lambolez, B., Lewis, D.A., Marin, O., Markram, H., Muñoz, A., Packer, A., Petersen, C.C.H., Rockland, K.S., Rossier, J., Rudy, B., Somogyi, P., Staiger, J.F., Tamas, G., Thomson, A.M., Toledo-Rodriguez, M., Wang, Y., West, D.C. and Yuste, R. (2008). Petilla terminology: nomenclature of features of GABAergic interneurons of the cerebral cortex. *Nat. Rev. Neurosci.*, **9**, 557–568.

Atallah, B.V., Bruns, W., Carandini, M. and Scanziani, M. (2012). Parvalbumin-expressing interneurons linearly transform cortical responses to visual stimuli. *Neuron*, **73**, 159–70.

Auerbach, A.A. and Bennett, M.V. (1969). A rectifying electrotonic synapse in the central nervous system of a vertebrate. *J. Gen. Physiol.*, **53**, 211–37.

Ayaz, A. and Chance, F.S. (2012). Gain Modulation of Neuronal Responses by Subtractive and Divisive Mechanisms of Inhibition. *J. Neurophysiol.*, **101**, 958–968.

Babloyantz, A. and Destexhe, A. (1986). Low-dimensional chaos in an instance of epilepsy. *Proc. Natl. Acad. Sci. U. S. A.*, **83**, 3513–7.

Barthó, P., Hirase, H., Monconduit, L., Zugaro, M., Harris, K.D. and Buzsáki, G. (2004). Characterization of neocortical principal cells and interneurons by network interactions and extracellular features. *J. Neurophysiol.*, **92**, 600–8.

Bartos, M., Vida, I. and Jonas, P. (2007). Synaptic mechanisms of synchronized gamma oscillations in inhibitory interneuron networks. *Nat. Rev. Neurosci.*, **8**, 45–56.

Battaglia, F.P. and Treves, A. (1998). Stable and rapid recurrent processing in realistic autoassociative memories. *Neural Comput.*, **10**, 431–50.

Bazhenov, M., Timofeev, I., Steriade, M. and Sejnowski, T.J. (2004). Potassium model for slow (2-3 Hz) in vivo neocortical paroxysmal oscillations. *J. Neurophysiol.*, **92**, 1116–1132.

Beaumont, M. and Maccaferri, G. (2011). Is connexin36 critical for GABAergic hypersynchronization in the hippocampus? *J. Physiol.*, **589**, 1663–80.

Behrens, C.J., ul Haq, R., Liotta, A., Anderson, M.L. and Heinemann, U. (2011). Nonspecific effects of the gap junction blocker mefloquine on fast hippocampal network oscillations in the adult rat in vitro. *Neuroscience*, **192**, 11–19.

Belluscio, M.A., Mizuseki, K., Schmidt, R., Kempter, R. and Buzsáki, G. (2012). Cross-frequency phase-phase coupling between θ and γ oscillations in the hippocampus. *J. Neurosci.*, **32**, 423–35.

Bem, J.L., Kerr, L. and Stuerchler, D. (1992). Mefloquine prophylaxis: an overview of spontaneous reports of severe psychiatric reactions and convulsions. *J. Trop. Med. Hyg.*, **95**, 167–179.

Bennett, M., Schatz, M.F., Rockwood, H. and Wiesenfeld, K. (2002). Huygens's clocks. *Proc. R. Soc. A Math. Phys. Eng. Sci.*, **458**, 563–579.

Bernardo, L.S. (1997). Recruitment of GABAergic inhibition and synchronization of inhibitory interneurons in rat neocortex. *J. Neurophysiol.*, 3134–3144.

Blatow, M., Rozov, A., Katona, I., Hormuzdi, S.G., Meyer, A.H., Whittington, M.A., Caputi, A. and Monyer, H. (2003). A novel network of multipolar bursting interneurons generates theta frequency oscillations in neocortex. *Neuron*, **38**, 805–817.

Blazquez-Llorca, L., Woodruff, A., Inan, M., Anderson, S.A., Yuste, R., DeFelipe, J. and Merchan-Perez, A. (2014). Spatial distribution of neurons innervated by chandelier cells. *Brain Struct. Funct.*, **220**, 2817–2834.

Borisyuk, G., Borisyuk, R., Khibnik, A. and Roose, D. (1995). Dynamics and bifurcations of two coupled neural oscillators with different connection types. *Bull. Math. Biol.*, **57**, 809–840.

Borisyuk, R. and Kirillov, A. (1992). Bifurcation analysis of a neural network model. *Biol. Cybern.*, **66**, 319–325.

Bragin, A., Jandó, G., Nádasdy, Z., Hetke, J., Wise, K. and Buzsáki, G. (1995). Gamma (40-100 Hz) oscillation in the hippocampus of the behaving rat. *J. Neurosci.*, **15**, 47–60.

Breakspear, M. and Knock, S. (2008). Kinetic Models of Brain Activity. *Brain Imaging Behav.*, **2**, 270–288.

Breakspear, M. and Stam, C.J. (2005). Dynamics of a neural system with a multiscale architecture. *Philos. Trans. R. Soc. London. Ser. B Biol. Sci.*, **360**, 1051–1074.

Breakspear, M., Roberts, J.A., Terry, J.R., Rodrigues, S., Mahant, N. and Robinson, P.A. (2006). A unifying explanation of primary generalized seizures through nonlinear brain modeling and bifurcation analysis. *Cereb. Cortex*, **16**, 1296–313.

Brenner, C.A., Sporns, O., Lysaker, P.H. and O'Donnell, B.F. (2003). EEG synchronization to modulated auditory tones in schizophrenia, schizoaffective disorder, and schizotypal personality disorder. *Am. J. Psychiatry*, **160**, 2238–2240.

Bressler, S.L., Coppola, R. and Nakamura, R. (1993). Episodic multiregional cortical coherence at multiple frequencies during visual task performance. *Nature*, **366**, 153–156.

Brink, P.R., Cronin, K. and Ramanan, S.V. (1996). Gap junctions in excitable cells. *J. Bioenerg. Biomembr.*, **28**, 351–358.

Bruzzone, R. and Dermietzel, R. (2006). Structure and function of gap junctions in the developing brain. *Cell Tissue Res.*, **326**, 239–248.

Bucurenciu, I., Kulik, A., Schwaller, B., Frotscher, M. and Jonas, P. (2008). Nanodomain Coupling between Ca2+ Channels and Ca2+ Sensors Promotes Fast and Efficient Transmitter Release at a Cortical GABAergic Synapse. *Neuron*, **57**, 536–545.

Bullock, W.M., Bolognani, F., Botta, P., Valenzuela, C.F. and Perrone-Bizzozero, N.I. (2009). Schizophrenia-like GABAergic gene expression deficits in cerebellar Golgi cells from rats chronically exposed to low-dose phencyclidine. *Neurochem. Int.*, **55**, 775–782.

Buzsáki, G. (2006). *Rhythms of the Brain*. Oxford University Press.

Buzsáki, G. and Chrobak, J.J. (1995). Temporal structure in spatially organized neuronal ensembles: a role for interneuronal networks. *Curr. Opin. Neurobiol.*, **5**, 504–510.

Buzsáki, G. and Draguhn, A. (2004). Neuronal Oscillations in Cortical Networks. *Science (80-.).*, **304**, 1926.

Buzsàki, G. and Eidelberg, E. (1981). Commissural projection to the dentate gyrus of the rat: evidence for feed-forward inhibition. *Brain Res.*, **230**, 346–350.

Canolty, R.T. and Knight, R.T. (2010). The functional role of cross-frequency coupling. *Trends Cogn. Sci.*, **14**, 506–15.

Canolty, R.T., Edwards, E., Dalal, S.S., Soltani, M., Nagarajan, S.S., Kirsch, H.E., Berger, M.S., Barbaro, N.M. and Knight, R.T. (2006). High gamma power is phase-locked to theta oscillations in human neocortex. *Science*, **313**, 1626–8.

Caputi, A., Rozov, A., Blatow, M. and Monyer, H. (2009). Two calretinin-positive gabaergic cell types in layer 2/3 of the mouse neocortex provide different forms of inhibition. *Cereb. Cortex*, **19**, 1345–1359.

Caputi, A., Melzer, S., Michael, M. and Monyer, H. (2013). The long and short of GABAergic neurons.

Cardin, J.A., Carlén, M., Meletis, K., Knoblich, U., Zhang, F., Deisseroth, K., Tsai, L.H. and Moore, C.I. (2009). Driving fast-spiking cells induces gamma rhythm and controls sensory responses. *Nature*, **459**, 663–667.

Cauli, B., Audinat, E., Lambolez, B., Angulo, M.C., Ropert, N., Tsuzuki, K., Hestrin, S. and Rossier, J. (1997). Molecular and physiological diversity of cortical nonpyramidal cells. *J. Neurosci.*, **17**, 3894–3906.

Cauli, B., Zhou, X., Tricoire, L., Toussay, X. and Staiger, J.F. (2014). Revisiting enigmatic cortical calretinin-expressing interneurons. *Front. Neuroanat.*, **8**, 52.

Chance, F.S. and Abbott, L.F. (2000). Divisive inhibition in recurrent networks. *Network*, **11**, 119–29.

Chance, F.S., Abbott, L.F. and Reyes, A.D. (2002). Gain modulation from background synaptic input. *Neuron*, **35**, 773–82.

Chepkova, A.N., Sergeeva, O.A. and Haas, H.L. (2008). Carbenoxolone impairs LTP and blocks NMDA receptors in murine hippocampus. *Neuropharmacology*, **55**, 139–147.

Chialvo, D.R. (2010). Emergent complex neural dynamics. *Nat. Phys.*, **6**, 744–750.

Chiovini, B., Turi, G.F., Katona, G., Kaszás, A., Erdélyi, F., Szabó, G., Monyer, H., Csákányi, A., Vizi, E.S. and Rózsa, B. (2010). Enhanced dendritic action potential backpropagation in parvalbumin-positive basket cells during sharp wave activity. *Neurochem. Res.*, **35**, 2086–2095.

Chu, Z., Galarreta, M. and Hestrin, S. (2003). Synaptic Interactions of Late-Spiking Neocortical Neurons in Layer 1. *J. Neurosci.*, **23**, 96–102.

Churchland, P.S. and Sejnowski, T.J. (1992). The computational brain. *MIT Press*, 544.

Cobb, S.R., Buhl, E.H., Halasy, K., Paulsen, O. and Somogyi, P. (1995). Synchronization of neuronal activity in hippocampus by individual GABAergic interneurons. *Nature*, **378**, 75–8.

Colgin, L.L., Denninger, T., Fyhn, M., Hafting, T., Bonnevie, T., Jensen, O., Moser, M.B. and Moser, E.I. (2009). Frequency of gamma oscillations routes flow of information in the hippocampus. *Nature*, **462**, 353–357.

Connors, B.W. (2012). Tales of a dirty drug: carbenoxolone, gap junctions, and seizures. *Epilepsy Curr.*, **12**, 66–8.

Connors, B.W. and Gutnick, M.J. (1990). Intrinsic firing patterns of diverse neocortical neurons.

Connors, B.W., Benardo, L.S. and Prince, D.A. (1983). Coupling between neurons of the developing rat neocortex. *J. Neurosci.*, **3**, 773–782.

Coombes, S. (2010). Large-scale neural dynamics: Simple and complex. *Neuroimage*, **52**, 731–739.

Cornell-Bell, A.H., Finkbeiner, S.M., Cooper, M.S. and Smith, S.J. (1990). Glutamate induces calcium waves in cultured astrocytes: long-range glial signaling. *Science (80-.).*, **247**, 470.

Couey, J.J., Witoelar, A., Zhang, S.J., Zheng, K., Ye, J., Dunn, B., Czajkowski, R., Moser, M.B., Moser, E.I., Roudi, Y. and Witter, M.P. (2013). Recurrent inhibitory circuitry as a mechanism for grid formation. *Nat. Neurosci.*, **16**, 318–24.

Coutinho, P., Qiu, C., Frank, S., Tamber, K. and Becker, D. (2003). Dynamic changes in connexin expression correlate with key events in the wound healing process. *Cell Biol. Int.*, **27**, 525–541.

Cowan, J.D., Neuman, J. and van Drongelen, W. (2016). Wilson-Cowan Equations for Neocortical Dynamics. *J. Math. Neurosci.*, **6**, 1.

Craig, M.T. and McBain, C.J. (2015). Fast Gamma Oscillations Are Generated Intrinsically in CA1 without the Involvement of Fast-Spiking Basket Cells. *J. Neurosci.*, **35**, 3616–3624.

Crevier, D. and Meister, M. (1998). Synchronous period-doubling in flicker vision of salamander and man. *J. Neurophysiol.*, **79**, 1869–1878.

Cruikshank, S.J., Hopperstad, M., Younger, M., Connors, B.W., Spray, D.C. and Srinivas, M. (2004). Potent block of Cx36 and Cx50 gap junction channels by mefloquine. *Proc. Natl. Acad. Sci. U. S. A.*, **101**, 12364–12369.

Cunningham, M.O., Davies, C.H., Buhl, E.H., Kopell, N.J. and Whittington, M.A. (2003). Gamma oscillations induced by kainate receptor activation in the entorhinal cortex in vitro. *J. Neurosci.*, **23**, 9761–9769.

Cunningham, M.O., Hunt, J., Middleton, S., LeBeau, F.E.N., Gillies, M.G., Davies, C.H., Maycox, P.R., Whittington, M.A. and Racca, C. (2006). Region-Specific Reduction in Entorhinal Gamma Oscillations and Parvalbumin-Immunoreactive Neurons in Animal Models of Psychiatric Illness. *J. Neurosci.*, **26**, 2767–2776.

Curley, A.A. and Lewis, D.A. (2012). Cortical basket cell dysfunction in schizophrenia. *J. Physiol.*, **590**, 715–24.

Cvitanovic, P. (1984). Universality in chaos (or, Feigenbaum for cyclists). *Acta Phys. Pol. A*, **65**, 203–239.

Dauwels, J., Vialatte, F., Musha, T. and Cichocki, A. (2010). A comparative study of synchrony measures for the early diagnosis of Alzheimer's disease based on EEG. *Neuroimage*, **49**, 668–93.

David, O. and Friston, K.J. (2003). A neural mass model for MEG/EEG: Coupling and neuronal dynamics. *Neuroimage*, **20**, 1743–1755.

Davis Jr, L. and Lorente, d.N. (1947). Contribution to the mathematical theory of the electrotonus. *Stud. Rockefeller Inst. Med. Res. Repr.*, **131**, 442.

Dayan, P. and Abbott, L.F. (2001). Theoretical Neuroscience: Computational and Mathematical Modeling of Neural Systems. *Comput. Math. Model. Neural ...*, 480.

de Almeida, L., Idiart, M. and Lisman, J.E. (2009). A second function of gamma frequency oscillations: an E%-max winner-take-all mechanism selects which cells fire. *J. Neurosci.*, **29**, 7497–503.

Deco, G., Jirsa, V.K., Robinson, P.A., Breakspear, M. and Friston, K.J. (2008). The dynamic brain: from spiking neurons to neural masses and cortical fields. *PLoS Comput. Biol.*, **4**, e1000092.

Deco, G., Jirsa, V.K., McIntosh, A.R., Sporns, O. and Kötter, R. (2009). Key role of coupling, delay, and noise in resting brain fluctuations. *Proc. Natl. Acad. Sci. U. S. A.*, **106**, 10302–7.

DeFelipe, J., Hendry, S.H. and Jones, E.G. (1989). Visualization of chandelier cell axons by parvalbumin immunoreactivity in monkey cerebral cortex. *Proc. Natl. Acad. Sci. U. S. A.*, **86**, 2093–2097.

DeFelipe, J., Hendry, S.H.C., Hashikawa, T., Molinari, M. and Jones, E.G. (1990). A microcolumnar structure of monkey cerebral cortex revealed by immunocytochemical studies of double bouquet cell axons. *Neuroscience*, **37**, 655–673.

DeFelipe, J., Ballesteros-Yáñez, I., Inda, M.C. and Muñoz, A. (2006). Double-bouquet cells in the monkey and human cerebral cortex with special reference to areas 17 and 18. *Prog. Brain Res.*, **154**, 15–32.

DelPino, I., García-Frigola, C., Dehorter, N., Brotons-Mas, J., Alvarez-Salvado, E., MartínezdeLagrán, M., Ciceri, G., Gabaldón, M., Moratal, D., Dierssen, M., Canals, S., Marín, O. and Rico, B. (2013). Erbb4 Deletion from Fast-Spiking Interneurons Causes Schizophrenia-like Phenotypes. *Neuron*, **79**, 1152–1168.

Dermietzel, R. (1998). Gap junction wiring: A 'new' principle in cell-to-cell communication in the nervous system? *Brain Res. Rev.*, **26**, 176–183.

Destexhe, A., Contreras, D. and Steriade, M. (2001). LTS cells in cerebral cortex and their role in generating spike-and-wave oscillations. *Neurocomputing*, **38-40**, 555–563.

Devinsky, O., Vezzani, A., Najjar, S., De Lanerolle, N.C. and Rogawski, M.A. (2013). Glia and epilepsy: Excitability and inflammation. *Trends Neurosci.*, **36**, 174–184.

Dhooge, A., Govaerts, W. and Kuznetsov, Y.A. (2003). MATCONT: a MATLAB package for numerical bifurcation analysis of ODEs. *ACM Trans. Math. Softw.*, **29**, 141–164.

Díaz, J., Razeto-Barry, P., Letelier, J.C., Caprio, J. and Bacigalupo, J. (2007). Amplitude modulation patterns of local field potentials reveal asynchronous neuronal populations. *J. Neurosci.*, **27**, 9238–9245.

Djurfeldt, M., Ekeberg, O. and Lansner, A. (2008). Large-scale modeling - a tool for conquering the complexity of the brain. *Front. Neuroinform.*, **2**, 1.

Donato, F., Rompani, S.B. and Caroni, P. (2013). Parvalbumin-expressing basket-cell network plasticity induced by experience regulates adult learning. *Nature*, **504**, 272–6.

Draguhn, A., Traub, R.D., Schmitz, D. and Jefferys, J.G.R. (1998). Electrical coupling underlies high-frequency oscillations in the hippocampus in vitro. *Nature*, **394**, 189–192.

Durstewitz, D. and Gabriel, T. (2007). Dynamical basis of irregular spiking in NMDA-driven prefrontal cortex neurons. *Cereb. Cortex*, **17**, 894–908.

Echtermeyer, C., Han, C.E., Rotarska-Jagiela, A., Mohr, H., Uhlhaas, P.J. and Kaiser, M. (2011). Integrating temporal and spatial scales: human structural network motifs across age and region of interest size. *Front. Neuroinform.*, **5**, 10.

El Boustani, S. and Sur, M. (2014). Response-dependent dynamics of cell-specific inhibition in cortical networks in vivo. *Nat. Commun.*, **5**, 1–14.

Erisir, A., Lau, D., Rudy, B. and Leonard, C.S. (1999). Function of specific K(+) channels in sustained high-frequency firing of fast-spiking neocortical interneurons. *J. Neurophysiol.*, **82**, 2476–2489.

Ermentrout, B. (1984). Period Doublings and Possible Chaos in Neural Models. *SIAM J. Appl. Math.*, **44**, 80–95.

Ermentrout, G.B. and Kopell, N.J. (1991). Multiple pulse interactions and averaging in systems of coupled neural oscillators. *J. Math. Biol.*, **29**, 195–217.

Ertel, S.I. and Ertel, E.A. (1997). Low-voltage-activated T-type Ca2+ channels. In *Trends Pharmacol. Sci.*, vol. 18, 37–42.

Evans, W.H. and Martin, P.E.M. (2002). Gap junctions: structure and function (Review). *Mol. Membr. Biol.*, **19**, 121–136.

Fanselow, E.E., Richardson, K.A. and Connors, B.W. (2008). Selective , State-Dependent Activation of Somatostatin-Expressing Inhibitory Interneurons in Mouse Neocortex. *J. Neurophysiol.*, **100**, 2640–2652.

Fazzari, P., Paternain, A.V., Valiente, M., Pla, R., Luján, R., Lloyd, K., Lerma, J., Marín, O. and Rico, B. (2010). Control of cortical GABA circuitry development by Nrg1 and ErbB4 signalling. *Nature*, **464**, 1376–1380.

Feigenbaum, M.J. (1978). Quantitative universality for a class of nonlinear transformations. *J. Stat. Phys.*, **19**, 25–52.

Fell, J. and Axmacher, N. (2011). The role of phase synchronization in memory processes. *Nat. Rev. Neurosci.*, **12**, 105–118.

Fellous, J.M., Rudolph, M., Destexhe, A. and Sejnowski, T.J. (2003). Synaptic background noise controls the input/output characteristics of single cells in an in vitro model of in vivo activity. *Neuroscience*, **122**, 811–829.

Fertziger, A.P. and Ranck, J.B. (1970). Potassium accumulation in interstitial space during epileptiform seizures. *Exp. Neurol.*, **26**, 571–585.

Fischer, I., Vicente, R., Buldú, J.M., Peil, M., Mirasso, C.R., Torrent, M.C. and García-Ojalvo, J. (2006). Zero-Lag Long-Range Synchronization via Dynamical Relaying. *Phys. Rev. Lett.*, **97**, 123902.

Foffani, G., Uzcategui, Y.G., Gal, B. and Menendez de la Prida, L. (2007). Reduced spike-timing reliability correlates with the emergence of fast ripples in the rat epileptic hippocampus. *Neuron*, **55**, 930–41.

Freeman, W.J. (1987). Simulation of chaotic EEG patterns with a dynamic model of the olfactory system. *Biol. Cybern.*, **56**, 139–150.

Froehlich, F. and McCormick, D.A. (2010). Endogenous electric fields may guide neocortical network activity. *Neuron*, **67**, 129–143.

Froemke, R.C., Merzenich, M.M. and Schreiner, C.E. (2007). A synaptic memory trace for cortical receptive field plasticity. *Nature*, **450**, 425–429.

Fukuda, T. and Kosaka, T. (2003). Ultrastructural study of gap junctions between dendrites of parvalbumin-containing GABAergic neurons in various neocortical areas of the adult rat. *Neuroscience*, **120**, 5–20.

Fukuda, T., Kosaka, T., Singer, W. and Galuske, R.A.W. (2006). Gap Junctions among Dendrites of Cortical GABAergic Neurons Establish a Dense and Widespread Intercolumnar Network. *J. Neurosci.*, **26**, 3434–3443.

Furshpan, E.J. and Potter, D.D. (1959). Transmission at the giant motor synapses of the crayfish. *J. Physiol.*, **145**, 289–325.

Gajda, Z., Gyengési, E., Hermesz, E., Ali, K.S. and Szente, M. (2003). Involvement of gap junctions in the manifestation and control of the duration of seizures in rats in vivo. *Epilepsia*, **44**, 1596–1600.

Galarreta, M. and Hestrin, S. (1999). A network of fast-spiking cells in the neocortex connected by electrical synapses. *Nature*, **402**, 72–75.

Galarreta, M. and Hestrin, S. (2001). Spike transmission and synchrony detection in networks of GABAergic interneurons. *Science*, **292**, 2295–9.

Galarreta, M., Erdélyi, F., Szabó, G. and Hestrin, S. (2004). Electrical Coupling among Irregular-Spiking GABAergic Interneurons Expressing Cannabinoid Receptors. *J. Neurosci.*, **24**, 9770–9778.

Garfield, R.E., Sims, S.M., Kannan, M.S. and Daniel, E.E. (1978). Possible role of gap junctions in activation of myometrium during parturition. *Am. J. Physiol. Physiol.*, **235**, C168—-C179.

Geiger, J.R.P., Lübke, J., Roth, A., Frotscher, M. and Jonas, P. (1997). Submillisecond AMPA receptor-mediated signaling at a principal neuron- interneuron synapse. *Neuron*, **18**, 1009–1023.

Genesio, R. and Tesi, A. (1992). Harmonic balance methods for the analysis of chaotic dynamics in nonlinear systems. *Automatica*, **28**, 531–548.

Gibson, J.R., Beierlein, M. and Connors, B.W. (1999). Two networks of electrically coupled inhibitory neurons in neocortex. *Nature*, **402**, 75–79.

Gigout, S., Louvel, J., Kawasaki, H., D'Antuono, M., Armand, V., Kurcewicz, I., Olivier, A., Laschet, J., Turak, B., Devaux, B., Pumain, R. and Avoli, M. (2006). Effects of gap junction blockers on human neocortical synchronization. *Neurobiol. Dis.*, **22**, 496–508.

Gilmore, R., Letellier, C. and Lefranc, M. (2008). Chaos topology. *Scholarpedia*, **3**, 4592.

Glausier, J.R., Fish, K.N. and Lewis, D.A. (2014). Altered parvalbumin basket cell inputs in the dorsolateral prefrontal cortex of schizophrenia subjects. *Mol. Psychiatry*, **19**, 30–6.

Gnatkovsky, V., Librizzi, L., Trombin, F. and De Curtis, M. (2008). Fast activity at seizure onset is mediated by inhibitory circuits in the entorhinal cortex in vitro. *Ann. Neurol.*, **64**, 674–686.

Goldberg, E.M., Clark, B.D., Zagha, E., Nahmani, M., Erisir, A. and Rudy, B. (2008). K+ Channels at the Axon Initial Segment Dampen Near-Threshold Excitability of Neocortical Fast-Spiking GABAergic Interneurons. *Neuron*, **58**, 387–400.

Goldberg, J.H., Tamas, G. and Yuste, R. (2003). Ca2+ imaging of mouse neocortical interneurone dendrites: Ia-type K+ channels control action potential backpropagation. *J. Physiol.*, **551**, 49–65.

Goldowitz, D. (2010). Allen Reference Atlas. A Digital Color Brain Atlas of the C57BL/6J Male Mouse - by H. W. Dong. *Genes. Brain. Behav.*, **9**, 128.

Gollo, L.L., Mirasso, C., Sporns, O. and Breakspear, M. (2014). Mechanisms of zero-lag synchronization in cortical motifs. *PLoS Comput. Biol.*, **10**, e1003548.

Goodyer, A.V.N. (1968). Factors Influencing Myocardial Contractility. *Yale J. Biol. Med.*, **41**, 294.

Green, J.D. (1964). The hippocampus. *Physiol. Rev.*, **44**, 561–608.

Grenier, F., Timofeev, I. and Steriade, M. (2003). Neocortical very fast oscillations (ripples, 80-200 Hz) during seizures: intracellular correlates. *J. Neurophysiol.*, **89**, 841–852.

Guckenheimer, J. and Kuznetsov, Y.A. (2007). Fold-Hopf bifurcation. *Scholarpedia*, **2**, 1855.

Gupta, A., Wang, Y. and Markram, H. (2000). Organizing principles for a diversity of GABAergic interneurons and synapses in the neocortex. *Science*, **287**, 273–8.

Hablitz, J.J. and Heinemann, U. (1987). Extracellular K+ and Ca2+ changes during epileptiform discharges in the immature rat neocortex. *Dev. Brain Res.*, **36**, 299–303.

Hablitz, J.J. and Heinemann, U. (1989). Alterations in the microenvironment during spreading depression associated with epileptiform activity in the immature neocortex. *Dev. Brain Res.*, **46**, 243–252.

Hamm, J.P., Bobilev, A.M., Hayrynen, L.K., Hudgens-Haney, M.E., Oliver, W.T., Parker, D.A., McDowell, J.E., Buckley, P.A. and Clementz, B.A. (2015). Stimulus train duration but not attention moderates γ-band entrainment abnormalities in schizophrenia. *Schizophr. Res.*, **165**, 97–102.

Hammond, C., Bergman, H. and Brown, P. (2007). Pathological synchronization in Parkinson's disease: networks, models and treatments. *Trends Neurosci.*, **30**, 357–364.

Han, X. and Boyden, E.S. (2007). Multilpe-color optical activation, silencing, and desynchronization of neural activity, with single-spike temporal resolution. *PLoS One*, **2**.

Heinemann, U. and Dieter Lux, H. (1977). Ceiling of stimulus induced rises in extracellular potassium concentration in the cerebral cortex of cat. *Brain Res.*, **120**, 231–249.

Heinemann, U., Stabel, J. and Rausche, G. (1990). Activity-dependent ionic changes and neuronal plasticity in rat hippocampus. *Prog Brain Res*, **83**, 197–214.

Hermann, L. (1881). *Handbuch der physiologie*, vol. 6. FCW Vogel.

Herrmann, C.S. (2001). Human EEG responses to 1-100 Hz flicker: Resonance phenomena in visual cortex and their potential correlation to cognitive phenomena. *Exp. Brain Res.*, **137**, 346–353.

Hestrin, S. and Galarreta, M. (2005). Electrical synapses define networks of neocortical GABAergic neurons.

Hillyard, S.A., Vogel, E.K. and Luck, S.J. (1998). Sensory gain control (amplification) as a mechanism of selective attention: electrophysiological and neuroimaging evidence. *Philos. Trans. R. Soc. Lond. B. Biol. Sci.*, **353**, 1257–1270.

Hines, M.L. and Carnevale, N.T. (1997). The NEURON simulation environment. *Neural Comput.*, **9**, 1179–1209.

Hodgkin, A.L. and Huxley, A.F. (1952). A quantitative description of membrane current and its applications to conduction and excitation in nerve. *J. Physiol.*, **117**, 500–544.

Hodgkin, A.L. and Rushton, W.A.H. (1946). The electrical constants of a crustacean nerve fibre. *Proc. R. Soc. Med.*, **134**, 444–479.

Horton, J.C. and Adams, D.L. (2005). The cortical column: a structure without a function. *Philos. Trans. R. Soc. B Biol. Sci.*, **360**, 837–862.

Hu, H. and Jonas, P. (2014). A supercritical density of Na(+) channels ensures fast signaling in GABAergic interneuron axons. *Nat. Neurosci.*, **17**, 686–93.

Hu, H., Martina, M. and Jonas, P. (2010). Dendritic mechanisms underlying rapid synaptic activation of fast-spiking hippocampal interneurons. *Sci. (New York, NY)*, **327**, 52–58.

Hu, H., Gan, J. and Jonas, P. (2014). Interneurons. Fast-spiking, parvalbumin GABAergic interneurons: from cellular design to microcircuit function. *Science*, **345**, 1255263.

Huang, G., Zhang, D., Meng, J. and Zhu, X. (2011). Interactions between two neural populations: A mechanism of chaos and oscillation in neural mass model. *Neurocomputing*, **74**, 1026–1034.

Hutcheon, B. and Yarom, Y. (2000). Resonance, oscillation and the intrinsic frequency preferences of neurons. *Trends Neurosci.*, **23**, 216–222.

Isaacson, J.S. and Scanziani, M. (2011). How inhibition shapes cortical activity. *Neuron*, **72**, 231–243.

Ishizuka, S. and Hayashi, H. (1996). Chaotic and phase-locked responses of the somatosensory cortex to a periodic medial lemniscus stimulation in the anesthetized rat. *Brain Res.*, **723**, 46–60.

Izhikevich, E.M. (2007). *Dynamical systems in neuroscience*. MIT press.

Jadi, M., Polsky, A., Schiller, J. and Mel, B.W. (2012). Location-dependent effects of inhibition on local spiking in pyramidal neuron dendrites. *PLoS Comput. Biol.*, **8**.

Jansen, B.H. and Rit, V.G. (1995). Electroencephalogram and visual evoked potential generation in a mathematical model of coupled cortical columns. *Biol. Cybern.*, **73**, 357–366.

Janssen, M.J., Leiva-Salcedo, E. and Buonanno, A. (2012). Neuregulin directly decreases voltage-gated sodium current in hippocampal ErbB4-expressing interneurons. *J. Neurosci.*, **32**, 13889–95.

Jensen, M.S. and Yaari, Y. (1997). Role of intrinsic burst firing, potassium accumulation, and electrical coupling in the elevated potassium model of hippocampal epilepsy. *J. Neurophysiol.*, **77**, 1224–1233.

Jin, Y., Castellanos, A., Solis, E.R. and Potkin, S.G. (2000). EEG resonant responses in schizophrenia: A photic driving study with improved harmonic resolution. *Schizophr. Res.*, **44**, 213–220.

Jirsa, V.K., Sporns, O., Breakspear, M., Deco, G. and Mcintosh, A.R. (2010). Towards the virtual brain: Network modeling of the intact and the damaged brain. *Arch. Ital. Biol.*, **148**, 189–205.

Jirsa, V.K., Stacey, W.C., Quilichini, P.P., Ivanov, A.I. and Bernard, C. (2014). On the nature of seizure dynamics. *Brain*, **137**, 2210–2230.

Johnston and Wu (1995). Foundations of cellular neurophysiology. *MIT Press*, 676.

Jones, E.G. (2001). The thalamic matrix and thalamocortical synchrony.

Kaiser, M. (2011). A tutorial in connectome analysis: topological and spatial features of brain networks. *Neuroimage*, **57**, 892–907.

Kaiser, M. and Hilgetag, C.C. (2006). Nonoptimal component placement, but short processing paths, due to long-distance projections in neural systems. *PLoS Comput. Biol.*, **2**, 0805–0815.

Kandler, K. and Katz, L.C. (1995). Neuronal coupling and uncouplng in the developing nervous system. **5**, 98–105.

Karnani, M.M., Jackson, J., Ayzenshtat, I., Tucciarone, J., Manoocheri, K., Snider, W.G. and Yuste, R. (2016). Cooperative Subnetworks of Molecularly Similar Interneurons in Mouse Neocortex. *Neuron*, 1–15.

Kawaguchi, Y. (1993). Groupings of nonpyramidal and pyramidal cells with specific physiological and morphological characteristics in rat frontal cortex. *J. Neurophysiol.*, **69**, 416–431.

Kawaguchi, Y. and Kubota, Y. (1996). Physiological and morphological identification of somatostatin- or vasoactive intestinal polypeptide-containing cells among GABAergic cell subtypes in rat frontal cortex.

Kawaguchi, Y. and Kubota, Y. (1997). GABAergic cell subtypes and their synaptic connections in rat frontal cortex. *Cereb. Cortex*, **7**, 476–486.

Kawaguchi, Y. and Kubota, Y. (1998). Neurochemical features and synaptic connections of large physiologically-identified GABAergic cells in the rat frontal cortex. *Neuroscience*, **85**, 677–701.

Keller, A.J. and Martin, K.A.C. (2015). Local Circuits for Contrast Normalization and Adaptation Investigated with Two-Photon Imaging in Cat Primary Visual Cortex. *J. Neurosci.*, **35**, 10078–10087.

Kiebel, S.J., Daunizeau, J. and Friston, K.J. (2008). A hierarchy of time-scales and the brain. *PLoS Comput. Biol.*, **4**.

Kim, S.Y., Lim, W. and Kim, Y. (2001). Universal Bicritical Behavior of Period Doublings in Unidirectionally Coupled Oscillators. *Prog. Theor. Phys.*, **106**, 17–37.

Kisvarday, Z.F., Martin, K.A.C., Whitteridge, D. and Somogyi, P. (1985). Synaptic connections of intracellularly filled clutch cells: a type of small basket cell in the visual cortex of the cat. *J. Comp. Neurol.*, **241**, 111–37.

Kisvarday, Z.F., Beaulieu, C. and Eysel, U.T. (1993). Network of GABAergic large basket cells in cat visual cortex (area 18): Implication for lateral disinhibition. *J. Comp. Neurol.*, **327**, 398–415.

Klausberger, T. and Somogyi, P. (2008). Neuronal diversity and temporal dynamics: the unity of hippocampal circuit operations. *Science*, **321**, 53–7.

Klimesch, W. (1999). EEG alpha and theta oscillations reflect cognitive and memory performance: a review and analysis. *Brain Res. Rev.*, **29**, 169–195.

Koch, C. (2004). *Biophysics of computation: information processing in single neurons*. Oxford university press.

Konstantoudaki, X., Papoutsi, A., Chalkiadaki, K., Poirazi, P. and Sidiropoulou, K. (2014). Modulatory effects of inhibition on persistent activity in a cortical microcircuit model. *Front. Neural Circuits*, **8**, 7.

Kopell, N.J. and Ermentrout, B. (2004). Chemical and electrical synapses perform complementary roles in the synchronization of interneuronal networks. *Proc. Natl. Acad. Sci. U. S. A.*, **101**, 15482–15487.

Korn, S.J., Giacchino, J.L., Chamberlin, N.L. and Dingledine, R. (1987). Epileptiform burst activity induced by potassium in the hippocampus and its regulation by GABA-mediated inhibition. *J. Neurophysiol.*, **57**, 325–40.

Kubota, Y. (2014). Untangling GABAergic wiring in the cortical microcircuit. *Curr. Opin. Neurobiol.*, **26**, 7–14.

Kuhlman, S.J., Olivas, N.D., Tring, E., Ikrar, T., Xu, X. and Trachtenberg, J.T. (2013). A disinhibitory microcircuit initiates critical-period plasticity in the visual cortex. *Nature*, **501**, 543–6.

Kuznetsov, A., Kuznetsov, S. and Sataev, I.R. (1997). A variety of period-doubling universality classes in multi-parameter analysis of transition to chaos. *Phys. D*, **109**, 91–112.

Kuznetsov, S., Kuznetsov, A. and Sataev, I.R. (2005). Multiparameter Critical Situations, Universality and Scaling in Two-Dimensional Period-Doubling Maps. *J. Stat. Phys.*, **121**, 697–748.

Lakatos, P., Karmos, G., Mehta, A.D., Ulbert, I. and Schroeder, C.E. (2008). Entrainment of Neuronal Oscillations as a Mechanism of Attentional Selection. *Science (80-.).*, **320**, 110–113.

Larkum, M.E., Nevian, T., Sandler, M., Polsky, A. and Schiller, J. (2009). Synaptic integration in tuft dendrites of layer 5 pyramidal neurons: a new unifying principle. *Science*, **325**, 756–760.

Laurent, G. (2002). Olfactory network dynamics and the coding of multidimensional signals. *Nat. Rev. Neurosci.*, **3**, 884–895.

Lea-Carnall, C.A., Montemurro, M.A., Trujillo-Barreto, N.J., Parkes, L.M. and El-Deredy, W. (2016). Cortical Resonance Frequencies Emerge from Network Size and Connectivity. *PLoS Comput. Biol.*, **12**, e1004740.

LeBeau, F.E.N. (2013). Cortical network oscillations in Alzheimer's disease: insights from rodent models. *Drug Discov. Today Ther. Strateg.*, **10**, e79–e83.

Lee, S., Hjerling-Leffler, J., Zagha, E., Fishell, G. and Rudy, B. (2010). The largest group of superficial neocortical GABAergic interneurons expresses ionotropic serotonin receptors. *J. Neurosci.*, **30**, 16796–808.

Lee, S.H., Kwan, A.C., Zhang, S., Phoumthipphavong, V., Flannery, J.G., Masmanidis, S.C., Taniguchi, H., Huang, Z.J., Zhang, F., Boyden, E.S., Deisseroth, K. and Dan, Y. (2012). Activation of specific interneurons improves V1 feature selectivity and visual perception. *Nature*, **488**, 379–83.

Lee, S.H., Kwan, A.C. and Dan, Y. (2014). Interneuron subtypes and orientation tuning. *Nature*, **508**, E1–E2.

Letzkus, J.J., Wolff, S.B.E., Meyer, E.M.M., Tovote, P., Courtin, J., Herry, C. and Lüthi, A. (2011). A disinhibitory microcircuit for associative fear learning in the auditory cortex. *Nature*, **480**, 331–335.

Lewis, D.A., Hashimoto, T. and Volk, D.W. (2005). Cortical inhibitory neurons and schizophrenia. *Nat. Rev. Neurosci.*, **6**, 312–324.

Lewis, D.A., Curley, A.A., Glausier, J.R. and Volk, D.W. (2012). Cortical parvalbumin interneurons and cognitive dysfunction in schizophrenia. *Trends Neurosci.*, **35**, 57–67.

Lewis, T.J. and Rinzel, J. (2003). Dynamics of spiking neurons connected by both inhibitory and electrical coupling. *J. Comput. Neurosci.*, **14**, 283–309.

Li, L., Bischofberger, J. and Jonas, P. (2007). Differential gating and recruitment of P/Q-, N-, and R-type Ca2+ channels in hippocampal mossy fiber boutons. *J. Neurosci.*, **27**, 13420–9.

Libchaber, A., Laroche, C. and Fauve, S. (1982). Period doubling cascade in mercury, a quantitative measurement. *J. Phys. Lettres*, **43**, 211–216.

Linkenkaer-Hansen, K., Nikouline, V.V., Palva, J.M. and Ilmoniemi, R.J. (2001). Long-Range Temporal Correlations and Scaling Behavior in Human Brain Oscillations. *J. Neurosci.*, **21**, 1370–1377.

Litwin-Kumar, A., Rosenbaum, R. and Doiron, B. (2016). Inhibitory stabilization and visual coding in cortical circuits with multiple interneuron subtypes. *J. Neurophysiol.*, jn.00732.2015.

Lodge, D.J., Behrens, M.M. and Grace, A.A. (2009). A loss of parvalbumin-containing interneurons is associated with diminished oscillatory activity in an animal model of schizophrenia. *J. Neurosci.*, **29**, 2344–2354.

Lopes da Silva, F.H., Blanes, W., Kalitzin, S.N., Parra, J., Suffczynski, P. and Velis, D.N. (2003). Epilepsies as dynamical diseases of brain systems: basic models of the transition between normal and epileptic activity. *Epilepsia*, **44 Suppl 1**, 72–83.

Louvel, J., Papatheodoropoulos, C., Siniscalchi, A., Kurcewicz, I., Pumain, R., Devaux, B., Turak, B., Esposito, V., Villemeure, J.G. and Avoli, M. (2001). GABA-mediated synchronization in the human neocortex: Elevations in extracellular potassium and presynaptic mechanisms. *Neuroscience*, **105**, 803–813.

Lovett-Barron, M., Turi, G.F., Kaifosh, P., Lee, P.H., Bolze, F., Sun, X.H., Nicoud, J.F., Zemelman, B.V., Sternson, S.M. and Losonczy, A. (2012). Regulation of neuronal input transformations by tunable dendritic inhibition. *Nat. Neurosci.*, **15**, 423–30, S1–3.

Lui, J.H., Hansen, D.V. and Kriegstein, A.R. (2011). Development and evolution of the human neocortex. *Cell*, **146**, 18–36.

Lytton, W.W. (2008). Computer modelling of epilepsy. *Nat. Rev. Neurosci.*, **9**, 626–637.

Lytton, W.W., Contreras, D., Destexhe, A. and Steriade, M. (1997). Dynamic interactions determine partial thalamic quiescence in a computer network model of spike-and-wave seizures. *J. Neurophysiol.*, **77**, 1679–96.

Ma, Y., Hu, H., Berrebi, A.S., Mathers, P.H. and Agmon, A. (2006). Distinct subtypes of somatostatin-containing neocortical interneurons revealed in transgenic mice. *J. Neurosci.*, **26**, 5069–82.

Makin, V.S., Makin, R.S., Vorobyev, A.Y. and Guo, C. (2008). Dissipative nanostructures and Feigenbaum's universality in the Metal-high-power ultrashort-pulsed polarized radiation nonequilibrium nonlinear dynamical system. *Tech. Phys. Lett.*, **34**, 387–390.

Malmierca, M.S., Hernández, O. and Rees, A. (2005). Intercollicular commissural projections modulate neuronal responses in the inferior colliculus. *Eur. J. Neurosci.*, **21**, 2701–2710.

Marín-Padilla, M. (1998). Cajal-Retzius cells and the development of the neocortex. *Trends Neurosci.*, **21**, 64–71.

Markram, H. (2006). The blue brain project. *Nat. Rev. Neurosci.*, **7**, 153–60.

Markram, H., Toledo-Rodriguez, M., Wang, Y., Gupta, A., Silberberg, G. and Wu, C. (2004). Interneurons of the neocortical inhibitory system. *Nat. Rev. Neurosci.*, **5**, 793–807.

Markram, H., Muller, E., Ramaswamy, S., Reimann, M.W., Abdellah, M., Sanchez, C.A., Ailamaki, A., Alonso-Nanclares, L., Antille, N., Arsever, S., Kahou, G.A.A., Berger, T.K., Bilgili, A., Buncic, N., Chalimourda, A., Chindemi, G., Courcol, J.D., Delalondre, F., Delattre, V., Druckmann, S., Dumusc, R., Dynes, J., Eilemann, S., Gal, E., Gevaert, M.E., Ghobril, J.P., Gidon, A., Graham, J.W., Gupta, A., Haenel, V., Hay, E., Heinis, T., Hernando, J.B., Hines, M., Kanari, L., Keller, D., Kenyon, J., Khazen, G., Kim, Y., King, J.G., Kisvarday, Z., Kumbhar, P., Lasserre, S., Le Bé, J.V., Magalhães, B.R.C., Merchán-Pérez, A., Meystre, J., Morrice, B.R., Muller, J., Muñoz-Céspedes, A., Muralidhar, S., Muthurasa, K., Nachbaur, D., Newton, T.H., Nolte, M., Ovcharenko, A., Palacios, J., Pastor, L., Perin, R., Ranjan, R., Riachi, I., Rodríguez, J.R., Riquelme, J.L., Rössert, C., Sfyrakis, K., Shi, Y., Shillcock, J.C., Silberberg, G., Silva, R., Tauheed, F., Telefont, M., Toledo-Rodriguez, M., Tränkler, T., Van Geit, W., Díaz, J.V., Walker, R., Wang, Y., Zaninetta, S.M., Defelipe, J., Hill, S.L., Segev, I. and Schürmann, F. (2015). Reconstruction and Simulation of Neocortical Microcircuitry. *Cell*, **163**, 456–492.

Martina, M. and Jonas, P. (1997). Functional differences in Na+ channel gating between fast-spiking interneurones and principal neurones of rat hippocampus. *J. Physiol.*, **505**, 593–603.

Martina, M., Schultz, J.H., Ehmke, H., Monyer, H. and Jonas, P. (1998). Functional and molecular differences between voltage-gated K+ channels of fast-spiking interneurons and pyramidal neurons of rat hippocampus. *J. Neurosci.*, **18**, 8111–8125.

Martina, M., Vida, I. and Jonas, P. (2000). Distal initiation and active propagation of action potentials in interneuron dendrites. *Science*, **287**, 295–300.

Mashimo, T., Ohmori, I., Ouchida, M., Ohno, Y., Tsurumi, T., Miki, T., Wakamori, M., Ishihara, S., Yoshida, T., Takizawa, A., Kato, M., Hirabayashi, M., Sasa, M., Mori, Y. and Serikawa, T. (2010). A Missense Mutation of the Gene Encoding Voltage-Dependent Sodium Channel (Nav1.1) Confers Susceptibility to Febrile Seizures in Rats. *J. Neurosci.*, **30**, 5744–5753.

Masuda, N. and Aihara, K. (2004). Global and local synchrony of coupled neurons in small-world networks. *Biol. Cybern.*, **90**, 302–309.

Masuda, N. and Kori, H. (2007). Formation of feedforward networks and frequency synchrony by spike-timing-dependent plasticity. *J. Comput. Neurosci.*, **22**, 327–345.

McBain, C.J., Traynelis, S.F. and Dingledine, R. (1990). Regional variation of extracellular space in the hippocampus. *Science*, **249**, 674–677.

McCormick, D.A., Connors, B.W., Lighthall, J.W. and Prince, D.A. (1985). Comparative electrophysiology of pyramidal and sparsely spiny stellate neurons of the neocortex. *J. Neurophysiol.*, **54**, 782–806.

McDonald, J.H. (2009). *Handbook of biological statistics*, vol. 2. Sparky House Publishing Baltimore, MD.

Mellios, N., Huang, H.S., Baker, S.P., Galdzicka, M., Ginns, E. and Akbarian, S. (2009). Molecular Determinants of Dysregulated GABAergic Gene Expression in the Prefrontal Cortex of Subjects with Schizophrenia. *Biol. Psychiatry*, **65**, 1006–1014.

Meunier, D., Lambiotte, R., Fornito, A., Ersche, K.D. and Bullmore, E.T. (2009). Hierarchical modularity in human brain functional networks. *Front. Neuroinform.*, **3**, 37.

Middleton, S.J., Racca, C., Cunningham, M.O., Traub, R.D., Monyer, H., Knöpfel, T., Schofield, I.S., Jenkins, A. and Whittington, M.A. (2008). High-Frequency Network Oscillations in Cerebellar Cortex. *Neuron*, **58**, 763–774.

Mitchell, S.J. and Silver, R.A. (2003). Shunting inhibition modulates neuronal gain during synaptic excitation. *Neuron*, **38**, 433–45.

Montbrió, E., Pazó, D. and Roxin, A. (2015). Macroscopic Description for Networks of Spiking Neurons. *Phys. Rev. X*, **5**, 021028.

Monteiro, L., Bussab, M. and Berlinck, J.C. (2002). Analytical results on a Wilson-Cowan neuronal network modified model. *J. Theor. Biol.*, **219**, 83–91.

Moody, W.J., Futamachi, K.J. and Prince, D.A. (1974). Extracellular potassium activity during epileptogenesis. *Exp. Neurol.*, **42**, 248–263.

Moran, R.J., Kiebel, S.J., Stephan, K.E., Reilly, R.B., Daunizeau, J. and Friston, K.J. (2007). A neural mass model of spectral responses in electrophysiology. *Neuroimage*, **37**, 706–720.

Morris, H.M., Hashimoto, T. and Lewis, D.A. (2008). Alterations in somatostatin mRNA expression in the dorsolateral prefrontal cortex of subjects with schizophrenia or schizoaffective disorder. *Cereb. Cortex*, **18**, 1575–1587.

Mountcastle, V. (1957). Modality and topographic properties of single neurons of cat's somatic sensory cortex. *J. Neurophysiol.*, **20**, 408–34.

Mountcastle, V. (1997). The columnar organization of the cerebral cortex. *Brain*, **120**, 701–722.

Moyer, K.E., Davis, A., Saggers, G.C., Mackay, D.R. and Ehrlich, H.P. (2002). Wound healing: the role of gap junctional communication in rat granulation tissue maturation. *Exp. Mol. Pathol.*, **72**, 10–16.

Mruczek, R.E.B. and Sheinberg, D.L. (2012). Stimulus selectivity and response latency in putative inhibitory and excitatory neurons of the primate inferior temporal cortex. *J. Neurophysiol.*, **108**, 2725–2736.

Nakazawa, K., Zsiros, V., Jiang, Z., Nakao, K., Kolata, S., Zhang, S. and Belforte, J.E. (2012). GABAergic interneuron origin of schizophrenia pathophysiology. *Neuropharmacology*, **62**, 1574–1583.

Nilsen, K.E., Kelso, A.R.C. and Cock, H.R. (2006). Antiepileptic Effect of Gap-junction Blockers in a Rat Model of Refractory Focal Cortical Epilepsy. *Epilepsia*, **47**, 1169–1175.

Nomura, M., Fukai, T. and Aoyagi, T. (2003). Synchrony of fast-spiking interneurons interconnected by GABAergic and electrical synapses. *Neural Comput*, **15**, 2179–2198.

Ogiwara, I., Miyamoto, H., Morita, N., Atapour, N., Mazaki, E., Inoue, I., Takeuchi, T., Itohara, S., Yanagawa, Y., Obata, K., Furuichi, T., Hensch, T.K. and Yamakawa, K. (2007). Nav1.1 localizes to axons of parvalbumin-positive inhibitory interneurons: a circuit basis for epileptic seizures in mice carrying an Scn1a gene mutation. *J. Neurosci.*, **27**, 5903–5914.

Ogiwara, I., Iwasato, T., Miyamoto, H., Iwata, R., Yamagata, T., Mazaki, E., Yanagawa, Y., Tamamaki, N., Hensch, T.K., Itohara, S. and Yamakawa, K. (2013).

Nav1.1 haploinsufficiency in excitatory neurons ameliorates seizure-associated sudden death in a mouse model of dravet syndrome. *Hum. Mol. Genet.*, **22**, 4784–4804.

Oláh, S., Füle, M., Komlósi, G., Varga, C., Báldi, R., Barzó, P. and Tamás, G. (2009). Regulation of cortical microcircuits by unitary GABA-mediated volume transmission. *Nature*, **461**, 1278–81.

Overstreet-Wadiche, L. and McBain, C.J. (2015). Neurogliaform cells in cortical circuits. *Nat. Rev. Neurosci.*, **16**, 458–468.

Palva, J.M., Palva, S. and Kaila, K. (2005). Phase synchrony among neuronal oscillations in the human cortex. *J. Neurosci.*, **25**, 3962–3972.

Papasavvas, C.A., Wang, Y., Trevelyan, A.J. and Kaiser, M. (2015). Gain control through divisive inhibition prevents abrupt transition to chaos in a neural mass model. *Phys. Rev. E*, **92**, 032723.

Pastoll, H., Solanka, L., van Rossum, M.C.W. and Nolan, M.F. (2013). Feedback Inhibition Enables Theta-Nested Gamma Oscillations and Grid Firing Fields. *Neuron*, **77**, 141–154.

Peinado, A., Yuste, R. and Katz, L.C. (1993). Extensive dye coupling between rat neocortical neurons during the period of circuit formation. *Neuron*, **10**, 103–114.

Penttonen, M. and Buzsáki, G. (2003). Natural logarithmic relationship between brain oscillators. *Thalamus Relat. Syst.*, **2**, 145–152.

Pereda, A.E. (2014). Electrical synapses and their functional interactions with chemical synapses. *Nat Rev Neurosci*, **15**, 250–263.

Pereda, A.E. and Faber, D.S. (1996). Activity-Dependent Short-Term Enhancement of Intercellular Coupling. *J. Neurosci.*, **16**, 983–992.

Pereda, A.E., Curti, S., Hoge, G., Cachope, R., Flores, C.E. and Rash, J.E. (2013). Gap junction-mediated electrical transmission: Regulatory mechanisms and plasticity. *Biochim. Biophys. Acta - Biomembr.*, **1828**, 134–146.

Perez Velazquez, J.L., Cortez, M.A., Snead, O. and Wennberg, R. (2003). Dynamical regimes underlying epileptiform events: role of instabilities and bifurcations in brain activity. *Phys. D Nonlinear Phenom.*, **186**, 205–220.

Peters, A. (1990). The axon terminals of vasoactive intestinal polypeptide (VIP)-containing bipolar cells in rat visual cortex. *J. Neurocytol.*, **19**, 672–685.

Peters, A. and Jones, E.G. (1984). Cerebral cortex. Vol. I: Cellular components of cerebral cortex.

Peyrache, A., Dehghani, N., Eskandar, E.N., Madsen, J.R., Anderson, W.S., Donoghue, J.A., Hochberg, L.R., Halgren, E., Cash, S.S. and Destexhe, A. (2012). Spatiotemporal dynamics of neocortical excitation and inhibition during human sleep. *Proc. Natl. Acad. Sci. U. S. A.*, **109**, 1731–6.

Pfeffer, C.K. (2014). Inhibitory neurons: Vip cells hit the brake on inhibition. *Curr. Biol.*, **24**, R18–R20.

Pfeffer, C.K., Xue, M., He, M., Huang, Z.J. and Scanziani, M. (2013). Inhibition of inhibition in visual cortex: the logic of connections between molecularly distinct interneurons. *Nat. Neurosci.*, **16**, 1068–76.

Pfeuty, B., Golomb, D., Mato, G. and Hansel, D. (2007). Inhibition potentiates the synchronizing action of electrical synapses. *Front. Comput. Neurosci.*, **1**, 8.

Piccolino, M., Neyton, J. and Gerschenfeld, H.M. (1984). Decrease of gap junction permeability induced by dopamine and cyclic adenosine 3':5'-monophosphate in horizontal cells of turtle retina. *J. Neurosci.*, **4**, 2477–88.

Pike, F.G., Goddard, R.S., Suckling, J.M., Ganter, P., Kasthuri, N. and Paulsen, O. (2000). Distinct frequency preferences of different types of rat hippocampal neurones in response to oscillatory input currents. *J. Physiol.*, **529 Pt 1**, 205–213.

Pinto, D.J., Brumberg, J.C., Simons, D.J. and Ermentrout, B. (1996). A quantitative population model of whisker barrels: re-examining the Wilson-Cowan equations. *J. Comput. Neurosci.*, **3**, 247–64.

Pittman-Polletta, B.R., Kocsis, B., Vijayan, S., Whittington, M.A. and Kopell, N.J. (2015). Brain Rhythms Connect Impaired Inhibition to Altered Cognition in Schizophrenia. *Biol. Psychiatry*, **77**, 1020–1030.

Porter, J.T., Cauli, B., Staiger, J.F., Lambolez, B., Rossier, J. and Audinat, E. (1998). Properties of bipolar VIPergic interneurons and their excitation by pyramidal neurons in the rat neocortex. *Eur. J. Neurosci.*, **10**, 3617–3628.

Pouille, F. and Scanziani, M. (2001). Enforcement of temporal fidelity in pyramidal cells by somatic feed-forward inhibition. *Science*, **293**, 1159–63.

Pouille, F., Marin-Burgin, A., Adesnik, H., Atallah, B.V. and Scanziani, M. (2009). Input normalization by global feedforward inhibition expands cortical dynamic range. *Nat. Neurosci.*, **12**, 1577–85.

Pouille, F., Watkinson, O., Scanziani, M. and Trevelyan, A.J. (2013). The contribution of synaptic location to inhibitory gain control in pyramidal cells. *Physiol. Rep.*, **1**, e00067.

Powell, T.P.S. and Mountcastle, V. (1959). Some aspects of the functional organization of the cortex of the postcentral gyrus of the monkey: a correlation of findings obtained in a single unit analysis with cytoarchitecture. *Bull Johns Hopkins Hosp*, **105**.

Prescott, S.A. and De Koninck, Y. (2003). Gain control of firing rate by shunting inhibition: roles of synaptic noise and dendritic saturation. *Proc. Natl. Acad. Sci. U. S. A.*, **100**, 2076–81.

Prönneke, A., Scheuer, B., Wagener, R.J., Möck, M., Witte, M. and Staiger, J.F. (2015). Characterizing VIP neurons in the barrel cortex of VIPcre/tdTomato mice reveals layer-specific differences. *Cereb. Cortex*, **25**, 4854–4868.

Qiu, C., Shivacharan, R.S., Zhang, M. and Durand, D.M. (2015). Can Neural Activity Propagate by Endogenous Electrical Field? *J. Neurosci.*, **35**, 15800–15811.

Quian Quiroga, R., Kraskov, A., Kreuz, T. and Grassberger, P. (2002). Performance of different synchronization measures in real data: A case study on electroencephalographic signals. *Phys. Rev. E*, **65**, 041903.

Rakic, P. (2009). Evolution of the neocortex: a perspective from developmental biology. *Nat. Rev. Neurosci.*, **10**, 724–735.

Rall, W. (1989). Cable theory for dendritic neurons. In *Methods Neuronal Model.*, 9–62.

Rash, J.E., Yasumura, T., Davidson, K.G., Furman, C.S., Dudek, F.E. and Nagy, J.I. (2001). Identification of cells expressing Cx43, Cx30, Cx26, Cx32 and Cx36 in gap junctions of rat brain and spinal cord. *Cell Commun. Adhes.*, **8**, 315–20.

Ren, J.Q., Aika, Y., Heizmann, C.W. and Kosaka, T. (1992). Quantitative analysis of neurons and glial cells in the rat somatosensory cortex, with special reference to GABAergic neurons and parvalbumin-containing neurons. *Exp. Brain Res.*, **92**, 1–14.

Renart, A., Brunel, N. and Wang, X.J. (2004). *Mean field theory of irregularly spiking neuronal populations and working memory in recurrent cortical networks*.

Rice, D.M., Potkin, S.G., Jin, Y., Isenhart, R., Heh, C.W.C., Sramek, J., Costa, J. and Sandman, C.A. (1989). EEG alpha photic driving abnormalities in chronic schizophrenia. *Psychiatry Res.*, **30**, 313–324.

Rodrigues, S., Barton, D., Szalai, R., Benjamin, O., Richardson, M.P. and Terry, J.R. (2009). Transitions to spike-wave oscillations and epileptic dynamics in a human cortico-thalamic mean-field model. *J. Comput. Neurosci.*, **27**, 507–26.

Roopun, A.K., Kramer, M.A., Carracedo, L.M., Kaiser, M., Davies, C.H., Traub, R.D., Kopell, N.J. and Whittington, M.A. (2008a). Period concatenation underlies interactions between gamma and beta rhythms in neocortex. *Front. Cell. Neurosci.*, **2**, 1.

Roopun, A.K., Kramer, M.A., Carracedo, L.M., Kaiser, M., Davies, C.H., Traub, R.D., Kopell, N.J. and Whittington, M.A. (2008b). Temporal Interactions between Cortical Rhythms. *Front. Neurosci.*, **2**, 145–54.

Rossignol, E., Kruglikov, I., Van Den Maagdenberg, A.M.J.M., Rudy, B. and Fishell, G. (2013). CaV2.1 ablation in cortical interneurons selectively impairs fast-spiking basket cells and causes generalized seizures. *Ann. Neurol.*, **74**, 209–222.

Rössler, O. (1976). An equation for continuous chaos. *Phys. Lett. A*, **57**, 397.

Rouveix, B., Bricaire, F., Michon, C., Franssen, G., Lebras, J., Bernard, J., Ajana, F., Vienne, J.L. and Others (1989). Mefloquine and an acute brain syndrome. *Ann. Intern. Med.*, **110**, 577–578.

Rozental, R., Srinivas, M. and Spray, D.C. (2001). How to close a gap junction channel. *Connexin Methods Protoc.*, 447–476.

Rudy, B. and McBain, C.J. (2001). Kv3 channels: Voltage-gated K+ channels designed for high-frequency repetitive firing.

Sanchez-Vives, M.V. and McCormick, D.A. (2000). Cellular and network mechanisms of rhythmic recurrent activity in neocortex. *Nat. Neurosci.*, **3**, 1027–34.

Schaefer, A.T., Larkum, M.E., Sakmann, B. and Roth, A. (2003). Coincidence detection in pyramidal neurons is tuned by their dendritic branching pattern. *J. Neurophysiol.*, **89**, 3143–3154.

Schevon, C.A., Weiss, S.A., McKhann, G., Goodman, R.R., Yuste, R., Emerson, R.G. and Trevelyan, A.J. (2012). Evidence of an inhibitory restraint of seizure activity in humans. *Nat. Commun.*, **3**, 1060.

Schmitz, D., Schuchmann, S., Fisahn, A., Draguhn, A., Buhl, E.H., Petrasch-Parwez, E., Dermietzel, R., Heinemann, U. and Traub, R.D. (2001). Axo-axonal coupling: A novel mechanism for ultrafast neuronal communication. *Neuron*, **31**, 831–840.

Schnitzler, A. and Gross, J. (2005). Normal and pathological oscillatory communication in the brain. *Nat. Rev. Neurosci.*, **6**, 285–96.

Schwab, K., Ligges, C., Jungmann, T., Hilgenfeld, B., Haueisen, J. and Witte, H. (2006). Alpha entrainment in human electroencephalogram and magnetoencephalogram recordings. *Neuroreport*, **17**, 1829–33.

Schwaller, B., Tetko, I.V., Tandon, P., Silveira, D.C., Vreugdenhil, M., Henzi, T., Potier, M.C., Celio, M.R. and Villa, A.E.P. (2004). Parvalbumin deficiency affects network properties resulting in increased susceptibility to epileptic seizures. *Mol. Cell. Neurosci.*, **25**, 650–63.

Schwartz, O. and Simoncelli, E.P. (2001). Natural signal statistics and sensory gain control. *Nat. Neurosci.*, **4**, 819–25.

Sessolo, M., Marcon, I., Bovetti, S., Losi, G., Cammarota, M., Ratto, G.M., Fellin, T. and Carmignoto, G. (2015). Parvalbumin-Positive Inhibitory Interneurons Oppose Propagation But Favor Generation of Focal Epileptiform Activity. *J. Neurosci.*, **35**, 9544–9557.

Seybold, B.A., Phillips, E.A.K., Schreiner, C.E. and Hasenstaub, A.R. (2015). Inhibitory Actions Unified by Network Integration. *Neuron*, **87**, 1181–1192.

Shepherd, G.M. (2003). *The synaptic organization of the brain*. Oxford University Press.

Sherman, S.M. and Guillery, R.W. (1998). On the actions that one nerve cell can have on another: distinguishing "drivers" from "modulators". *Proc. Natl. Acad. Sci. U. S. A.*, **95**, 7121–6.

Shu, Y., Hasenstaub, A.R. and McCormick, D.A. (2003). Turning on and off recurrent balanced cortical activity. *Nature*, **423**.

Silver, R.A. (2010). Neuronal arithmetic. *Nat. Rev. Neurosci.*, **11**, 474–89.

Simon, A., Oláh, S., Molnár, G., Szabadics, J. and Tamás, G. (2005). Gap-junctional coupling between neurogliaform cells and various interneuron types in the neocortex. *J. Neurosci.*, **25**, 6278–6285.

Sims, S.M., Daniel, E.E. and Garfield, R.E. (1982). Improved electrical coupling in uterine smooth muscle is associated with increased numbers of gap junctions at parturition. *J. Gen. Physiol.*, **80**, 353–375.

Smith, M. and Pereda, A.E. (2003). Chemical synaptic activity modulates nearby electrical synapses. *Proc. Natl. Acad. Sci. U. S. A.*, **100**, 4849–54.

Snyders, J., Knoth, K.M., Roberds, S.L. and Tamkun, M.M. (1992). Time-, voltage-, and state-dependent block by quinidine of a cloned human cardiac potassium channel. *Mol. Pharmacol.*, **41**, 322–330.

Sohal, V.S., Zhang, F., Yizhar, O. and Deisseroth, K. (2009). Parvalbumin neurons and gamma rhythms enhance cortical circuit performance. *Nature*, **459**, 698–702.

Somjen, G.G. (2004). *Ions in the brain: normal function, seizures, and stroke*. Oxford University Press.

Somjen, G.G. and Giacchino, J.L. (1985). Potassium and calcium concentrations in interstitial fluid of hippocampal formation during paroxysmal responses. *J. Neurophysiol.*, **53**, 1098–108.

Somogyi, P. and Klausberger, T. (2005). Defined types of cortical interneurone structure space and spike timing in the hippocampus. *J. Physiol.*, **562**, 9–26.

Somogyi, P., Tamás, G., Lujan, R. and Buhl, E.H. (1998). Salient features of synaptic organisation in the cerebral cortex. In *Brain Res. Rev.*, vol. 26, 113–135.

Sparta, D.R., Hovelsø, N., Mason, A.O., Kantak, P.A., Ung, R.L., Decot, H.K. and Stuber, G.D. (2014). Activation of prefrontal cortical parvalbumin interneurons facilitates extinction of reward-seeking behavior. *J. Neurosci.*, **34**, 3699–705.

Spiegler, A., Knösche, T.R., Schwab, K., Haueisen, J. and Atay, F.M. (2011). Modeling brain resonance phenomena using a neural mass model. *PLoS Comput. Biol.*, **7**, e1002298.

Sprott, J. (1994). Some simple chaotic flows. *Phys. Rev. E*, **50**, R647.

Srinivas, M., Hopperstad, M.G. and Spray, D.C. (2001). Quinine blocks specific gap junction channel subtypes. *Proc. Natl. Acad. Sci. U. S. A.*, **98**, 10942–7.

Stam, C.J., van der Made, Y., Pijnenburg, Y.A.L. and Scheltens, P. (2003). EEG synchronization in mild cognitive impairment and Alzheimer's disease. *Acta Neurol. Scand.*, **108**, 90–96.

Stark, E., Eichler, R., Roux, L., Fujisawa, S., Rotstein, H.G. and Buzsáki, G. (2013). Inhibition-Induced theta resonance in cortical circuits. *Neuron*, **80**, 1263–1276.

Steriade, M. (1999). Coherent oscillations and short-term plasticity in corticothalamic networks.

Steriade, M. and Contreras, D. (1998). Spike-Wave Complexes and Fast Components of Cortically Generated Seizures. I. Role of Neocortex and Thalamus. *J. Neurophysiol.*, **80**, 1439–1455.

Steriade, M., Nuñez, A. and Amzica, F. (1993). A novel slow (< 1 Hz) oscillation of neocortical neurons in vivo: depolarizing and hyperpolarizing components. *J. Neurosci.*, **13**, 3252–3265.

Strogatz, S.H. (1994). *Nonlinear dynamics and chaos: with applications to physics, biology and chemistry*. Perseus Books, Reading.

Stuart, G.J. and Sakmann, B. (1994). Active propagation of somatic action potentials into neocortical pyramidal cell dendrites. *Nature*, **367**, 69–72.

Suffczynski, P., Kalitzin, S.N. and Lopes da Silva, F.H. (2004). Dynamics of non-convulsive epileptic phenomena modeled by a bistable neuronal network. *Neuroscience*, **126**, 467–84.

Swadlow, H.A. and Waxman, S.G. (2012). Axonal conduction delays. *Scholarpedia*, **7**, 1451.

Szabadics, J., Varga, C., Molnár, G., Oláh, S., Barzó, P. and Tamás, G. (2006). Excitatory effect of GABAergic axo-axonic cells in cortical microcircuits. *Science*, **311**, 233–5.

Tabak, J., O'Donovan, M.J. and Rinzel, J. (2006). Differential control of active and silent phases in relaxation models of neuronal rhythms. *J. Comput. Neurosci.*, **21**, 307–28.

Tabak, J., Rinzel, J. and Bertram, R. (2011). Quantifying the relative contributions of divisive and subtractive feedback to rhythm generation. *PLoS Comput. Biol.*, **7**, e1001124.

Tan, G.H., Liu, Y.Y., Hu, X.L., Yin, D.M., Mei, L. and Xiong, Z.Q. (2012). Neuregulin 1 represses limbic epileptogenesis through ErbB4 in parvalbumin-expressing interneurons. *Nat. Neurosci.*, **15**, 258–66.

Taniguchi, H., Lu, J. and Huang, Z.J. (2013). The spatial and temporal origin of chandelier cells in mouse neocortex. *Science*, **339**, 70–4.

Testa, J., Pérez, J. and Jeffries, C. (1982). Evidence for universal chaotic behavior of a driven nonlinear oscillator. *Phys. Rev. Lett.*, **48**, 714.

Thomson, A.M. and Bannister, A.P. (2003). Interlaminar connections in the neocortex. *Cereb. Cortex*, **13**, 5–14.

Thut, G., Veniero, D., Romei, V., Miniussi, C., Schyns, P. and Gross, J. (2011). Rhythmic TMS causes local entrainment of natural oscillatory signatures. *Curr. Biol.*, **21**, 1176–1185.

Timofeev, I., Bazhenov, M., Sejnowski, T.J. and Steriade, M. (2002). Cortical hyperpolarization-activated depolarizing current takes part in the generation of focal paroxysmal activities. *Proc. Natl. Acad. Sci. U. S. A.*, **99**, 9533–9537.

Tort, A.B.L., Kramer, M.A., Thorn, C., Gibson, D.J., Kubota, Y., Graybiel, A.M. and Kopell, N.J. (2008). Dynamic cross-frequency couplings of local field potential oscillations in rat striatum and hippocampus during performance of a T-maze task. *Proc. Natl. Acad. Sci. U. S. A.*, **105**, 20517–20522.

Tort, A.B.L., Komorowski, R.W., Manns, J.R., Kopell, N.J. and Eichenbaum, H. (2009). Theta-gamma coupling increases during the learning of item-context associations. *Proc. Natl. Acad. Sci.*, **106**, 20942–20947.

Tovar, K.R., Maher, B.J. and Westbrook, G.L. (2009). Direct actions of carbenoxolone on synaptic transmission and neuronal membrane properties. *J. Neurophysiol.*, **102**, 974–978.

Tremblay, R., Lee, S. and Rudy, B. (2016). GABAergic Interneurons in the Neocortex: From Cellular Properties to Circuits. *Neuron*, **91**, 260–292.

Tresser, C., Coullet, P. and de Faria, E. (2014). Period doubling. *Scholarpedia*, **9**, 3958.

Treue, S. and Martinez-Trujillo, J.C. (1999). Feature-based attention influences motion processing gain in macaque visual cortex. *Nature*, **399**, 575–579.

Trevelyan, A.J. (2009). The direct relationship between inhibitory currents and local field potentials. *J. Neurosci.*, **29**, 15299–15307.

Trevelyan, A.J. (2016). Do Cortical Circuits Need Protecting from Themselves? *Trends Neurosci.*, **39**, 502–511.

Trevelyan, A.J., Sussillo, D., Watson, B.O. and Yuste, R. (2006). Modular propagation of epileptiform activity: evidence for an inhibitory veto in neocortex. *J. Neurosci.*, **26**, 12447–55.

Trevelyan, A.J., Bruns, W., Mann, E.O., Crepel, V. and Scanziani, M. (2013). The information content of physiological and epileptic brain activity. *J. Physiol.*, **591**, 799–805.

Trotter, Y. and Celebrini, S. (1999). Gaze direction controls response gain in primary visual-cortex neurons. *Nature*, **398**, 239–242.

Tsodyks, M.V., Skaggs, W., Sejnowski, T.J. and McNaughton, B. (1997). Paradoxical effects of external modulation of inhibitory interneurons. *J. Neurosci.*, **17**, 4382–4388.

Uhlhaas, P.J. and Singer, W. (2006). Neural Synchrony in Brain Disorders: Relevance for Cognitive Dysfunctions and Pathophysiology. *Neuron*, **52**, 155–168.

Uhlhaas, P.J. and Singer, W. (2010). Abnormal neural oscillations and synchrony in schizophrenia. *Nat. Rev. Neurosci.*, **11**, 100–13.

Uusisaari, M., Smirnov, S., Voipio, J. and Kaila, K. (2002). Spontaneous epileptiform activity mediated by GABAA receptors and gap junctions in the rat hippocampal slice following long-term exposure to GABAB antagonists. *Neuropharmacology*, **43**, 563–572.

Uva, L., Avoli, M. and De Curtis, M. (2009). Synchronous GABAA-receptor-dependent potentials in limbic areas of the in-vitro isolated adult guinea pig brain. *Eur. J. Neurosci.*, **29**, 911–920.

Vergara, C., Latorre, R., Marrion, N.V. and Adelman, J.P. (1998). Calcium-activated potassium channels. *Curr. Opin. Neurobiol.*, **8**, 321–329.

Verselis, V.K., Ginter, C.S. and Bargiello, T.A. (1994). Opposite voltage gating polarities of two closely related connexins. *Nature*, **368**, 348–351.

Vessey, J.P., Lalonde, M.R., Mizan, H.A., Welch, N.C., Kelly, M.E.M. and Barnes, S. (2004). Carbenoxolone inhibition of voltage-gated Ca channels and synaptic transmission in the retina. *J. Neurophysiol.*, **92**, 1252–1256.

Vicente, R., Gollo, L.L., Mirasso, C.R., Fischer, I. and Pipa, G. (2008). Dynamical relaying can yield zero time lag neuronal synchrony despite long conduction delays. *Proc. Natl. Acad. Sci.*, **105**, 17157–17162.

Vida, I., Bartos, M. and Jonas, P. (2006). Shunting inhibition improves robustness of gamma oscillations in hippocampal interneuron networks by homogenizing firing rates. *Neuron*, **49**, 107–117.

Vierling-Claassen, D., Siekmeier, P., Stufflebeam, S. and Kopell, N.J. (2008). Modeling GABA alterations in schizophrenia: a link between impaired inhibition and altered gamma and beta range auditory entrainment. *J. Neurophysiol.*, **99**, 2656–71.

Viriyopase, A., Bojak, I., Zeitler, M. and Gielen, S. (2012). When Long-Range Zero-Lag Synchronization is Feasible in Cortical Networks. *Front. Comput. Neurosci.*, **6**, 1–22.

Vogels, T.P. and Abbott, L.F. (2005). Signal propagation and logic gating in networks of integrate-and-fire neurons. *J. Neurosci.*, **25**, 10786–10795.

Vogels, T.P., Rajan, K. and Abbott, L.F. (2005). Neural network dynamics. *Annu. Rev. Neurosci.*, **28**, 357–76.

Vogels, T.P., Sprekeler, H., Zenke, F., Clopath, C. and Gerstner, W. (2011). Inhibitory plasticity balances excitation and inhibition in sensory pathways and memory networks. *Science*, **334**, 1569–73.

Vogels, T.P., Froemke, R.C., Doyon, N., Gilson, M., Haas, J.S., Liu, R., Maffei, A., Miller, P., Wierenga, C.J., Woodin, M.A., Zenke, F. and Sprekeler, H. (2013). Inhibitory synaptic plasticity: spike timing-dependence and putative network function. *Front. Neural Circuits*, **7**, 119.

von der Malsburg, C. (1995). Binding in models of perception and brain function. *Curr. Opin. Neurobiol.*, **5**, 520–526.

von Stein, A., Chiang, C. and König, P. (2000). Top-down processing mediated by interareal synchronization. *Proc. Natl. Acad. Sci. U. S. A.*, **97**, 14748–14753.

Vu, E.T. and Krasne, F.B. (1992). Evidence for a computational distinction between proximal and distal neuronal inhibition. *Science (80-.).*, **255**, 1710–2.

Walsh, J.P., Cepeda, C., Hull, C.D., Fisher, R.S., Levine, M.S. and Buchwald, N.A. (1989). Dye-Coupling in the neostriatum of the rat: II. Decreased coupling between neurons during development. *Synapse*, **4**, 238–247.

Wang, Y., Gupta, A., Toledo-Rodriguez, M., Wu, C.Z. and Markram, H. (2002). Anatomical, physiological, molecular and circuit properties of nest basket cells in the developing somatosensory cortex. *Cereb. Cortex*, **12**, 395–410.

Wang, Y., Toledo-Rodriguez, M., Gupta, A., Wu, C., Silberberg, G., Luo, J. and Markram, H. (2004). Anatomical, physiological and molecular properties of Martinotti cells in the somatosensory cortex of the juvenile rat. *J. Physiol.*, **561**, 65–90.

Wang, Y., Goodfellow, M., Taylor, P.N. and Baier, G. (2012). Phase space approach for modeling of epileptic dynamics. *Phys. Rev. E*, **85**, 061918.

Wang, Z. and McCormick, D.A. (1993). Control of firing mode of corticotectal and corticopontine layer V burst-generating neurons by norepinephrine, acetylcholine, and 1S,3R-ACPD. *J. Neurosci.*, **13**, 2199–216.

Wendling, F., Bartolomei, F., Bellanger, J.J. and Chauvel, P. (2002). Epileptic fast activity can be explained by a model of impaired GABAergic dendritic inhibition. *Eur. J. Neurosci.*, **15**, 1499–1508.

White, E.L. (1989). Cortical Circuits: Synaptic Organization of the Cerebral Cortex.

White, T.P., Joseph, V., O'Regan, E., Head, K.E., Francis, S.T. and Liddle, P.F. (2010). Alpha-gamma interactions are disturbed in schizophrenia: A fusion of electroencephalography and functional magnetic resonance imaging. *Clin. Neurophysiol.*, **121**, 1427–1437.

Whittington, M.A. and Traub, R.D. (2003). Interneuron Diversity series: Inhibitory interneurons and network oscillations in vitro. *Trends Neurosci.*, **26**, 676–682.

Whittington, M.A., Traub, R.D. and Jefferys, J.G. (1995). Synchronized oscillations in interneuron networks driven by metabotropic glutamate receptor activation.

Williams, S.R. and Stuart, G.J. (2000). Backpropagation of physiological spike trains in neocortical pyramidal neurons: implications for temporal coding in dendrites. *J. Neurosci.*, **20**, 8238–46.

Wilson, H.R. and Cowan, J.D. (1972). Excitatory and inhibitory interactions in localized populations of model neurons. *Biophys. J.*, **12**, 1–24.

Wilson, H.R. and Cowan, J.D. (1973). A mathematical theory of the functional dynamics of cortical and thalamic nervous tissue. *Kybernetik*, **13**, 55–80.

Wilson, H.R. and Kim, J. (1998). Dynamics of a divisive gain control in human vision. *Vision Res.*, **38**, 2735–2741.

Wilson, N.R., Runyan, C.A., Wang, F.L. and Sur, M. (2012). Division and subtraction by distinct cortical inhibitory networks in vivo. *Nature*, **488**, 343–348.

Wolff, S.B.E., Gründemann, J., Tovote, P., Krabbe, S., Jacobson, G.A., Müller, C., Herry, C., Ehrlich, I., Friedrich, R.W., Letzkus, J.J. and Lüthi, A. (2014). Amygdala interneuron subtypes control fear learning through disinhibition. *Nature*, **509**, 453–8.

Woodruff, A.R., McGarry, L.M., Vogels, T.P., Inan, M., Anderson, S.A. and Yuste, R. (2011). State-Dependent Function of Neocortical Chandelier Cells. *J. Neurosci.*, **31**, 17872–17886.

Wright, J. and Liley, D.T.J. (1996). Dynamics of the brain at global and microscopic scales: Neural networks and the EEG. *Behav. Brain Sci.*, **19**, 285.

Xu, H., Jeong, H.Y., Tremblay, R. and Rudy, B. (2013). Neocortical Somatostatin-Expressing GABAergic Interneurons Disinhibit the Thalamorecipient Layer 4. *Neuron*, **77**, 155–167.

Xu, X., Roby, K.D. and Callaway, E.M. (2010). Immunochemical characterization of inhibitory mouse cortical neurons: Three chemically distinct classes of inhibitory cells. *J. Comp. Neurol.*, **518**, 389–404.

Yatani, A., Wakamori, M., Mikala, G. and Bahinski, A. (1993). Block of transient outward-type cloned cardiac K+ channel currents by quinidine. *Circ. Res.*, **73**, 351–359.

Yazaki-Sugiyama, Y., Kang, S., Cateau, H., Fukai, T. and Hensch, T.K. (2009). Bidirectional plasticity in fast-spiking GABA circuits by visual experience. *Nature*, **462**, 218–221.

Yeragani, V.K., Cashmere, D., Miewald, J., Tancer, M. and Keshavan, M.S. (2006). Decreased coherence in higher frequency ranges (beta and gamma) between central and frontal EEG in patients with schizophrenia: A preliminary report. *Psychiatry Res.*, **141**, 53–60.

Ylinen, A., Bragin, A., Nádasdy, Z., Jandó, G., Szabó, I., Sik, A. and Buzsáki, G. (1995). Sharp wave-associated high-frequency oscillation (200 Hz) in the intact hippocampus: network and intracellular mechanisms. *J. Neurosci.*, **15**, 30–46.

Zhang, M., Ladas, T.P., Qiu, C., Shivacharan, R.S., Gonzalez-Reyes, L.E. and Durand, D.M. (2014). Propagation of epileptiform activity can be independent of synaptic transmission, gap junctions, or diffusion and is consistent with electrical field transmission. *J. Neurosci.*, **34**, 1409–19.

Zhu, Y., Stornetta, R.L. and Zhu, J.J. (2004). Chandelier Cells Control Excessive Cortical Excitation : Characteristics of Whisker-Evoked Synaptic Responses of Layer 2 / 3 Nonpyramidal and Pyramidal Neurons. *New York*, **24**, 5101–8.

Zuckermann, E.C. and Glaser, G.H. (1968). Hippocampal epileptic activity induced by localized ventricular perfusion with high-potassium cerebrospinal fluid. *Exp. Neurol.*, **20**, 87–110.